# EXPERIMENTAL STUDIES OF NONLINEAR INTEGRABLE OPTICS WITH ELLIPTIC POTENTIALS

By

John Wieland

A DISSERTATION

Submitted to
Michigan State University
in partial fulfillment of the requirements
for the degree of

Physics—Doctor of Philosophy

November 26, 2025

## ABSTRACT

The stable transport of charged particle beams is the core challenge in designing and operating accelerators. The current paradigm for transverse focusing is based on quadrupole and dipole elements, described as a linear integrable Hamiltonian by Courant and Snyder. The operational limits of high intensity accelerators are often determined by collective instabilities within the beam. Nonlinear elements may be added to suppress certain forms of these collective effects, but restrict the range of stable trajectories. These shortcomings motivate extending to a nonlinear integrable system which can offer the benefits of suppressing collective instabilities without limiting the stable trajectories. Danilov and Nagaitsev proposed a novel nonlinear integrable system with elliptical potentials, which could be implemented as magnetic elements in an accelerator.

Such a system has been implemented for practical verification in the integrable optics test accelerator (IOTA), a small storage ring constructed for beam dynamics studies. Electron beam studies in IOTA treat the low-emittance beam as a macroparticle for detailed probing of the expected single particle dynamics. This dissertation details new measurements of the nonlinear integrable system relevant for practical implementation. Turn-by-turn measurements of the kicked beam responses are used for phase space reconstruction and analysis of the predicted nonlinear dynamics. The stability and aperture for various nonlinear configurations are measured with beam losses. Amplitude dependent detuning, a core figure of merit for suppressing instabilities, is measured and compared with high fidelity particle tracking simulations. The synchrotron radiation images of circulating beam allow direct measurements of the topology and lifetime in configurations where nonlinear focusing terms dominate.

## ACKNOWLEDGEMENTS

Full acknowledgements to follow in final version.

## TABLE OF CONTENTS

# CHAPTER 1

# INTRODUCTION

## 1.1 Background

Charged particle accelerators have been productive experimental tools for fundamental physics experiments, from Rutherford's use of naturally accelerated alpha particles for the discovery of the nucleus to the contemporary multinational physics collaborations centered at the Large Hadron Collider. In addition to their useful nature as tools, particle accelerators provide an interesting system to study dynamics in a controlled environment. These same dynamical studies then have direct impacts on the construction of new machines for fundamental studies. As the experiments drive increasing energy and power demands on the beams, careful control of losses becomes more important as ever smaller loss fractions exceed safety and machine protection limits.

To tackle the challenge of controlling energetic subatomic particles we first have to choose our tools. Some of the earliest "accelerator" experiments relied on energetic decay products, leveraging the weak nuclear force. This approach is quickly limited by the characteristic energies of these decays. Gravity can be easily dismissed as too weak and effectively fixed on the earth's surface. Bulk material interactions can be used to affect the path of particles, but they cannot accelerate and tend to cause significant losses. The default choice has been electromagnetic fields, dating back to early cathode ray experiments. These fields are easy to produce and control and can both steer and provide energy to charged particles. Naturally this restricts our ability to work with neutral particle beams, but this can be typically overcome with a charged primary beam to produce a neutral secondary beam as is the case in successful neutron spallation and neutrino beam facilities [30, 1].

Scaling the electrostatic fields from our early cathode ray tubes are a straightforward starting point for accelerating particles. A large voltage applied across carefully shaped electrodes can simultaneously accelerate and focus a beam. This was the guiding principle for early Van de Graaff machines like the Westinghouse atom smasher and the Cockroft-

Walton style proton sources popularly used in the mid 20th century. This approach still finds use in pelletrons and "tandem" accelerators for low energy nuclear experimentation. However, the limits of breakdown gradients quickly restrict the energy from such devices. Using an oscillating electric field is a practical approach to bypassing this in two ways. First, the gradients of oscillating fields may be much higher than static fields. Second, by selectively timing the particles to be accelerated, the particle can gain energy from the gradient at the frequency of the oscillation. There are a few ways this is currently accomplished. The first is simply physically shielding the particles from the negative gradient, as is done in the Alvarez or drift tube linear accelerator (linac) [3]. If the velocity of a traveling Electromagnetic (EM) wave is matched to that of the desired accelerated particle, the beam can always see a positive gradient and "surf" the wave. This is the approach of a traveling wave linac, typified by the original SLAC linac. Another early approach is to accelerate the particles in a single increasing field period. This is the approach of a betatron, where a ramping magnetic field generates a circular accelerating gradient until the field ramp is unsustainible. Betatrons were popular early industrial electron sources. Another approach is to adjust the path length of the beam between standing wave structures (usually called cavities) and the phase of these cavities to always arrive in a positive gradient. There are two main approaches using this technique. Either a sequence of cavities with proper phase are used sequentially, a resonant cavity linac. Or, the particles are recirculated to a cavity many times, the case with a broad variety of cyclic machines.

So far the problem of imparting energy to the particles has been given precedence, but naturally the particles must also be steered and focused for useful purposes. Here, we can consider magnetic fields as well as electric. While not possible to be used for energy gain, magnetic fields are the preferred option for steering and control. While electrostatic fields are used in some low energy applications, the proportional scaling of the force with momentum from a magnetic field pay dividends as beam energy increases and is the dominant approach for accelerator applications. We can consider then the earliest cyclic machine, the cyclotron.

This consists of a single resonant electric gap in a static perpendicular magnetic field. By properly scaling the field strength, in the nonrelatavistic approximation, the classical cyclotron frequency means that the particle will continue to cycle at the correct frequency to see a positive gradient and gain energy. As a result, a modest field on the gap seen many times can result in a significant energy gain for the beam. The trade off is that now we have a periodic system which must support stable motion in the plane transverse to the direction of acceleration. This is not unique to cyclic machines, but the stability conditions are less stringent in linear machines, as they are one pass.

The energy limitations imposed by the relativistic effects in fixed field cyclotrons straightforwardly motivated ramping the magnetic field in time with the nominal energy to produced a fixed reference trajectory. This breaks the isochronous condition and introduces a synchronous frequency for a given design energy. The resulting "synchrotrons" represent the current standard in high-energy accelerators, holding the absolute beam energy record since the late 60's. Advantages in alternating gradient focusing and later separated function magnets resulted in greatly reduced beam sizes and increased control over the dynamics. However, as intensities and energies increased, the requirements on the beam control increased commensurately. These conditions require close control of chromaticity and the working point to suppress certian collective instabilities. Additional elements to provide for Landau damping to suppress general collective instabilities all add nonlinear perturbations which serve to limit the stable region of dynamics. In high intensity machines, self forces in the form of space charge serve to significantly perturb the dynamics and increase vulnerability to parametric resonances. These shortcomings have long motivated searches for nonlinear integrable focusing systems in accelerators. Such a potential has been implemented at the Integrable Optics Test Accelerator (IOTA). This thesis describes the system, and presents experimental results on studies of the practicality of the nonlinear focusing system.

## 1.2 General Beamline Hamiltonian

The problem of system stability is of course not unique to accelerators and has a long history of study for dynamical systems. Accordingly, we can construct a Hamiltonian of the system. To evaluate the inherent stability of the system, we will construct the Hamiltonian for a single particle in external confining potentials in two dimensions. Notably, this does not include the self fields of the particle, or of the interactions of many particles in a beam. We are specifically interested in a Hamiltonian which describes a relativistic particle in electromagnetic fields. This results in the general Hamiltonian 1.1 where $\Phi$ and $\vec{A}$ are the typical scalar and vector potentials related to the electric and magnetic fields by 1.2

$$H_{EM} = E_\Phi = c\sqrt{(\vec{P} - q\vec{A}) + m^2c^2} + q\Phi \tag{1.1}$$

$$\begin{aligned} \vec{E} &= -\nabla\Phi - \frac{\partial \vec{A}}{\partial t} \\ \vec{B} &= \nabla \times \vec{A} \end{aligned} \tag{1.2}$$

Here the canonical momentum $\vec{P}$ is related to the mechanical momentum by 1.3

$$\vec{P} = \gamma m\vec{v} - q\vec{A} \tag{1.3}$$

And this Hamiltonian is then the total energy of the particle including the contribution from the scalar potential, I will call this $E_\Phi$ to differentiate it from the total energy in the absence of the scalar potential.

The presented derivations for the equations of motion are based on the tradition of the solution found in [17], and generally follow the approach outlined in [64] with some elements from [39]. We would like to refine this expression by changing to a simpler local coordinate system. When studying the dynamics of a particle accelerator, it is useful to investigate the motion of the particles with respect to some reference trajectory rather than their absolute coordinates in the lab frame. To start with, we adopt a Frenet-Serret (Fig.

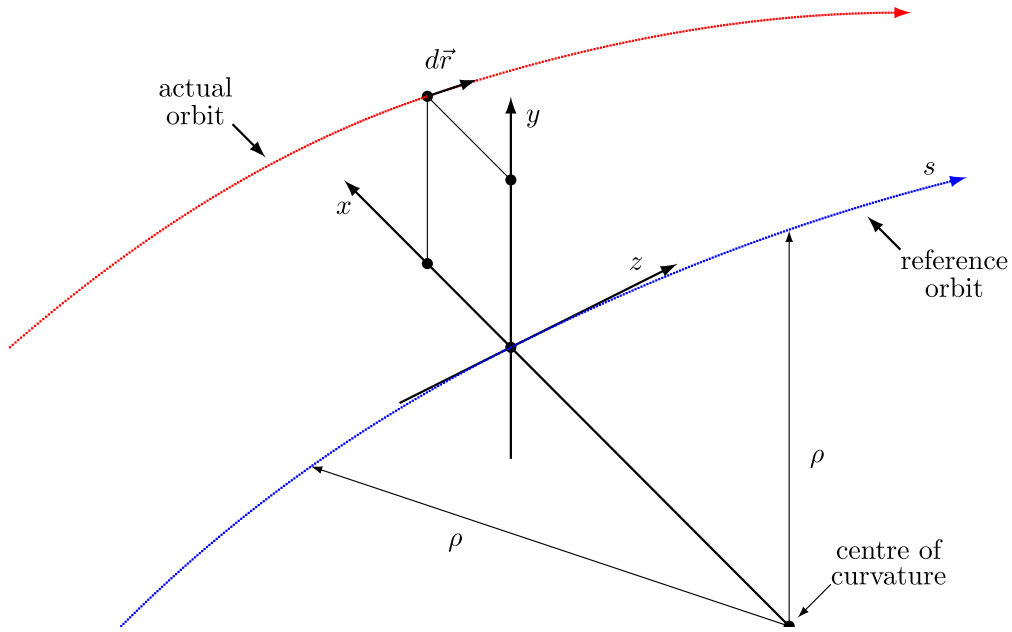


Figure 1.1 Illustration of Frenet-Serret style Coordinate System From MAD-X Documentation [22]

1.1) coordinate system where the coordinate axes are defined with respect to a tangent vector of an arbitrary curved path. In the case of many accelerator systems, the situation is simpler than this. In practice, bending is only in a single plane, typically horizontal in the lab frame. Additionally, if bending is only generated from the motion of charged particles in a static magnetic field, the bent path will be circles of a characteristic bending radius $\rho$. The result of this transformation only ends up modifying the momentum along the curved trajectory by a factor of $1 + \frac{x}{\rho}$ and gives us the Hamiltonian $H_{f.s.}$ in 1.4. This coordinate transformation does not affect the value of the Hamiltonian, so it is still equivalent to the total energy of the test particle with the scalar field contribution. In general, this is the case for transfer lines, linacs, synchrotrons and storage rings. There are other style machines, such as cyclotrons and fixed field alternating gradient accelerators which demand a different treatment of the dynamics, but are beyond the scope of this dissertation.

$$H_{f.s.} = E_\Phi = c\sqrt{\left(\frac{p_s}{1 + x/\rho} - qA_s\right)^2 + (P_x - qA_x)^2 + (P_y - qA_y)^2 + m^2c^2} + q\Phi \qquad (1.4)$$

Since an accelerator is composed of sequential elements along this reference trajectory, it

is useful to change the independent variable to the spacial coordinate along the trajectory. Inspecting the form of the action shows that to change from $t$ as the independent variable to $s$ requires a new Hamiltonian of the form $H_s(x, p_x, y, p_y, t, -E_\Phi; s) = -p_s$. We can then simply rearrange Eq. 1.4 to arrive at Eq. 1.5.

$$H_s = -\left(1+\frac{x}{\rho}\right)\sqrt{\left(\frac{E_\Phi - q\Phi}{c}\right)^2 - (P_x - qA_x)^2 - (P_y - qA_y)^2 - m^2c^2} - \left(1+\frac{x}{\rho}\right)qA_s \quad (1.5)$$

There is one more coordinate transformation we would like to make. Currently, our longitudinal canonical coordinate is absolute position alont the Frenet-Serret trajectory, which will increase quickly along the beam line and become cumbersome. We would like to define the position of the beam with respect to some reference particle, which has the ideal quantities we would like in our accelerated beam. Correspondingly, we define a particle on our reference trajectory with a momentum $p_o$ (Eq.1.6) directed along the reference trajectory.

$$p_o = \beta_o \gamma_o mc \quad (1.6)$$

We can then scale the overall Hamiltonian by this reference momentum in Eq. 1.7. The equations of motion are still satisfied with the inclusion of the already substituted variable changes in Eq. 1.8.

$$H_p = \frac{H_s}{p_o} = -\left(1+\frac{x}{\rho}\right)\frac{q}{p_o}A_s - \left(1+\frac{x}{\rho}\right)\sqrt{\left(\frac{\tilde{E}_\Phi - \frac{q}{p_o}\Phi}{c}\right)^2 - \left(p_x - \frac{q}{p_o}A_x\right)^2 - \left(p_y - \frac{q}{p_o}A_y\right)^2 - \frac{m^2c^2}{p_o^2}} \quad (1.7)$$

$$
\begin{aligned}
p_x &= \frac{P_x}{p_o} \\
p_y &= \frac{P_y}{p_o} \\
\tilde{E_\Phi} &= \frac{E_\Phi}{p_o}
\end{aligned}
\tag{1.8}
$$

The last coordinate transformation we will make is to shift the longitudinal position of the test particle with respect to our reference particle. Using a generating function of the form Eq. 1.9.

$$
G_2(x, p_x, y, p_y, t, p_t; s) = xp_x + yp_y + \left(ct - \frac{s}{\beta_o}\right)\left(p_t - \frac{1}{\beta_o}\right) \tag{1.9}
$$

The $x, y$ coordinates are not affected by the transformation, but we have the following new longitudinal coordinates in Eq. 1.10. Here we follow the direction convention chosen in ImpactX as it will be the native coordinate system for our simulation results later on.

$$
\begin{aligned}
\tilde{ct} &= ct - \frac{s}{\beta_o} \\
\tilde{p_t} &= \frac{1}{\beta_o} - \frac{\tilde{E_\Phi}}{c} \\
\tilde{H_p} &= H_p - \frac{\tilde{p_t}}{\beta_o} + \frac{1}{\beta_o^2}
\end{aligned}
\tag{1.10}
$$

After substitution and removing the constant $\frac{1}{\beta_o^2}$ term, we have the Hamiltonian in Eq. 1.11

$$
\begin{aligned}
H_A = &- \left(1 + \frac{x}{\rho}\right)\frac{q}{p_o}A_s - \frac{\tilde{p_t}}{\beta_o} \\
&- \left(1 + \frac{x}{\rho}\right)\sqrt{\left(\frac{1}{\beta_o} - \tilde{p_t} - \frac{q}{p_o c}\Phi\right)^2 - \left(p_x - \frac{q}{p_o}A_x\right)^2 - \left(p_y - \frac{q}{p_o}A_y\right)^2 - \frac{m^2c^2}{p_o^2}}
\end{aligned}
\tag{1.11}
$$

We then have arrived at the general Hamiltonian for a particle along our reference trajectory with respect to a nominal reference particle in arbitrary electromagnetic fields.

From here, we now need to decide on which fields to apply to our particle for stable acceleration. We are interested in representing the basic accelerator components, i.e. transverse magnets and radiofrequency cavities. For this case, we can take $\Phi, A_x, A_y = 0$, which yields the Hamiltonian in 1.12. Components that do not meet these conditions, like a solenoid, can be treated analogously to the following approach, but are omitted for brevity.

$$H = -\left(1 + \frac{x}{\rho}\right)\sqrt{\left(\frac{1}{\beta_o} - p_t\right)^2 - p_x^2 - p_y^2 - \frac{m^2c^2}{p_o^2}} - \frac{p_t}{\beta_o} - \left(1 + \frac{x}{\rho}\right)\frac{q}{p_o}A_s \tag{1.12}$$

With the scalar potential set to zero, we arrive at a common set of canonical coordinates used for studies of accelerator dynamics (Eq. 1.13). The relevant difference here from our coordinates above is that now the longitudinal momentum $p_t$ is the difference in the relativistic energy (Eq. 1.14) of the test and reference particle. These definitions are now completely consistent with those used in ImpactX. The longitudinal spacial coordinate $\tilde{ct}$ (the time of arrival difference scaled by speed of light) will retain the scaling parameter to remind its dimensinality is length, but will be reffered to as $ct$ without the tilde for consistency with plotting moving forward.

$$\begin{aligned} x &= x \\ p_x &= \frac{P_x}{p_o} \\ y &= y \\ p_y &= \frac{P_y}{p_o} \\ ct &= c(t - t_o) \\ p_t &= \frac{E_o - E}{p_o c} \end{aligned} \tag{1.13}$$

$$E = \gamma mc^2 \Rightarrow E_o = \gamma_o mc^2 \tag{1.14}$$

There are two prominent alternative coordinate definitions in use. The first is an alternative longitudinal coordinate parameterization using the difference in momentum instead of

energy, usually called $\delta$, which also changes the longitudinal coordinate definition to spacial offset. The relationship between these coordinates and the coordinates in Eq. 1.13 is given in Eq. 1.15 and expanded upon in Appendix A.

$$\begin{aligned} \delta &= \frac{p - p_o}{p_o} = \sqrt{p_t^2 - \frac{2}{\beta_o} p_t + 1} - 1 \approx -\frac{p_t}{\beta_o} \\ z &= ct \frac{\sqrt{\beta_o^2 + \beta_o^2 p_t^2 - 2\beta_o p_t}}{\beta_o p_t - 1} \approx -\beta_o ct \end{aligned} \tag{1.15}$$

The other coordinate convention which deserves mention is the use of $x' = \frac{dx}{ds}$. This is an easy to understand coordinate, but it is in general non-canonical and so is avoided in our Hamiltonian-based approach. This value converges with our definition of $p_x$ in the ultrarelatavistic case.

Recognizing $\frac{m^2c^2}{p_o^2} = \frac{1}{\beta_o^2 \gamma_o^2}$ we can make one more simplification now that $\Phi = 0$, giving us the Hamiltonian in Eq. 1.16.

$$H = -\left(1 + \frac{x}{\rho}\right) \sqrt{1 + p_t^2 - \frac{2p_t}{\beta_o} - p_x^2 - p_y^2} - \frac{p_t}{\beta_o} - \left(1 + \frac{x}{\rho}\right) \frac{q}{p_o} A_s \tag{1.16}$$

The exact form of $A_s$ must now be selected to find our equations of motion. Before we do so, we will consider the general form of this expansion we are interested in.

### 1.3 Multipole Expansion

To determine the fields used, we first consider what is convenient to generate. In general, a beam typically needs an evacuated beam pipe to travel in, so we would like to consider magnetic fields that we generate outside of a region of beam travel. As a result, we can consider a series solution for Laplace's equations for magnetic fields in two dimensions for a region with periodic cylindrical boundary conditions, Eq. 1.17

$$\begin{aligned} B_r(r, \theta) &= \sum_{n=1}^{\infty} \tilde{A}_n(z) \, (r)^{n-1} \sin(n\theta) \\ B_\theta(r, \theta) &= \sum_{n=1}^{\infty} \tilde{B}_n(z) \, (r)^{n-1} \cos(n\theta) \end{aligned} \tag{1.17}$$

We can apply an alternative combined representation with complex variables introduced by Beth [10] 1.18. There are two different conventions for numbering the multipole orders. The convention used in this thesis is the "European" convention, the "US" convention shifts down the multipole term by an integer so the exponent simply becomes the summation variable.

$$B_\theta + iB_r = \sum_{n=1}^{\infty} C_n(z) e^{in\theta} (r)^{n-1} \tag{1.18}$$

Using the substitutions in Eq. 1.19 we can convert the field representation to Cartesian coordinates in Eq. 1.20. Then, this can be matched to our Hamiltonian coordinates.

$$\begin{aligned} B_\theta + iB_r &= (B_y + iB_x)e^{i\theta} \\ re^{i\theta} &= x + iy \end{aligned} \tag{1.19}$$

$$B_y + iB_x = \sum_{n=1}^{\infty} C_n(z)(x + iy)^{n-1} \tag{1.20}$$

The term $C_n(z)$ contains the multipole terms, and is in general a complex quantity with real "normal" and complex "skew" terms. The skew fields end up being the normal fields rotated by a factor of $\frac{\pi}{2n}$ for a given order. Figure 1.2 shows the first few multipole fields, both normal and skew. As there are no magnetic monopoles, each multipole term represents another radially symmetric addition of a pair of north and south poles. The multipole terms are named according to a mix of Latin and Greek numeric prefixes, $n = 1$ is dipole, $n = 2$ is quadrupole, $n = 3$ is a sextupole etc.

Of course, the three dimensional consequence of Gauss's law mean that the magnetic field extends beyond the length of the pole, and has a nonlinear falloff along the beam path. However, In practice we are typically only concerned with the effective integral of the field, the length of the magnets and the fringe field especially are usually short compared to the characteristic wavelengths of the betatron motion and only become relevant in large aperture magnets with long fringing fields. We can then exclude the $z$ dependence of our multipole

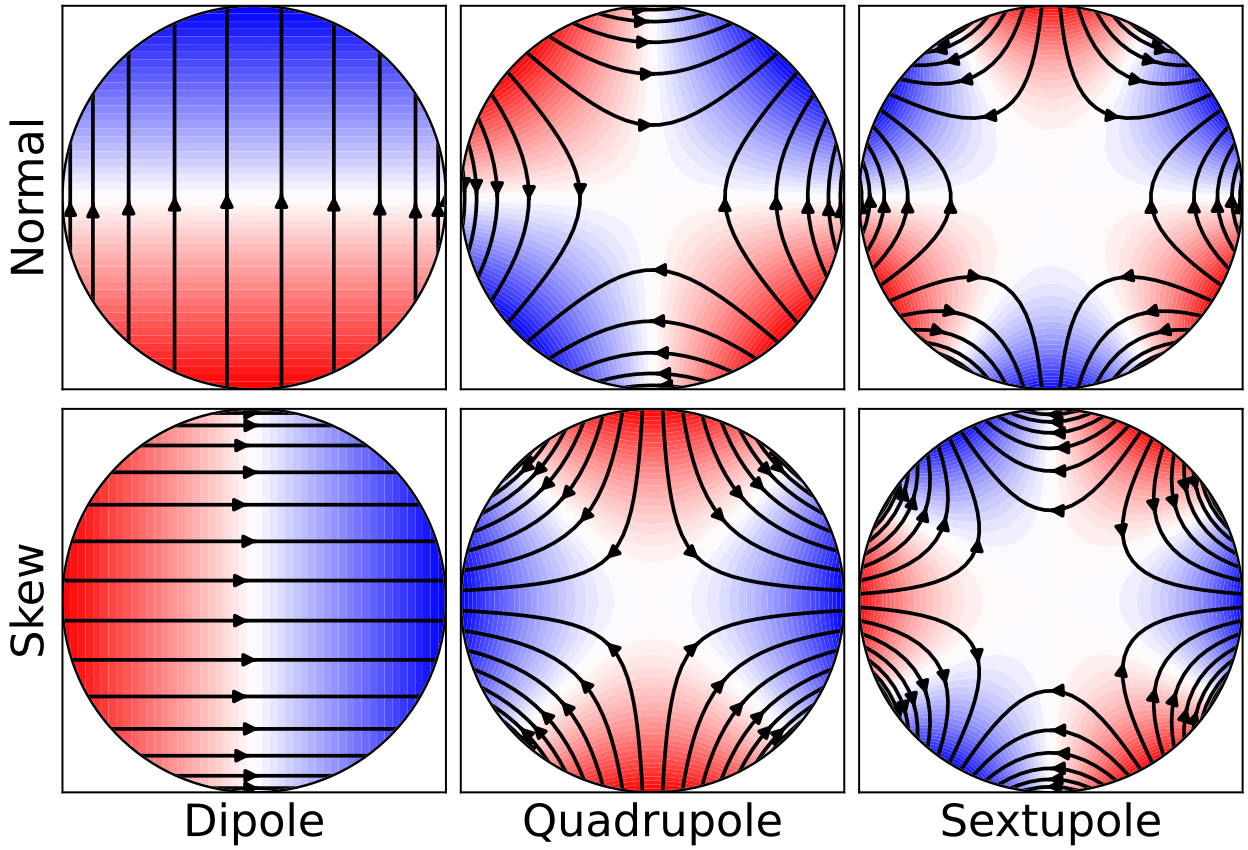


Figure 1.2 First three multipoles

terms and arrive at the general definition for our two dimensional multipole expansion in Eq. 1.21. Here, the $B_n$ terms are the normal components and the $A_n$ terms are skew.

$$B_y + iB_x = \sum_{n=1}^{\infty}(B_n + iA_n)(x + iy)^{n-1} \tag{1.21}$$

There are a few different parameterizations of this multipole expansion including reference radii and reference fields. We will only consider scaling to our magnetic rigidity in Eq. 1.22.

$$B\rho = \frac{p_o}{q} \tag{1.22}$$

This is a useful quantity which indicates the effect of fields on a particle irrelevant of species. For a given fixed magnetic field, the radius of the characteristic circle of its motion is given by the rigidity over the field strength. So, a high rigidity particle will be bent less than a low rigidity particle in the same field. We can then define a multipole scaling to this

rigidity in Eq. 1.23. We will only consider normal terms in the derivations later, but the same approach can be done for skew terms.

$$k_n = \frac{B_n}{B\rho} \tag{1.23}$$

This expansion has been about a straight reference path which contrasts with our earlier transformation to the Frenet-Serret frame. There do exist treatments of multipoles defined in a curved reference frame [68], but this is of relatively minor concern. In practice, we can see that our dipole magnet is the only term which results in bending of the reference trajectory. So, these curved trajectory cases only are relevant inside an element with a deliberate dipole term. This brings up the notion of separated and combined function machines. The first generation of machines used a fixed magnetic field for the entire radius, sometimes with short gaps for injection and extraction. Vertical focus either relied on the field falloff due to realistic magnet construction, or a deliberately added gradient to the median plane, effectively a mixed dipole and quadrupole term in our multipole expansion. First generation alternating gradient accelerators kept this approach, simply implementing two types of "combined function" magnets with consistent dipole terms and alternating quadrupole terms for much stronger net focusing. It quickly became clear that it was preferable to separate the bending and focusing components of the fields for greater flexibility in design. As a result, most modern machines exhibit bending only in pure dipole magnets and higher order fields are placed in straight sections. Combined function magnets are typically used when particular cost or space concerns renders them more practical.

An additional consideration for the dipole fields is the incident angle on the element. There are two broad approaches, a rectangular bending magnet, and a sector bend. The sector bend has poles with faces perpendicular to the direction of travel. Without this, there is effective focusing based on the longer and shorter path lengths in the constant field depending on the initial horizontal coordinate. Figure 1.3 shows the difference between a sector and rectangular dipole magnet. This can be exploited for focusing effects as was done

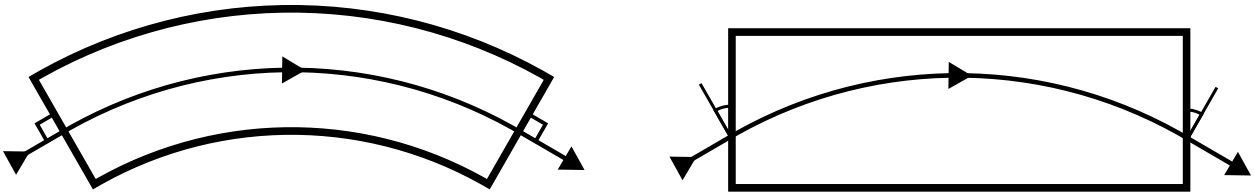

Figure 1.3 Sector and Rectangular bending dipoles

in the Zero Gradient Synchrotron, but is not relevant for the content of this these as all dipoles considered are sector bends.

For the purposes of evaluating our Hamiltonian, we can then represent the vector potential with respect to the multipole expansion terms in Eq. 1.24.

$$A_s = -\mathbb{R}\left[\sum_{n=1}^{\infty} \frac{B_n + iA_n}{n}(x+iy)^n\right] \tag{1.24}$$

### 1.4 Linearized Hamiltonian

Based on the form of the multipole expansion, we can see that only our dipole and quadrupole elements will affect the dynamics to the first order. While in general, we can use potentials of any order, we are not guaranteed an analytical solution. The first order solutions to the equations of motion are possible to find analytically and will serve as the foundation for our dynamical analysis moving forward.

We will look for a solution to the equations of motion for a static quadrupole field. This has the vector potential in Eq. 1.25.

$$A_s = -\frac{B_2}{2}(x^2 - y^2) \tag{1.25}$$

We also have no bending of the reference trajectory here, so $\rho \to \infty$. Recalling our relationship for the rigidity $B\rho = \frac{p_o}{q}$, the resulting Hamiltonian is Eq. 1.26

$$H = -\sqrt{1 + p_t^2 - \frac{2p_t}{\beta_o} - p_x^2 - p_y^2} - \frac{p_t}{\beta_o} + \frac{k_2}{2}(x^2 - y^2) \tag{1.26}$$

We will now make the first big assumption towards our solution. If we expand the square root term in the Hamiltonian and truncate to lowest order in the dynamical variables (Eq. 1.27) we are making the paraxial approximation. The argument is that since our canonical momentum coordinates are all defined as a ratio with respect to the reference particle, when it is relativistic, the motion of these particles is all nearly parallel and these quantities are small, so higher orders can safely be ignored. Naturally, this assumption breaks down for low energy beams, but is generally good for most practical accelerators.

$$\sqrt{1 + p_t^2 - \frac{2p_t}{\beta_o} - p_x^2 - p_y^2} \Rightarrow 1 - \frac{p_t^2}{2\beta_o^2\gamma_o^2} - \frac{p_t}{\beta_o} - \frac{p_x^2}{2} - \frac{p_y^2}{2} + O(3) \tag{1.27}$$

Resubstituting and dropping the constant factor, we arrive at the Hamiltonian in Eq. 1.28

$$H = \frac{p_x^2}{2} + \frac{p_y^2}{2} + \frac{p_t^2}{2\beta_o^2\gamma_o^2} + \frac{k_2}{2}(x^2 - y^2) \tag{1.28}$$

Note that the resulting Hamiltonian has no mixed terms, so the equations of motion are naturally separated into the different dimensions. This is in part due to our selection of external field, if we selected a skew quadrupole the transverse dimensions would be coupled. We can see that any static, non-bending, multipole field will not result in any coupling to the longitudinal dimensions in the paraxial approximation. For the quadrupole, the most relevant effect is the effective field for different momentum, the transverse "Chromaticity" in analogy to light optics. This is properly treated at higher orders, but we will first resolve this to lowest order. Applying Hamilton's equations of motion gives us three systems of linear differential equations.

$$\begin{aligned} \frac{dx}{ds} &= p_x \\ \frac{dp_x}{ds} &= -k_2 x \end{aligned} \tag{1.29}$$

Substituting and rearranging we arrive at Hills equation, Eq. 1.30

$$\frac{d^2x}{ds^2} + k_2 x = 0 \tag{1.30}$$

Which has three general solutions for different ranges of $k_2$.

$$x(s) = a\cos\left(\sqrt{k_2}s\right) + b\sin\left(\sqrt{k_2}s\right), \qquad k_2 > 0 \tag{1.31}$$

$$x(s) = as + b, \qquad k_2 = 0 \tag{1.32}$$

$$x(s) = a\cosh\left(\sqrt{k_2}s\right) + b\sinh\left(\sqrt{k_2}s\right), \qquad k_2 < 0 \tag{1.33}$$

For a quadrupole of a given length $L$, we can define a matrix Eq. 1.34 which represents the three linear solutions for our different dimensions if it acts on a state vector of our canonical coordinates.

$$\mathrm{M}_{quad} = \begin{pmatrix} \cos\left(\sqrt{k_2}L\right) & \frac{1}{\sqrt{k_2}}\sin\left(\sqrt{k_2}L\right) & 0 & 0 & 0 & 0 \\ -\sqrt{k_2}\sin\left(\sqrt{k_2}L\right) & \cos\left(\sqrt{k_2}L\right) & 0 & 0 & 0 & 0 \\ 0 & 0 & \cosh\left(\sqrt{k_2}L\right) & \frac{1}{\sqrt{k_2}}\sinh\left(\sqrt{k_2}L\right) & 0 & 0 \\ 0 & 0 & \sqrt{k_2}\sinh\left(\sqrt{k_2}L\right) & \cosh\left(\sqrt{k_2}L\right) & 0 & 0 \\ 0 & 0 & 0 & 0 & 1 & \frac{L}{\beta_o^2\gamma_o^2} \\ 0 & 0 & 0 & 0 & 0 & 1 \end{pmatrix} \tag{1.34}$$

The same approach can be applied to our other separated function, first order elements in the paraxial approximation, for a drift space (Eq. 1.35) and a sector dipole magnet (Eq. 1.36).

$$\mathrm{M}_{drift} = \begin{pmatrix} 1 & L & 0 & 0 & 0 & 0 \\ 0 & 1 & 0 & 0 & 0 & 0 \\ 0 & 0 & 1 & L & 0 & 0 \\ 0 & 0 & 0 & 1 & 0 & 0 \\ 0 & 0 & 0 & 0 & 1 & \frac{L}{\beta_o^2 \gamma_o^2} \\ 0 & 0 & 0 & 0 & 0 & 1 \end{pmatrix} \tag{1.35}$$

$$\mathrm{M}_{dipole} = \begin{pmatrix} \cos\left(\frac{L}{\rho}\right) & \rho \sin\left(\frac{L}{\rho}\right) & 0 & 0 & 0 & -\frac{\rho}{\beta_o}\left(1 - \cos\left(\frac{L}{\rho}\right)\right) \\ -\frac{1}{\rho}\sin\left(\frac{L}{\rho}\right) & \cos\left(\frac{L}{\rho}\right) & 0 & 0 & 0 & -\frac{1}{\beta_o}\sin\left(\frac{L}{\rho}\right) \\ 0 & 0 & 1 & L & 0 & 0 \\ 0 & 0 & 0 & 1 & 0 & 0 \\ \frac{1}{\beta_o}\sin\left(\frac{L}{\rho}\right) & \frac{\rho}{\beta_o}\left(1 - \cos\left(\frac{L}{\rho}\right)\right) & 0 & 0 & 1 & \frac{\rho}{\beta_o^2}\sin\left(\frac{L}{\rho}\right) - L \\ 0 & 0 & 0 & 0 & 0 & 1 \end{pmatrix} \tag{1.36}$$

Note that the dipole preserves coupling between the longitudinal and horizontal planes at the first order, unlike the quadrupole. This gives rise to first order dispersion, or longitudinally dependent energy coupling in the horizontal motion.

These solutions are quite powerful, as they let us stack linear transformations in a row to construct mathematical representations of a transfer line. There is an additional advantage to this form, since the equations of motion were derived from the Hamiltonian of our system, we are guaranteed that these transformations are symplectic. Formally, a "symplectic form is a two-form which is closed and nondegenerate" [34]. More usefully in a physics context, a symplectic transformation is one which is guaranteed to preserve our physical quantities, such as total energy. A sequence of symplectic mappings is also symplectic, so we can be certain that any sequence of our above matrix elements will maintain the symplectic condition. Symplecticity is a rich topic in the context of dynamical systems, but beyond the

scope of this thesis, the author recommends the following references for further edification [26, 65].

### 1.5 Courant-Snyder Parameterization

While the transformations we have acquired are generally applicable, we would like to evaluate the conditions for a stable periodic system like we need for a cyclic machine. At this point we will make another simplification of the dynamics by investigating the stability of the transverse and longitudinal dimensions separately. This is of course not strictly true, but the characteristic timescales of synchrotron oscillations are often orders of magnitude slower than the transverse oscillations. We will choose the horizontal $x$ motion to investigate. Analogous methods can be used for the $y$ plane.

We begin with defining a matrix of a periodic "cell" (Eq. 1.37), or sequence of elements $\mathrm{M}_1 \ldots \mathrm{M}_n$ with total length $L$. This could be the representation of a whole cyclic accelerator, or smaller sequence of elements intended for a superperiodic construction.

$$\mathbb{M}(s) = \mathrm{M}(s_o + L|s_o) = \mathrm{M}_n\mathrm{M}_{n-1}\ldots\mathrm{M}_2\mathrm{M}_1 \tag{1.37}$$

Our periodic condition then becomes that motion is bounded for repeated applications of this matrix. The solutions to Hill's equations (including the dipole case where longitudinal coupling is excluded) yield matrices with a determinant of one. As the determinant of a product of matrices is the product of their individual determinants, we know that the determinant of our particular cell must be 1. If we decompose $\mathbb{M}$ into eigenvalues $\lambda_1, \lambda_2$ and eigenvectors $\vec{v}_1, \vec{v}_2$, the unit determinant leads to two useful relationships. First $\lambda_1 + \lambda_2 = \mathrm{Trace}(\mathbb{M})$, and second $\lambda_1 = 1/\lambda_2$. Substituting and rearranging yields Eq. 1.38.

$$\lambda_1^2 - \mathrm{Trace}(\mathbb{M})\lambda_1 + 1 = 0 \tag{1.38}$$

If we describe a canonical state vector as a linear combination of our eigenvectors, we can get a straightforward requirement on our eigenvalues with repeated application of the transfer map (Eq. 1.39).

$$\vec{q_n} = \mathbb{M}^n \vec{q_o} = \mathbb{M}^n (a\vec{v}_1 + b\vec{v}_2) = a\lambda_1^n \vec{v}_1 + b\lambda_2^n \vec{v}_2 \tag{1.39}$$

This relationship clearly demonstrates that for stable long term motion, these eigenvalues cannot grow with repeated iterations. Courant and Snyder proposed the following general parameterization of our transfer matrix in Eq. 1.40, consisting of "Lattice functions" $\alpha_x, \beta_x, \gamma_x$ and phase advance $\phi_x$.

$$\mathbb{M}_{CS} = \begin{pmatrix} \cos(\phi_x) + \alpha_x \sin(\phi_x) & \beta_x \sin(\phi_x) \\ -\gamma_x \sin(\phi_x) & \cos(\phi_x) - \alpha_x \sin(\phi_x) \end{pmatrix} \tag{1.40}$$

If we calculate the trace of this parameterization and substitute into Eq. 1.38, we find values of the eigenvalues to be Eq. 1.41

$$\begin{aligned} \lambda_1 &= e^{i\phi_x} \\ \lambda_2 &= e^{-i\phi_x} \end{aligned} \tag{1.41}$$

Where $\phi_x$ is complex if $|\text{Trace}(\mathbb{M})| > 2$ and real if $|\text{Trace}(\mathbb{M})| < 2$. We can see from Eq. 1.39, our motion is only bounded for real values of $\phi_x$ and our stability condition for a periodic transfer matrix $\mathbb{M}$ becomes $|\text{Trace}(\mathbb{M})| < 2$.

By leveraging the fact that the periodic linearized equations of motion have a determinant of 1, we can arrive at the relationship in Eq. 1.42. We can also see from the Courant-Snyder parameterization Eq. 1.43 holds for any stable transfer matrix. This defines the fractional component of $\phi_x$, but leaves it ambiguous to integer multiples of $2\pi$. In practice, the ambiguity can be cleared up by calculating this parameter for individual constituents of the periodic transfer matrices.

$$\beta_x \gamma_x = 1 + \alpha_x^2 \tag{1.42}$$

$$\cos(\phi_x) = \text{Trace}(\mathbb{M}) \tag{1.43}$$

We can further investigate the form of these parameters by splitting the general periodic matrix, in Eq. 1.44, where the matrix "A" and "S" are given in Eq. 1.45. "S" is a block antisymmetric matrix, and reduces to just the antisymmetric matrix in two dimensions like we have here.

$$\mathbb{M}_{CS} = \mathrm{I}\cos(\phi_x) + \mathrm{SA}\sin(\phi_x) \tag{1.44}$$

$$\mathrm{A} = \begin{pmatrix} \gamma_x & \alpha_x \\ \alpha_x & \beta_x \end{pmatrix}, \quad \mathrm{S} = \begin{pmatrix} 0 & 1 \\ -1 & 0 \end{pmatrix}, \quad \mathrm{I} = \begin{pmatrix} 1 & 0 \\ 0 & 1 \end{pmatrix} \tag{1.45}$$

Within our periodic cell $\mathbb{M}$, we can consider the transformation in Eq. 1.46 by some transfer matrix in the cell which moves the overall start point. By examining the trace of this transformation, we can see that $\phi_x$ of our periodic matrix is unchanged by this shift in start point.

$$\mathbb{M}(s_1) = \mathrm{M}(s_1|s_o)\mathbb{M}(s_o)\mathrm{M}(s_1|s_o)^{-1} \tag{1.46}$$

If we apply this transformation to 1.44, as $\phi_x$ unadjusted by the shift, the overall effect is summarized in Eq. 1.47.

$$SA(s_1) = M(s_1|s_o)SA(s_o)M(s_1|s_o)^{-1} \tag{1.47}$$

We can now leverage the underlying symplecticity of our transfer matrices, which mandates the condition in Eq. 1.48.

$$\mathrm{M}^T\mathrm{SM} = \mathrm{S} \tag{1.48}$$

Recognizing that $\mathrm{S}^T = \mathrm{S}^{-1}$ and using the symplectic condition, we can rearrange and invert Eq. 1.47 to arrive at the transformation of $\mathrm{A}^{-1}$ at different points in the cell in Eq. 1.49.

$$A(s_1)^{-1} = M(s_1|s_o)A(s_o)^{-1}M(s_1|s_o)^T \tag{1.49}$$

After inverting "A" we can solve Eq. 1.49 for the transformation of our Courant-Snyder parameters $\beta_x, \alpha_x, \gamma_x$ with respect to the components of the transfer matrix "M" in Eq. 1.50.

$$\begin{pmatrix} \beta_x(s_1) \\ \alpha_x(s_1) \\ \gamma_x(s_1) \end{pmatrix} = \begin{pmatrix} M_{11}^2 & -2M_{11}M_{12} & M_{12}^2 \\ -M_{11}M_{21} & M_{11}M_{22} + M_{12}M_{21} & -M_{12}M_{22} \\ M_{21}^2 & -2M_{21}M_{22} & M_{22}^2 \end{pmatrix} \begin{pmatrix} \beta_x(s_o) \\ \alpha_x(s_o) \\ \gamma_x(s_o) \end{pmatrix} \tag{1.50}$$

This is a useful result, as it means for any stable, periodic, sequence of our linear beamline elements, we can uniquely define the Courant-Snyder parameters and transfer them to any other point in the lattice. The result in 1.50 is even useful without a periodic system, as the effective lattice parameters of a known initial beam distribution (described later in this section) can be transformed along a sequence of linear elements for a linac or transfer line.

We would now like to find the equations of motion for this parameterization. We can construct an invariant action for our canonical coordinates and Courant-Snyder parameters.

$$J = \frac{1}{2}(\vec{q}_x)^T \mathrm{A}\vec{q}_x = \frac{1}{2}(\gamma_x x^2 + 2\alpha_x x p_x + \beta_x p_x^2) \tag{1.51}$$

Which we verify is invariant by inspecting the transformation of our canonical state vectors $\vec{q}_x$ and matrix "A" under a transfer matrix in Eq 1.52.

$$J(s_1) = \frac{1}{2}\vec{q}_x(s_1)^T \mathrm{A}(s_1)\vec{q}_x(s1) = \frac{1}{2}\vec{q}_x(s_o)^T \mathrm{M}^T(\mathrm{M}^T)^{-1}\mathrm{A}(s_o)\mathrm{M}^{-1}\mathrm{M}\vec{q}_x(s_o) = J(s_o) \tag{1.52}$$

Determining the angle variable with respect to the Cournant-Snyder parameters is an extended derivation which requires inspecting the general solution to Hill's equation using the Floquet transform in comparison with the current periodic condition. This would be longer than the entire derivation of the Courant-Snyder parameters up to this point, so it

is omitted here and only the important results are quoted. First, is the relationship of the angle variable $\varphi_x$ to the coordinates in eq. 1.53.

$$\tan(\varphi_x) = -\beta_x \frac{x}{p_x} - \alpha_x \tag{1.53}$$

Second, the relationship to the $\beta_x$ parameter, to the focusing term $K(s)$ in Eq. 1.54. Here $K(s)$ is a stand in for all of our Hill's equation conditions, both focusing and defocusing and the weak focusing effect from dipoles.

$$\begin{aligned} &\frac{d^2}{ds^2}\sqrt{\beta_x(s)} + K(s)\sqrt{\beta_x(s)} = \frac{1}{\sqrt{\beta_x^3(s)}} \ \ or, \\ &\frac{\beta_x(s)}{2}\frac{d^2\beta_x(s)}{ds^2} - \frac{1}{4}\left(\frac{d\beta_x(s)}{ds}\right)^2 + K(s)\beta_x^2(s) = 1 \end{aligned} \tag{1.54}$$

Third we can recognize an additional relationship between the $\alpha_x$ and $\beta_x$ functions in Eq. 1.55

$$\alpha_x(s) = -\frac{1}{2}\frac{d\beta_x(s)}{ds} \tag{1.55}$$

Finally we can relate the angle variable to the $\beta_x$ function (Eq. 1.56) and our phase advance $\phi_x$ (Eq. 1.57.

$$\frac{d\varphi_x(s)}{ds} = \frac{1}{\beta_x(s)} \tag{1.56}$$

$$\phi_x(s_1|s_o) = \varphi(s_1) - \varphi(s_o) \Rightarrow \phi_x(s_1|s_o) = \int_{s_o}^{s_1} \frac{1}{\beta_x(s)} ds \tag{1.57}$$

The result is that we only need the function $\beta_x(s)$ and its derivative to fully parameterize the linear motion of our single particles in an accelerator. We can further expand on this by finding the equations of motion with respect to this phase angle $\varphi_x$ by inverting Equations 1.53 and 1.52 to arrive Equations 1.58 and 1.59.

$$x = \sqrt{2\beta_x J_x}\cos(\varphi_x) \tag{1.58}$$

$$p_x = -\sqrt{\frac{2J_x}{\beta_x}}(\sin(\varphi_x) + \alpha_x \cos(\varphi_x)) \tag{1.59}$$

We can see that the combination of these equations of motion paramaterize an ellipse for our Poincaré section at any given point along the beamline. Figure 1.4 shows such an ellipse with the relevant relationship to the Courant-Snyder parameters. This graphic makes clear some useful intuitive relationships of the paramaterization. We can see that the $\beta_x$ describes the transverse envelope of motion for the lattice at a given location, and is defined to be strictly positive. The $\gamma_x$ function must also be strictly positive and parameterizes something of a "momentum envelope", though this is much less useful than the amplitude. The phase advance $\phi_x$ can be seen as sort of betatron oscillation time parameter. Regions with small beta functions, or small beam envelopes have large phase advances and represent large advances in the betatron oscillations.

The area of this ellipse is $2\pi J_x$, but is usually related to the "emittance" in Eq. 1.60 as $\pi\epsilon_x$. There is some inconsistency in application of the emittance in accelerator literature, sometimes it is only considered to be an aggregate property of a particle bunch and other times it may relate to a single particle equivalent dynamical value. I will distinguish the aggregate property as e.g. $\epsilon_{x,rms}$, defined in section 1.6, to distinguish it from the dynamical value $\epsilon_x$.

$$\epsilon_x = 2J_x \tag{1.60}$$

Based on these result we can introduce the "normalized" (they still have dimension of $\sqrt{m}$) Cournat-Snyder parameters in 1.61.

$$\begin{aligned} x_N &= \frac{x}{\sqrt{\beta_x}} \\ p_{xN} &= \frac{\alpha_x x}{\sqrt{\beta_x}} - \sqrt{\beta_x} p_x \end{aligned} \tag{1.61}$$

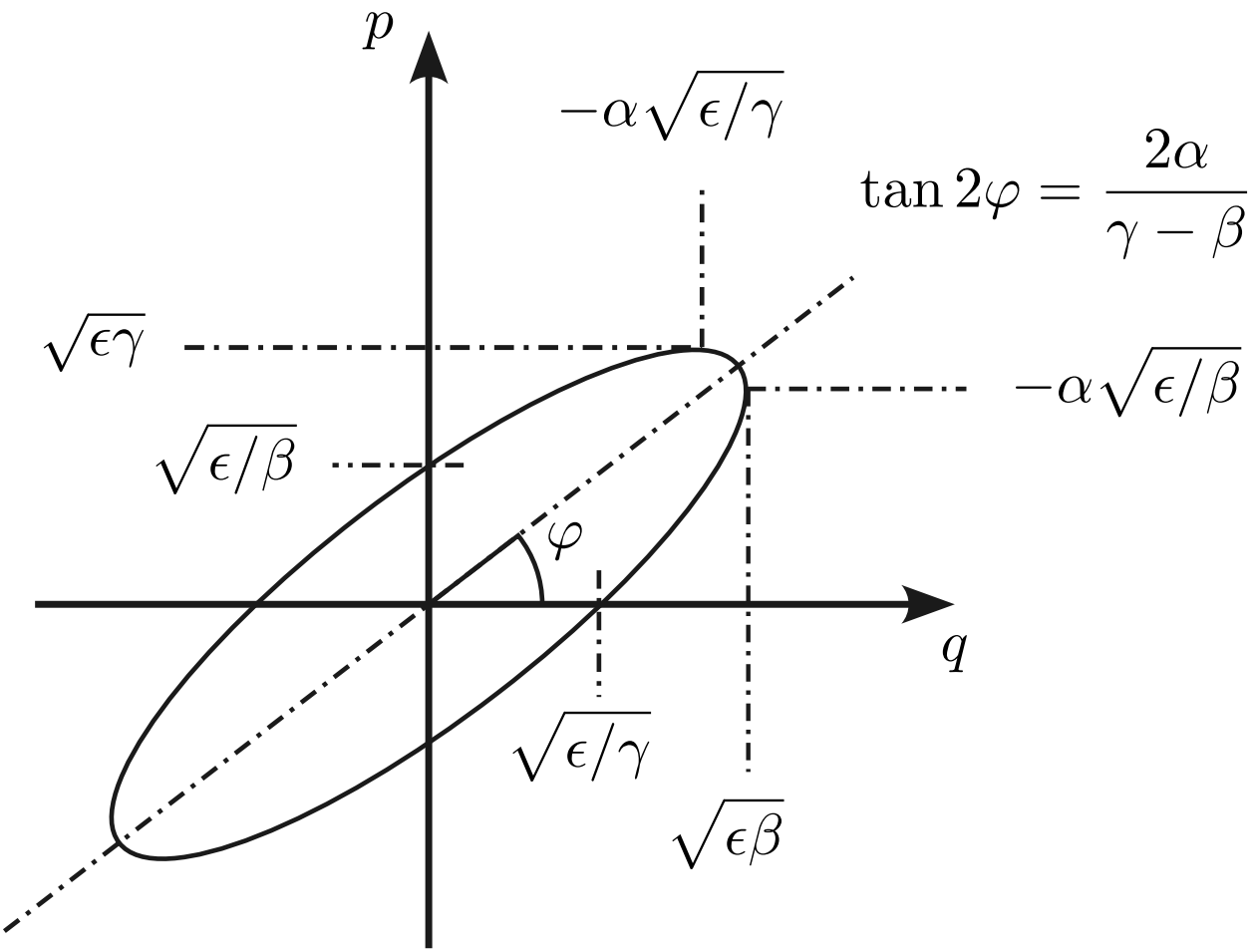


Figure 1.4 Poincare section ellipse of linear betatron motion with associated relationships to Courant-Snyder parameters [32]

This normalization reduces the equations of motion to that of circles with radius equal to the square root of the emittance. These coordinates are also sometimes referred to as Floquet coordinates in accelerator literature.

$$\begin{aligned} x_N &= \sqrt{\epsilon_x}\cos(\varphi_x) \\ p_{xN} &= -\sqrt{\epsilon_x}\sin(\varphi_x) \end{aligned} \tag{1.62}$$

We can also observe that the definition of the emittance simplifies in these coordinates (Eq. 1.63), and our linearized Hamiltonian reduces to Eq. 1.64.

$$\epsilon_x = p_{xN}^2 + x_N^2 \tag{1.63}$$

$$H = \frac{p_{xN}^2}{2\beta_x} + \frac{x_N^2}{2\beta_x} \tag{1.64}$$

There is one more important dynamical quantity that needs to be defined. The betatron tune $Q_x$ is the total phase advance over the full periodicity of an accelerator, defined in Eq. 1.65 where $C$ is the overall machine circumference. While some machines may be constructed of periodic cells, the overall tune is the fundamental periodic condition and necessary to understand the overall machine's stability.

$$Q_x = \int_{s_o}^{s_o+C} \frac{1}{\beta_x(s)} ds \tag{1.65}$$

All of this parameterization was of course in one dimension, the same can be applied to the y-plane assuming they are uncoupled. An extended parameterization to include coupling has been considered and there are two main approaches. One by Edwards-Teng [25] and one by Mais-Ripkin [11]. A good overview including many extensions to these parameterizations is provided in [59]. For the purposes of this dissertation, these coupled parameterizations are extraneous.

At this point, I would like to reiterate the assumptions along the way, and comment on the impacts:

1. The equations of motion are for single particles in external electromagnetic field - interaction with the environment and other particles due to the particles self fields are not considered.

2. The motion is defined with respect to a reference particle traveling with a design momentum along a desired design trajectory - requires definition of this reference.

3. The confining potentials are hard edged constant magnetic fields - impacts of realistic magnetic field fall-off are assumed to be small.

4. The transverse momentum is assumed to be small compared to the longitudinal momentum, which lets us linearize with the paraxial approximation - approach is valid only for situations where individual trajectories are mostly parallel to the reference.

5. The transverse "betatron" oscillations are assumed to be much faster than the longitudinal "synchrotron" oscillations and the Courant-Snyder parameterization is for particles with the design momentum - nonlinear energy dependent effects are not considered.

With these caveats in mind, this approach has been very powerful and is the guiding principle for first order accelerator design since its introduction. There is a wide variety of lattice simulation codes dating back to the 60's specifically designed to calculate these lattice parameters for evaluating stability, steering, and aperture restrictions of linear lattices.

### 1.6 First Order Bunch Properties

In practice we rarely accelerate single particles, and so we would like to parameterize the collective properties of a particle bunch. If we have some bunch of particles we can relate their individual betatron oscillations to the ensemble average or first moment in Eq. 1.66.

$$\langle x \rangle = \sqrt{\beta_x} \langle \sqrt{\epsilon_x} \cos(\varphi_x) \rangle \tag{1.66}$$

Here we can extract the beta function since we know it is a longitudinally dependent parameter of the lattice and not our individual particles. For a typical bunch we can assume a uniform distribution of oscillation phases, and we know from our equations of motion that the emittance and betatron phase are uncorrelated, so we can see that this mean is typically zero. This form can be exploited by adding a correlated emittance and phase term to the bunch with a "Kicker" element. This adds a coherent term to Eq. 1.66 and can be measured as the bunch centroid evolving according to the lattice dynamics. If we look at the second moments, we can extract more information on the bunch distribution. We start with the transverse coordinate, Eq. 1.67.

$$\langle x^2 \rangle = \beta_x \langle \epsilon_x \cos{(\varphi_x)}^2 \rangle \tag{1.67}$$

If we evaluate again for a uniform distribution of the betatron phase, we arrive at Eq. 1.68

$$\langle x^2 \rangle = \frac{\beta_x}{2} \langle \epsilon_x \rangle \tag{1.68}$$

We then define our rms emittance in Eq. 1.69.

$$\epsilon_{x,rms} = \frac{1}{2} \langle \epsilon \rangle \tag{1.69}$$

Using the same approach, we can relate the emittance to the two other moments of the distribution.

$$\begin{aligned} \langle x p_x \rangle &= -\alpha_x \epsilon_{x,rms} \\ \langle p_x^2 \rangle &= \gamma_x \epsilon_{x,rms} \end{aligned} \tag{1.70}$$

Based on the relationship between the Courant-Snyder parameters in Eq. 1.71.

$$\epsilon_{x,rms} = \sqrt{\langle x^2 \rangle \langle p_x^2 \rangle - \langle x p_x \rangle^2} \tag{1.71}$$

These values can be directly related to measurable quantities. This of course requires knowledge of the beam distribution, but the core of most beams is Gaussian and Eq. 1.72 is generally useful.

$$\sigma_x = \sqrt{\beta_x \epsilon_{x,rms}} \tag{1.72}$$

In most accelerator literature, these rms quantites are referred to as the geometric emittance, as opposed to the other common "normalized" emittance. The normalization in question is a multiplicaiton by the relatavistic factors to ensure that the emittance is preserved through acceleration. This is irrelevant in a non-accelerating ring, so emittances presented

are all geometric. Finally, by a quick dimensional analysis the units of emittance are simply [m] in our canonical coordinates. However, this convention is not universal, and often times the momentum dimensions are scaled with metric prefixes, as in the commonplace [mm-mrad]. As such, the emittance will be presented as [m-rad] to remain consisent, even though the [rad] label is not strictly accurate in our choice of coordinates.

### 1.7 Nonlinear Perturbations

Our treatment of the dynamics thus far has been exclusively linear. In practical machines, higher order multipoles are often added to compensate for deficiencies in the linear lattice construction. In most modern circular accelerators, the transverse chromaticity is compensated, or at least controlled with sextupole magnets. Octupole magnets may also be added to add an amplitude dependent detuning, which in turn drives tune spread in the bunch and can provide Landau damping. In addition to deliberately introduced nonlinear perturbations, our linear elements have small intrinsic nonlinearities. Most notably, there is an exact, nonlinear mapping for the dipole which has higher order terms which become relevant for dipoles with short radii of curvature [13]. Additionally, the fringe fields of linear elements will possess intrinsic nonlinearities, though this is strongly dependent on the design [6]. For example, the quadrupole fringe field in the hard-edge approximation has contributions of the same order as an octupole magnet [27]. These contributions all serve to perturb the dynamics, we can briefly consider the next order case of a sextupole magnet. If we add the sextupole term to our general Hamiltonian in Eq. 1.16, and take the case for the curvature to be zero we arrive at Eq. 1.73.

$$H = -\sqrt{1 + p_t^2 - \frac{2p_t}{\beta_o} - p_x^2 - p_y^2} - \frac{p_t}{\beta_o} + \frac{k_3}{3}(3xy^2 - x^3) \tag{1.73}$$

Even in the linearized case, we cannot find an analytic solution for the equations of motion for this system. There are a number of analytical techniques for analyzing the motion of these nonlinear systems, with Lie algebra approaches being the most common, but this is beyond the scope of this thesis. We can instead consider a quick numerical example using

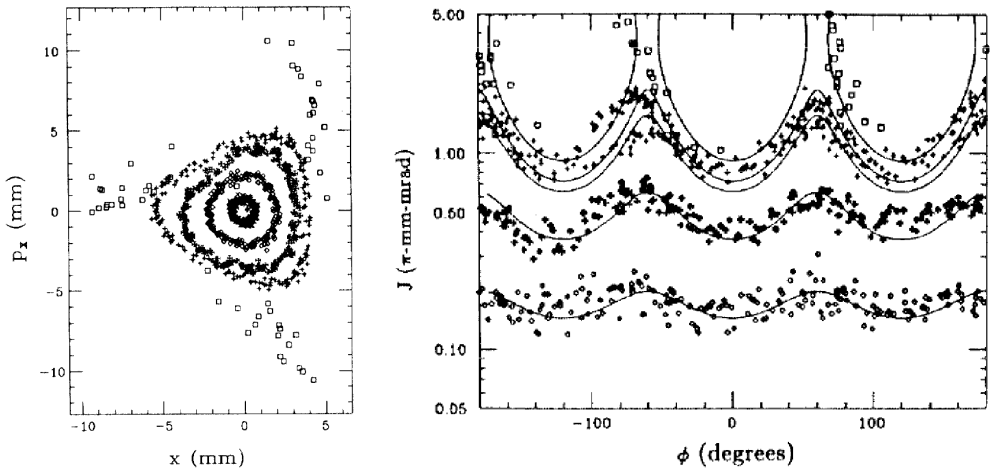


Figure 1.5 Phase space in canonical and action angle coordinates for linear system with strong sextupole perturbations [14].

a thin mapping of the integrated effect of the sextupole term in Eq 1.74, analogous to our matrix treatment of the linear dynamics. For illustrative purposes, we will continue to restrict ourselves to the horizontal plane.

$$\Delta p_x = L k_3 x^2 \tag{1.74}$$

Figure 1.5 shows the Poincare map for beam measurements in the Indiana University Cooler Synchrotron with sextupole effects. It demonstrates two important effects of the sextupole perturbation, there is an amplitude limit to stable motion, referred to as the dynamic aperture in accelerator literature. It also shows significant deviation of the trajectories from the linear elliptical traces, indicating that the emittance is not conserved.

## 1.8 Nonlinear Resonances

There is an additional effect of nonlinear perturbations to the linear dynamics, they serve to drive additional resonances. The general condition for a resonance is given in Eq 1.75, where $n$,$m$, and $k$ are integers.

$$nQ_x + mQ_y = k\pi \tag{1.75}$$

At these characteristic frequencies contributions add coherently and drive unstable mo-

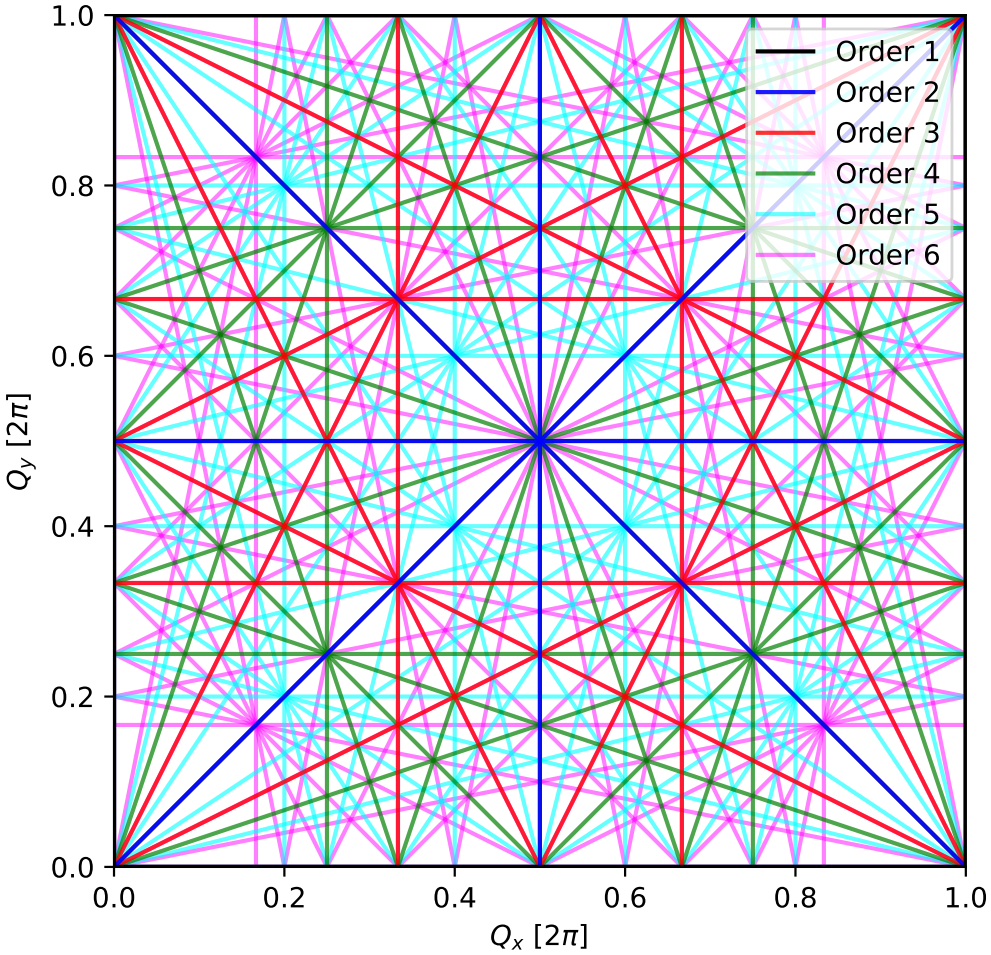


Figure 1.6 Resonance lines in tune space up to the 6$^{\text{th}}$ order

tion. The order of resonance is determined by the sum of $n$ and $m$. If $n + m = 3$ this is a third integer resonance and can be driven by sextupoles. Resonances are not limited to nonlinear driving components, quadrupoles drive half integer resonances, all multipole terms drive integer resonances. The basic resonance condition results in the dense map of resonance lines up to the order 6 in tune space in Figure 1.6.

Not every resonance is dangerous, only those which are driven strongly by the particular lattice configuration cause instabilites. Carefully picking the working point, or central tune of a lattice is an important design consideration.

## 1.9 Integrable Systems

We have seen that uncontrolled nonlinear perturbations can significantly reduce the stability of our system. An integrable system is one which has as many independent conserved quantities as degrees of freedom in the configuration space. This serves to regularize the motion and means there cannot be chaotic trajectories, though it does not guarantee that trajectories are bounded. Additionally, the KAM theorem ensures that most trajectories away from resonances of a perturbed integrable system remain stable and quasi-periodic [44]. This is an important result, as it means a realistic, flawed implementation of an integrable system will still demonstrate broad stability. The predictability of integrable systems means they have long been a subject of study in dynamics. Many forms of integrable systems have been found [31], though they generally are physically impossible to impractical to implement in accelerators. Particle accelerators are one of the few areas where careful study of the controlled dynamical systems can take place.

The linear Courant-Snyder system is an integrable system, with an independently conserved emittance in each degree of freedom. This also holds in the coupled linear system, though the parameterization is more complicated. In the context of accelerator dynamics, the advantages of this integrability are clear. It indicates that the design orbits are stable, generally robust to small permutations, and can be parameterized from the conserved quantities. The drawbacks of perturbative nonlinearites introduced to the linear system to mitigate higher order effects, have motivated a long history of searches for practical nonlinear integrable accelerators. McMillan introduced a basic set of one dimensional thin lens solutions [40], and Danilov found a practical 1-D solution using the Beam-Beam force as the nonlinear confining potential [20]. The experiments in this thesis focus on another development of Danilov and Nagaitsev formulated in 2010 [19].

## 1.10 Nonlinear Integrable Optics

Danilov and Nagaitsev discovered a two dimensional nonlinear integrable system relevant for accelerators [19]. To derive this system, we begin with a Hamiltonian in transverse

space using Courant-Snyder normalized parameters, so there is no time dependence of the Hamiltonian. If we add a general nonlinear potential constructed out of these normalized coordinates, it too will be time independent and the Hamiltonian will be a constant of motion, as in Eq. 1.76.

$$H = \frac{p_{xN}^2}{2} + \frac{p_{yN}^2}{2} + \frac{x_N^2}{2} + \frac{y_N^2}{2} + V(x_N, y_N, s) \tag{1.76}$$

We can make the form of $V(x_N, y_N, s)$ more straightforward to define in lab coordinates if we elect to place the nonlinear potential in a position with matched horizontal and vertical beta functions. The basic way to accomplish this is in a drift space. In order to arrive at this condition, we can define a periodic cell consisting of a matched drift and a so called "t-insert" which evaluates to a matrix with equal focusing in both planes, dependent on the desired phase advance in the drift. We can construct this matching lattice out of whatever elements are convenient.

The general problem is then to find a potential which can generate a second invariant of motion $I$. We absorb the linear potential terms into an overall potential to yield Eq. 1.77.

$$H = \frac{p_{xN}^2}{2} + \frac{p_{yN}^2}{2} + U(x_N, y_N) \tag{1.77}$$

The approach used by Danilov and Nagaitsev looked for forms of $I$ quadratic in the normalized momentum. Three solutions were found, though two were determined to have practical issues impeding physical implementation. Most notably, the phase space trajectories could not circle the origin, and would require some sort of "C"-shaped vacuum chamber. The choice of constants leading to the first solution yields Eq. 1.78 as the constraint on $U$ for a second integral.

$$x_N y_N \left( \frac{\partial^2 U}{\partial x_N^2} - \frac{\partial^2 U}{\partial y_N^2} \right) + (y_N^2 - x_N^2 + c^2) \frac{\partial^2 U}{\partial x_N y_N} + 3 y_N \frac{\partial U}{\partial x_N} - 3 x_N \frac{\partial U}{\partial x_N} = 0 \tag{1.78}$$

This is Darbroux's equation [21], and has the general solution of Eq. 1.79, where $\xi$ and $\eta$ are elliptical coordinates given in Eq. 1.80 and $f(\xi)$ and $g(\eta)$ are arbitrary functions. Note that there is a constant $c$ introduced with units of the square root of length.

$$U(x_N, y_N) = \frac{f(\xi) + g(\eta)}{\xi^2 - \eta^2} \tag{1.79}$$

$$\begin{aligned} \xi &= \frac{1}{2c}\left[\sqrt{(x_N + c)^2 + y_N^2} + \sqrt{(x_N - c)^2 + y_N^2}\right] \\ \eta &= \frac{1}{2c}\left[\sqrt{(x_N + c)^2 + y_N^2} - \sqrt{(x_N - c)^2 + y_N^2}\right] \end{aligned} \tag{1.80}$$

These can be related back to our transverse coordinates with the relationships in Eq. 1.81

$$\begin{aligned} x_N &= c\xi\eta \\ y_N &= c\sqrt{(\xi^2 - 1)(1 - \eta^2)} \end{aligned} \tag{1.81}$$

These functions result in a second invariant of motion of the form in Eq. 1.82

$$I = (x_N p_{yN} - y_N p_{xN})^2 + c^2 p_{xN}^2 + 2c^2 \frac{f(\xi)\eta^2 + g(\eta)\xi^2}{\xi^2 - \eta^2} \tag{1.82}$$

The particular form of the $f(\xi)$ and $g(\eta)$ functions were selected to also satisfy Laplace's equation so the potential $U$ could be generated by static magnetic fields. The first solution to consider is the linear potential Eq. 1.83, which we recast into this form in Eq. 1.84

$$\frac{f_1(\xi) + g_1(\eta)}{\xi^2 - \eta^2} = \frac{x_N^2}{2} + \frac{y_N^2}{2} \tag{1.83}$$

$$\begin{aligned} f_1(\xi) &= \frac{c^2}{2}\xi^2(\xi^2 - 1) \\ g_1(\eta) &= \frac{c^2}{2}\eta^2(1 - \eta^2) \end{aligned} \tag{1.84}$$

The more difficult case is to find a nonlinear solution to these constraints. This was found to be the functions in 1.85. Here $b$, $d$ and $\tilde{t}$ are arbitrary constants with units of length.

$$\begin{aligned} f_2(\xi) &= \xi\sqrt{\xi^2-1}(d+\tilde{t}\arccosh(\xi)) \\ g_2(\eta) &= \eta\sqrt{1-\eta^2}(b+\tilde{t}\arccos(\eta)) \end{aligned} \tag{1.85}$$

Inspection of the form of the nonlinear potential functions reveals that selecting $d=0$ and $b=-\tilde{t}\frac{\pi}{2}$ results in a magnetic field with not dipole term in the multipole expansion and therefore no bending in the nonlinear region. We also introduce a unitless nonlinear scaling parameter $t$ such that $\tilde{t}=tc^2$. Making all of these substitutions we arrive at a form of these potentials in Eq. 1.86.

$$\begin{aligned} f_2(\xi) &= tc^2\xi\sqrt{\xi^2-1}\arccosh(\xi) \\ g_2(\eta) &= tc^2\eta\sqrt{1-\eta^2}\left(\arccos(\eta)-\frac{\pi}{2}\right) = -tc^2\eta\sqrt{1-\eta^2}\arcsin(\eta) \end{aligned} \tag{1.86}$$

We can then consider the linear combination of these individual solutions, i.e. $f(\xi) = f_1(\xi)+f_2(\xi)$, and after substitution and simplification, we arrive at the form of the equations in Equations 1.87 and 1.88.

$$H_{DN} = \frac{p_{xN}^2}{2}+\frac{p_{yN}^2}{2}+\frac{x_N^2}{2}+\frac{y_N^2}{2}+ tc^2\frac{\xi\sqrt{\xi^2-1}\arccosh(\xi)-\eta\sqrt{1-\eta^2}\arcsin(\eta)}{\xi^2-\eta^2} \tag{1.87}$$

$$I_{DN} = (x_N p_{yN}-y_N p_{xN})^2+c^2p_{xN}^2+c^2x_N^2+ 2tc^4\xi\eta\frac{\eta\sqrt{\xi^2-1}\arccosh(\xi)-\xi\sqrt{1-\eta^2}\arcsin(\eta)}{\xi^2-\eta^2} \tag{1.88}$$

This parameterization is presented as it was the form used in the original derivation, and most clearly arises from the underlying partial differential equations. However it is quite

cumbersome, and encounters issues in numerical tracking for small values of $y_N$. A separate parameterization in complex coordinates was proposed in [42], and will be used for the rest of this thesis. To begin with, the coordinates in this representation are scaled by the geometric parameter $c$ to be fully unitless, and a complex coordinate $z$ is introduced, Eq. 1.89.

$$\begin{aligned} x_c &= \frac{x_N}{c} = \frac{x}{c\sqrt{\beta(s)}} \\ p_{xc} &= \frac{p_{xN}}{c} = p_x \frac{\sqrt{\beta(s)}}{c} + \frac{\alpha(s)x}{c\sqrt{\beta(s)}} \\ z_c &= x_c + iy_c \end{aligned} \tag{1.89}$$

The resulting Hamiltonian and second integral of motion are given in Equations 1.90 and 1.91

$$H_c = \frac{1}{2}\left(p_{xc}^2 + p_{yc}^2 + x_c^2 + y_c^2\right) - t\mathbb{R}\left[\frac{z_c}{\sqrt{1-z_c^2}}\arcsin(z_c)\right] \tag{1.90}$$

$$I_c = (x_c p_{yc} - y_c p_{xc})^2 + p_{xc}^2 + x_c^2 - t\mathbb{R}\left[\frac{2x_c}{\sqrt{1-z_c^2}}\arcsin(z_c)\right] \tag{1.91}$$

Since the normalization changed these quantities are related to the original Hamiltonian and second invariant by the relations in 1.92

$$\begin{aligned} H_{DN} &= c^2 H_c \\ I_{DN} &= c^4 I_c \end{aligned} \tag{1.92}$$

We can plot the potential $U$ with respect to our fully normalized coordinates $x_c, y_x$ in Figure 1.7.

This plot allows us to clearly illustrate the impact of the two arbitrary constants in the DN system. The $c$ parameter describes the locations of singularities in the nonlinear potential, specifically when $x_c = 1$ and $y_c = 0$. The dimensionless $t$ parameter encodes the relative strength of nonlinear insert, and has the strongest impact on the dynamics. Practically, the

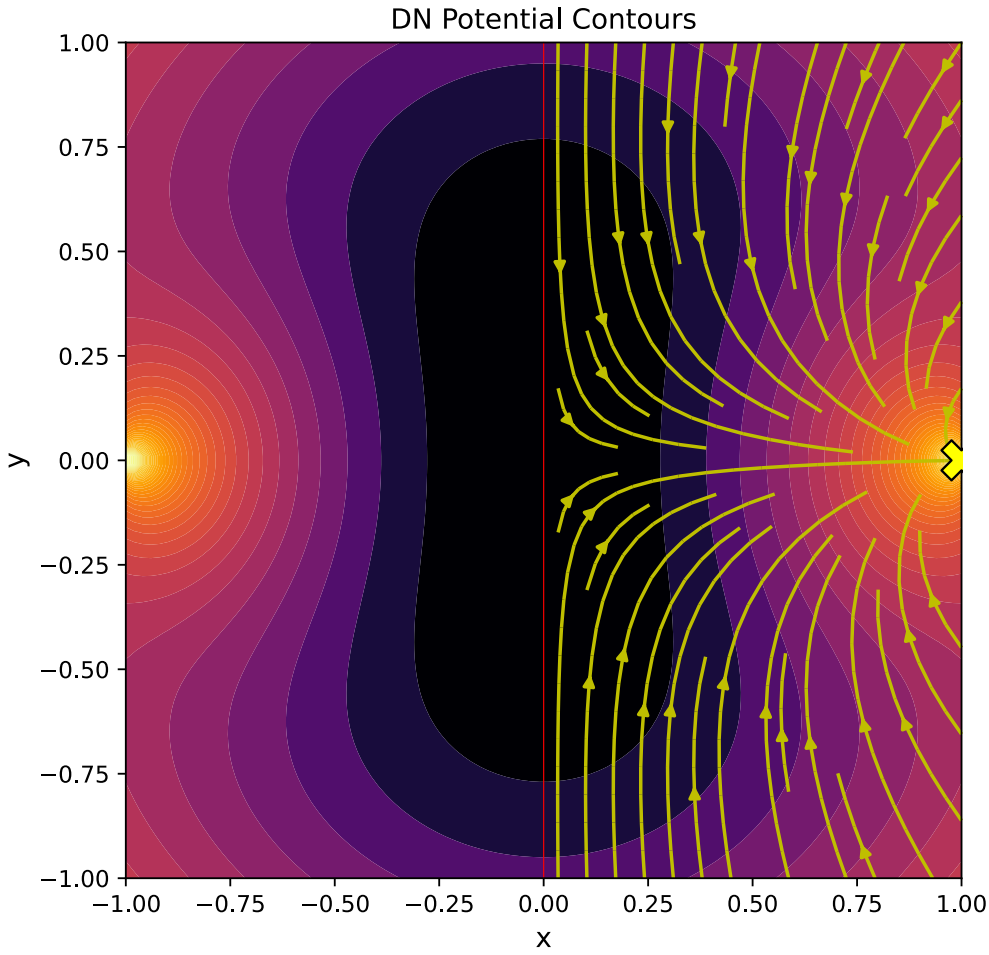


Figure 1.7 Potential of Danilov-Nagaitsev Integrable System. Yellow arrows indicate direction of potential scaling with $t$-parameter, and the cross indicates the location of the pole where $x = c$

$t$-parameter is selected to vary in the range $-0.5 \leq t \leq 0$, here a value of $t = 0$ recovers our Courant-Snyder case. The impact on the dynamics for further $t$ ranges are considered in [43].

As the potential satisfies Laplace's equation it can be represented with a string of magnets with properly shaped poles. The details of the implementation of such a magnet are discussed in section 2.6.

When the system was first introduced, it naturally generated some interest. This combination of bounded trajectories and strong nonlinearities is a generic recepie for a large

tune footprint with no limiting dynamic aperture, a desirable configuration for high intensity beams with intense space charge. In particular, simulations with intense space charge in the NIO system were perfomed [60] and indicated strong suppression of halo formation for space charge dominated beams. This motivate constructing the IOTA ring for dedicated studies of a realistic NIO system.

# CHAPTER 2

# INTEGRABLE OPTICS TEST ACCELERATOR

## 2.1 Facility Overview

The Integrable Optics Test Accelerator (IOTA) was constructed at the Fermi National Accelerator Laboratory (Fermilab) for dedicated beam studies, particularly implementations of nonlinear integrable optics (NIO) [4]. There are two main operational modes of IOTA, with 150 MeV electrons, and with 2.5 MeV protons. The design parameters for IOTA are given in Table 2.1. The electron beams have a quick damping time and low emittance due to synchrotron radiation and are useful probes of the phase space of the dynamical systems. The proton beams exhibit strong space charge effects at modest circulating currents and are useful for investigating schemes for suppression of damaging collective effects analogous to those seen in high intensity machines. IOTA is housed in the Fermilab Accelerator Science and Technology (FAST) facility and is not connected to the main sequence of proton accelerators at Fermilab. The location of the FAST facility on the Fermilab campus is marked in figure 2.1. In addition to IOTA, the FAST facility houses a superconducting electron linac, and a low energy proton injector.

## 2.2 FAST Electron Linac

The electron linac started as a test bed for the ILC [16, 12], and has since evolved to support a broad range of beam physics studies [18, 35]. Most importantly for the studies in this thesis, it is the source of the electron beams in IOTA. Figure 2.2 shows a component-level outline of the linac. The general linac bunch parameters are given in table 2.2.

| **Nominal IOTA Parameters** | **Electron Value** | **Proton Value** |
|---|---|---|
| Circumference | 39.96 [m] | |
| Energy | 150 [MeV] | 2.5 [MeV] |
| Circulating Current | 2.4 [mA] | 8 [mA] |
| Revolution Frequency | 7.5 [MHz] | 2.1 [MHz] |
| Magnetic Rigidity $B\rho$ | 0.5 [T-m] | 0.23 [T-m] |

Table 2.1 IOTA Design Parameters

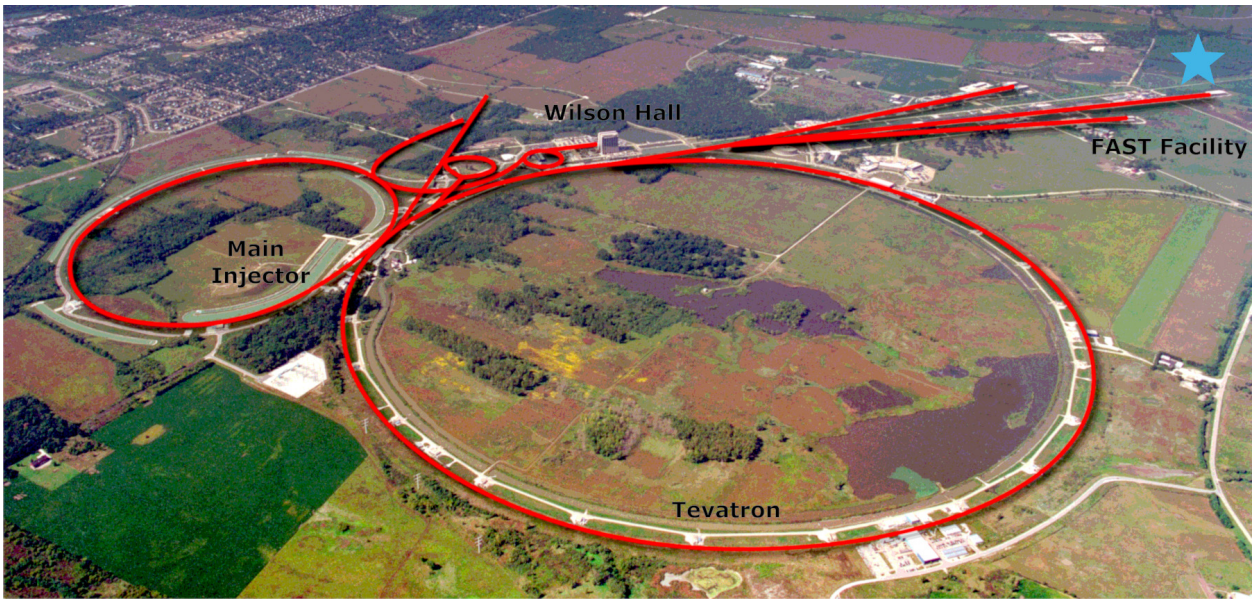


Figure 2.1 Location of FAST facility indicated by blue star at the end of a decommissioned fixed target beamline

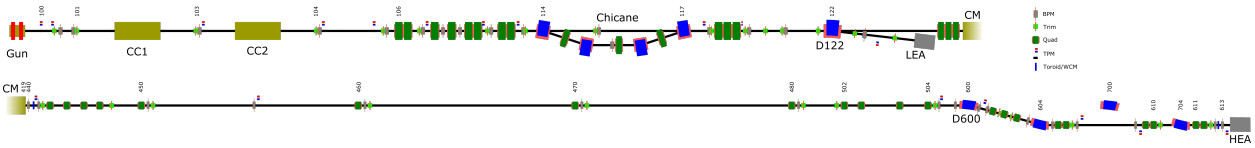


Figure 2.2 Placeholder Overview of FAST Linac

| **FAST Linac Parameter** | **Design Value/Range** |
|---|---|
| Beam energy to low energy absorber | 20-52 [MeV] |
| Beam energy to IOTA/high energy absorber | 100-300 [MeV] |
| Bunch Charge | $< 1\times10^{-5}$ - 3.2 [nC] |
| Normalized Emittance (for 0.1 nC bunch) | 0.6 [mm-mrad] |

Table 2.2 FAST Electron Linac Parameters

The electron source is a gallium-arsenide photocathode inside a 1.3 GHz room temperature copper RF gun. The laser pulses for the photocathode are supplied from a supporting laser lab capable of laser pulse shaping and timing for granular control of the resulting electron bunch. The beam then travels through a low energy beam transport (LEBT) line consisting of two independent 1.3 GHz superconducting 9 cell "capture" cavities. The electron LEBT also contains a few experimental stations and an optional chicane for beam studies. At the end of the LEBT the beam can be either steered to a low energy absorber or onward to the 1.3 GHz TESLA style cryomodule, which contains 8 sequential 9 cell superconducting cavities. Beyond the cryomodule is a long transport line initially intended for further cryomodules, to a switchyard. Here the beam may be steered to further linac experiments, the high energy absorber, or injected into IOTA. Figure 2.3 shows the lattice functions through the electron linac to the end of the IOTA injection septum. This long transport line presented some difficulties in tuning for injection, exacerbated by a failure in a quadrupole coil which removed it from the lattice. The $\beta$ functions necessarily grow to large values which amplifies the impact of the quadrupole errors, especially the limited control resolution in quadrupole power supply. While an accurate transverse match into IOTA is not crucial as the captured beam will damp to the equilibrium emittance, this touchy injection line was the cause of some headache in experimental operation, often limiting the injected current available.

## 2.3 IOTA Proton Injector

The IOTA proton injector (IPI) delivers 2.5 MeV proton beams to IOTA for space charge dominated studies. The hardware for the proton injection line is mostly repurposed from the Fermilab High Intensity Neutrino Source (HINS) [62] project of the late 2000's, consisting of a Duoplasmatron proton source, a solenoidal LEBT line, a radiofrequency quadrupole (RFQ), and a typical strong focusing medium energy beam transport (MEBT) line [24] to IOTA. The IPI line has been constructed and is undergoing commissioning at the time of the writing of this thesis, so it is not yet possible to quote its exact performance characteristics.

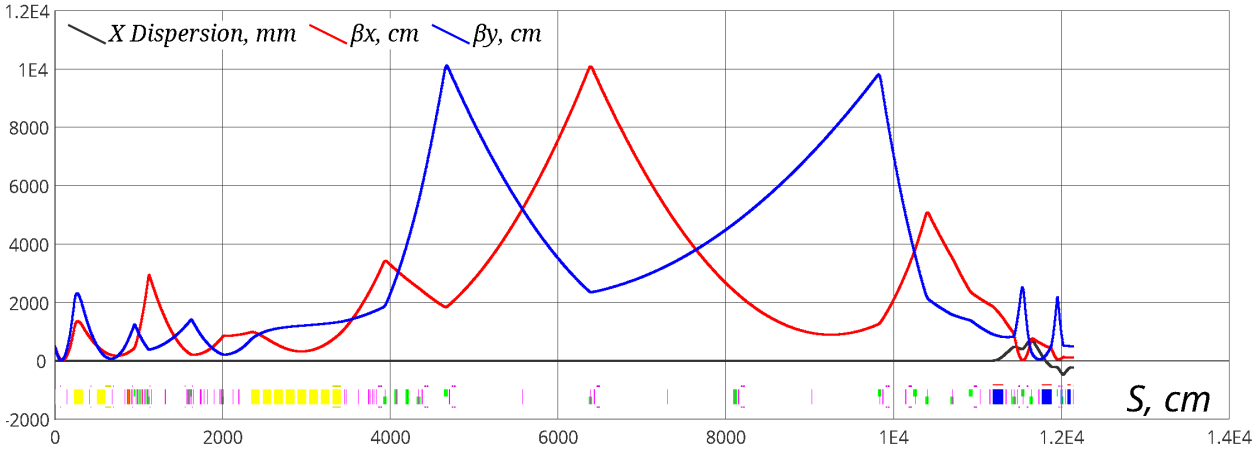


Figure 2.3 Lattice functions of the FAST electron linac for IOTA studies

The proton source is a 50 keV duoplasmatron. This particular source was characterized in the past [58] for the HINS project, and these are the approximate emittance values used in simulation studies. However, the source was slightly reconfigured for its new installation location, so the past characterization is not entirely accurate. Some additional characterization was performed with an Allison-type emittance scanner [2] to verify approximate ion species fractions, but it was not possible to separate proton emittance information. This will be evaluated with an Allison scanner downstream of the RFQ.

The 325 MHz RFQ accelerates the beam to the final energy of 2.5 MeV. As the HINS linac was intended to be focused entirely with superconducting solenoids, the incoming and outgoing beams from the RFQ needed to be axially symmetric. This was accomplished through deliberately shaped electrodes for matching at the end of the otherwise typical RFQ vanes, and leads to unusual matching conditions into the RFQ using round beams.

The MEBT is mostly a straightforward strong focusing transfer line with two notable exceptions, debunching cavity and an oversized dipole with strong edge focusing. The dipole was designed for operations with up to 1.2 GeV electrons for the superconducting linac at the facility. In order to properly steer the low rigidity protons into IOTA, the protons enter the dipole not at the pole face, but rather at the side of the pole with an effective entrance angle of 75°. This combined with the relatively large bending angle of the dipole results in

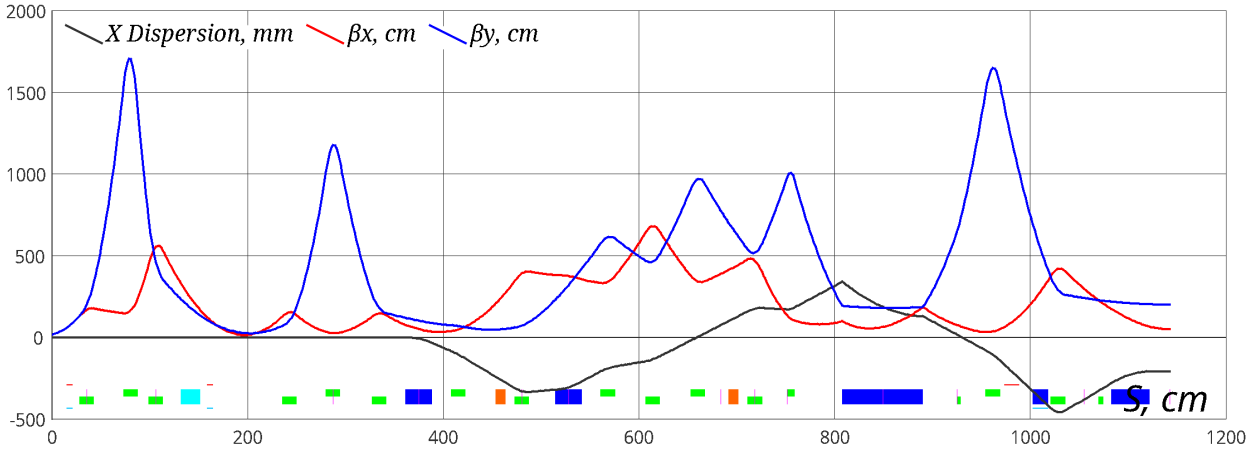


Figure 2.4 IPI MEBT lattice functions

strong edge focusing. This strongly limits the degrees of freedom in matching the MEBT to IOTA, and means there are not free knobs for tuning injection into IOTA. In practice, the plan is to add small permanent magnet quadrupoles to the end of the MEBT to match the desired input distribution. The lattice functions for the IPI MEBT are given in 2.4, note the sharp kinks at the edges of the longest dipole, this is the effect of the strong edge focusing effects. The debuncher cavity is used to reduce the energy spread of the beam for studies in IOTA, and helps preserve the RFQ bunched beam through the end of the MEBT. It operates at the same 325 MHz as the RFQ with accelerating gradients up to 50 kV.

## 2.4 IOTA Design

IOTA shows significant design inheritance from the VEPP-2000 collider at the Budker Institute for Nuclear Physics [56]. IOTA is of a stretched octagonal layout with four thirty degree and four sixty degree sector dipoles forming the fundamental geometry. IOTA originally was intended to be a regular octagon, but was eventually stretched to better fill the available lab space and provide a longer insert region for the optical stochastic cooling program. IOTA is broadly mirror symmetric across the stretched sides, which informs the element naming scheme outlined in 2.5.

The main dipole coils are all wired in series to provide identical excitation, as is pretty typical. In addition there are dipole correction coils wound in the main poles to act as an

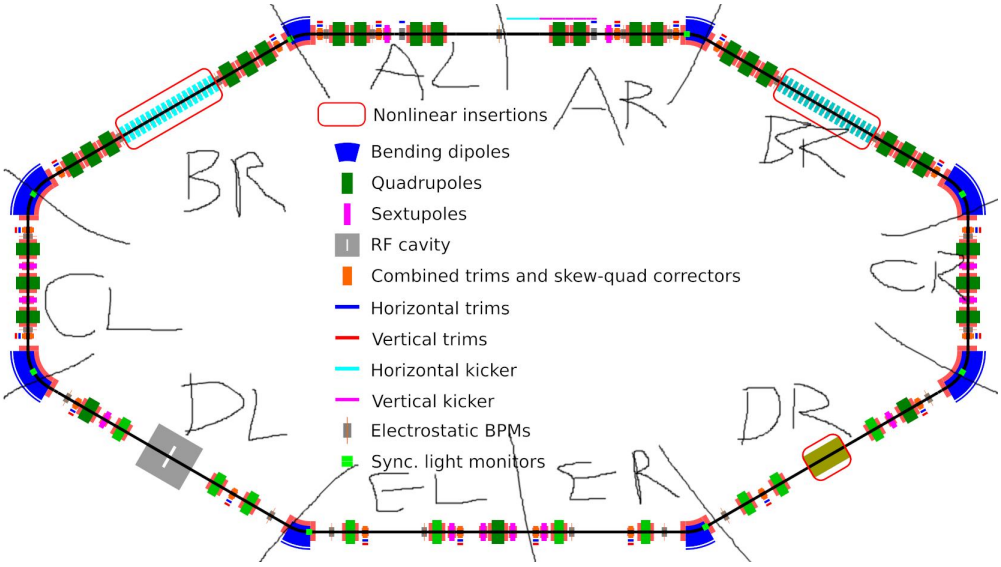


Figure 2.5 Placeholder IOTA drawing

| **Dipole Parameters** | **30° Dipole** | **60° Dipole** |
|---|---|---|
| Design Bending Angle | 30° | 60° |
| Design Bending Radius | 74.7 [cm] | 72.4 [cm] |
| Design Path Length | 39.114 [cm] | 75.799 [cm] |
| Pole Gap | 6.49 [cm] | 6.1 [cm] |

Table 2.3 IOTA Design Parameters

additional correctors. Notably the dipoles have "flux compensation" coils added to the pole face to reduce the length and intensity of the fringe fields. This was applied after IOTA commissioning to correct for excessive sagitta into the dipoles. The dipole parameters are outlined in 2.3.

Primary focusing is provided by 39 quadrupoles of two types. High current quadrupoles are of a refurbished AmPS design [54], and the rest of ring is filled out with commercially available quadrupoles purchased from Radiabeam. All quadrupoles are individually powered for flexible tuning of the lattice. IOTA has 20 Pansofsky [28] style combined function correctors for local correction of the closed orbit and skew quadrupole terms to minimize coupling. For longitudinal focusing and making up for synchrotron radiation losses, IOTA has a single ferrite loaded quarter wave RF cavity operating at 30 MHz with a tunable voltage range.

Adjustment of the RF voltage was used to reduce momentum acceptance for fast and convinient beam scraping to current ranges the BPMs were sensitive to. Injection into IOTA is facilitated by a horizontally bending Lambertson type magnetic septum [36], and a vertical travelling wave stripline kicker [5]. Additionally, there a vertical corrector intended for injection bump manipulation, but is practically simply implemented as additional corrector knobs. In addition to the linear elements, IOTA has 12 sextupoles of three types. There are 4 "prototype" type sextupoles constructed in house, 6 "long" type sextupoles manufactured by Elytts to the same magnetic parameters as the "prototypes" and 2 "short" sextupoles which aim for the same magnetic properties with shorter poles to fit a tight spot in the lattice. The basic IOTA geometry has three experimental insert locations. For the experiments described in this thesis, all three were filled. The first is the NIO insert described in detail in 2.6 in the BR straight. The BL straight housed a string of octupoles which satisfy one invariant of motion like the NIO system and are considered quasi-integrable. The octupole program lies outside of the scope of this thesis except for the magnetic alignment covered in appendix C. The final insert in DR was a permanent magnet undulator used for the CLARA experiment on electron radiation [57].

The IOTA beam diagnostics for the electron experiments consisted of 21 button style beam position monitors, a direct current current transformer (DCCT), a photomultiplier tube (PMT) for synchrotron radiation intensity and time of arrival, and five cameras for observing the synchrotron radiation profiles [23]. The BPM's were of two configurations, 20 nominal and one larger aperture BPM for increased admittance near the injection location. The BPMs sampled at 32 times the revolution frequency of the machine and applied a linear fit to the difference over the sum of the individual button digitized signals as described in [52]. After obtaining the position from the button signals, a seventh order two dimensional polynomial was applied to the measured position to account for the nonlinear response of the BPM. The factors for the polynomial mapping were obtained based on pulsed wire data in a single BPM, and applied uniformly to all. The BPMs could provide turn-by-turn (TBT)

data for "7000" turns, and 1000 turn averaged closed orbit data. Additionally 1000 turn raw button signals were available for a selectable single BPM in a special diagnosis mode. The particular preamplifier configuration on the IOTA BPMs means that there is a practical sensitivity band. Above circulating currents of 0.5 mA, individual BPM buttons were likely to saturate for kicked beams and impact TBT position data. This effect was screened for in postprocessing, and set the upper operating current. Below a circulating beam current of 0.1 mA, the BPM sensitivity became too poor for TBT collections and was usually the cutoff for a reinjection. The DCCT was used for monitoring the current of the circulating beam. The DCCT samples the current in the kHz range, and these values are averaged and reported at a 15 Hz rate in the data acquisition system. The PMT was calibrated to act as a supplemental current measurement, though discoloration on the tube's surface impacted its sensitivity and limited its accurate current measurements to un-kicked beams. The synchrotron light cameras are mounted on the top of five of the IOTA dipoles and can monitor the transverse profile of the beam and its intensity. The camera system is quite flexible and the exposure can be adjusted all the way down to sensitivity to single orbiting electrons. The exposure is not calibrated, however, so only relative intensity measurements can be made. The cameras also act as an excellent operational diagnostic as they can be live during beam operation and you can easily "see" the circulating beam. Figure 2.6 shows a clean publicity shot of IOTA before all components were installed.

## 2.5 IOTA Lattice

The dominant consideration for the design of the IOTA lattice is fulfilling the NIO insert requirements. These are:

1. The beta functions in the insert must be symmetric between the x and y planes, which enforces a symmetric drift of matched phase advance which defines the overall ring's fractional tune.

2. The dispersion throughout the nonlinear insert must be zero.

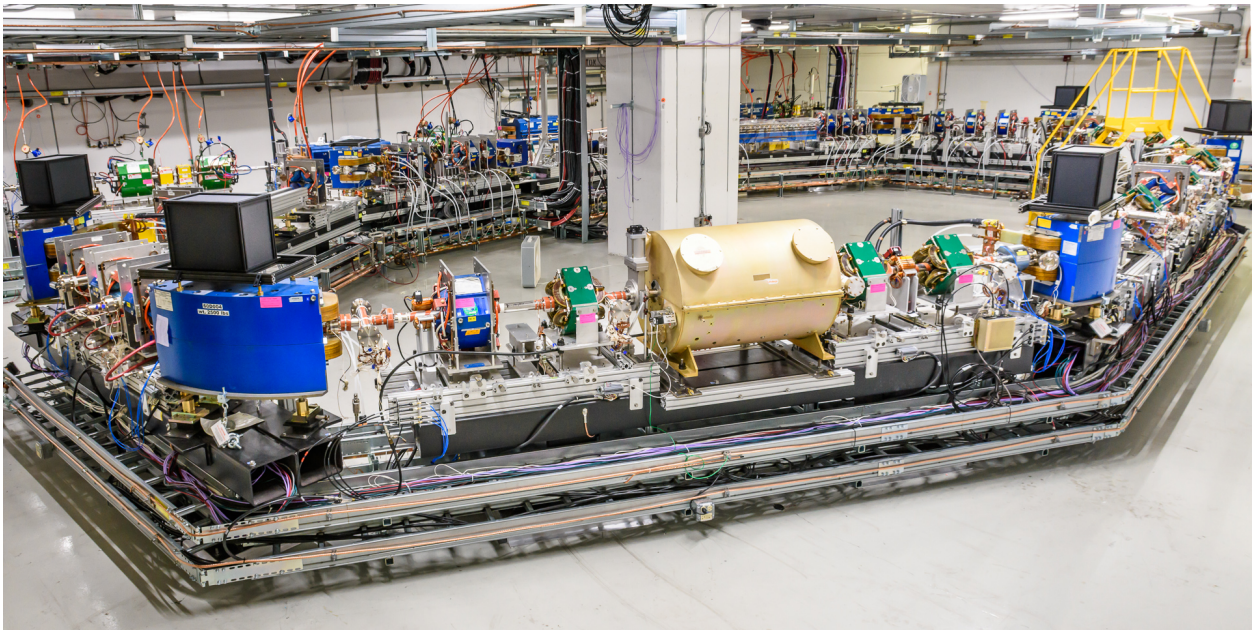

Figure 2.6 IOTA Ring photographed before all cabling is installed

The dispersion consideration comes from analytical studies of the NIO system including energy dependent effects [61]. The important results are that the dispersion must be made zero in the insert, and that the chromaticties in each plane must at least be matched. For IOTA the nonlinear insert length was chosen to be 1.8 m, and the fractional working point was selected to be $Q_{x,y} = 0.3$. In the current IOTA lattice the integer working points are symmetrically 5, but this is not a srict requirement. These parameters then fix the beta and alpha lattice functions in the drift. While the insert length is fixed, the working point can in principle be adjusted, though the nonlinear insert design depends on this factor so it is practically fixed. The basic transverse lattice requirements of the NIO system require 6 degrees of freedom to fully match. With the addition of dispersion suppression, this brings us to 8 degrees of freedom (assuming no coupling). IOTA is usually tuned to be mirror symmetric for convenience, which gives 20 quadrupole knobs, so there is available flexibility in the lattice for significant adjustments. In practice these knobs are not totally free as the beta functions and phase advance across the lattice must be kept reasonable for stable operation and good sensitivity of the BPMs. The idealized IOTA lattice functions as solved

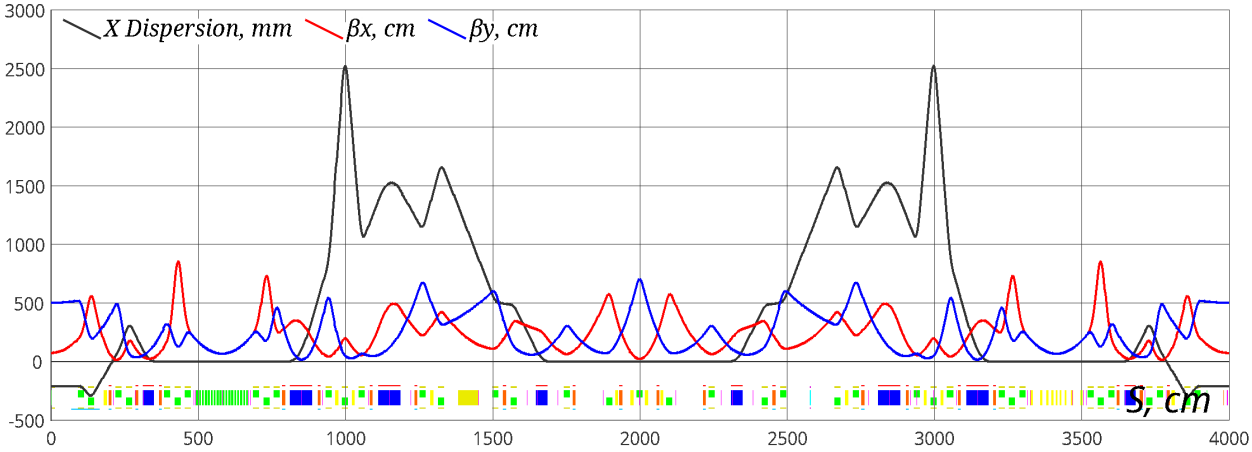


Figure 2.7 Nominal IOTA lattice functions

| **IOTA Lattice Parameter** | **Six D Simulation Value** |
|---|---|
| Transverse Tunes $Q_x, Q_y$ | 5.3, 5.3 [$2\pi$] |
| Natural Chromaticity $C_x, C_y$ | -10.5, -9.33 [1] |
| Momentum Compaction $\alpha_p$ | 0.086 [1] |
| RF Harmonic | 4 [1] |
| RF Voltage | 310 [V] |
| RMS bunch Length $\sigma_z$ | 21 [cm] |
| RMS momentum spread $\sigma_\delta$ | 1.28 [1] |
| Synchrotron Tune $Q_s$ | $3.33\times10^{-4}$ [$2\pi$] |
| Radiation Damping Times$^\dagger$ $x, y, s$ | 2.8, 0.65, 0.24 [s] |
| Equalibrium Emittances$^\dagger$ $x, y$ | $1.67\times10^{-7}$,0 [m-rad] |

Table 2.4 IOTA Run 4 Lattice Parameters.
$^\dagger$Calculated from linear radiation integrals [39, pg.438] without quantum excitation

in SixDSimulation are plotted in figure 2.7. This is the fundamental lattice used in the simulation studies presented in this thesis. Table 2.4 gives the lattice properties of this nominal configuration.

In the real accelerator there are of course small perturbations and misalignments of the physical elements. To actually tune the IOTA lattice the linear optimization of closed orbits (LOCO) algorithm is used to iterativley adjust the lattice to best fit the simulation model [53]. In the case of IOTA, there had to be slight adjustments to the lattice model to arrive at the final fit. Most notably, the undulator magnet was included in the lattice, the BPM

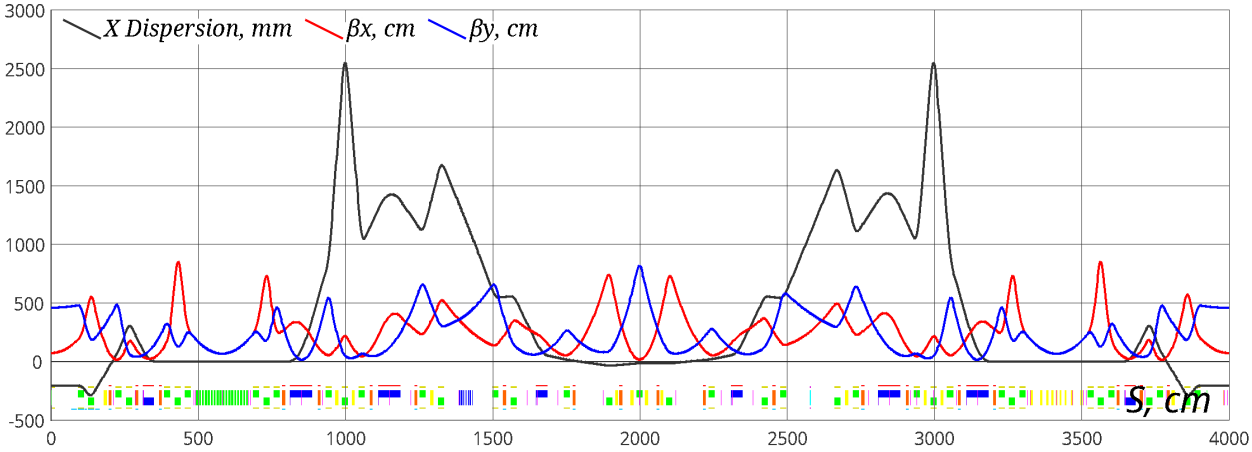


Figure 2.8 Experimentally fitted IOTA lattice functions

locations had to shift a bit, and small gradient terms were added to the dipoles. The resulting lattice functions are plotting in 2.8, notice that the symmetry in the dispersion has been broken due to the dipole gradients. This lattice is used for experimental analysis as it represents the best match to the real accelerator conditions.

## 2.6 IOTA NIO Insert Design

Once the insert drift parameters are fixed, the actual nonlinear insert magnets must be designed. To define the pole geometry, we introduce an additional function from [42]. This is a complex representation of the vector and magnetic scalar potentials (not the relativistic scalar potential), scaled by the rigidity.

$$F(z_c) = \frac{A_s}{B\rho} + i\frac{\Phi_m}{B\rho} = \frac{tc^2}{\beta(s)}\frac{z_c}{\sqrt{1-z_c^2}}\arcsin(z_c) \tag{2.1}$$

We can also expand this function about the origin. Note that this expansion is only valid inside the radius $x_c^2 + y_c^2 = 1$. This is of no practical concern as it only mandates that our expansion is good inside singularities of the potential, where we are interested in the dynamics anyway.

$$F(z_c) = \frac{tc^2}{\beta(s)}\sum_{n=1}^{\infty}\frac{2^{2n-1}n!(n-1)!}{(2n)!}z_c^{2n} \tag{2.2}$$

In a space with only the $A_s$ component of the vector potential, we know our magnetic field terms are given by Eq. 2.3, with chain rule considered since our potential depends on the normalized coordinates.

$$\begin{aligned} B_x =& \frac{\partial A_s}{\partial y} = \frac{1}{c\sqrt{\beta(s)}} \frac{\partial A_s}{\partial y_c} \\ B_y =& -\frac{\partial A_s}{\partial x} = -\frac{1}{c\sqrt{\beta(s)}} \frac{\partial A_s}{\partial x_c} \end{aligned} \tag{2.3}$$

To construct a Beth representation of our field we can combine our field terms in Eq. 2.4.

$$B_y + iB_x = -\frac{\partial A_s}{\partial x} + i\frac{\partial A_s}{\partial y} = -\frac{1}{c\sqrt{\beta(s)}} \left( \frac{\partial A_s}{\partial x_c} - i\frac{\partial A_s}{\partial y_c} \right) \tag{2.4}$$

A consequence of the Cauchy-Riemann equations yields Eq. 2.5

$$\frac{\partial F}{\partial z_c} = \left( \frac{\partial}{\partial x_c} - i\frac{\partial}{\partial y_c} \right) \frac{A_s}{B\rho} \tag{2.5}$$

Substituting, we arrive at Eq. 2.6, or the multipole expansion (in lab coordinates) Eq. 2.7.

$$B_y + iB_x = -\frac{B\rho}{c\sqrt{\beta(s)}} \frac{\partial F}{\partial z_c} = -\frac{tcB\rho}{\beta(s)^{3/2}} \left( \frac{z_c}{1 - z_c^2} + \frac{\arcsin(z_c)}{(1 - z_c^2)^{3/2}} \right) \tag{2.6}$$

$$B_y + iB_x = -\frac{tc^2 B\rho}{\beta(s)} \sum_{n=1}^{\infty} \frac{2^{2n-1} n!(n-1)!}{c^{2n}\beta(s)^n (2n-1)!} (x + iy)^{2n-1} \tag{2.7}$$

There are two important takeaways from the multipole expansion, there are only even multipoles in the expansion (quadrupole, octupole, dodecapole, etc.), and the lowest multipole order is that of a quadrupole. So, the first order effect of the nonlinear insert can be treated in our linear dynamics for coarse tuning purposes and alignment. Figure 2.9 shows the fractional deviation of the magnitude of the magnetic field of the multipole decomposition (Eq. 2.7), from the exact analytic form (Eq. 2.6) for increasing cutoff orders. Three points

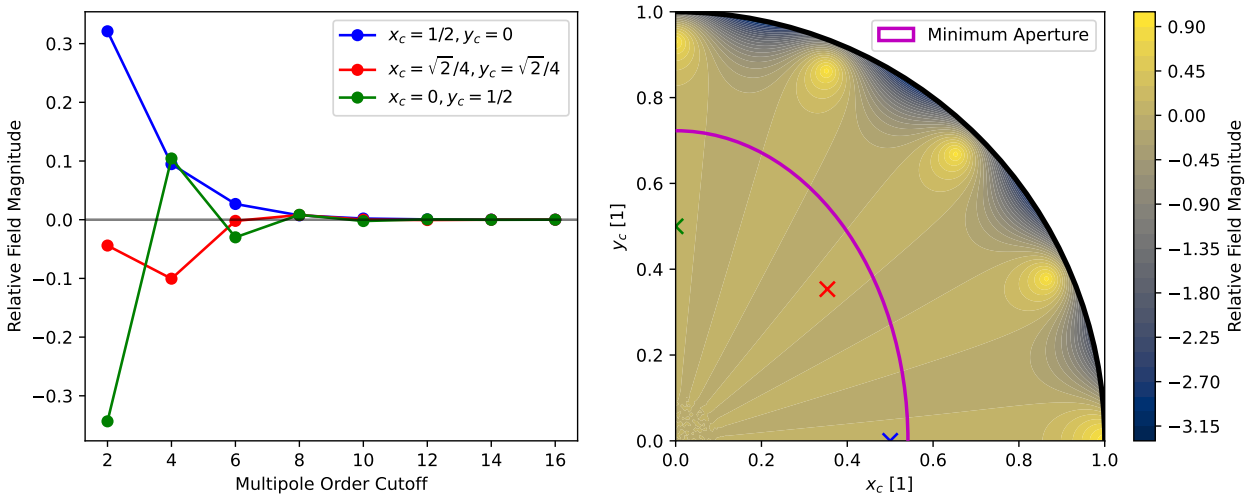


Figure 2.9 Relative field magnitude deviation between exact form and expansion with different truncated orders. Right plot is truncated at the 16th order term, same as last point in left plot. Transverse location of traces from left plot correspond to crosses in right plot.

of comparison are taken, $(x_c = 1/2, y_c = 0)$, $(x_c = 0, y_c = 1/2)$, and $(x_c = \sqrt{2}/4, y_c = \sqrt{2}/4)$. A comparison for a multipolar cutoff at the 16th order, or our 32-pole term, is also plotted. Notice the breakdown of the field match at large amplitudes, even with these high order multipole terms considered.

The design of the nonlinear inserts use iron dominated magnets to shape the field, we can set to the scalar magnetic potential to a constant value and invert for the coordinates. In practice this is done numerically. The nonlinear insert used in these studies placed the pole at a scalar potential value of 0.5, in the $B\rho$ normalized units. Figure 2.10 shows the scalar magnetic potential gradient in the region where the multipole expansion holds, with the selected contour for the insert in red.

Once the transverse profile has been defined the necessary longitudinal scaling needs to be considered. The ideal DN potential smoothly scales with the beta function in the insert drift, but this is impractical to implement with magnets. For the real insert, a series of magnets approximately integrate the potential. The basic implementation is to assume some number of thin kicks scaled by the hard edge equivalent length of the magnets. For the first version of the magnet, this was done with 18 magnets equally spaced along the length

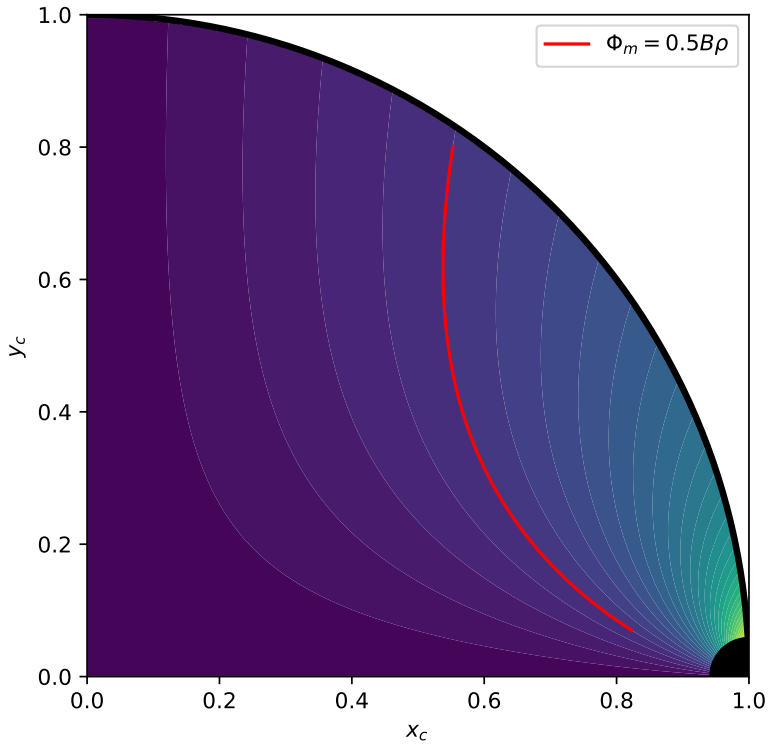


Figure 2.10 Normalized magnetic potential of NIO system, contour used in IOTA magnets is highlighted in red. The region near the singularity is masked to make the gradient more distinct.

of the insert. Figure 2.11 shows the effective potential for the ideal case and the 18 element piecewise approach.

Based on the form of the normalization employed to constructh the Hamiltonian, the poles must be shaped according to the beta function at the given location to match the same contour in the magnetic potential. As a result the insert is composed of 9 unique pairs of magnets arranged symmetrically about the center. Figure 2.12 shows the physical contours of the magnet families in the insert, the increase in size as the index increases from the center corresponds to a larger aperture.

The nonlinear insert was designed in part to exploit the nonlinearities of the magnet at small amplitudes, so the $c$ parameter was chosen to be quite small; $c = 0.009\sqrt{m}$ (some literature claims a different physically implemented c-parameter, but this value has been confirmed with the engineering drawings). This means that the singularity of the potential

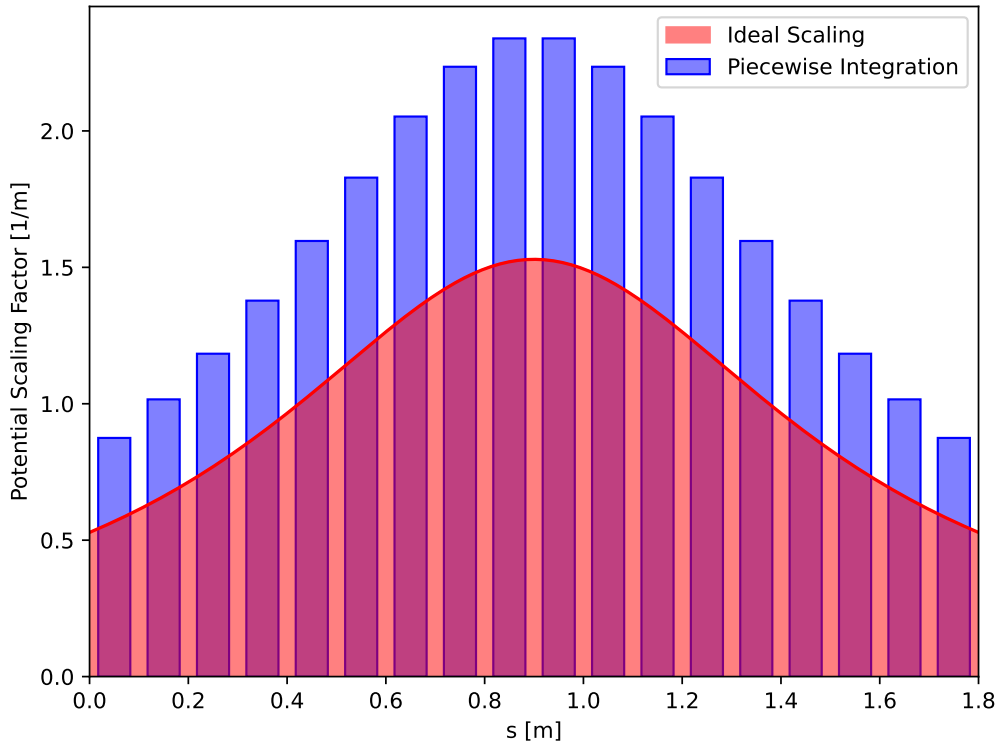


Figure 2.11 Comparison of ideal longitudinal scaling of potential with physical piecewise approximation.

| **NIO Insert Parameter** | **Nominal Value** |
|---|---|
| Insert Length | 1.8 [m] |
| Insert Phase Advance | 0.3 [$2\pi$] |
| Number of Magnets | 18 [1] |
| Magnet Length | 6.5 [cm] |
| $c$ parameter | 0.009 [$\sqrt{\text{m}}$] |
| Turns Per Coil | 40 [1] |
| Minimum X Aperture Radius | 3.94 [mm] |
| Minimum Y Aperture Radius | 5.26 [mm] |

Table 2.5 NIO Insert Parameters

is at about 7 mm at the center of the insert, and necessitates a carefully designed beam pipe to maximize the available aperture within the small poles. The core parameters of the insert are outlined in table 2.5

The mechanical, magnetic, and vacuum design and fabrication of the insert was performed by Radiabeam (in collaboration with the IOTA group) under a Department of Energy small

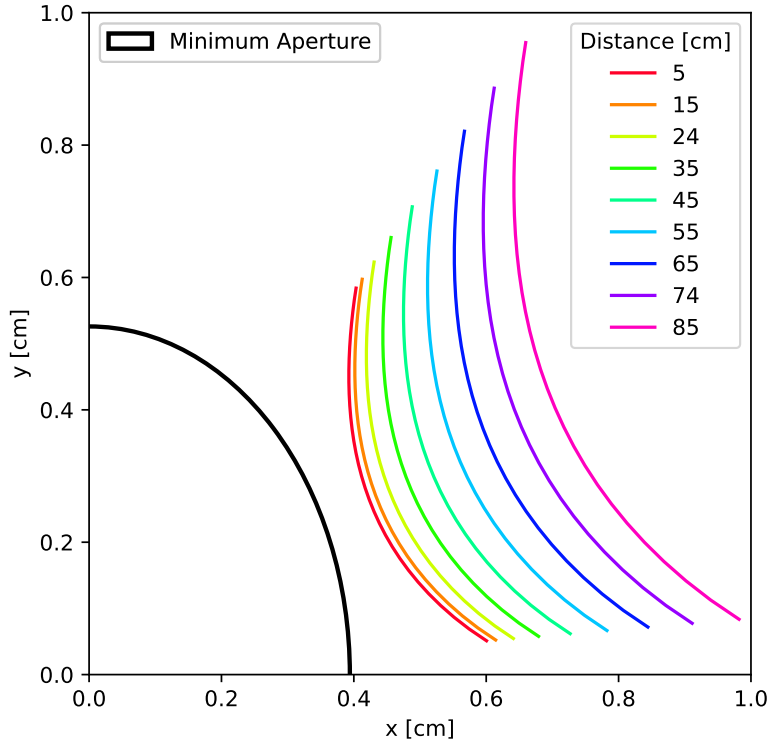


Figure 2.12 Lab coordinate pole contours of DN magnet. Distances are measured from the center of the nonlinear insert

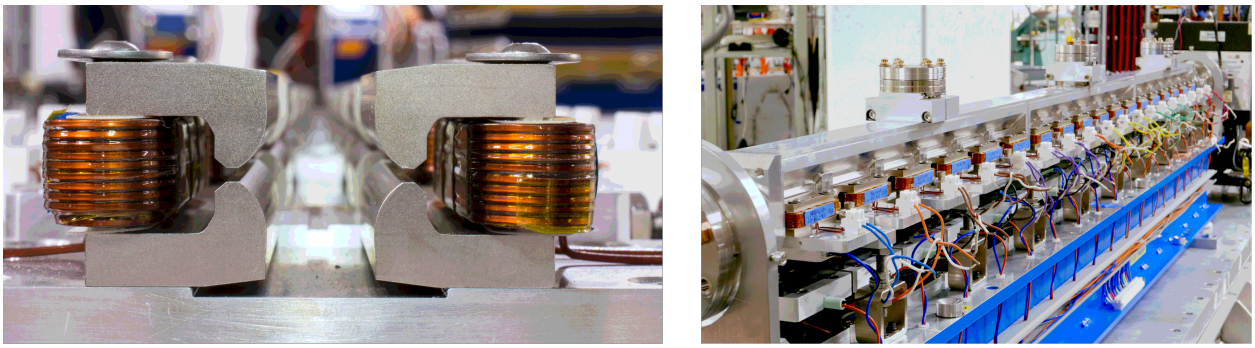

Figure 2.13 Pictures of IOTA NIO insert, note the pole contours and the longitudinal structure.

business innovation research (SBIR) grant [41, 48, 49, 50]. The actual magnet is pictured in figure 2.13. Based on experience with the first insert, a second version of the insert was constructed, though no beam studies have yet been performed. Some details on its design and magnetic mapping are included in appendix B.

# CHAPTER 3

# SIMULATION STUDIES

## 3.1 Simulation Codes

There is a veritable zoo of commonly used codes for simulating the dynamics of charged particle accelerators, all with different focuses, operating assumptions, supported hardware, and dynamics models. A few different simulation software programs were used for simulation studies of IOTA and the NIO system, two main codes, and a few supplemental codes. The main lattice code for design and control of the linear optics was Six D Simulation (SixDSim), a java based application written and maintained by Aleksandr (Sasha) Romanov, the resident IOTA lattice expert. SixDSim performs lattice function calculations for periodic and channel mode accelerator systems in the full six dimensions, so first order dispersive and path lengthening effects are automatically considered. SixDsim provides general lattice construction and optimizing functionality with a graphical environment (a rarity in accelerator codes). In addition to offline lattice design and manipulation, SixDsim has support for control system integration and was the main driving engine for the linear optimization of linear optics (LOCO) which defined the IOTA bare lattice for experiments. It also allowed for application of complicated custom knobs for fine tuning the lattice between time intensive LOCO iterations. As such, the SixDsim lattice model contained the best fit of the experimental IOTA lattice and was used for extraction of lattice functions used in calculations.

The other primary code used for IOTA simulations was Impact-X [32], a particle tracking code under active development with a particular focus on particle-in-cell space charge modelling and efficient operation on large scale computing environments. Impact-X was selected for two main reasons, the first is its implementation of the DN NIO lenses, and its advanced space charge models. The space charge simulation capabilities ended up being moot, as the proton program at IOTA was sufficiently delayed to fall outside the scope of this dissertation. The implementation of the DN lenses in Impact-X is based on the complex representation formulated in [42], which has some benefits for numerical stability near the x-

axis in configuration space. This is unlike other common tracking codes MAD-X and Xsuite which implement the original parameterization of the DN lens. Generally, Impact-X is a robust symplectic tracking code with modern Python scripting support and expanding physics capabilities. The whole complement of tracking simulations presented were performed with Impact-X.

MAD-X is the closest the accelerator community has to a standard, and as such is the code in which the generic IOTA lattice is described. The cpymad wrapper for MAD-X was used as the benchmark for lattice functions in the tracking codes to evaluate proper lattice implementation, due to its straightforward implementation into python workflows. Xsuite is the new tracking code developed at CERN to replace and supplement the many legacy codes in use. For this work Xsuite was used for additional lattice benchmarking and as an educational tool. TRACK is a non-symplectic tracking code optimized for multi charge state acceleration of heavy ion beams in arbitrary external fields. The HINS RFQ re-used for the IOTA injector was designed in part with TRACK, so this most accurate physics model was used for that component of the proton injector simulation. Finally, a self programmed python tracking code was used for initial evaluation of invariant conservation in various nonlinear insert configurations. This was a valuable educational experience, but not a recommended long term approach. All of these personally constructed simulations were re-performed with equivalent Impact-X lattices for better reproducibility and clarity.

### 3.2 NIO Toy Simulations

The first simulations we will consider will be of the DN NIO system to demonstrate the underlying dynamics. The simulations are constructed in the drift-kick style, with the kick for the DN insert defined by the instantaneous change in momentum in a Ruth-like formulation in equation 3.1 [42].

$$\Delta p_x - i\Delta p_y = \Delta s \frac{tc}{\beta^{3/2}} \left( \frac{z_c}{1 - z_c^2} + \frac{\arcsin(z_c)}{(1 - z_c^2)^{3/2}} \right) \tag{3.1}$$

The simplest insert configuration is a nonlinear insert drift with a thin matrix element

providing the equal focusing. For ease of comparison, we match the IOTA NIO configuration with a 1.8 m drift with a phase advance of 0.3. This uniquely constrains the lattice functions in the drift and sets the values in the focusing matrix. We will also add a limiting aperture of a circle with a radius of 0.95 times the lab frame location of the singularities in the DN potential. We are only interested in the dynamics between the singularities as this is the physically practical region. [43] touches on the predicted dynamics outside of these constraints. We choose aperture of 0.95 of the limit to avoid numerical issues near the singularities.

To best approximate the nominal smooth longitudinal scaling of the DN potential, we integrate the insert with a sequence of 1800 kicks, effectively subdividing the insert into millimeter-scale steps. The particles are initialized and monitored at the center of the insert. In the bare lattice this corresponds to the $\beta^*$ location where the $\alpha$ lattice functions are zero. This makes interpretation easy as the maximum amplitude of the oscillation shares the zero momentum condition. As we ramp the t-insert, the symmetry of the insert means the first order effect of the nonlinear magnets keeps the effective $\alpha$ zero at the center. The first simulation considered uses an initial grid of points which uniformly fills the central aperture in the transverse configuration space. Impact-X is a strictly 6-D code, so it is impossible to completely exclude the longitudinal dynamics, but the $ct$ and $p_t$ coordinates are uniformly zero, so any effects are the result of numerical error. The drifts in the nonlinear insert are strictly linear, and do not include chromatic effects. Figure 3.1 shows the resulting amplitude dependent detuning for this full configuration space range for a t-parameter of $t = -0.238$. The color indicates the relative initial coordinates, i.e. red points indicate only $y$ initial coordinates and blue the same for $x$. The tune was measured for each macroparticle with the NAFF algorithm [38, 67] and a first order Hann window [29]. We see a very large tune footprint with a characteristic "butterfly wing" profile. The largest detuning axis is dependent on the horizontal amplitude. There are some spurious features related to large horizontal excitations. We see a thin line of tunes crossing the main footprint from the lower

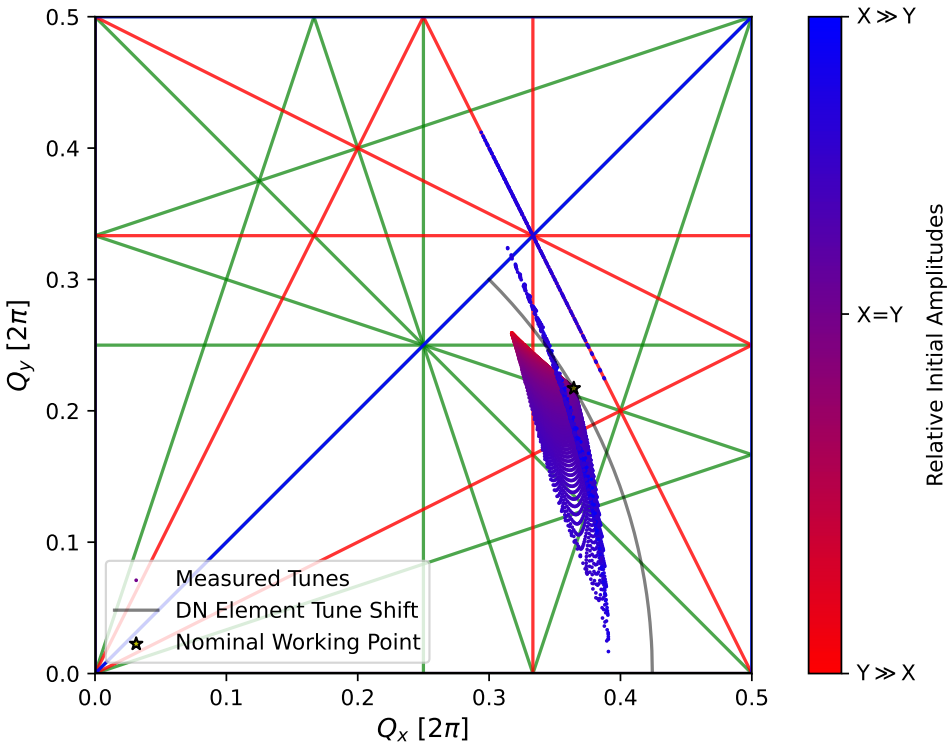


Figure 3.1 Amplitude dependent detuning in tune space for idealized NIO system at $t = -0.238$. Color indicates relative initial transverse coordinates.

"point", and a number of tunes on the $2Q_x + Q_y = 6$ resonance line. The interpretation of this effect becomes more obvious in the tune versus amplitude space.

Figure 3.2 displays the tunes versus the initial amplitude. The amplitude is calculated as the initial emittance for the bare lattice, to easily compare between different simulations. All points are present in each plot, so the perpendicular amplitudes are also present for a given labeled amplitude axis. The color scaling for relative ratio of kick amplitude has been retained. In addition to the general tune dependence on different amplitudes, we have a clear indicator on these extra features. Both features are present at excitations leading to detuning near the vertical integer resonance. Notably, since the system is fully integrable, all of these orbits remain stable. The interpretation of the tune becomes difficult in this region, as the TBT frequency approaches zero. The system is strongly nonlinear, so the assumption of a dominant frequency breaks down. The measured tunes for amplitudes predicted to detune beyond the also pose a practical challenge, standard signal processing methods are

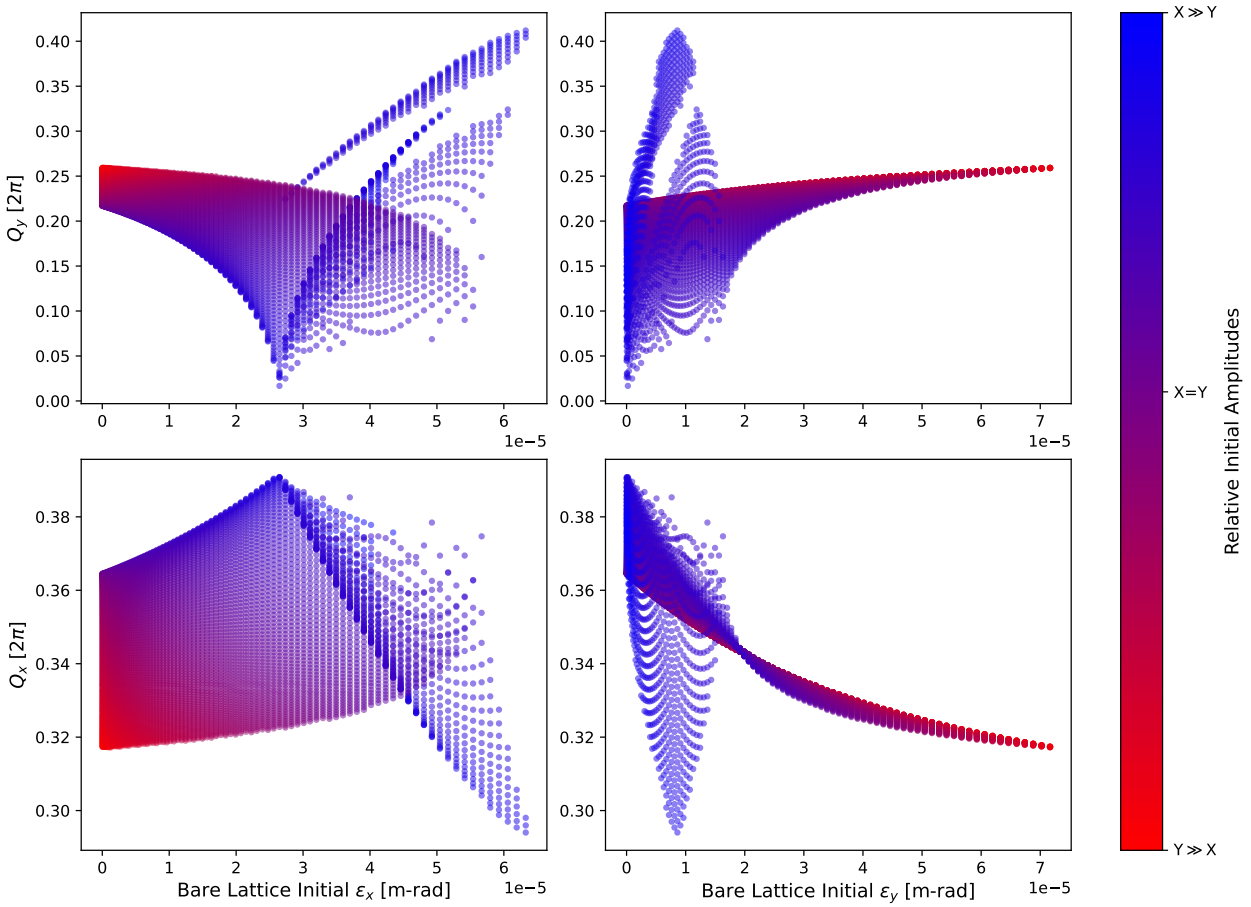


Figure 3.2 Tune versus initial amplitude for idealized NIO system at $t = -0.238$. Color indicates relative initial transverse coordinates.

sensitive only to the fractional component of the tune, so we are insensitive to whether the tune "rebounds" or passes down by an integer.

The characteristic Poincarè sections of the DN NIO system are shown in Figure 3.3 in fully normalized coordinates. The system exhibits these "Spirograph" like patterns near the circle which would be traced by the basic Courant-Snyder system in the phase space. The most notable effect in the configuration space is the nonlinear coupling which results in this "Hourglass" shape that the particle traces. This has some impacts on admittance considered in section 5.5.

We can gain some further insight by looking at the phase space and Fourier spectrum of a particle near the integer resonance. Figure 3.4 shows the result of the FFT for such a particle. We see that there is a broader spectrum with many peaks, so our monotonal

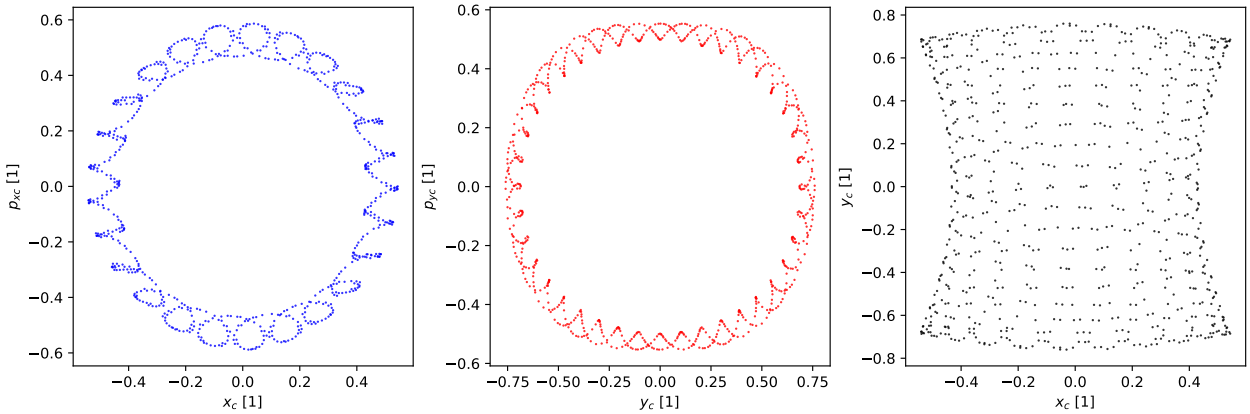


Figure 3.3 Poincare sections for a single particle of the horizontal and vertical phase spaces, and the configuration space for the idealized NIO system at $t = -0.238$

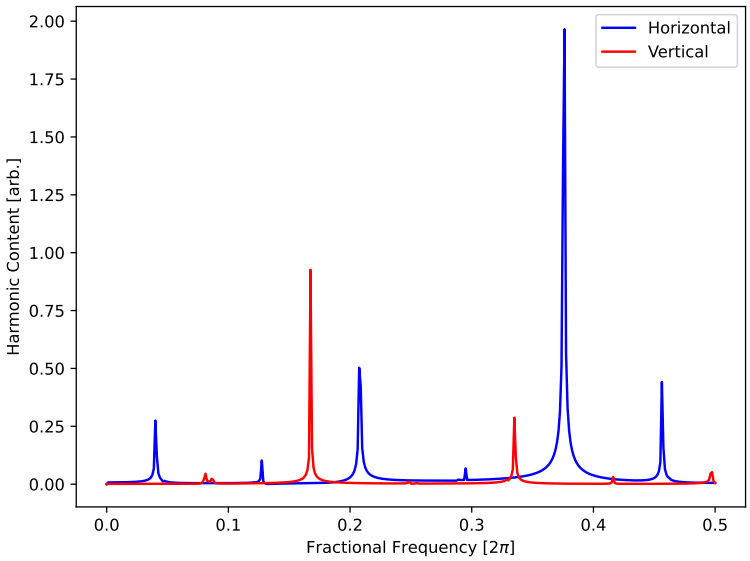


Figure 3.4 Fourier spectrum of simulated particle near vertical integer resonance

definition of tune begins to break down somewhat.

Figure 3.5 shows the phase space of this same particle. The motion becomes strongly nonlinear, especially vertically, where we are no longer orbiting around the original closed orbit.

A final figure of merit to consider is the quality of the conservation of the analytically predicted invariants. Figure 3.6 shows the calculated DN system Hamiltonian and the second invariant turn by turn from an example particle, normalized by the mean. In the ideal case this would be flat. We see some slight jitter presumably from numerical noise and a slightly

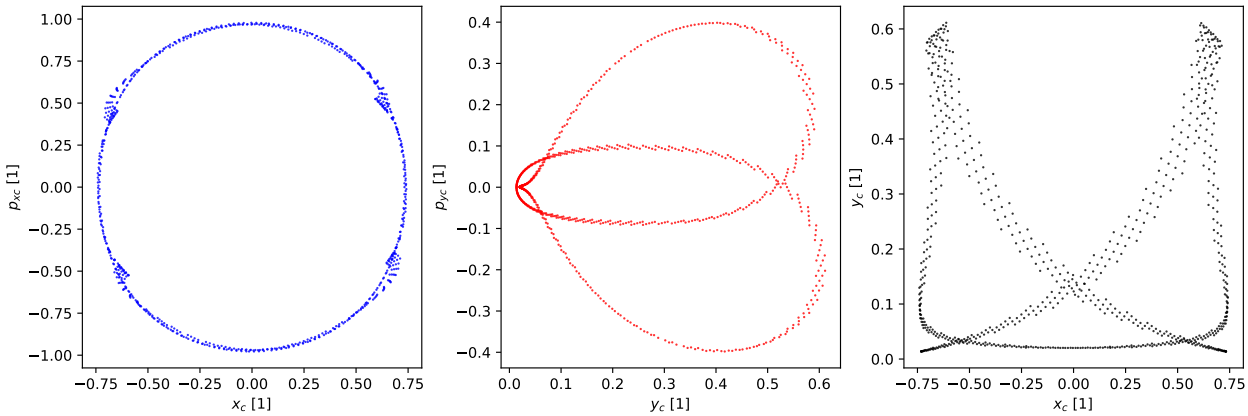


Figure 3.5 Phase space Poincare sections for simulated macroparticle near vertical integer resonance

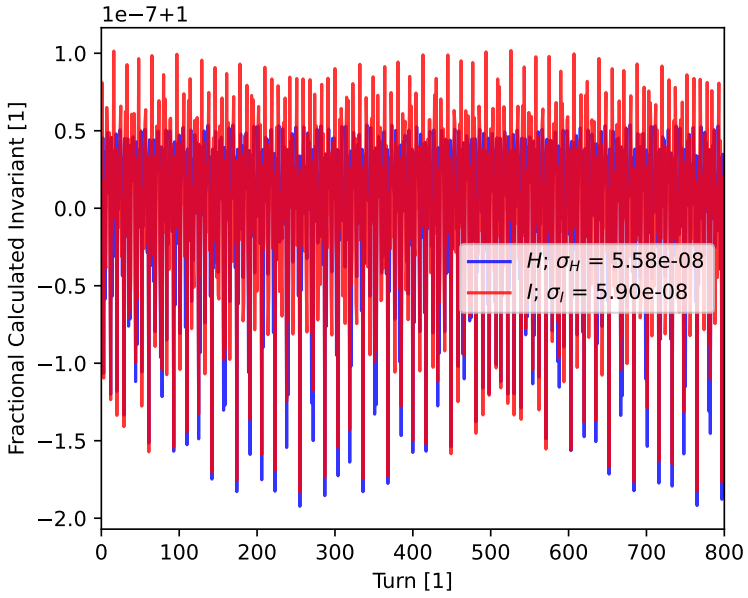


Figure 3.6 Calculated analytic invariant quantities turn-by-turn from simulated particle in toy NIO system at $t = -0.238$

imperfect integration of the potential. This calculated quantity will be used for evaluating quality of other integrators and lattices moving forward as it is a direct indicator of the match of the system to the ideal DN NIO system.

We now need to consider more realistic nonlinear insert configurations. It is impractical to manufacture a magnet that smoothly tapers with the required longitudinal scaling. To simulate the realistic IOTA insert, we need kicks which correspond to our 18 elements. This

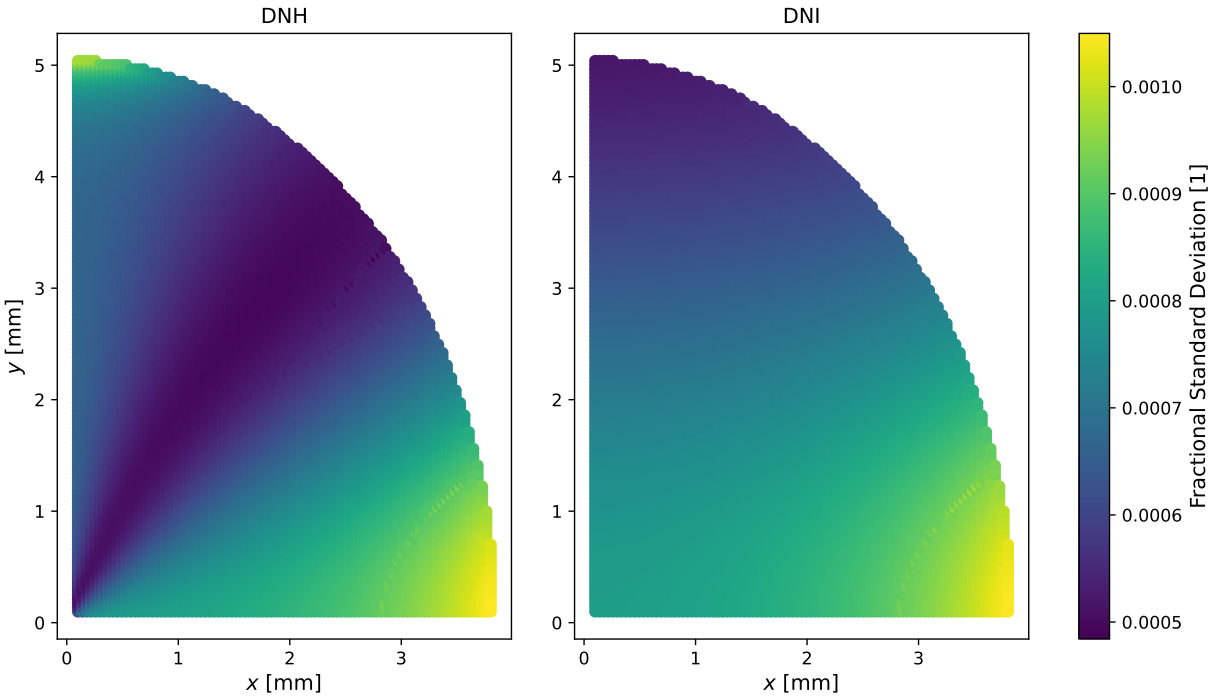


Figure 3.7 Invariant quantities conservation for the full IOTA aperture with 18 thin NIO kicks at $t = -0.238$

will not perfectly match the necessary integration of the potential, so we evaluate the quality of invariant conservation for this reduced number of elements. The following simulation consists of the IOTA style nonlinear insert with 18 equally spaced nonlinear thin kicks. We apply an aperture at the center of the insert consistent with the minimizing aperture in IOTA. Figure 3.7 shows the resulting invariant conservation for the whole simulated grid of macro particles. Here the color scale is the standard deviation of the invariants turn-by-turn and divided by the mean of the invariant quantity over the range, like in figure 3.6. The horizontal and vertical axes correspond to the simulated particles initial position in quadrant one, as the potential is symmetric about both axes. The aperture of IOTA is visible as the elliptical cutoff in the transverse dimensions. We see that the overall conservation quality has gone down, but our standard deviation is still below $1.1\times10^{-3}$. In general, the quality of invariant conservation and approximation of the DN system improves for a larger number of integration steps or slices, though we are limited to what we can practically build.

The $t = -0.238$ is the nominal t-parameter studied further in this dissertation, but we

are also interested in the quality of conservation in more nonlinear-dominated configurations. Identical simulations were performed with the 18 element configuration for a t-parameter $t = -0.45$, which is almost at the vertical integer resonance. The conservation of both invariant quantities was below a fractional standard deviation of $2.5\times10^{-3}$ for this t-parameter.

The equal spacing configuration is the simplest approach to the system, but alternative configurations have been found have superior quality of integration. [9] proposes two alternative integration schemes, an equi-phase insert configuration, and an Yoshida-style [65] higher order integrator. The equi-phase style integration can be straightforwardly implemented as a new insert. Instead of placing elements equally spaced in lab frame position, the elements are equally spaced in bare lattice phase advance. A simulation using 11 equi-phase elements instead of 18 at a t-parameter of $t = -0.238$ showed invariant conservation below a fractional standard deviation of $4\times10^{-3}$. The upper limit on the conservation deviation is dominated by a single region in the configuration space near the horizontal aperture limit. The majority of the range has conservation better than $1.5\times10^{-3}$ like the 18 element equal space case. This is a significant advantage in practically constructing these inserts, as we can arrive at similar NIO system quality with fewer expensive magnets. This configuration is the basis for the second IOTA insert covered in appendix B.

### 3.3 IOTA Tracking Simulation Lattices

For better fidelity simulations of experimental design and comparison, we need to include the full IOTA lattice. The physical dimensions the Impactx IOTA lattice used are based on the publicly released version of the Mad-X lattice. The linear dynamics were benchmarked to this lattice configuration with simple Gaussian beam simulations as Impact-X does not have direct first-order lattice calculation capabilities. The lattice was configured to accept quadrupole settings from SixDSim lattices. In all Impact-X simulations, the fully symmetric model of IOTA was used, matching the lattice in figure 2.7. This is without BPM offsets, dipole gradients, and the undulator corrections for easiest interpretability.

Impact-X supports a number of higher order effects which we can optionally include in the

simulations to verify their impacts on invariant conservation and stability. The base condition considered above uses the linearized versions of the linear elements, i.e. drifts, quads, and dipoles. With respect to longitudinal effects, this means that we are considering dispersion but not chromaticity. To begin to consider chromaticity, we change the quadrupole model to a drift kick model which integrates the full nonlinearities present, and the drifts to the exact model which includes the full geometric nonlinear term in momentum. The combination of this drift model and thin kicks is a sufficient Hamiltonian splitting for arbitrary transverse kicks, so adding nonlinear elements in this lattice properly includes their chromatic effects as well. In this configuration we can evaluate the chromaticity of the lattice, by directly measuring the tune dependence on energy. We see a discrepancy in the natural chromaticity of the Impact-X lattice compared with SixDSim. Additionally, the impacts of the sextupole families based on the nominal calibrations fail to accurately compensate the chromaticity, this likely stems from improper calibration of the sextupole current to strength. Regardless, based on the measured impacts of the sextupoles in Impact-X, we can fully compensate the natural chromaticity in the simulated lattice. For bunched beam simulations in the chromatic lattice we implement a thin linear model of the RF. The bunch length is small compared to the RF bucket, and synchrotron dynamics are not typically relevant compared to momentum deviation and simple stability, so the linear approximation is sufficient. In addition to chromatic effects, we can introduce models of the expected residual nonlinearities in the bare lattice. The two elements considered in Impact-X are quadrupole fringe fields [27] and the "geometric" nonlinearites from the short bending radii of the dipoles [13]. In addition to the larger nonlinear contributions full, nonlinear drift-kick models of the sextupoles can be implemented. We have one more configuration to consider, which is a first-order version of the NIO insert. This is used to evaluate the general lattice with only the first order impacts of the NIO insert. Since the insert is modeled with thin kicks, in Impact-X this is accomplished by simply replacing the DN kicks with thin quadrupole kicks, not the typical linearized thick quadrupole models used elsewhere in the ring. We now have many basic lattice configurations

| Nickname | Lattice Description |
|---|---|
| toy | Thin, equal focusing matrix for linear matching. 1800 equally spaced thin kicks for NIO insert. |
| linmin | Linearized IOTA model, linear thick quads, linear thick dipoles, linear drifts. Minimizing aperture matching that in real IOTA. 18 thin kicks for NIO insert matching physical insert, with linear drifts between. |
| crom | Nonlinear drift-kick quadrupoles, exact nonlinear drifts, linear thick dipoles. Minimizing aperture matching that in real IOTA. Thin sextupoles may be used, treated seperately. Thin linear RF model included for bunched beam simulations. 18 thin kicks for NIO insert matching physical insert, with exact nonlinear drifts between. |
| nonlin | Nonlinear drift-kick quadrupoles with thin fringe field models, exact nonlinear drifts, exact nonlinear dipoles. Minimizing aperture matching that in real IOTA. Drift-kick sextupoles may be used, treated separately. Thin linear RF model included for bunched beam simulations. 18 thin kicks for NIO insert matching physical insert, with exact nonlinear drifts between. |
| quadnio | Same matching lattice configuration as "nonlin", but 18 NIO kicks in insert are replaced with proportionately scaled thin quadrupole kicks. |

Table 3.1 IOTA Simulation Lattice Configurations

which will be swapped between in the upcoming chapters, the have been given nicknames and associated descriptions in table 3.1. Sextupole strength configurations are in general more flexible and treated separately.

In addition to the linear lattice benchmarking, identical simulations using the "linmin" lattice to those carried out with the thin matrix yielded similar invariant conservation levels as seen in Figure 3.7. We can look at the detuning range given by the realistic aperture in Figure 3.8 for $t = -0.238$ in "linmin". The overall detuning shape is the same, but the range is much smaller, especially from the reduction in horizontal aperture. The interpretation problem of the tunes near the integer resonance disappears in this realistic configuration, which simplifies the experimental analysis.

### 3.4 Energy Dependence Simulation

We can evaluate the impacts of realistic momentum deviation on the system with controlled offsets. In the following simulations, we consider an initial distribution consisting of

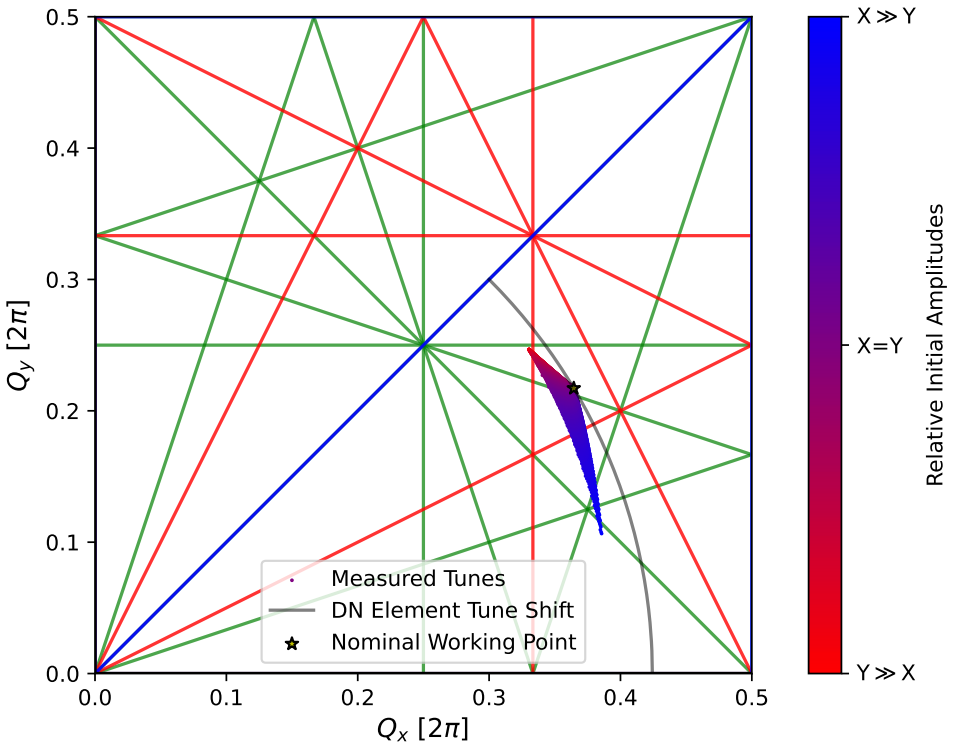


Figure 3.8 Amplitude dependent detuning for IOTA with $t = -0.238$

transverse particles which fill the available aperture at a select group of initial momentum offsets. We are primarily interested in the relative stability at these locations, so there is no RF applied, and the macroparticles are permitted to slip longitudinally as in a coasting beam. Before we commit to these simulations, we will verify that the grid in $x$-$y$ is a sufficient initial condition to sample the whole phase space. For the linear Hamiltonian, this will uniformly cover the available phase space, but the full phase space of nonlinear systems is not necessarily sampled by a uniform distribution in one phase space variable. We have some confidence, because the underlying system is integrable it is smoothly differentialble in phase space variables, so there should be no isolated regions in phase space. This assumption breaks down with perturbations to the system in the form of additional nonlinearities. To verify, a simulation in the "crom" with 4-D initial conditions was performed. The base structure consisted of a $x$-$y$ grid, and for each point in configuration space a smaller range of $p_x, p_y$ points was added. The energy offsets were also included to evaluate their impacts. Figure 3.9 shows the fractional standard deviation in the DN Hamiltonian plotted against

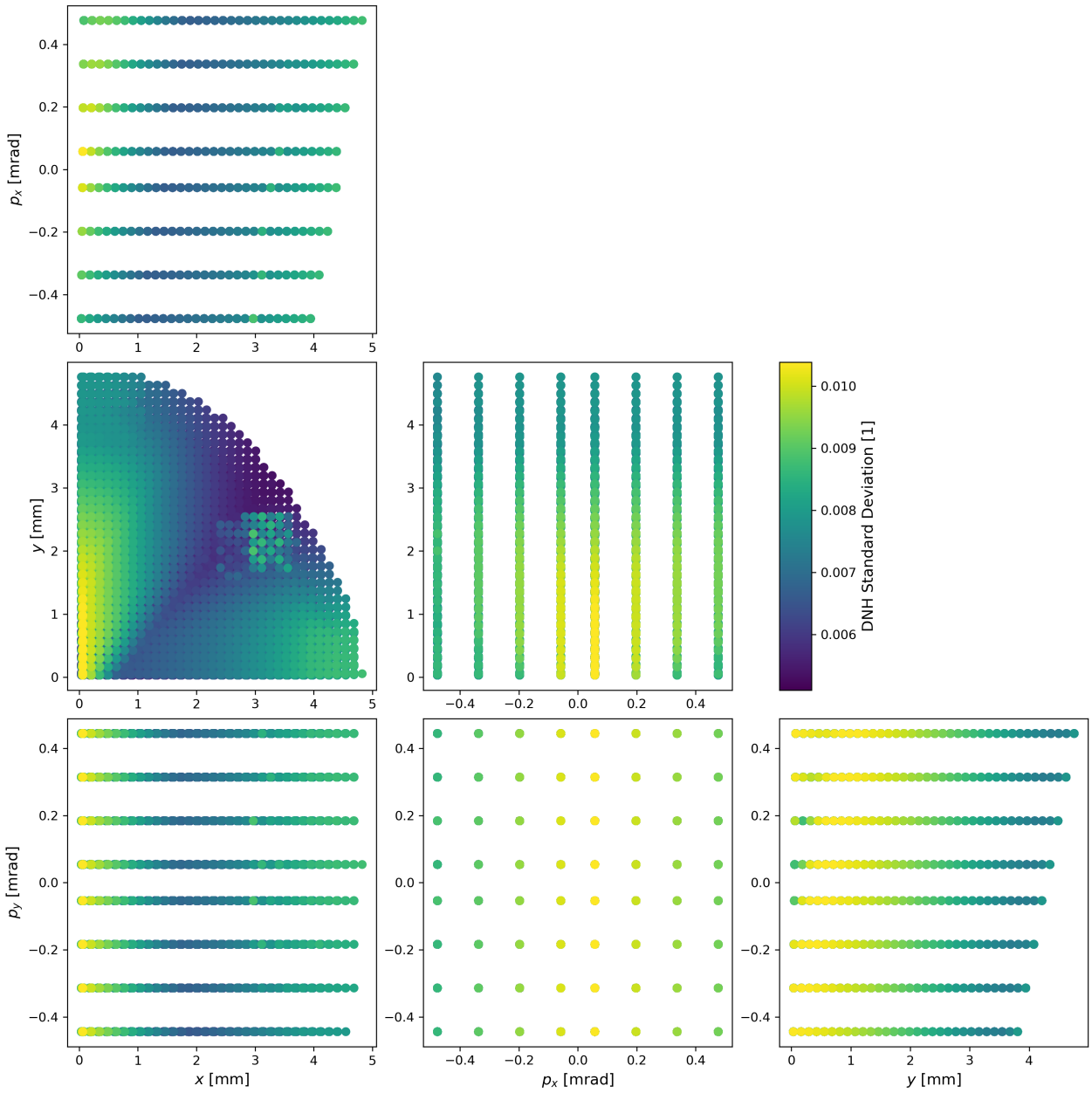


Figure 3.9 DN Hamiltonian fractional standard deviation against transverse phase space variables

the initial positions in phase space. The plotted points have no momentum deviation. All simulated particles are plotted, so naturally, some are obscured by later points, here they have been sorted by conservation so the "worst" points rise to the top.

We see that generally, conservation is reasonable with the nonlinear contributions from chromatic drifts and quads. More importantly, we can see that there is no significant corre-

lation on invariant conservation against initial momentum. The only point of concern is the cluster of unusual poor conservation around $x = 3, y = 2$. This picture becomes more clear if we instead plot the conservation with respect to the maximum amplitude as calculated by the effective emittances. Figure 3.10 shows the fractional invariant conservation for both DN invariants, Hamiltonian on the left and second invariant on the right. Here the color scales are unified, if invariant standard deviation is below $5\times10^{-3}$ it is colored dark blue, and if over $5\times10^{-2}$ orange. The horizontal and vertical coordinates are the maximum amplitudes at the IOTA minimum aperture calculated by using the first order effect of the nonlinear insert to calculate the effective emittances. The third plot from the top on the left corresponds to the same points, and we see that this region of poorer conservation in 3.9 corresponds clearly to a line in the reduced quality conservation in combined amplitude, presumably stemming from a nonlinear resonance.

We can further compare this conservation picture with a similar plot of the invariant conservation for only initial position seeds in 3.11. All of the same features are present at a higher resolution for many fewer simulated particles due to the reduced dimensionality.

We now want to evaluate the impacts of chromatic compensation with sextupoles on the dynamic aperture and invariant conservation. This is the generic approach to matching the chromaticities and maximizing decoherence times for the bare lattice in experiment. This should nominally compensate for the energy dependence of the invariant conservation seen in figure 3.11. Figure 3.12 shows the resulting conservation plots. We see that conservation is significantly impacted, the threshold for the orange points has been raised to a fractional standard deviation of $5\times10^{-1}$ for reasonable comparison. Clearly this means that the NIO system is not well represented here. Additionally, the sextupole effects introduce a significant reduction in the dynamic aperture, especially in regions detuning to the sextupole resonant lines.

We can also simulate the impacts of expected nonlinearities in our lattice with the "nonlin" lattice configuration. Here we do not include sextupole contributions. This condition

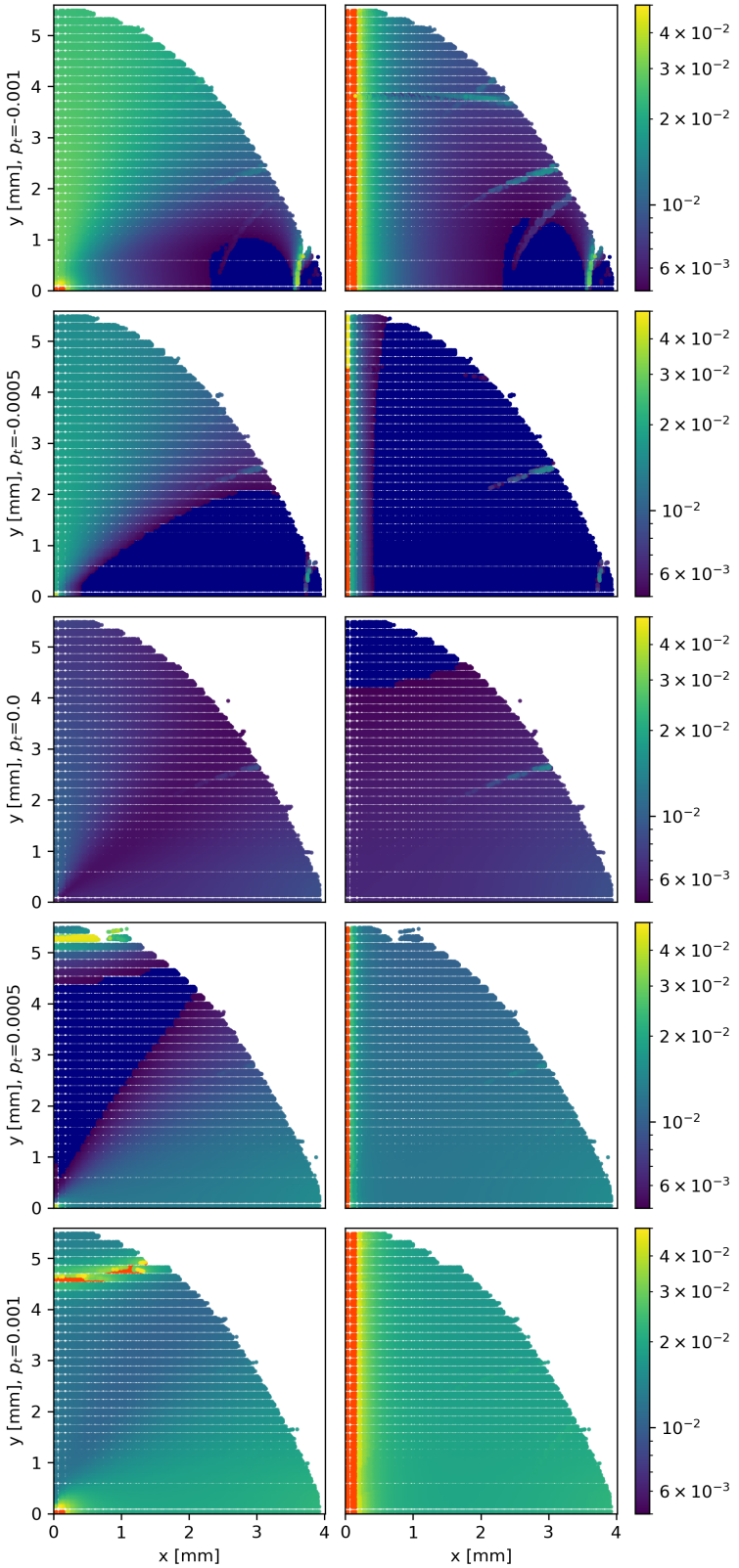


Figure 3.10 DN Invariants fractional standard deviation against maximum amplitudes calibrated by effective Courant-Snyder emittances and initial momentum offsets

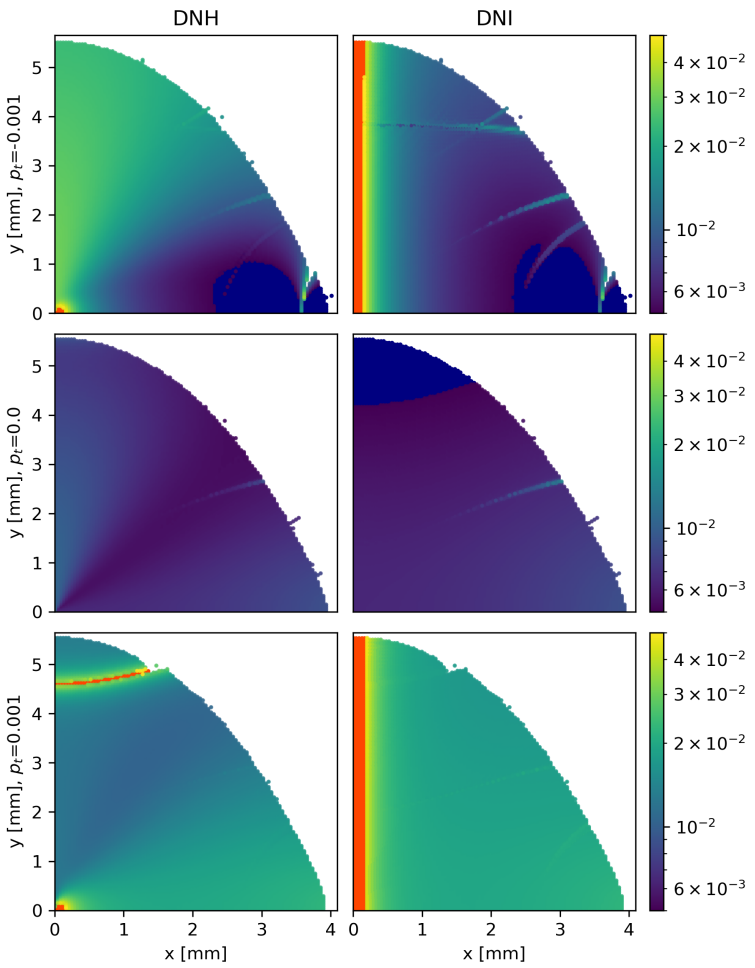


Figure 3.11 DN Invariants conservation for flat initial positions with all momentum $p_x, p_y$ zero. Orange points indicate values with over $5{\times}10^{-2}$ fractional deviation in the invariants. Blue points indicate values below $5{\times}10^{-3}$ fractional deviation in the invariants.

is milder than the sextupole impacts, we can revert to the orange upper limit at $5{\times}10^{-2}$. Generally, outside of the impacted upper regions

Finally, we can consider the expected nonlinearities and the sextupole compensation. We need to increase the orange threshold to $5{\times}10^{-1}$ again. invariant conservation is poor, and dynamic aperture is significantly reduced, though the main impacts seem to stem from the sextupole terms. It is difficult to evaluate the invariant conservation dependence on the energy offset. This is the nearest simulation configuration to the expected dynamics in IOTA. As the invariant conservation is quite poor for these noiseless measurements, this throws into doubt the possibility to directly measure the conservation of invariant quantities from turn

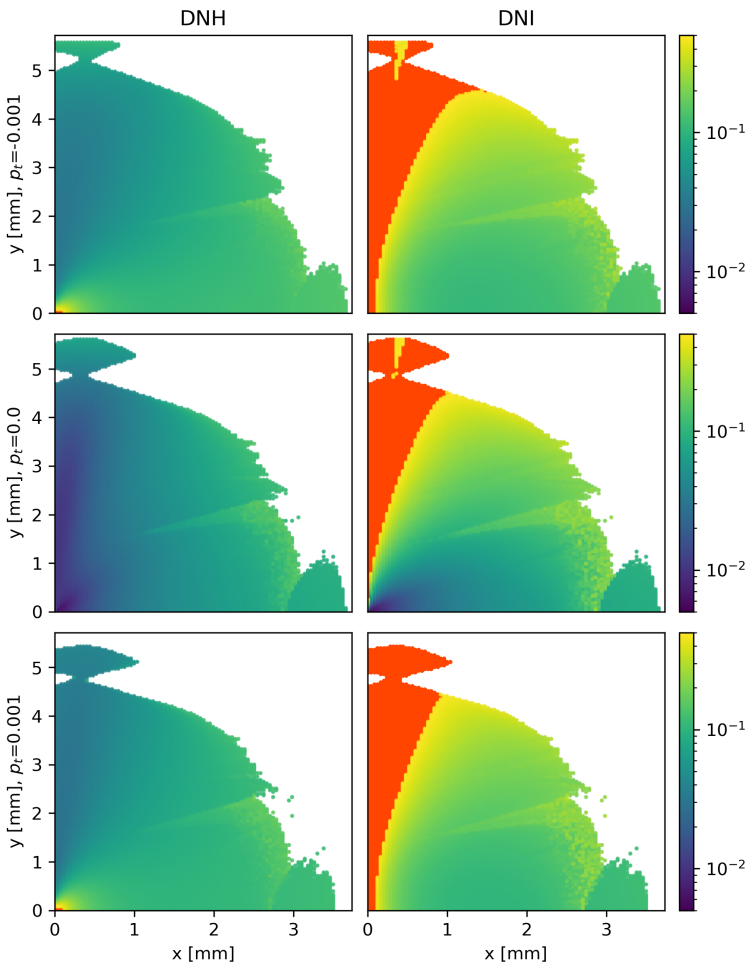


Figure 3.12 DN Invariants conservation for flat initial positions with sextupole compensation of chromaticity. Orange points indicate values with over $5\times10^{-1}$ fractional deviation in the invariants.

by turn measurements, especially with sextupoles. Unfortunately, these simulations were performed after the experimental measurements, and were not available for guiding the experimental design.

### 3.5 Bunch Simulations

The IOTA electron experiments leverage the fact the electron beam is small and can act as a macroparticle probe of the dynamics. Some simulations were performed to verify that this assumption holds in the strongly amplitude dependent NIO system. To evaluate this, a 10,000 particle bunch with emittances comparable to those measured in the bare iota lattice was initialized. An "index" particle was also placed with zero amplitude. The whole bunch

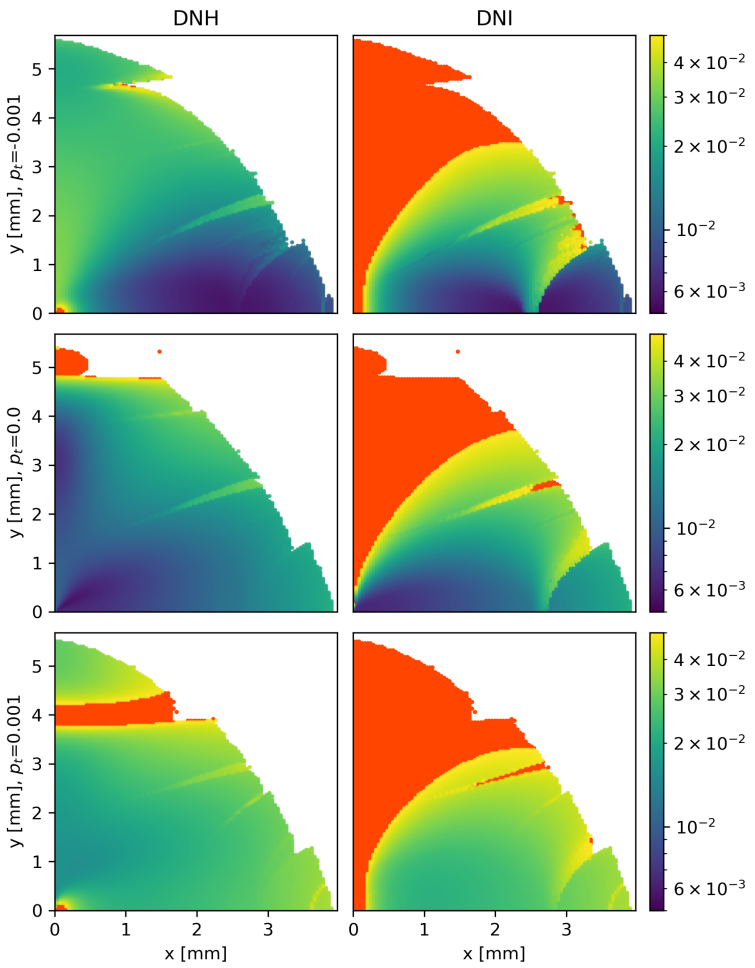


Figure 3.13 DN Invariants conservation for flat initial positions with expected residual nonlinearities. Orange points indicate values with over $5{\times}10^{-2}$ fractional deviation in the invariants.

and index were then given coherent instantaneous momentum, analogous to the action of a kicker. The individual particles, index particle, and beam centroid could then be tracked through the ring. The index represents the actual point probe of the dynamics for a given amplitude, and the centroid is a close approximation of the signal on the BPMs. These simulations are interesting in the context of a bunched beam which necessarily includes chromatic effects. The first simulation is for an initial kick of $\delta p_x = 2{\times}10^{-3}$ [1] and $deltap_y = 2{\times}10^{-3}$ in the "crom" lattice without sextupole compensation. The initial and final configuration in $x$-$y$ configuration space is plotted in Figure 3.15. This is a good illustration of the relatively flat beam and the mostly linear response of the kicked beam, the final state after 1200 turns

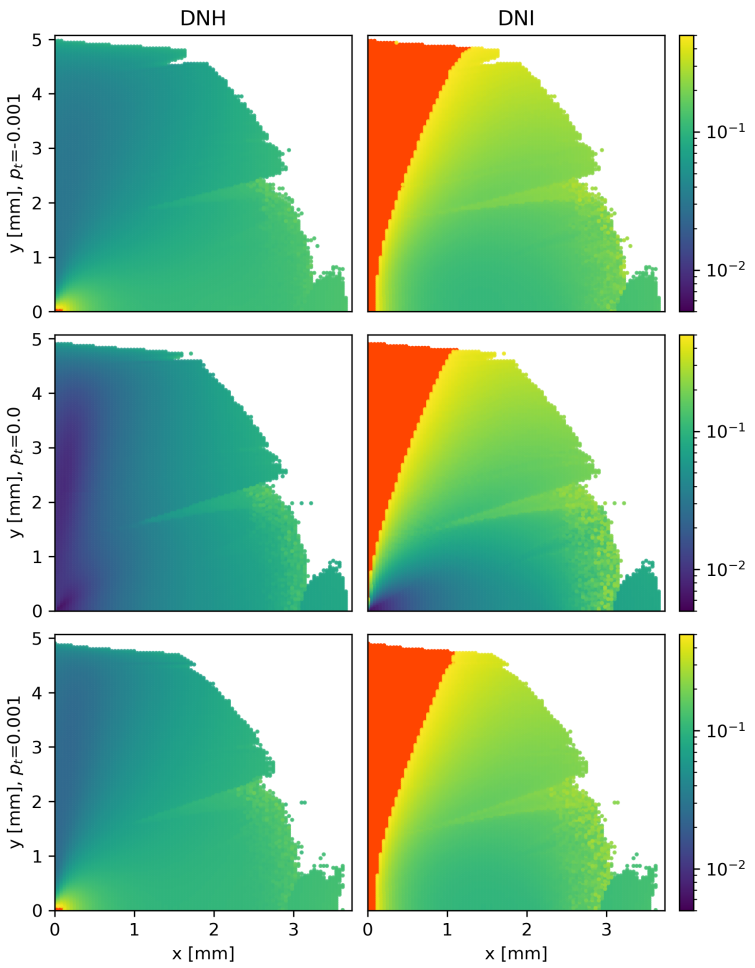


Figure 3.14 DN Invariants conservation for flat initial positions with expected residual nonlinearities. Orange points indicate values with over $5\times10^{-1}$ fractional deviation in the invariants.

is the typical four pointed distribution.

We can look at the calculated centroids TBT in Figure 3.16, this is analogous to the signal we expect to see on the BPMs. Immediately the decoherence from the tune footprint of the beam is obvious and gives us an idea of what we may expect in experiment. This also informs the range we can measure the tune over.

To evaluate the quality of the bunch probe, we can investigate the tune for the index particle, which is on momentum with exactly the kick amplitude, the centroid of the bunch, and the individual simulated particles. Figure 3.17 shows the calculated tunes for the index, centroid, and the tune footprint of the beam. For this configuration, we see that the beam

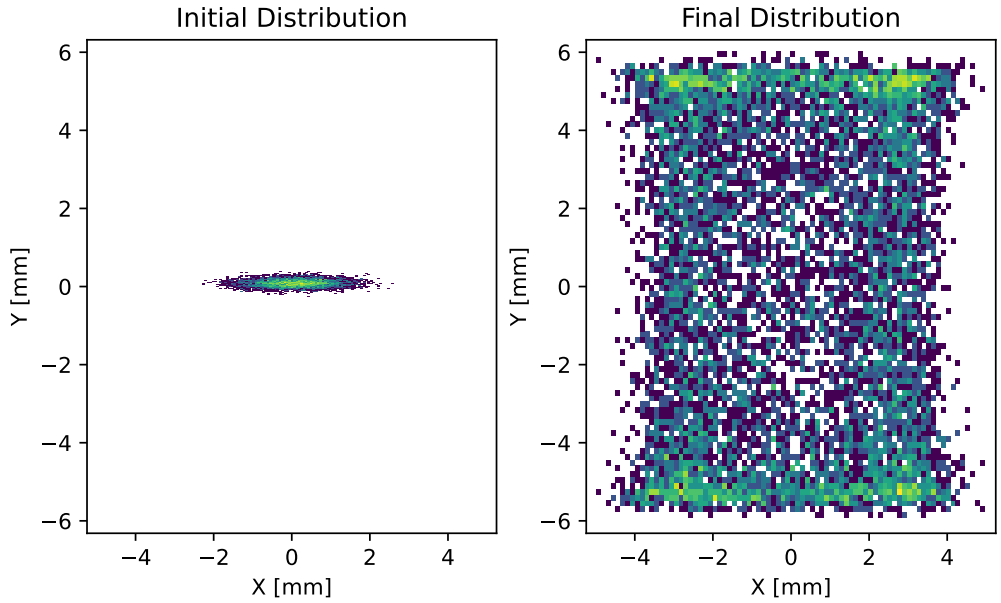


Figure 3.15 Transverse density profile of kicked bunch simulation for initial distribution and final distribution after 1200 turns.

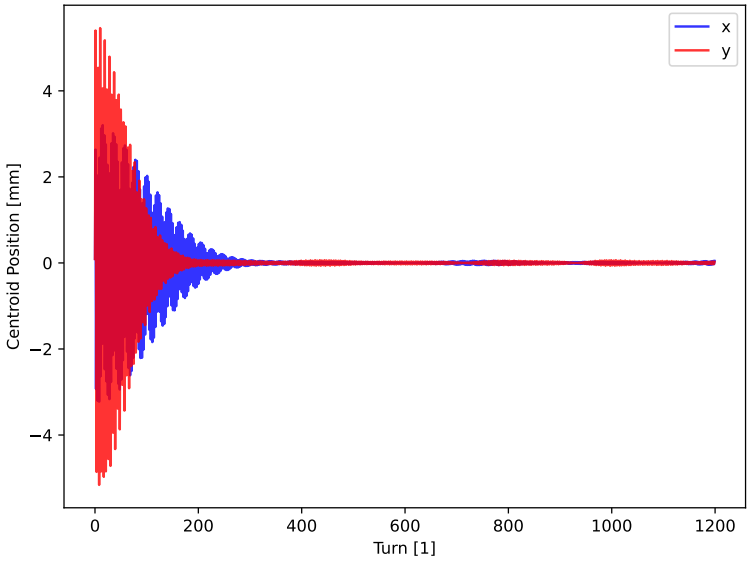


Figure 3.16 Bunch centroids calculated from simulated distribution, "crom" lattice without sextupole compensation.

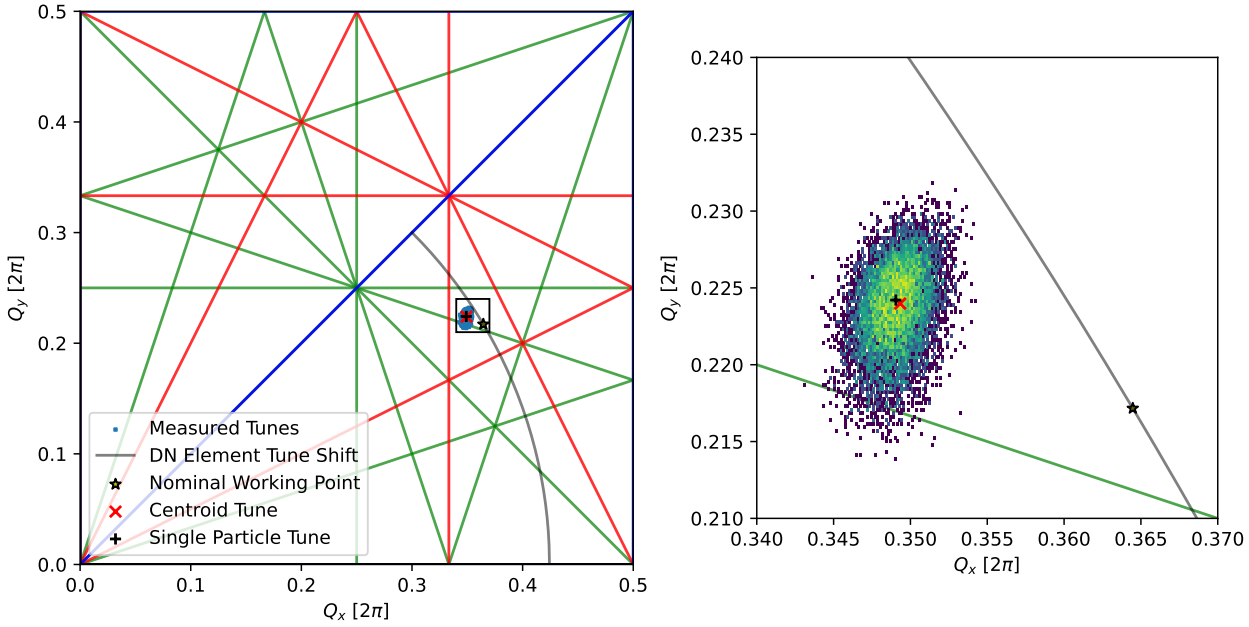


Figure 3.17 Amplitude dependent detuning for kicked bunch, in "chrom" lattice without sextupole compensation. Black cross indicates nominal single particle tune, red cross indicates tune measured from bunch centroid, density plot is tune footprint of simulated bunch.

centroid tune closely resembles the equivalent single particle probe of our index particle. The index particle tune is calculated over the full range of 1200 turns, as it is the nominal on-momentum dynamics probe. The tune footprint measurements are over 400 turns to minimize the impacts of synchrotron motion on the detuning. Finally the centroid tune is calculate over 60 turns to accurately capture the large amplitude region before strong detuning.

We can look at the tune distributions directly in Figure 3.18, and see that in this relatively clean lattice configuration the tune footprint is well distributed about the nominal and centroid tunes. The detuning is dominated by the nonlinear insert and the chromatic tune footprint only mildly impacts the distribution.

The next obvious comparison is the tune measurements with our chromatic compensation. Nominally this should reduce the tune footprint due to energy spread and improve our coherence times. Additionally, this is the expected necessary condition for a stable working

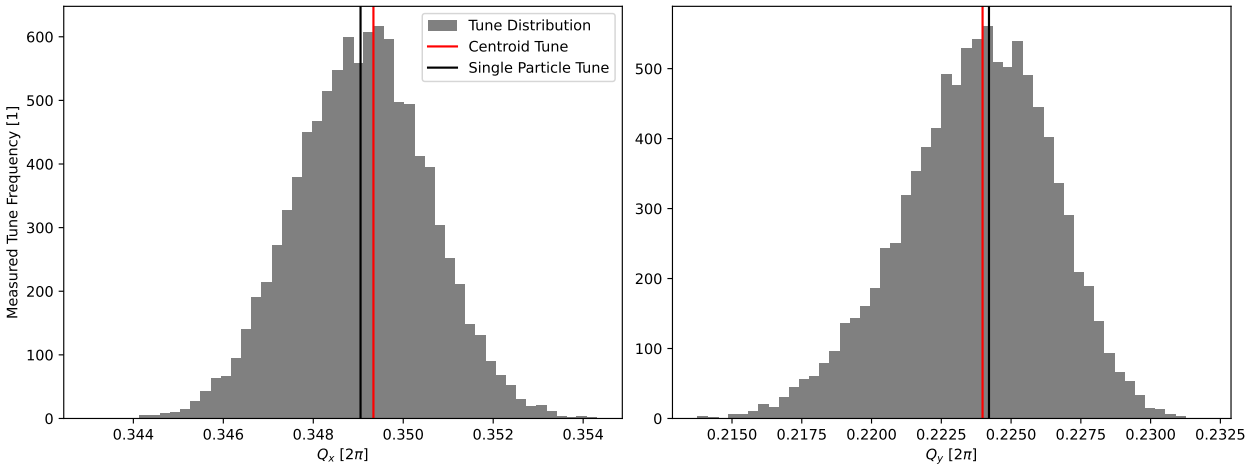


Figure 3.18 Distribution of simulated tune footprint for "crom" lattice without sextupole compensation.

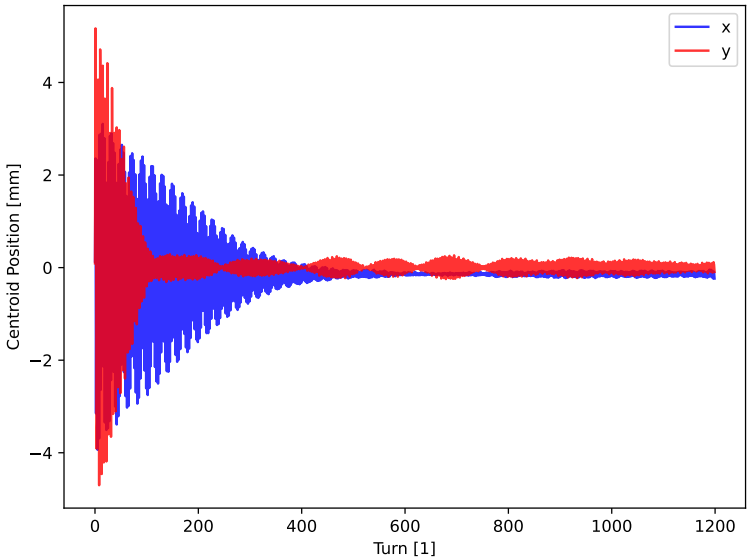


Figure 3.19 Bunch centroids calculated from simulated distribution, "crom" lattice with sextupole compensation.

point with the nonlinear insert. Figure 3.19 shows the resulting centroid decoherence with fully compensated chromaticity in the "crom" lattice. In this clean configuration, we see negligible change in the vertical decoherence and an increase in the horizontal length.

Inspecting the tune footprint in Figure 3.20, we see the impacts of the nonlinearities, some large amplitude particles are captured on the sextupole coupling resonance. Nonetheless, for the same tune calculation ranges the centroid still closely matches the nominal "index"

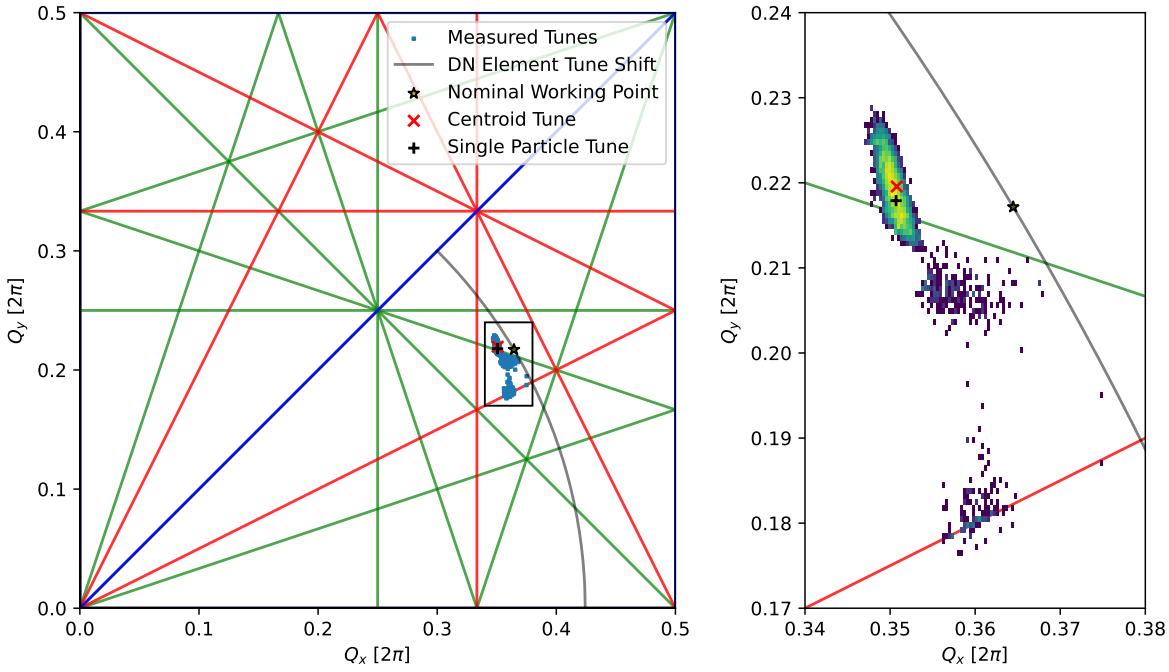


Figure 3.20 Amplitude dependent detuning for kicked bunch, in "chrom" lattice with sextupole compensation.

particle.

Finally we consider the tune footprint for the full "nonlin" lattice with sextupole chromatic compensation in 3.21. Here the resonant capture effects are quite strong, we see significant components of the beam trapped on the third and fourth order coupling resonances for our nominal kick away from these locations. Nonetheless, with short samples of the turns, the centroid tune measurements remain robust and comparable with the nominal tune.

The importance of selecting relevant turn ranges for tune calculation is well illustrated in Figure 3.22. This is the same lattice condition as above, "nonlin" with full sextupole chromatic compensation with different kick amplitudes of $\delta p_x = 2.2{\times}10^{-3}$ [1] and $deltap_y = 1.2{\times}10^{-3}$ [1] to get a larger fraction of the beam on the sextupole coupling line. The index and tune footprint calculation ranges are the same, but the centroid tune is calculated over 200 turns, so the resonantly captured particles begin to dominate the measurement. We see that the centroid tune becomes resonantly captured and does not represent the nominal

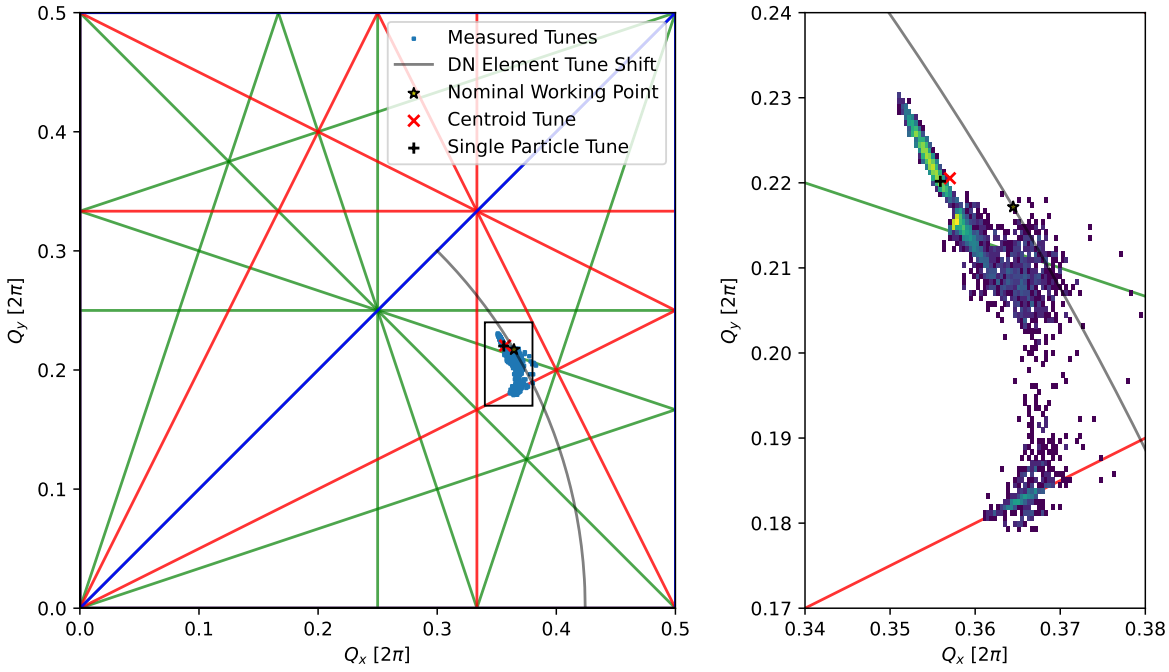


Figure 3.21 Amplitude dependent detuning for kicked bunch, in "nonlin" lattice with sextupole compensation.

"index" amplitude. This effect is reproduced in experiment, as further discussed in sections 4.1 and 5.4.

### 3.6 Theoretical Lattice Improvement Simulations

Based on experimental results, a number of potential improvements to the bare lattice configuration were considered in simulation. The simplest impact evaluated was to minimize the emittance of the electron beam. This has the effect of making the beam more point-like, and most importantly reduces its tune footprint. A reduced footprint means extended coherent centroid oscillations and improved sensitivity for all major turn-by-turn measurements. The main contributor to emittance is the dispersion in the 60 degree dipoles. For the NIO lattice, the dispersion and its derivative must be zero at the end of these dipoles on the face near the insert to match the NIO condition. In the dipole the derivative of the dispersion monotonically increases, so the simplest approach to reduce these integrals in the 60 degree dipoles is to configure them as a so called double bend achromat [39, pg.133]. An example lattice which retains the core NIO requirements with a DBA like structure in the 60

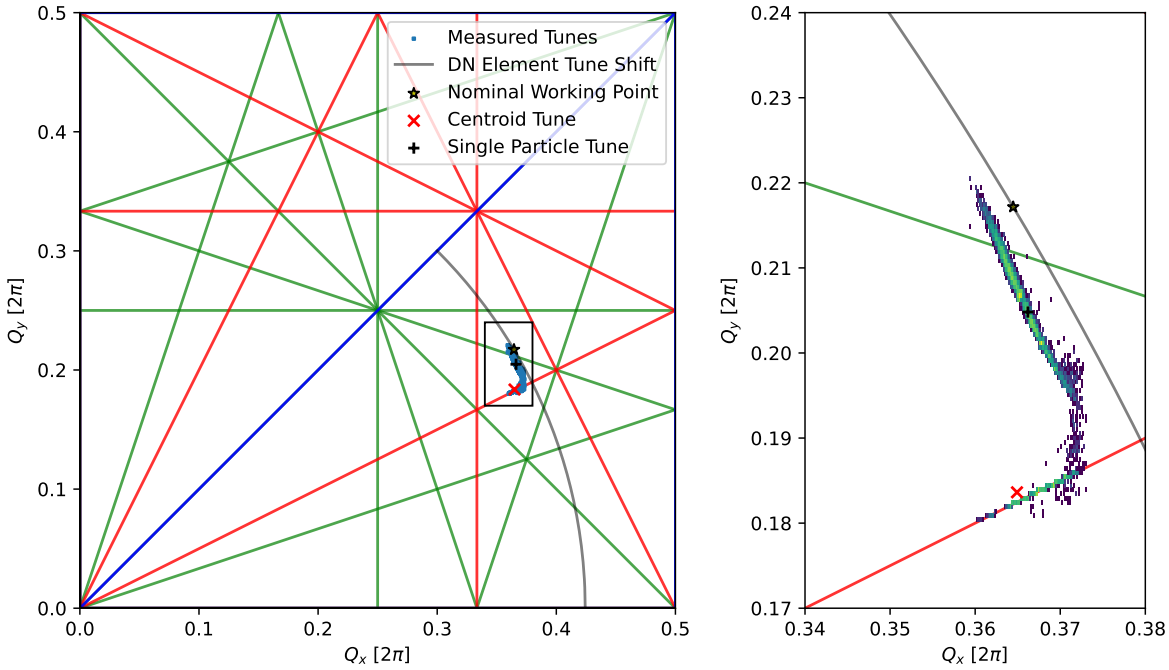


Figure 3.22 Amplitude dependent detuning for kicked bunch, in "nonlin" lattice with sextupole compensation. Amplitude selected to demonstrate resonant capture of centroid tune measurement away from nominal single particle tune.

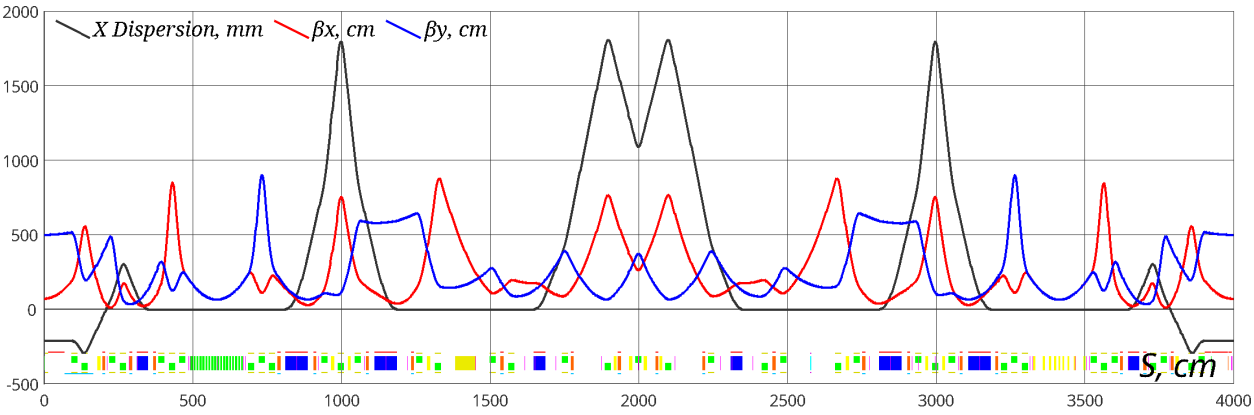


Figure 3.23 SixDsim lattice plot of the lower emittance DBA-style IOTA configuration.

degree dipoles is presented in Figure 3.23. This lattice results in over an order of magnitude reduction in equilibrium emittance in the horizontal plane, from $1.67\times10^{-5}$ to $1.01\times10^{-6}$ [cm-rad] as calculated by SixDsim using the radiation integrals [39, pg.438].

The resulting detuning impacts on a simulated TBT response can be seen in Figure 3.24. The tune footprints for an example kick amplitude of beams at the equilibrium emmittance

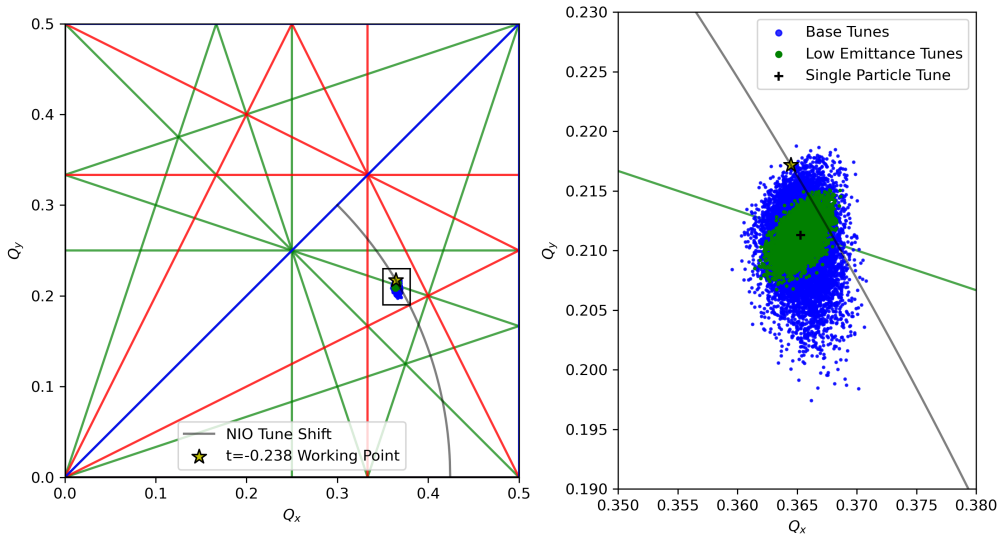


Figure 3.24 Single bunch kicked beam tune footprints before and after lattice emittance minimization.

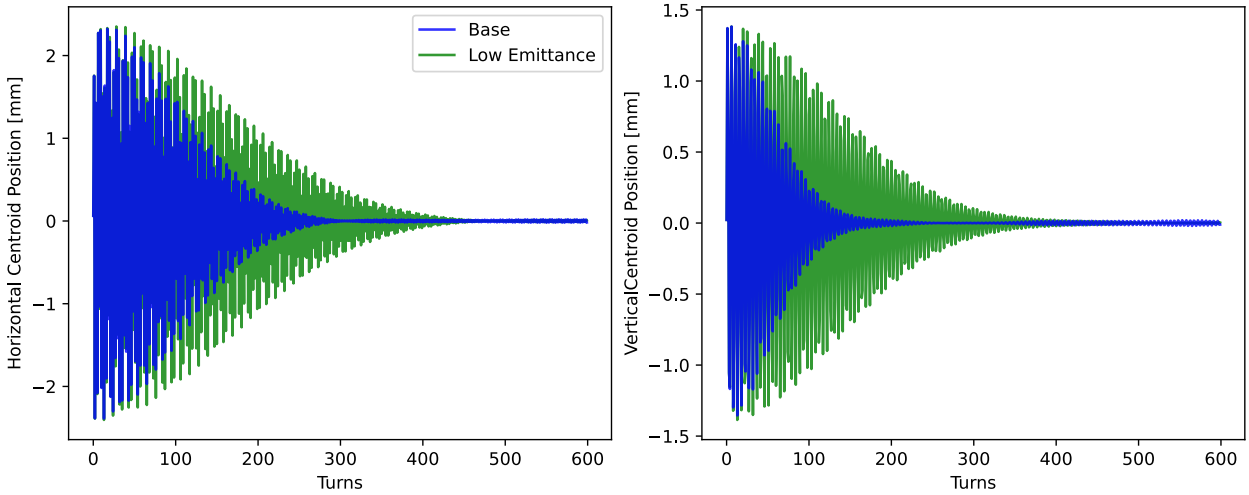


Figure 3.25 Decoherence profiles for kicked beam simulations before and after lattice emittance minimization.

for the generic NIO and low-emittance lattices are plotted in blue and green respectively.

The results on the decoherence as measured by the mean of the transverse coordinates are given in Figure 3.25. We see about a factor of two improvement on the vertical decoherence, a relevant factor as this is often the limiting number in the tune and phase space reconstruction.

This lattice represents only the first pass on the optimization, but is readily applicable for the IOTA lattice and within the bounds of the current quadrupoles. In addition to the

emittance minimization, tuning of the natural chromaticities of IOTA was considered. The main consideration for NIO lattice operation is matched chromaticities in the horizontal and vertical planes. The natural chromaticites in IOTA are already near each other. A lattice was optimized to bring these chromaticities to match, though the symmetry of IOTA had to be broken. This was accomplished with a general optimization using the full range of IOTA quadrupoles, there is not a simple linearly scaling knob to adjust the natural chromaticities in this way. Due to the imperfect matching between the SixDSim and Impact-X calibrations, the quality of the NIO condition degraded somewhat. The resulting invariant conservation versus energy spread is given in Figure 3.26. We can see that the overall conservation in the zero energy condition is slightly compromised, likely due to this imperfect bare lattice. But, more importantly, the invariant conservation for off momentum particles is improved, especially for higher amplitudes.

## 3.7 IOTA Proton Injector Simulations

While electron experiments are the primary focus, the IOTA proton injector line was being formalized and constructed during the course of this work. Some simulations were undertaken for evaluating the impact of space charge effects in the proton injector beamline.

The IOTA proton source was characterized in the past [58], and these emittances were used as the starting point for the simulation. The source configuration has since changed, so these values are not expected to be the exact configuration in the current beamline. As a result a range of currents and their associated measured emittances were used to initialize the simulations. Currents of 8, 2, and 0 [mA] were simulated. We expect space charge neutralization in the LEBT, so these output emittances were used directly as the inputs to the RFQ simulations, in conjunction with the well understood matched incoming lattice functions.

The RFQ simulations were performed with the TRACK code, as it was the original code used to design the RFQ in question [51]. The HINS linac was intended to be focused entirely with superconducting solenoids, so the incoming and outgoing beams from the RFQ needed

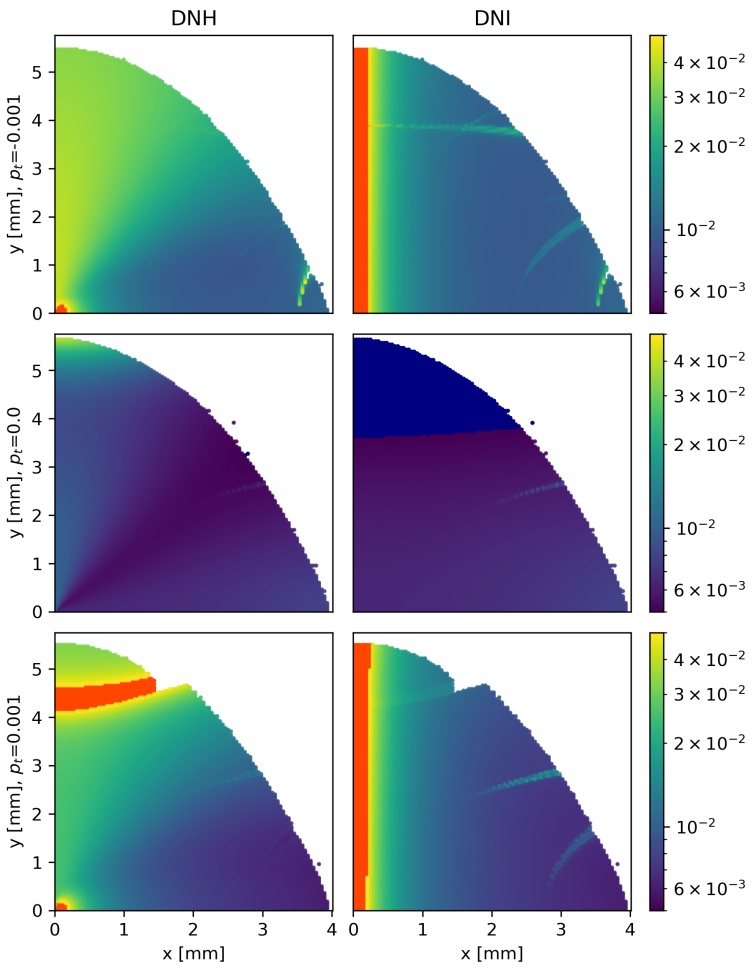


Figure 3.26 Invariant conservation for lattice with approximately matched natural chromaticities

to be axially symmetric. This was accomplished through deliberately shaped electrodes for matching at the end of the otherwise typical RFQ vanes. These elements are represented as custom 3-D EM fields in TRACK and necessitated reviving the original simulation files. Space charge was modeled with particle in cell kicks. Table 3.2 summarizes the essential quantities for the RFQ outputs at the extremum currents. Figure 3.27 shows the output Poincare sections of the outputs for the extremum currents as well. The input distribution was transverse waterbags with a DC longitudinal structure, so of most interest is negligible transverse emittance growth and reasonable bunching. As we can see, the output longitudinal envelope is current independent in this range. The slight reduction in 8 [mA] emittance can be attributed to small mismatch losses. The longitudinal "cyclone" structure in the 0 [mA] is

| Current [mA] | Input $\epsilon_{x,y}$ [mm-mrad] | Output $\epsilon_{x,y}$ [mm-mrad] | Output $\epsilon_{ct}$ [mm-mrad] |
|---|---|---|---|
| 0 | 2.05 | 2.1 | 9.1 |
| 8 | 6.8 | 6.5 | 8.5 |

Table 3.2 TRACK RFQ simulation results

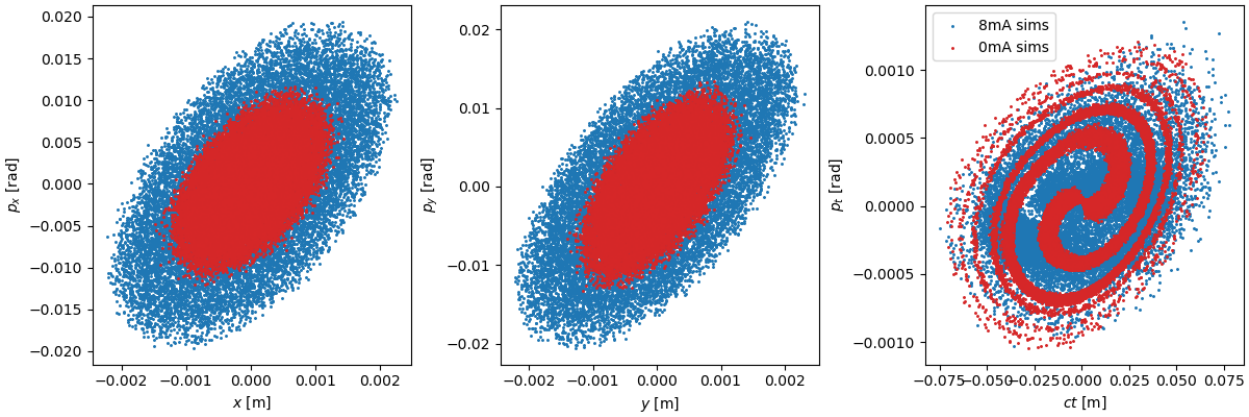


Figure 3.27 Output bunch profiles from TRACK RFQ simulation

not expected to significantly affect the dynamics downstream and can be seen to reasonably smear out with more current.

The second order moments were calculated for these output distributions and used as the seeds for input distributions, both waterbag and Gaussian, into Impact-X simulations of the MEBT. At the range of currents considered, there are negligible transverse impacts, and we are primarily interested in the evolution of the longitudinal structure. The MEBT simulations ran from the output of the RFQ to just beyond the extent of the vertical injection kicker in IOTA, so the resulting distributions could be direcly used for injection simulations. The ImpactX PIC solver does not have periodic boundary conditions, so to mitigate unpredictable results at the edge of the grid, the tracked bunch was "bookended" by identical bunches at the RFQ wavelength, as in figure 3.28. The analysis was only considered for the central bunch, but the self-fields are calculated for all of the bunches.

Figure 3.29 shows the resulting bunch lengthening in the MEBT for different input distributions and currents space charge. For the largest growth configuration, this is almost

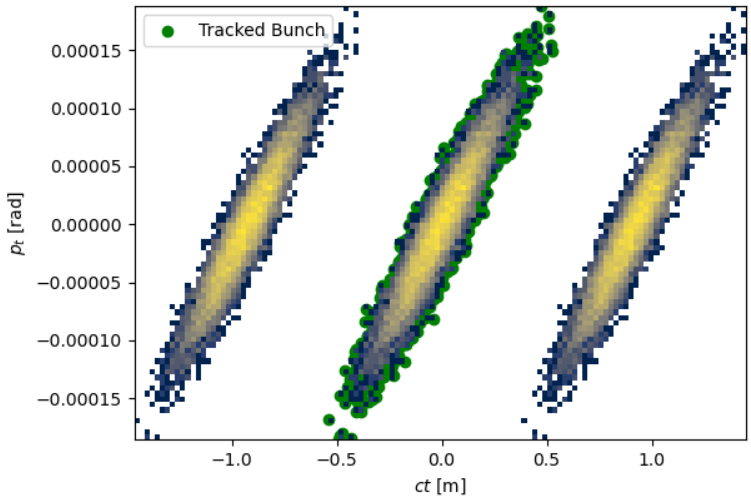


Figure 3.28 "Bookended" bunches for MEBT space charge simulation

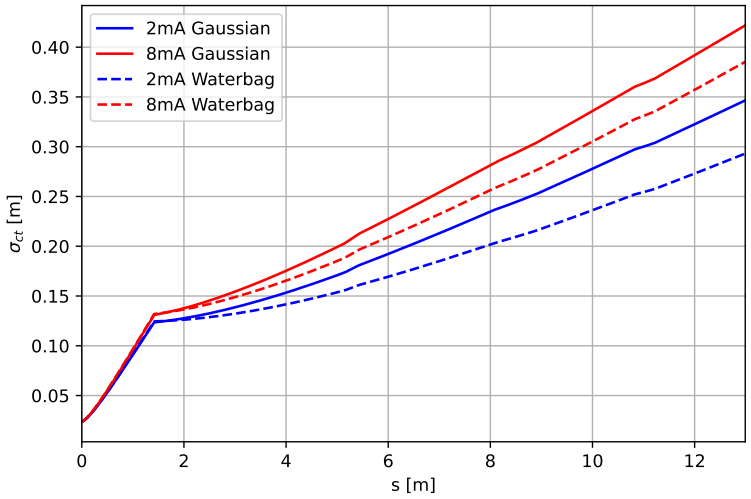


Figure 3.29 MEBT bunch lengthening

fully debunched. While we do not need bunched beam to stably circulate in IOTA, the residual bunch structure is the intended mode for tuning injection into IOTA. In principle, the debunching cavity (visible as the sharp kink in the growth curve) may be moved slightly downstream to increase its action on the bunch length.

Using the resulting emittances from the MEBT simulation, the injection efficiency into IOTA was simulated. The tuning knobs at the end of the MEBT are strongly constrained by the large edge focusing from the final dipole. To optimized the injection efficiency into IOTA, the lattice functions at the injection were allowed to vary. Based on these results,

| Input | Initial Losses | Optimized Losses |
|---|---|---|
| Results using minimum source input emittance | | |
| 0 mA Gaussian | 1.31% | - |
| 2 mA Gaussian | 2.49% | 2.05% |
| 8 mA Gaussian | 15.42% | 12.02% |
| 8 mA Waterbag | 12.74% | 7.83% |
| Results using maximum source input emittance | | |
| 8 mA Gaussian | 39.78% | 37.55% |
| 8 mA Waterbag | 44.21% | 41.75% |

Table 3.3 Bare lattice space charge injection optimization results

the intent is to best match the MEBT by adding small permanent magnet quadrupoles, but the range of this tuning is naturally limited. Based on preliminary simulations of injection into IOTA the beam debunches very quickly. The Impact-X space charge models available at the time of the simulation did not handle coasting beam well (this functionality has recently been added), so only the first 8 turns were simulated, after which every case was fully debunched. To optimize injection, the transverse lattice parameters were applied as the independent parameters to a Bayesian optimization algorithm with losses over the initial turns as the figure of merit. The optimization algorithm in question was from the Xopt package [55]. Table 3.3 shows the optimization results for injection losses before and after tuning. Matching is improved for the lower initial emittance case considered, but if the source output is at the upper end of the earlier measurements, we can expect substantial losses on injection.

Finally, the same approach was used for a full NIO lattice with the nonlinear insert excited. If beam lifetime is short, this may be the preferred approach instead of ramping the insert strength after injection. Table 3.4 shows the similar results as above for the NIO lattice. Only the low initial emittance was considered as the losses are so large in the previous case, and matching optimization seems to have negligible results. We see a similar scale of improvement with the NIO insert for the higher space charge conditions. The resulting lattice functions from this optimization are expected to guide injection tuning

| Input | Initial Losses | Optimized Losses |
|---|---|---|
| 0 mA Gaussian | 1.46% | - |
| 2 mA Gaussian | 3.23% | 2.05% |
| 8 mA Gaussian | 27.41% | 17.22% |

Table 3.4 NIO lattice

as commissioning continues.

# CHAPTER 4

# EXPERIMENTAL ANALYSIS METHODS

## 4.1 Tune Measurements

Tune measurements provide long term coherent information on the dynamics and the strong dependence on amplitude is the chief experimental indicator of nonlinearities in the focusing. While decoherence limits the available turns for measurements, the variations in amplitude do not alter the fundamental frequency, which gives us a longer coherent signal. The tune was previously defined only for the linear system in the context of phase advance. The definition of the tune is more nebulous then for a strongly nonlinear system, as the motion is necessarily anharmonic. For nonlinear dynamical systems, the Poincare rotation number is a related quantity [46], but difficult to relate to measurable quantities. For the experimental measurements, we interpret the dominant frequency of the transverse oscillation spectrum as the tune.

Different tune measurement algorithm were considered for the particular limitations of the available data. The simplest approach is simply taking the Fourier transform of turn by turn (TBT) BPM data and picking the peak frequency. As we have discrete sampling of the motion, a discrete Fourier transform is a simple first approach. Practically, the fast Fourier transform (FFT) is used as the default discrete transform. There are a number of methods to improve the resolution of the frequency measurements. In principle a windowing function can be applied to improve resolution of the peak frequency at the cost of suppressing sidebands. However, for the IOTA data, there are two important considerations. A window suppresses the amplitude of a fraction of the sample window. In the case of the short coherent measurements, the reduction in available signal was more detrimental than the advantages of the window. And for low signal to noise ratios the benefits of a window disappear. For example, the common Hann window does not provide any benefits for signal to noise ratios less than $1\times10^3$ [7], well above those seen in IOTA. To bypass some of the limitations on the discrete sample resolution of the FFT, Jacobsen interpolation [33] applies

a quadratic interpolation to the FFT peak and its nearest neighbors for finer peak resolution. The implementation used is based on that from the PyLHC [15] analysis library. The other approach considered is the Numerical Analysis of Fundamental Frequencies (NAFF) proposed by Laskar for the evaluation of long term stability of planetary systems [38]. NAFF starts with a guess from the FFT spectrum, and seeks to iteratively optimize the magnitude of a single Fourier transform as in equation 4.1. In principle this can be used to extract successive harmonics of the motion, but we are interested only in the dominant frequency, so typically only one term is considered. The implementation of NAFF used in this analysis is PyNAFF [67], this uses Hardy's method (Eq. 4.2 [63, p.151]) for the numerical integration as opposed to a simple Riemann sum. In addition to the offline methods, live tune measurements on circulating beam used a least squares approach, where an assumed functional form with free parameters for tune, phase, coupling, and decoherence times, is fit to the data.

$$\Psi(T) = \frac{1}{2T}\int_{-T}^{T} f(t)e^{-i\omega t}dt \tag{4.1}$$

$$\int_{x_n}^{x_{n+6}} f(x)dx \approx \frac{\Delta x}{100}\left(28(f(x_n)+f(x_{n+6})) + 162(f(x_{n+1})+f(x_{n+5})) + 220f(x_{n+3})\right) \tag{4.2}$$

To evaluate the methods, a comparison was made with both a synthetic signal and the simulated bunch centroid signal from an Impact-X simulation. Figure 4.1 shows the evaluation signals, the amplitude does not impact the tune evaluation. The synthetic signal consisted of a convolution of a single harmonic base signal, a logistic function for decoherence and a Gaussian noise distribution with a RMS of ten percent of the signal amplitude.

The first evaluation was on the convergence of the various methods. Figure 4.2 shows the convergence of tune measurements for the various considered algorithms with increasing length of the sample window. The limitations of the FFT resolution from the available signal are clear, but they inform the initial values for the interpolation and the NAFF. The vertical simulation signals are considered here as they exhibit faster decoherence. The relatively long

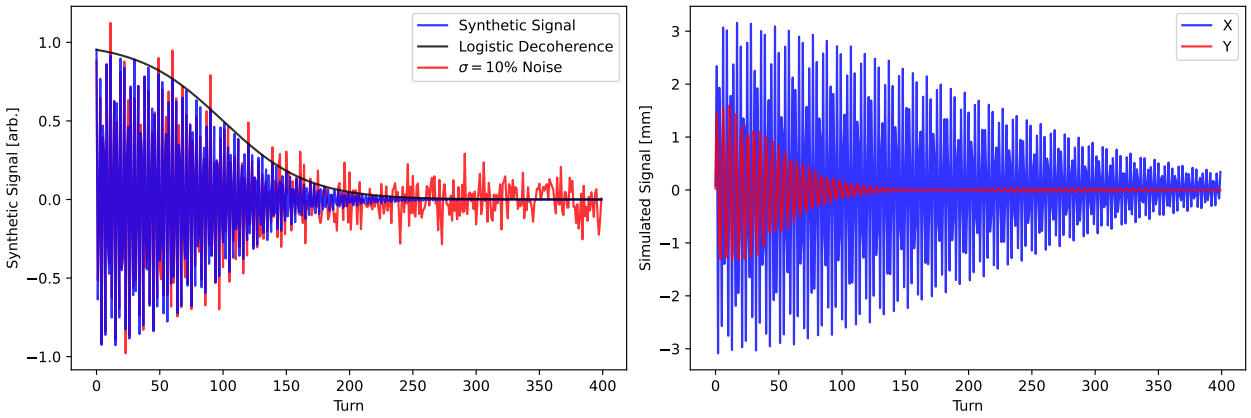


Figure 4.1 Evaluation signals, fully synthetic and simulated

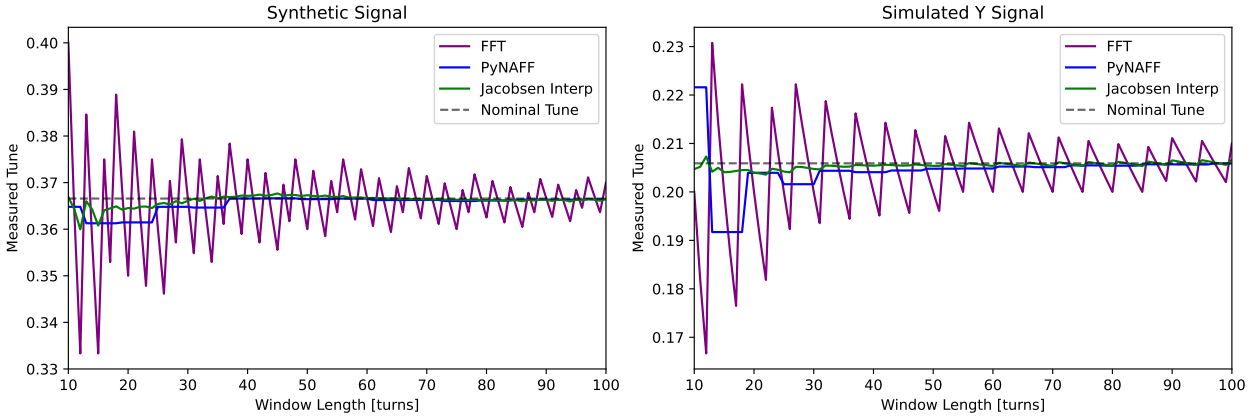


Figure 4.2 Convergence of tune measurements with length of signal window

coherence time of the horizontal signal means that convergence rate is less important, and we are interested in best performance for very fast decoherence.

The available resolution of the FFT can be improved by padding the input signal with zero values. This is the same effect as increasing the length of the signal and applying a rectangular window the length of the original signal. Figure 4.3 shows the convergence of the faster methods with and without padding. Here all signals were padded to an equal signal length of 256 turns. We see that the convergence of the padded FFT is improved, but the windowing effect introduces a systematic, limited offset of the tune determined by the length of the padding. The Jacobsen interpolation with a padded signal also suffers a similar effect, converging on a systematically offset tune.

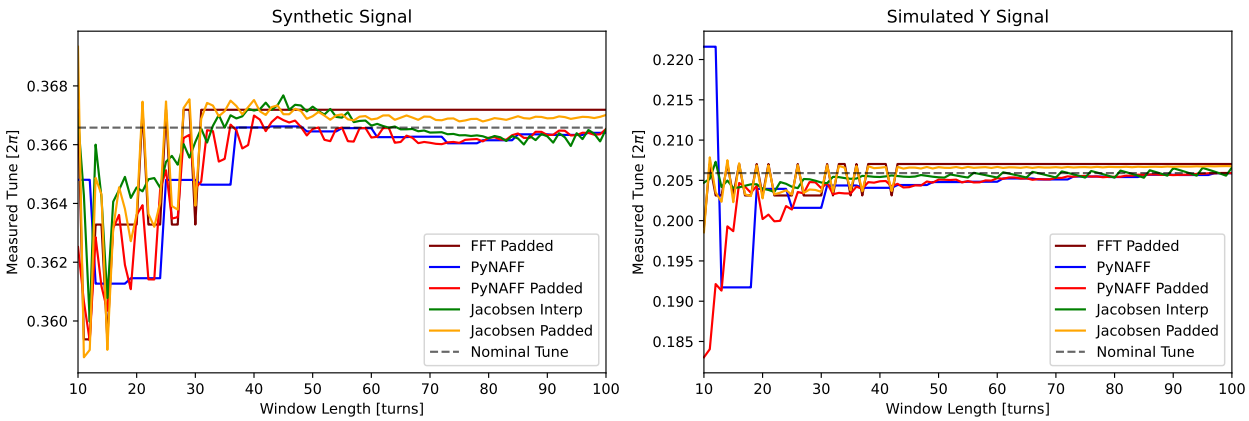


Figure 4.3 Convergence of tune measurements with zero padding

We then have three approaches which reliably converge before the 100 turn limit of our sample plots, Jacobsen interpolation without padding, and NAFF with and without padding. In evaluating the quality of the convergence, the noise seed on the simulated signal was found to have a significant effect on these methods. The convergence of the tune measurement was evaluated for the same underlying synthetic signal and decoherence as before but with one thousand different noise seeds for the random noise. The synthetic signal was used as there is a guarantee of a single underlying frequency unlike the simulation signal. The ensemble properties of the convergence are plotted in Figure 4.4. The left plot shows the mean of the absolute difference of the measured tune from the nominal, $|Q_{meas} - Q_{nominal}|$ and the right plot is the standard deviation of the measured tunes for each window length. We see that the average convergence is about the same, with a slight preference for Jacobsen interpolation. The padded NAFF measurements have slightly lower variation.

There is an additional consideration, we can evaluate the accuracy of the measurements while adjusting the initial phase. There is a periodic variation of the measured tune for this change in initial. This necessarily means sampling a lower amplitude region of the signal as you go along the decoherence. With the padded signal we can also do a similar transformation. By rolling the padding to the front as well as behind with the same overall signal length, different phases given by the resolution of the binning. Figure 4.5 shows the change in the tune measurements for varying the initial turn of a sixty turn sample window

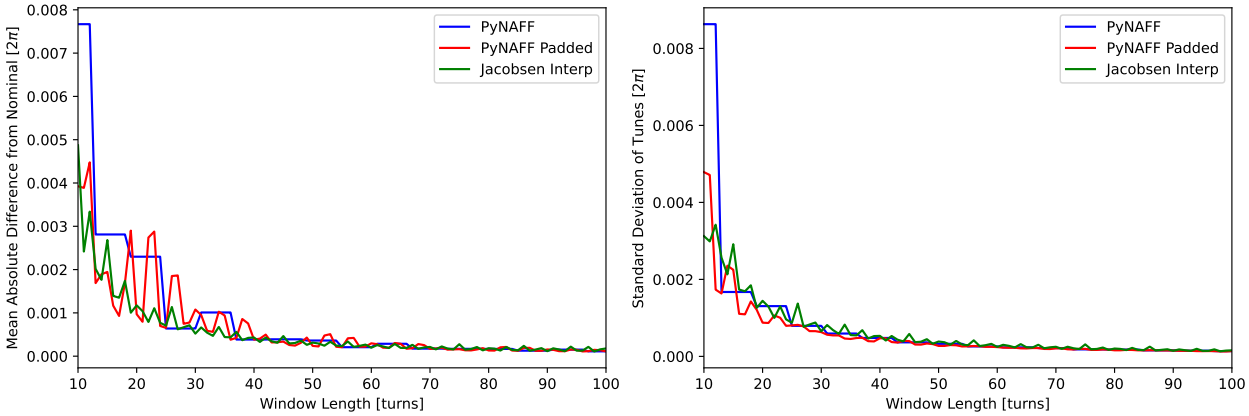


Figure 4.4 Convergence of tune measurements with zero padding

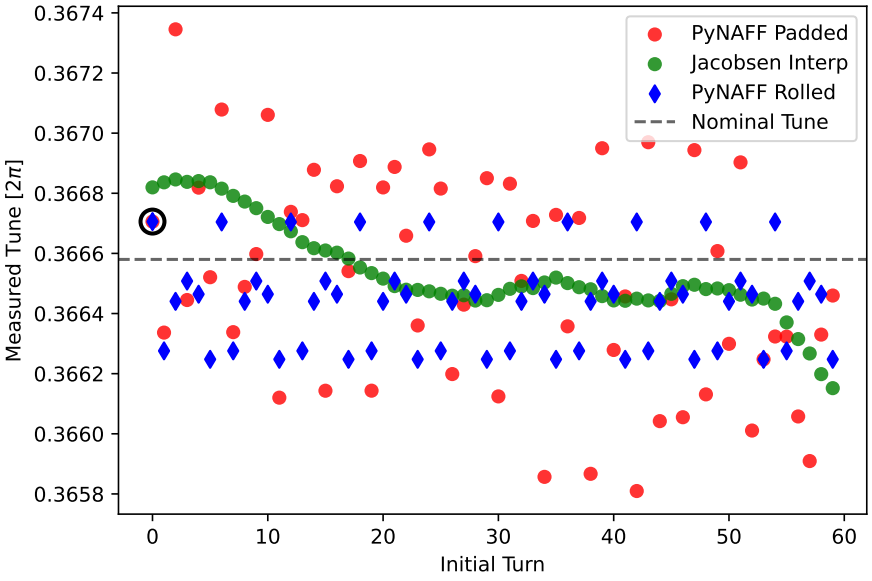


Figure 4.5 Variation of tune measurements with initial phase

and "rolling" the padded signal. Note that the first value of the NAFF padded and the NAFF rolled circled in black are exactly the same as they are evaluating the same signal. This comparison is not apples-to-apples but it does imply a benefit of the NAFF padded evaluation. For a given signal length the uncertainty due to the initial phase is regular and can be evaluated without sampling different, presumably lower amplitude areas of the original signal.

The different tune measurement algorithms have different characteristic statistical uncertainties that scale with the available sample window. Without interpolation, the uncertainty

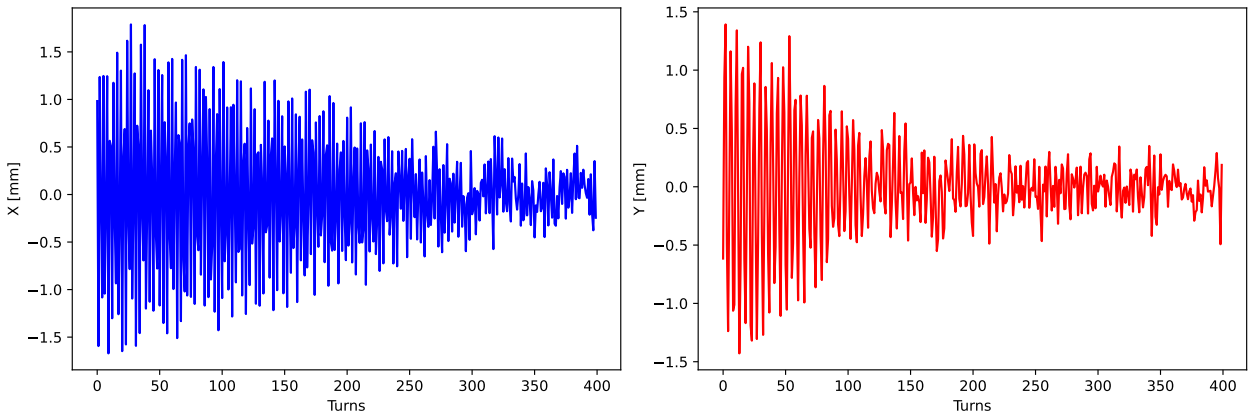


Figure 4.6 Example kick for tune evaluation, BPM B1R signal

in the FFT lines goes as $\frac{1}{N}$ where N is sample points, in our case available turns. Both the unwindowed NAFF and interpolation approaches have analytic uncertainties that go as $\frac{1}{N^2}$ [66, 8]. The magnitude of the variation due to initial phase was added to the uncertainty of the tune measurements. We then have the following steps for a single signal tune measurement:

1. Zero pad signal to predetermined length
2. Evaluate the tune with NAFF
3. "Roll" the signal to shift initial phase
4. Evaluate rolled signal with NAFF
5. Repeat roll and evaluation a predetermined number of times, and estimate initial phase uncertainty from variance in rolled tune measurements

This algorithm is applied to the real TBT bpm sample (Figure. 4.6) in Figure 4.7.

The above comparisons assume a single signal, but multiple BPM signals are available and we would like to combine them, there were two approaches considered. The first is a BPM stacking approach, where a quasi-periodic signal is constructed [66] by stacking sequential BPMs. This approach did not yield good results for the experimental IOTA data.

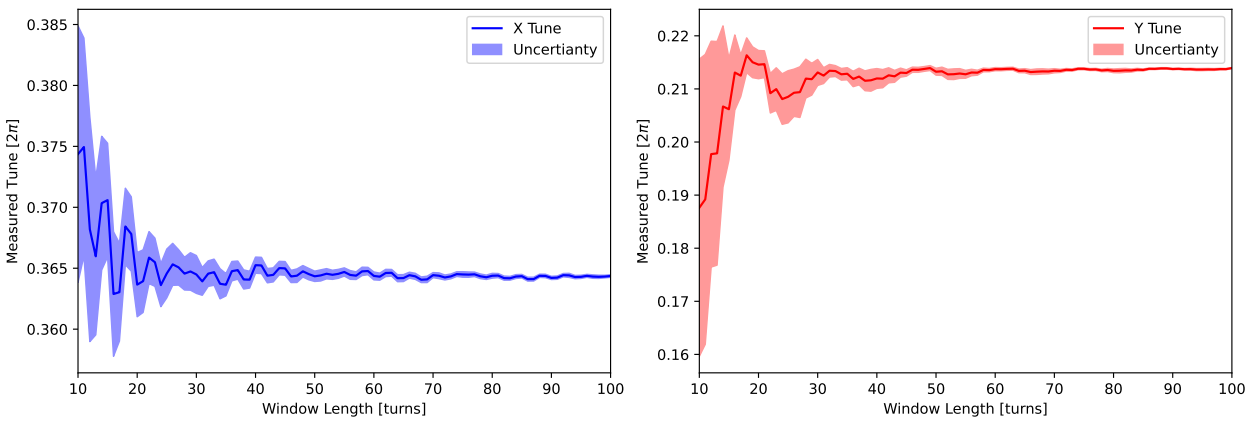


Figure 4.7 Tune measurement convergence for measured TBT data, with estimated uncertainty

The other considered approach to investigate multiple BPM response was to select the dominate components of a PCA decomposition of all combined BPM signals. PCA was selected as the scikit-learn implementation of PCA was significantly more performant than the numpy implementation of SVD, with the same resulting singular values. Figure 4.8 shows the matrix resulting from the convolution of the BPM-specific terms in the PCA with the singular values of a single kick, the same kick as shown in 4.6. Each column corresponds to a BPM, with the center line indicating the split between the horizontal and vertical BPM labels.

The rows indicate different temporal signals. To provide some insight, in the case of simple harmonic motion we would expect four terms, two components for each phase in each plane. Each BPM signal is then composed of the relevant fraction of these phase components with scaling proportional to the beta function at that location. Figure 4.9 shows the first four temporal components of the same decomposition.

We can then discriminate on the direction of a tune component by looking at the relative magnitudes of the temporal components in the horizontal and vertical BPMs. A tune measurement technique, NAFF in this case, can then be applied to these individual components. This has the slight drawback of making phase measurements of individual BPMs more difficult, but this is not typically considered for the analysis anyways. The other drawback of

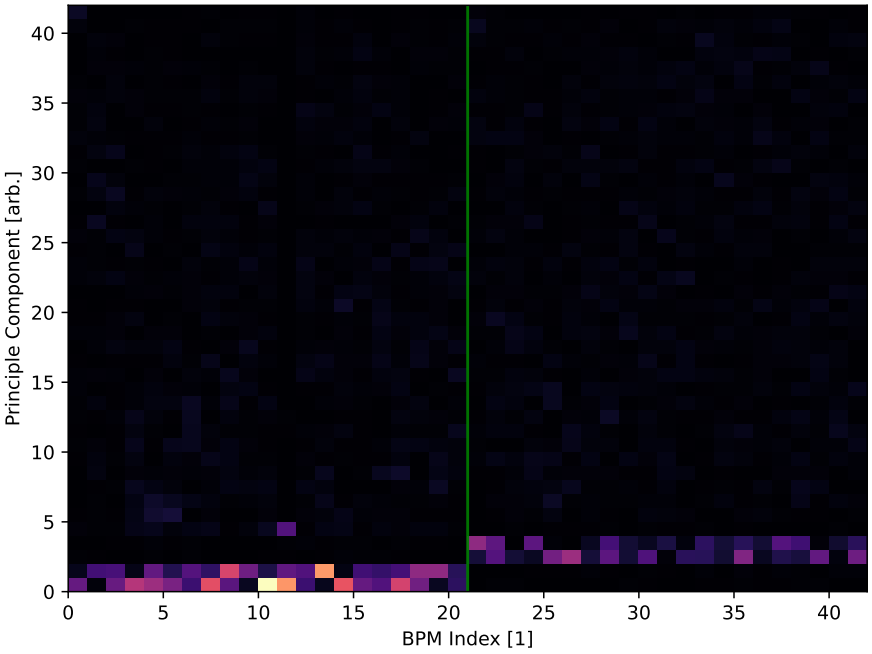


Figure 4.8 PCA decomposition of TBT signals

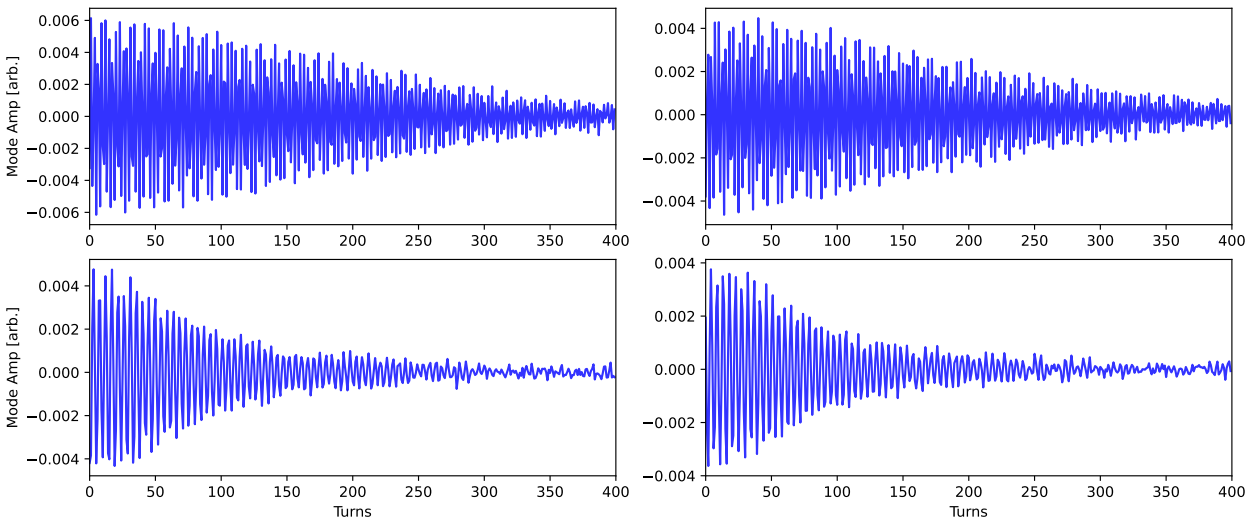


Figure 4.9 First four PCA temporal modes from decomposition above

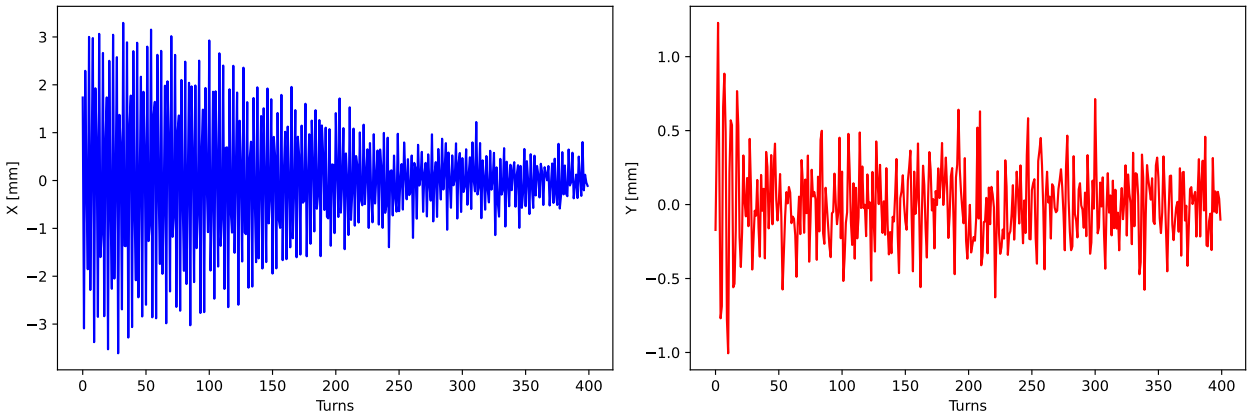


Figure 4.10 Example resonant capture kick

this apporach is that it requires the same number of turns to be considered for each plane. The nature of the PCA decomposition with all BPM signals means that if there is a strong discrepancy between the decoherence times in different planes (which is not uncommon), neccesarially we have to throw away coherent data in one plane or consider a longer range of decohered signal in the other.

Another effect on tune measurements is resonant capture, briefly discussed in section 3.5, where a small fraction of the beam becomes trapped in a resonant condition and continues to oscillate at the characteristic frequency of the resonance. As the rest of the beam quickly decoheres due to tune spread, this dominates tune measurements with long sample windows. This can be seen in the spectrogram with short vertical decoherence with a long faint line. Figure 4.10 shows the profile for a kick demonstrating resonant capture. The vertical decoherence is very fast, about 20 turns. However, a small portion of the beam continues to coherently oscillate as can be seen in the spectogram in Figure 4.11. This spectogram has a window length of 60 turns. The dominant peak in the first window is with the decohering main tune line, but we see a faint line with one bin lower tune and long coherence right on the third order difference line $Q_x - 2Q_y = 0$.

This resonant capture effect means we prefer to keep the tune measurement windows as short as gives reasonable tune resolution. This effect has been demonstrated in simulation, with kicked bunch measurements, and can be seen in single-electron measurements.

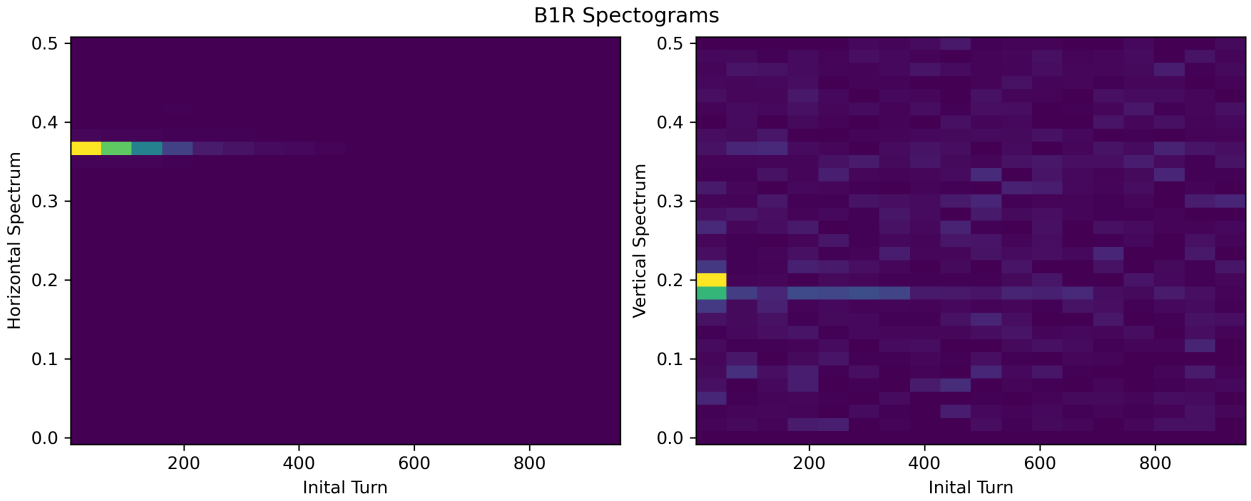


Figure 4.11 Resonant capture spectogram

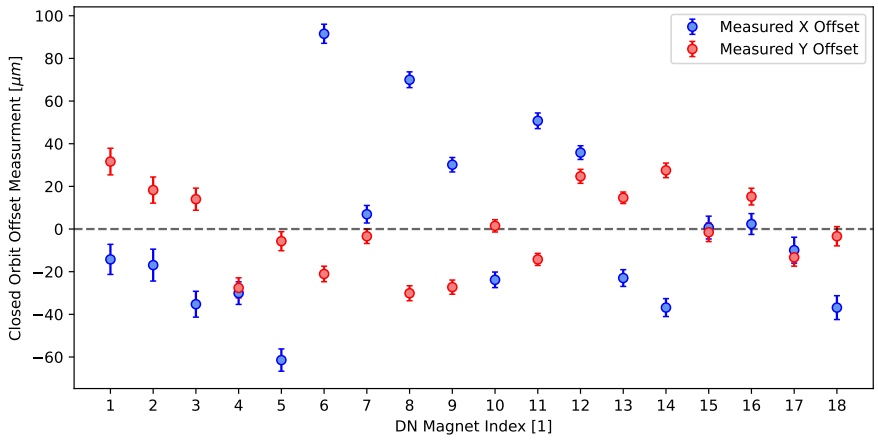


Figure 4.12 Closed orbit offsets in DN magnet after manual alignment, assuming quadrupole terms

## 4.2 Nonlinear Insert Calibration

The nonlinear insert had to be calibrated and aligned to best match the nominal potential. This was done with beam based measurements. Recalling from section 2.6 that the lowest order component of the nonlinear insert is a quadrupole, and that the proper implementation of the DN NIO system requires consistent longitudinal scaling to properly match the potential, we treat the individual DN magnets as quadrupoles for small amplitudes. LOCO was applied to center the individual elements, the measured closed orbit offsets after centering *assuming quadrupole terms* are presented in 4.12.

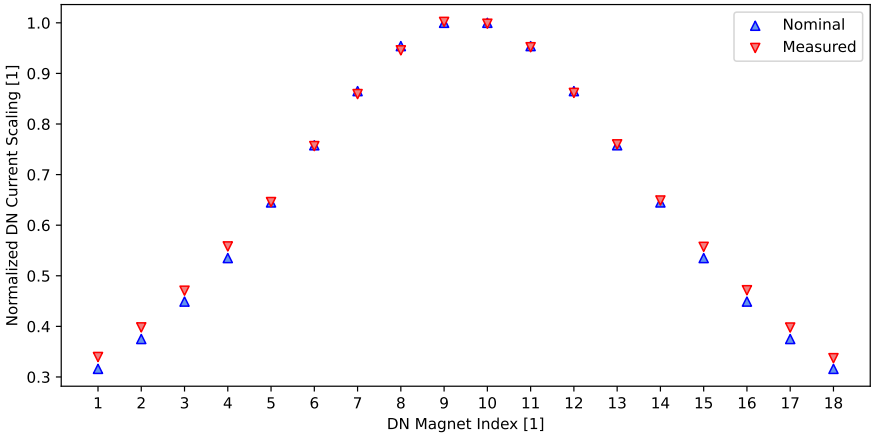


Figure 4.13 Relative DN insert current scaling profile compared to calculated ideal values

Each magnet was energized individually and a small amplitude kick was applied to the beam to measure the tune shift. This was done for multiple current setpoints to fit a tune shift vs current. The individual scaling of the nonlinear t-parameter to current was calibrated for each magnet using the tune shift due to a quadrupole error in the lattice, (eq. 4.3) set equal to the quadrupole term of the DN potential (eq. 4.4), and solved for t.

$$\Delta Q_x = \pm \frac{1}{4\pi} \int \beta_x(s) \frac{\Delta B_2}{B\rho} ds \tag{4.3}$$

$$\Delta B_2 = \frac{-2B\rho\Delta t}{\beta^2(s)} \tag{4.4}$$

The resulting data gives a relative current scaling profile for the overall insert Fig. 4.13. This calibration assumes good accuracy of the beta functions in the nonlinear insert at the time of the calibration.

This approach gives good relative scaling of the magnets, but we want to additionally evaluate the calibration of the insert as a whole. The tune shift assuming only the quadrupole terms of the DN element is given in Eq. (4.5) [45].

$$\begin{aligned} Q_x &= Q_o\sqrt{1+2t} \\ Q_y &= Q_o\sqrt{1-2t} \end{aligned} \tag{4.5}$$

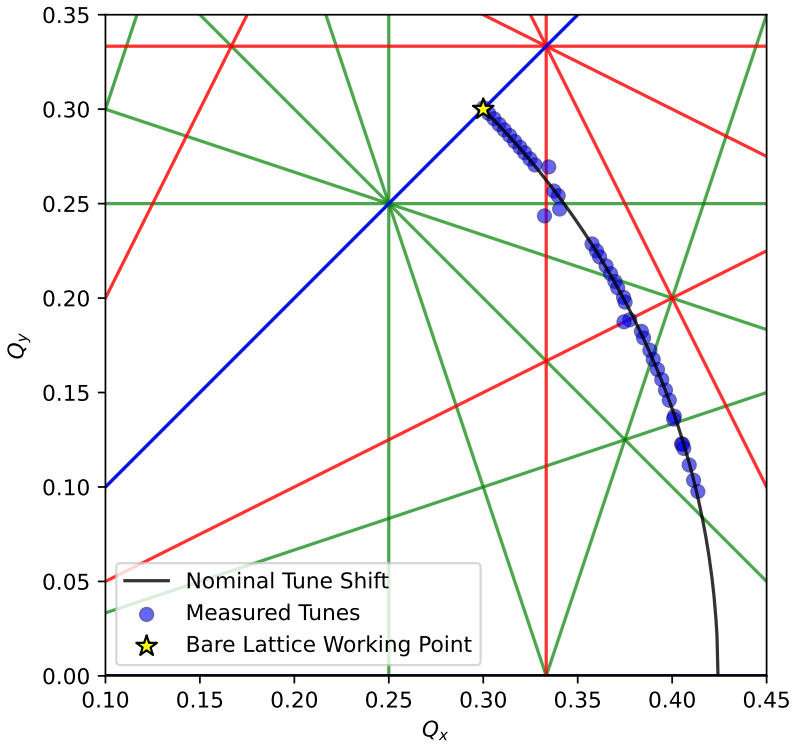


Figure 4.14 Measured nonlinear insert tune shift detuning

The tune shift of the insert was measured by adjusting the t-parameter of the entire DN insert, according to the previously calibrated current ratios and kicking the beam to small amplitudes to measure the tune. The measured tunes are plotted with the quadrupolar detuning in Figure 4.14. The impact of the sextupoles used to compensate chromaticity can be seen as the dominant effect on the tune near the third order resonances (red lines on tune diagram).

The ratio of the tune shift between the planes is good indicator of proper implementation of the longitudinal scaling of the potential and beta function match in the insert. The absolute t-parameter scaling was calibrated by measuring tune shift vs nominal t-parameter, as presented in Figure 4.15. The gap in the data between t=0.2 t=0.3 was an unfortunate result of the BPM system freezing and failing to update TBT data, and was simply excluded.

The initial data indicated a discrepancy in the tune dependence of the t-parameter. The proportion The ideal detuning expression was fit to the data with a t-scaling factor as the only free parameter Eq. (4.6).

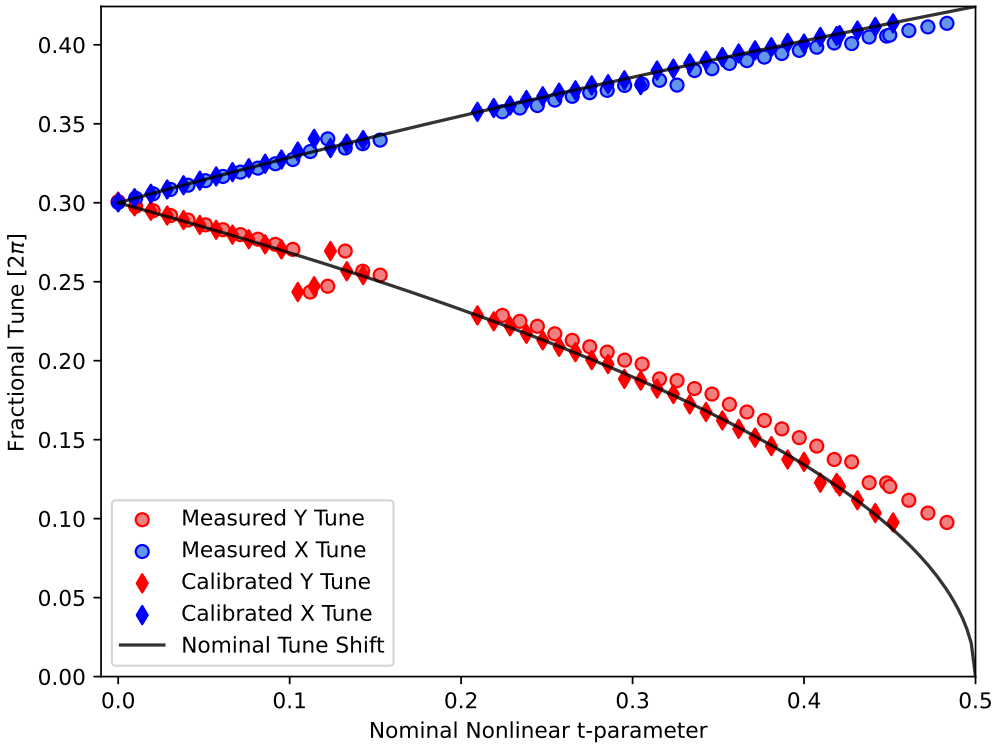


Figure 4.15 Tune shift vs t-parameter in both planes, before and after scaling

$$Q = Q_o\sqrt{1 \pm 2at} \tag{4.6}$$

The fit resulted in a calibrated t-parameter scaling of $a \approx 0.935$. The source of this discrepancy is not clear, but may be a result of magnet crosstalk, as the relative calibration was measured with single elements and the magnet spacing is close.

### 4.3 Momentum Reconstruction

For studying the evolution of the phase space, the four dimensional $(x, p_x, y, p_y)$ transverse coordinates of the beam need to be reconstructed. There are a few standard ways to accomplish this. The simplest approach is a pair of BPMs with a $\phi = \pi/2$ phase advance between them. This is a straightforward start, but we have more than two BPMs and would like to combine the signals. A successful approach this is the N-BPM method [37], which can reconstruct the momentum from measured beta functions. The most accurate beta function measurements use the relative phase advance between BPMs can adjust a model prior for

the betas. In the case of IOTA with the NIO insert, the tune and therefore phase advance is highly nonlinear and not a reliable parameter to combine with the bare lattice. Instead we leverage the linear model of the lattice generated using LOCO. The momentum and position at a virtual BPM could then be reconstructing using a least squares approach.

The BPMs are all located in the linear matching section of the lattice. We can then reconstruct the position and momentum at a virtual BPM turn by turn, using the linear model from LOCO. The main nonlinearity in IOTA stems from the insert, though there is nonlinearity stemming from the sextupoles, fringe fields, and sharp bending dipoles. Using higher order maps including the calibrated sextupole terms was considered, but expanding the method using second order transfer maps yielded poor convergence of the fits of the motion. Additionally, such a method would require more accurate understanding of the residual nonlinearities in the matching lattice than we currently have for IOTA. We have an advantage in that the nonlinear effects outside of the insert are perturbative compared to the linear focusing terms, so we only expect them to be coherent over many turns. This motivates carefully evaluating the goodness of fit to our linear model later in this section. So then, for the fitting, the matching section was essentially treated in a channel mode from the end of the nonlinear insert to the beginning of it.

To perform the least squares fit the lmfit python package [47] was used. The nonlinear least squares efforts are irrelevant for the linear transport model, but the interface is much improved over other pythonic options, e.g. scipy. For our fits the free parameters are the position and momentum at a virtual BPM. Our model is the linear transfer matrices to each BPM from the virtual BPM location. In principle, these could be coupled, but the coupling is deliberately locally corrected with the IOTA skew quad correctors. The resulting transfer matrices have coupling on the order of the machine precision, so we simply exclude these terms to reduce the dimensionality of the fit. Accordingly, we perform a fit for each plane. The data for the fit is the BPM measured position at each BPM in a given turn. To ascribe an uncertainty to our reconstructed coordinates we need an understanding of the uncertainty

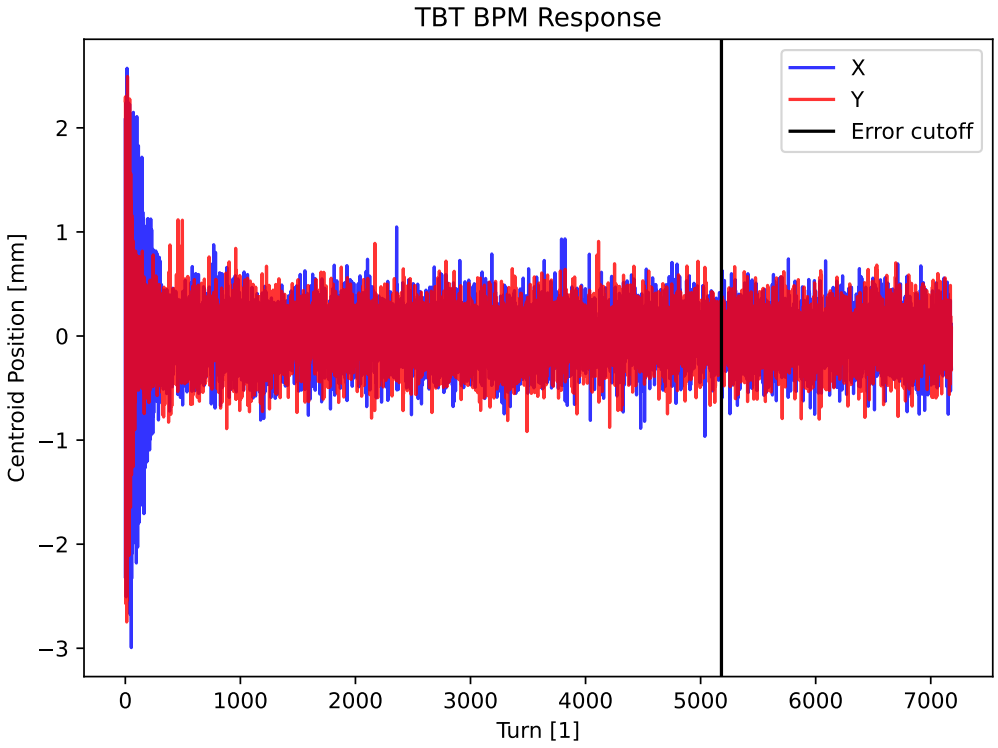


Figure 4.16 Full range IOTA example kick with error estimation cutoff

in our BPM measurements.

The uncertainty of the BPM measurements is evaluated from the variation in the tails long after the signal has fully decohered. Note that the radiation damping time for the beam 3 orders of magnitude longer than this sample time. The individual particles are still at mostly full amplitude and our beam is "large". This may impact the centroid measurements if the nonlinear BPM calibration factors are off, as a fraction of the beam near the buttons may be undersampled or saturate the acquisition electronics. Some preprocessing was applied to the BPM signals to excluded these effects. For NIO lattice configurations, the tail was defined to be 2000 turns from the end, well past the expected coherence limit. Figure 4.16 shows the full sample range of an example kick in IOTA with a line indicating the noise sample threshold.

The error in the BPM measurements is then evaluated to be the variance in this remaining signal. Figure 4.17 shows the histogram of coordinates in the last thousand turns in Figure 4.16. The standard deviation and interquartile range are both calculated and compared. The

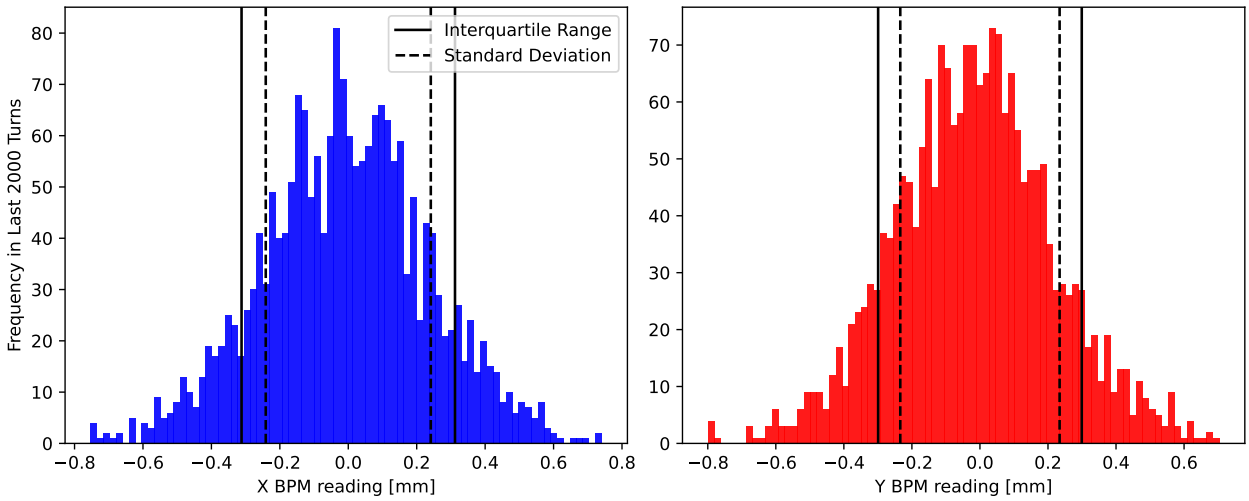


Figure 4.17 BPM noise over last 2000 turns, standard deviation and interquartile range markers included

interquartile range is less susceptible to outliers, and can be directly related to the standard deviation if the distribution is Gaussian. A comparison of these metrics for a large sample of real IOTA kicks showed good correspondence, indicating that the bpm noise is well modeled with the normal distribution. For fitting, the BPM noise was evaluated for each BPM and kick individually and applied as the noise for each turn.

Figure 4.18 shows the resulting error evaluation for a full collection. This is a smaller example collection from the rest considered in this section to be a little easier to read. The vertical and horizontal BPM signals are separated with the red line. We can see that the oddball BPM A1C has a suppressed uncertainty from its improper calibration. The other standout bpm is the unusually high noise on the horizontal signals on E2L, an issue with the hardware. We can see a steady growth in the uncertainty over the collection as the circulating current decreases. The individual fits capture the relative uncertainty for their given kick.

The reduced chi square of each turn was used to evaluate the goodness of fit to the linear model. In the ideal case a reduced chi square value of one indicates a good fit. In practice, estimation of uncertainty and data preprocesing can impact this value, and we are mostly interested in a reasonably contained rang of reduced chi-square values. Initially, the range

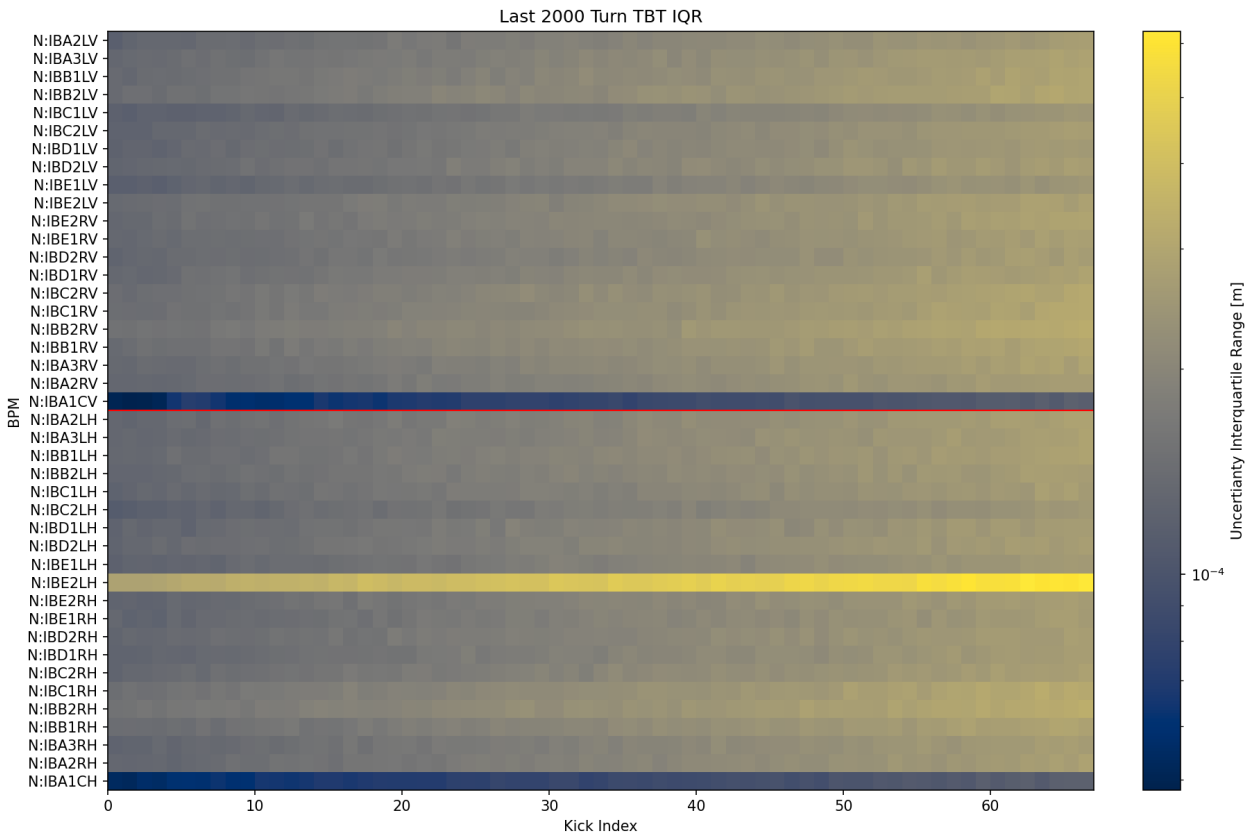


Figure 4.18 BPM noise over last 2000 turns, IQR evaluation for a full collection

of the goodness of fit was very large, with large outliers above and below the central value near one. Excluding turns with large BPM noise significantly improved this metric, and let us consider the impact of other data preprocessing steps on the goodness of fit.

First we consider the linear BPM calibration factors from the LOCO procedure. The real BPMs are not perfectly made or aligned to the principle modes of the beam dynamics. To first order these calibrations are included in the LOCO fits. The resulting parameterization with individual bpm constants is given in eq. 4.7.

$$x_{meas} = KK_x \left(x \cos(ang + ang_x) + y \sin(ang + ang_x)\right) \tag{4.7}$$

In Figure 4.19 we compare the reduced chi square of the fits to the data before and after the linear calibration. The turns are all from the same large dataset for a fixed lattice configuration with many amplitudes and reinjections. The colored region shows the full

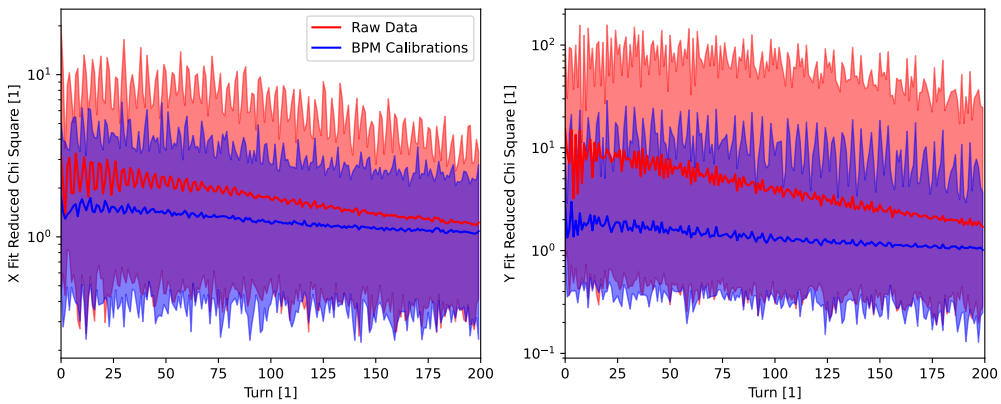


Figure 4.19 Goodness of Fit

extent of the reduced chi square values, and the solid line is an average to give a sense of the distribution. These values are plotted against turn number, in general we can see a trend towards lower reduced chi square values as the signal to noise ratio goes down with decoherence. In these plots a good result is a narrow band, and a lower relative reduced chi squared value indicates better match to the model. We see the distribution get much narrower, and the central values move closer to our nominal value of one.

Individual BPMs can be dropped from the fitting algorithm in the case of a acquisition error or saturation in the BPM. We know that the A1C BPM has a different geometry and incorrectly applied scaling map, so we investigate the impact on goodness of fit by uniformly dropping it in Figure 4.20. We see a slight reduction in the size of the band as compared to just applying the calibration. As a result, this BPM was excluded from any momentum reconstruction calculations.

To reduce the uncorrelated noise a principle component analysis was applied to all of the BPMs. The PCA was applied to all BPMs to account for possible coupling. Based on the singular values, the first 8 components of the PCA were used. Figure 4.21 shows the impact on the goodness of fit between the calibration and dropping A1C and these two steps plus the PCA cleaning step. We see a reduction in the band and a correlated drop in the average reduced chi square away from one. This is an expected side effect, since we are now over estimating the uncertainty from before the PCA cleaning. The uncertainty is not

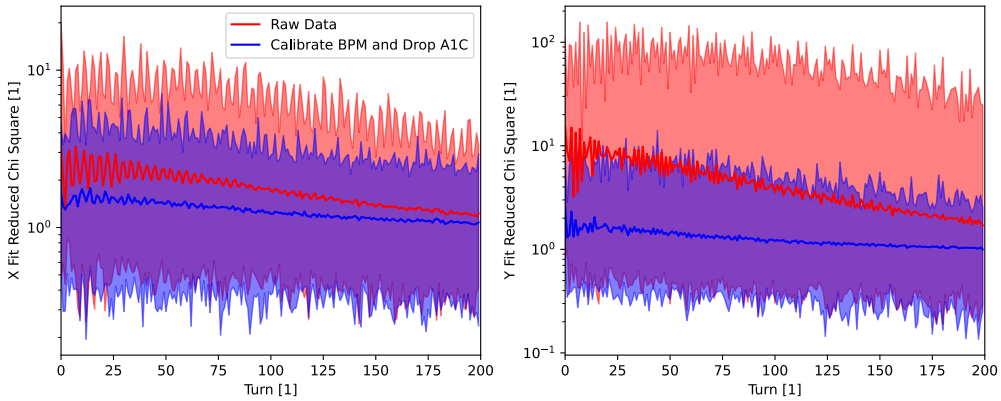


Figure 4.20 Goodness of fit

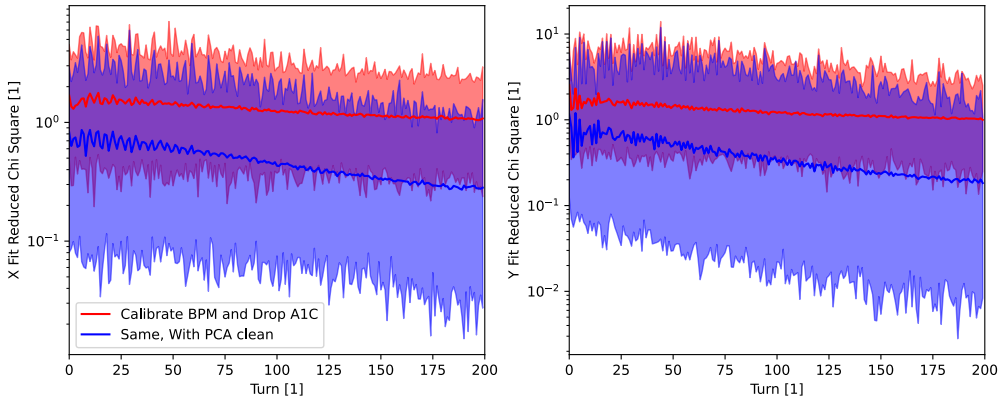


Figure 4.21 Goodness of fit

re-estimated because the interpretation of the tails after PCA is inconsistent, and we prefer to evaluate the PCA on as short of a section of the kick as possible.

While BPM A1C was consistently excluded, the other BPMs were evaluated and found to be reliable. Figure 4.22 shows the comparison after all of our preprocessing steps with and without BPM B2L as an example. We see no significant deviation in the goodness of fit, and retain all of the rest of the BPMs unless there is some readily identifiable acquisition error with the particular kick sample.

After evaluating and settling on our preprocessing steps we can evaluate the distribution of our reduced chi square values over the course of the collection. Figure 4.23 shows this distribution for the first 25 and last 25 turns to account for the decoherence related shift. We see the characteristic reduced chi distribution is preserved. The grey histogram corresponds

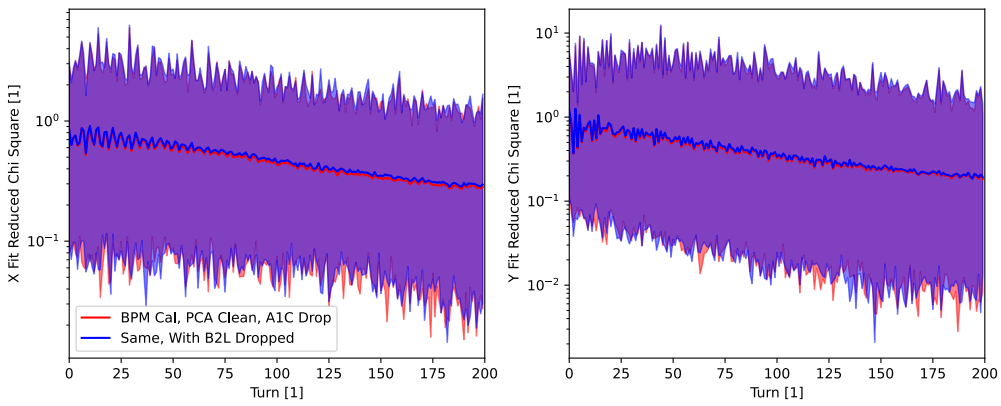


Figure 4.22 Goodness of fit

to every fitted turn, the colored curves indicate increasingly aggressive cuts. The first cut excludes BPMs with saturation and errors, and the further cuts are on TBT noise. The reduced chi distribution is preserved and the tails smooth out with the calibration cuts. The green trace corresponds to the sets analyzed in the preprocessing comparisons above.

To illustrate the result with data, Figure 4.24 shows the result of a fit for a single turn. The position and momentum are fit from the blue measured points. The fitted position is given by the green diamond, and the effective propagated position from that virtual bpm is illustrated with the green trace.

## 4.4 Kick Amplitude Calibration

The position reconstruction is also valuable for calibrating the amplitude from the kicker. When evaluating the amplitude dependent detuning, we need a consistent way to define the amplitude for different configurations. The position reconstruction with the nonlinear insert is difficult to interpret and depends on the insert setting. We prefer instead to evaluate the effective linear emittance imparted from a kick. To calculate this, we reconstruct the position and momentum for the first turn in the bare lattice and look at the correlation with the kicker setting. Figure 4.25 shows the reconstructed position and momentum for a few bare lattices with different sextupole configurations. The kicker response is reasonably linear, but we see a difference in calibration between bare lattices. From operational experience, we know some sextupoles have error terms with feed down effects on the linear lattice D. As a

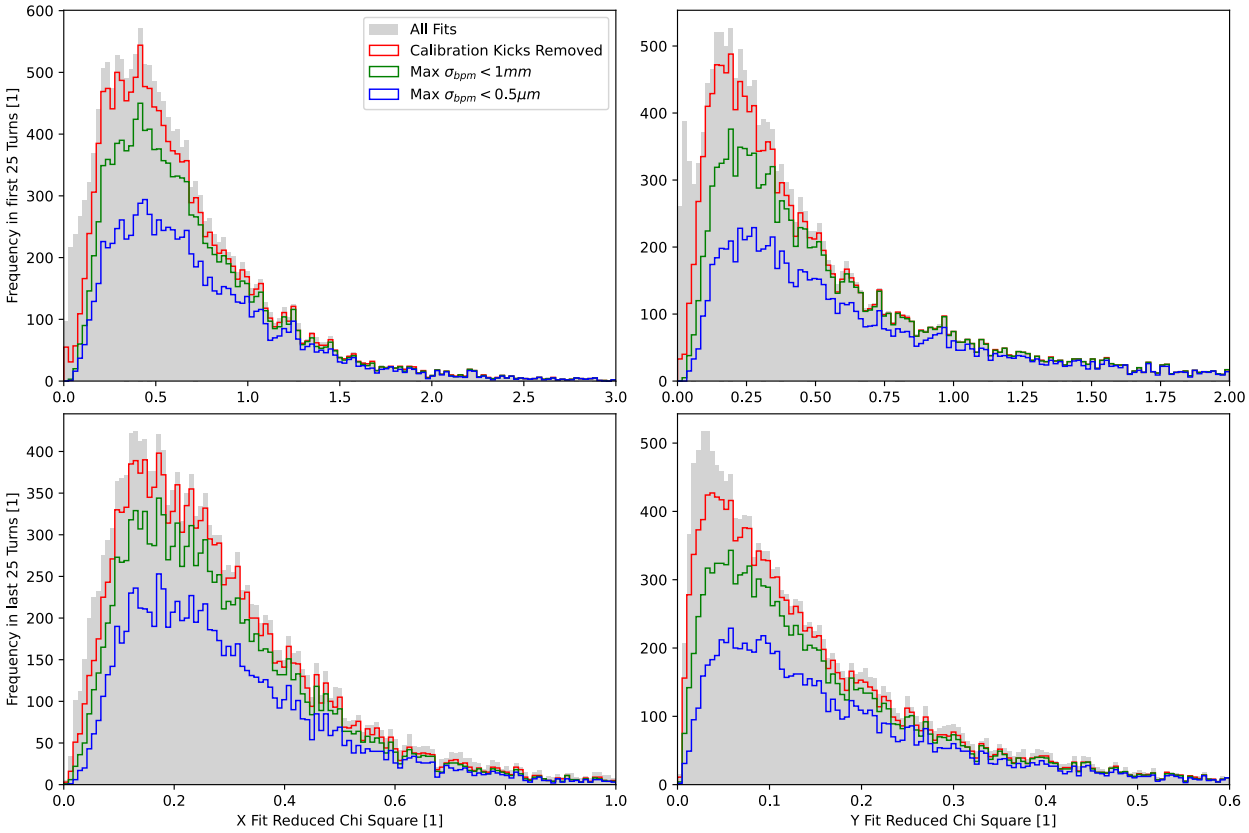


Figure 4.23 Reduced chi square distributions for fully processed data sets, histograms for first 25 turns and last 25 turns to account for general reduction due to decoherence

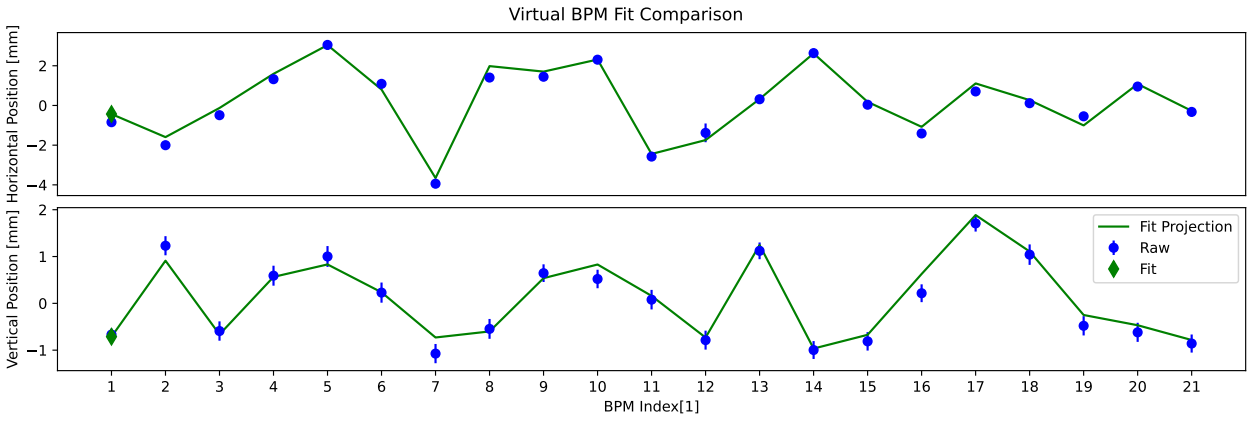


Figure 4.24 Reconstructed position threaded through the rest of the machine

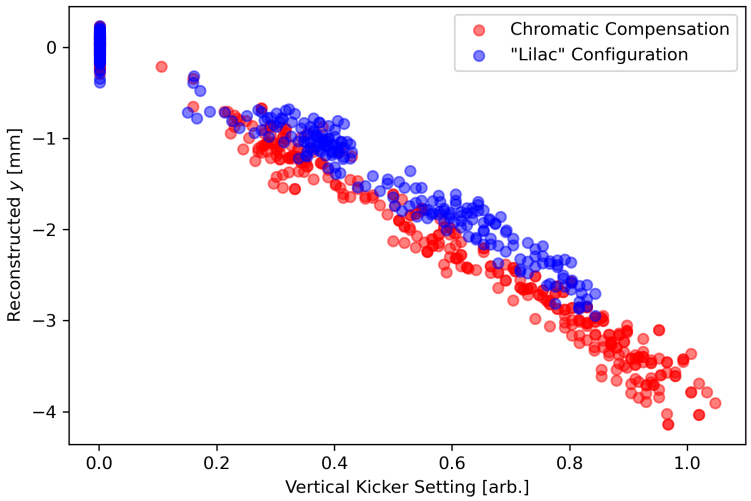


Figure 4.25 Reconstructed vertical position for lilac sextupole configuration lattices and those with only chromatic compensation

| **Reconstructed Coordinate** | **Horizontal Kicker** | **Vertical Kicker** |
|---|---|---|
| $x$ [m] | $-6.8\times10^{-4} \pm 1.5\times10^{-6}$ | $-2.5\times10^{-4} \pm 3.3\times10^{-6}$ |
| $p_x$ [1] | $1.1\times10^{-4} \pm 4.9\times10^{-6}$ | $-3.3\times10^{-3} \pm 1.6\times10^{-5}$ |
| $y$ [m] | $1.9\times10^{-3} \pm 6.8\times10^{-6}$ | $1.3\times10^{-4} \pm 1.5\times10^{-5}$ |
| $p_y$ [1] | $5.2\times10^{-5} \pm 4.8\times10^{-6}$ | $-3.9\times10^{-3} \pm 1.6\times10^{-5}$ |

Table 4.1 Kicker Calibration scaling for "Lilac" bare lattice

result only the lattice with a current LOCO optimization is reliable, for the collections we are interested in, this is the "lilac" configuration considered moving forward.

Considering with a large collection of mixed kicks for this bare lattice configuration, a few models were considered, but a coupled linear model with a fixed zero intercept performed the best according to the goodness of fit metric. Figure 4.26 shows the reconstructed position and momentum at the virtual BPM and the lines corresponding to no perpendicular kicker setting. The calibration parameters are given in 4.1. The coupling can be interpreted as a slight roll misalignment of the kicker about the longitudinal axis.

This amplitude calibration could be used directly or to generate the initial values for a short position reconstruction between the kicker and the nonlinear insert.

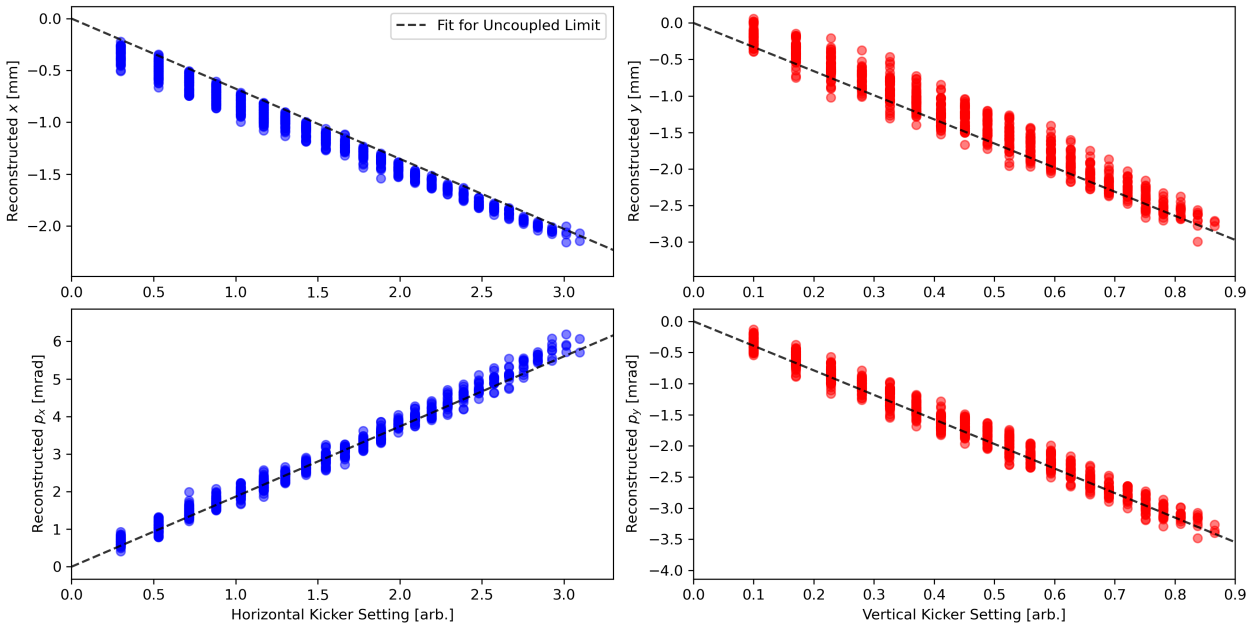


Figure 4.26 Reconstructed First Turn position and momentum with fitted kicker setting calibrations

## 4.5 Dynamic Aperture Evaluation

The dynamic aperture (DA), or amplitude limit on stable motion, is a crucial metric of the real nonlinear system with full perturbations. The dynamic aperture is evaluated for simulated beams as the limit of asymptotically stable trajectories. For experimental measurements, the interpretation becomes more difficult. The DA measurements settled on were performed by measuring the losses of kicked circulating beam at increasing amplitudes. Two methods were used to evaluate the dynamic aperture, a fast coarse approach implemented online for optimization purposes, and a more granular method emplying postprocessing.

The coarse apporoach consisted of fitting a logistic funciton to the charactersitic current curve of repeated losses versus kick amplitude. The offset of the logistic function could be used as a relative metric for the location of the aperture. Figure 4.27 shows the raw output in the Fermilab ACNET control system that was used for the fitting. The green trace is the DCCT current, the red trace is a rolling average of the same measurment, and the yellow trace is the calibrated current as measured by the PMT. The spikes in the PMT signal correspond to kicks, as the center of the PMT window is discolored, so when the beam size

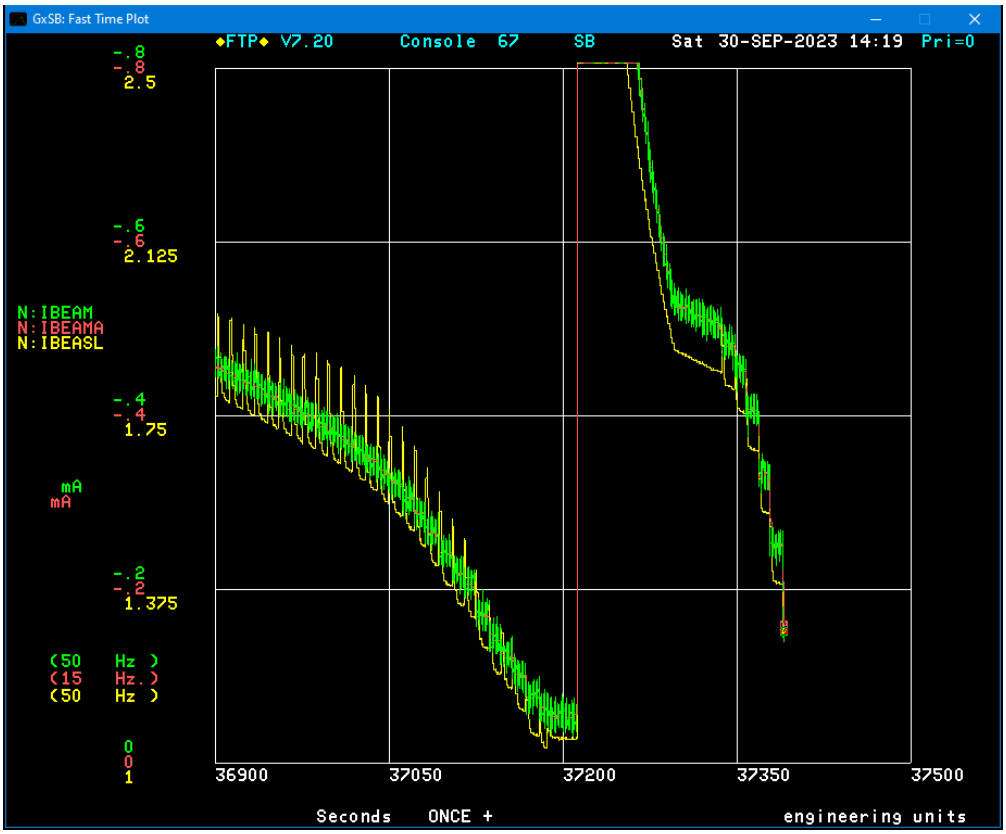


Figure 4.27 ACNET control system readout of currents during a logistic fit DA scan

increases after a kick the spot size increases beyond this artificially suppressed region on the diagnostic. This ended up being an additional useful indicator of successfull kicks in the machine. This method relies on many assumptions, the losses between the kicks are consistent, the kick timing is regular, and the initial current is consistent. However, it was relatively fast, and resulted in a simple single figure of merit, both very useful features for input into an optimizer

For the more granualar, postprocessed DA scans, a bunch was injected and scraped to a standard initial current in the BPM sensitivity range. The beam was iteratively kicked along fixed ratio "spokes" as current was logged. Once the current reached a minimum threshold, another bunch was injected and the scan of another spoke began. Figure 4.28 illustrates the resulting geometry of the kick amplitudes.

Both the BPMs and DCCT were used to monitor beam current after a kick. The sum of

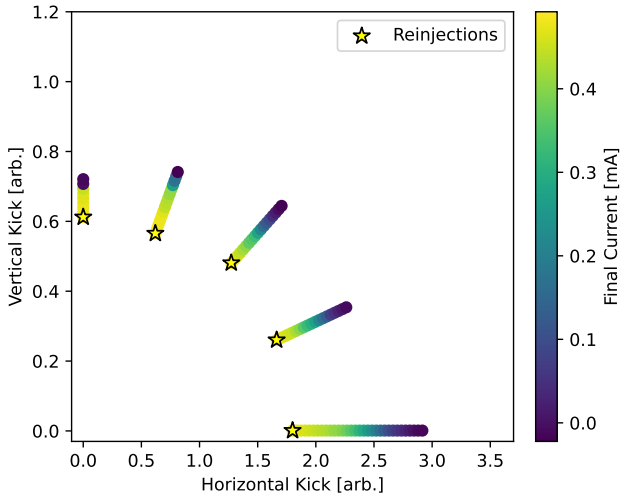


Figure 4.28 Dynamic Aperture Scan configuration

the individual BPM button responses can be used as a TBT indicator of losses. The BPM TBT output contains 20 turns of information before the kicker fires, which can be used as a baseline. For loss comparisons, the mean of the BPM signal for the first and last 20 turns was compared. The sample range of the BPMs was around 7000 turns which corresponds to a timescale of just under a millisecond. The sum signal from all of the BPMs was combined TBT to form a global sum signal. The sum signal noise was evaluated as the standard deviation of these sample ranges.

The DCCT signal was sampled before and after the kick on a timescale of a second. Loss timescales differed, some losses on kick were visible in the first few turns of the sum signal, and some losses were too slow to be in the sum signal but were visible in the DCCT.

To ensure that losses occurred in the time span between the DCCT samples, and were not dominated by the natural circulating beam lifetime, the difference between the second sample and the first sample of the next kick were calculated and verified to be at the level of noise in the DCCT signal. Figure 4.29, shows the difference in current after a DA kick and the initial value before the next kick on the order of a few seconds. DCCT noise was evaluated as the standard deviation without any circulating beam at $6.7{\times}10^{-3}$ [mA].

Figure 4.30 shows the DCCT and BPM sum signal for increasing kicks along a particular

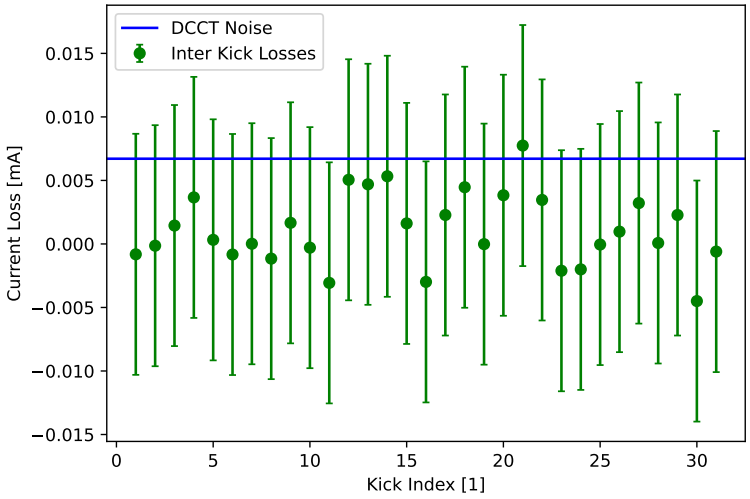


Figure 4.29 Change in DCCT current between DA scan kicks

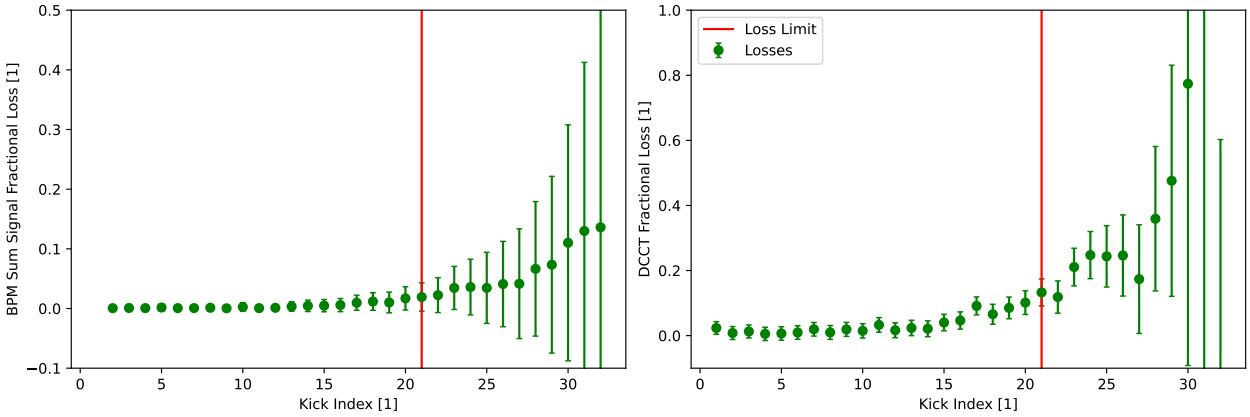


Figure 4.30 Percent Losses after individual kicks in a DA scan

spoke. A consistent qualitative metric was applied, the loss limit was defined as a percent loss greater than 25% or two subsequent kicks with percent losses greater than 10%. The red line indicates the determined DA limit for the particular spoke.

## 4.6 Synchrotron Radiation Profiles

In addition to their very useful capacity as live beam monitoring instruments, the synchrotron radiation cameras were used to evaluate the stability of the beam at the integer resonance condition. These measurements were taken with very low circulating beam currents, the cameras are sensitive down to single orbiting electrons, but the exposure has to be periodically adjusted to maintain sensitivity. The transverse profile and the intensity were

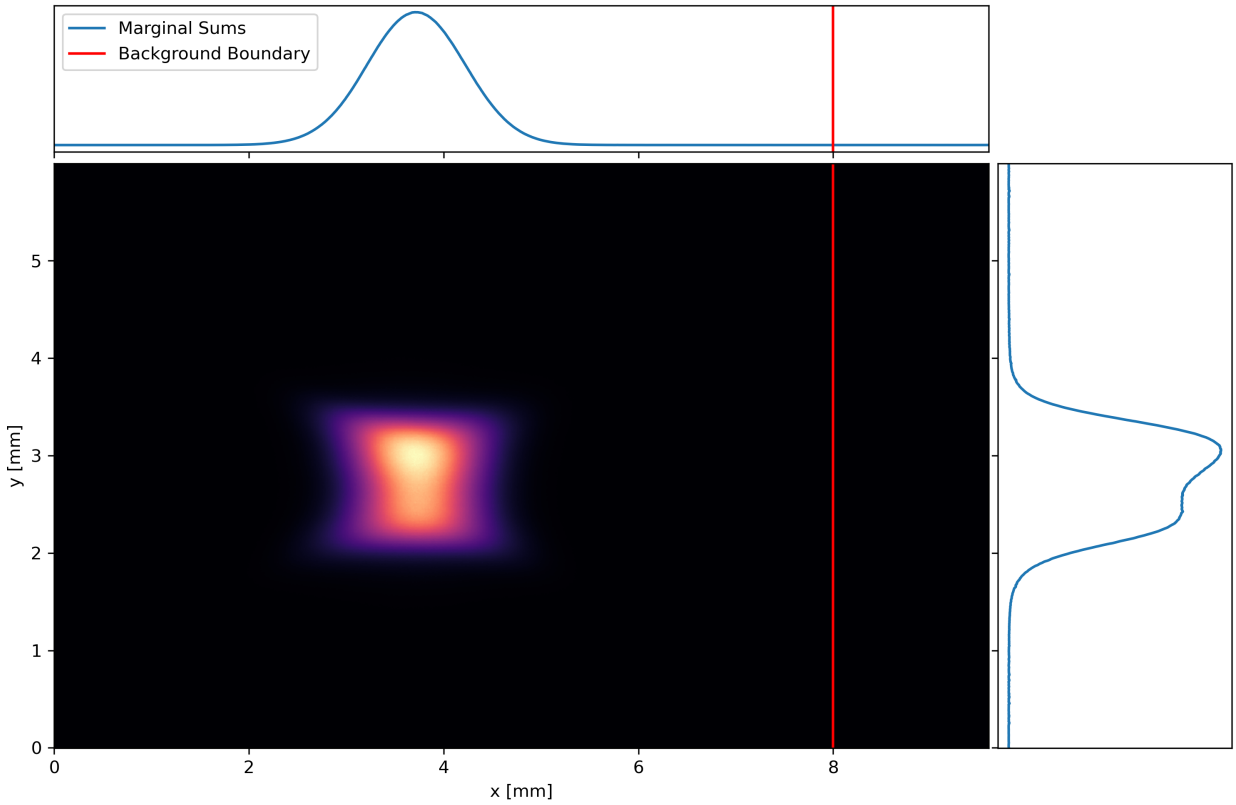


Figure 4.31 Example Synchtrotron Radiation profile in M1L beyond integer resonance, axes ticks are simply for scale, not absolute position

the points of reference. The images were preprocessed with a media filter to remove potential hot pixels, and a background subtraction was applied. Figure 4.31 shows an example camera profile with the marginal sums and a line indicating where the boundary of the background sample.

To evaluate the lifetime from camera images, the relative intensity (simply the sum of the full image) and timestamps of the image could be fit with an exponential decay, eq. 4.8. The uncertainty of the lifetime was determined from the uncertainty in the fit.

$$I(t) = I_o e^{-\frac{t}{\tau}} \tag{4.8}$$

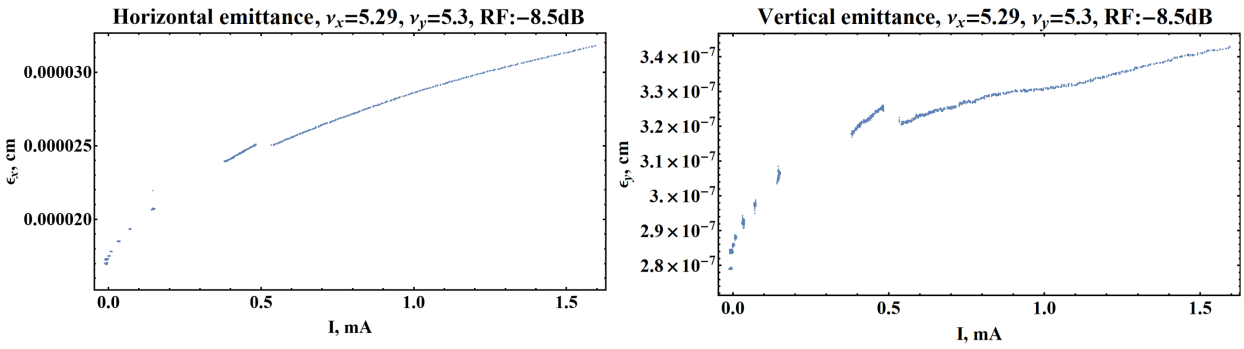


Figure 4.32 Measured emittance versus circulating current in split tune bare IOTA lattice

The synchrotron radiation profiles were also used to measure the equalibrium emittance of the circulating beam for the IOTA bare lattice. Figure 4.32 shows the emittance dependence as fitted to the camera profiles. The emittance analysis presented was performed by A. Romanov. We see there is some dependence on the circulating current due to intra-beam effects. The lattice in question is the IOTA bare lattice with a small perturbation to split the tunes off of the coupling resonance. The majority of the measumrents are taken off of this coupling line, and the beam is much flatter off the coupling from the disparate synchrotron damping in the different planes. As the t-insert is ramped the emittances are of course not strictly conserved, but are nearly transformed to the first order, and is reasonably comparable for small t-parameters. Generally, for most evaluations a central emittance qauntity of $\epsilon_x = 2.2\times10^{-7}$ [m-rad] and $\epsilon_y = 3.2\times10^{-9}$ [m-rad] is used, as this represents a pretty typical operating current for a particular injection. Recall we are sensitive between 0.5 [mA] and 0.1 [mA] for BPM data.

# CHAPTER 5

# EXPERIMENTAL STUDIES

## 5.1 Working Point stability of Different NIO configurations

As discussed in section 2.6, the NIO system requires chromatic compensation for stable operation. The base stability was investigated for different bare lattice configurations. Circulating beam was established and the nonlinear insert t-parameter was slowly ramped to establish stability. Figure 5.1 shows the ramp for the naive bare lattice without sextupole compensation of any kind. We see complete losses near the horizontal third order resonance $3Q_x = 1$. This is indicative of residual third order nonlinearities in the IOTA bare lattice. The source of these nonlinearities is not clear, but may stem from the dipole fringe fields, or the geometric nonlinearities from the tight bending radius in the dipoles. The chromaticity of the bare lattice also deviates from the model predicted value by a significant margin of over a unit, another indicator of spurious third order terms.

Chromaticity was then empirically compensated with a minimal set of two families of sextupoles. Figure 5.2 shows a similar ramp after the compensation. The sextupole resonance is still present, but the stability is not strongly impacted and we can go all of the way to the integer resonance condition. We see a new loss location occur around $t = -0.46$, and some potential losses near $t = -0.3$. This motivates investigating the losses with a slowly varying t-parameter.

This slow ramp of the NIO insert is presented in Figure 5.3. In this scan a second region of losses becomes more clear near the integer resonant condition. The nearest resonant line in tune space is $2Q_x + 2Q_y = 11$, in addition to a number of $6^{th}$ order lines. Whatever the cause of losses near this working point, it meant that this region had to be quickly stepped beyond when investigating dynamics at the integer resonance. Practically, the NIO insert was ramped to just above the limit of losses then "snapped" beyond this point. There are no significant losses near $t = -0.30$ during the slower scan. This location corresponds to a third order coupling resonance, which does not drive losses but impacts turn-by-turn

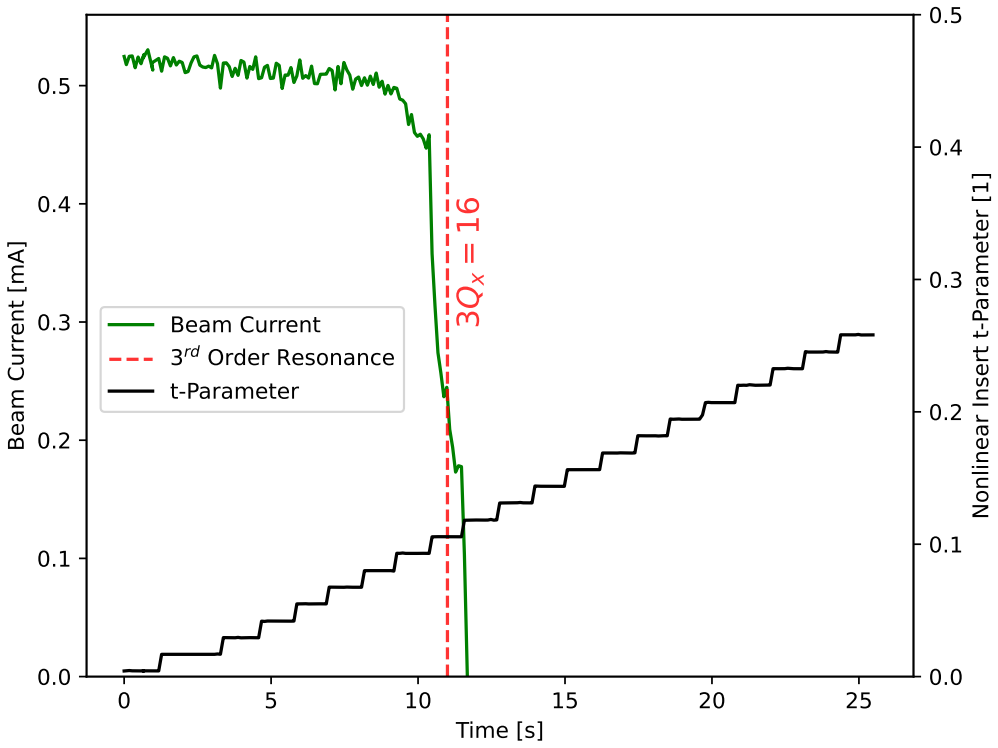


Figure 5.1 Circulating current in IOTA while ramping t-parameter for no sextupole compensation

measurements.

Figure 5.4 shows quickly ramping does not incur significant losses. This is an improvement over the lattice tune in the previous runs. In the past, ad hoc sextupole knobs had to be adjusted as the insert was ramped to stably operate at various tunes. The fast ramp is the approach used in regular operation, an immediate "snap" to a desired t-parameter proved too destabilizing. Additionally, a ramp provides for more iterative checking of the generally unreliable control system. This measurement was collected before the full DN calibration was finalized, so it does not quite arrive at the integer resonance equivalent setting like the scans above.

## 5.2 NIO Studies Kicked Beam Collections

Measurements of kicked beam data is convenient and information rich with electron operation. Synchrotron radiation damping means the beam occupies a relatively small portion of the phase space and the motion of the centroid closely approximates the motion of a single

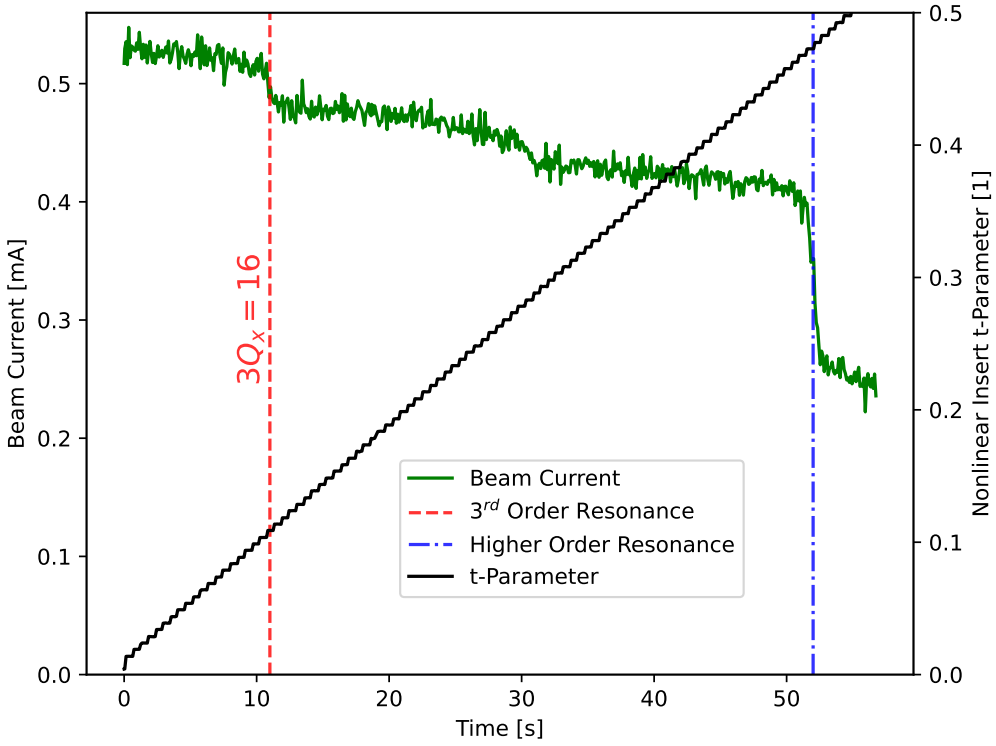


Figure 5.2 Circulating current in IOTA while ramping t-parameter with chromatic compensation

particle at the same amplitude. The radiation damping also means that the beam "resets" after a kick as the beam damps back down to its equilibrium emitttance quickly. In the case of IOTA, the damping time is significantly longer than the BPM sample range, and on the order of the kicker reset timing. We do not introduce significant damping systematics in the TBT data, and can effectively kick as quickly as the hardware safely allows to maximize the available lifetime between re-injections. For kicked beam measurements we have access to all 21 BPMs on a TBT basis and the current measurements, nearly our full diagnostic complement. The synchrotron radiation cameras lack the acquisition systems and speed for kicked beam measurements, but the live monitoring provides useful operational information on kick success, amplitude, and damping. There were two primary configurations for kicked beam measurements in the experimental run. The first was a simple grid in the parameter space of the kicker setpoints. Early in the run, coarse calibration of the kickers was performed to evaluate their respective strengths. These ratios were used to roughly scale to a grid in beam

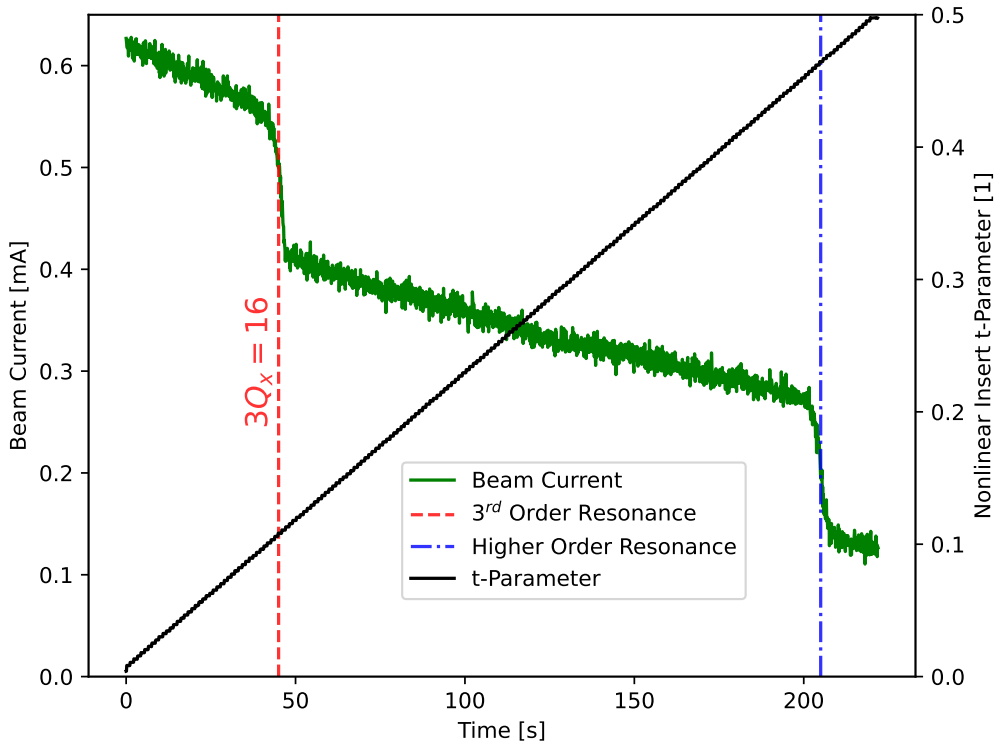


Figure 5.3 Circulating current in IOTA while slowly ramping t-parameter with chromatic compensation

configuration space. As described in section 4.4, the absolute calibration varies based on the exact lattice configuration, and likely drifts from collection to collection with the overall lattice drift. So, while the coarse calibration does not yield a uniform grid in configuration space, if the kick difference is small the density is sufficient to sample the full available phase space. Two grid ordering approaches were used. For fast measurements, the points were ordered according to the magnitude of their amplitude. This approach seeks to maximize the number of kicks per injection before beginning to lose beam on aperture, physical or dynamic. The second configuration of grid kicks used a raster approach, a single horizontal or vertical kicker setting was selected, and the perpendicular kicker iterated amplitudes until the beam was fully lost on the aperture. The kicks were rastered in both direction, first sweeping one direction then the other. This approach is necessarily slower, but yields the maximum range of samples in configuration space, and was only applied to a few lattice configurations which had been evaluated to have reasonable apertures and large detuning

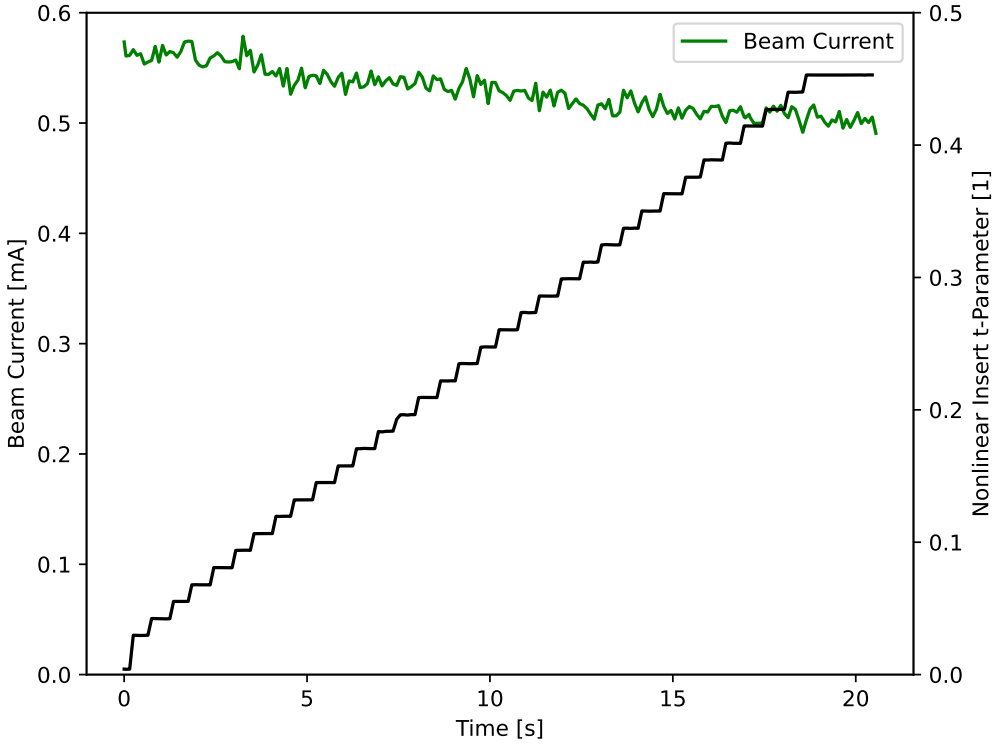


Figure 5.4 Circulating current in IOTA while quickly ramping t-parameter with chromatic compensation

ranges. Figure 5.5 shows an example of the kicker settings for a grid scan with current. The color scale is simply an incrementing counter of individual kicks. It shows the perpendicular rastering, we can see some cases where losses occur more quickly in one direction than the other, and the earlier kicks on the vertical raster lines peek out from behind. The two points not on the regular grid spacing are "calibration" kicks used for collection purposes, but not analyzed.

The other primary collection for kicked beam measurement used was a spoke style scan intended for aperture measurements. For these scans a fixed kicker amplitude ratio was employed, with iteratively larger kicks applied along that "spoke". Initially a binary search style method was evaluated for kick efficient measurement of the aperture. However, in practice, re-injections were time intensive and unreliable, so methods with expected losses at the end were preferable. For each spoke, the beam was re-injected, scraped to a consistent initial current, then kicked along the spoke starting at an expected lossless amplitude. The

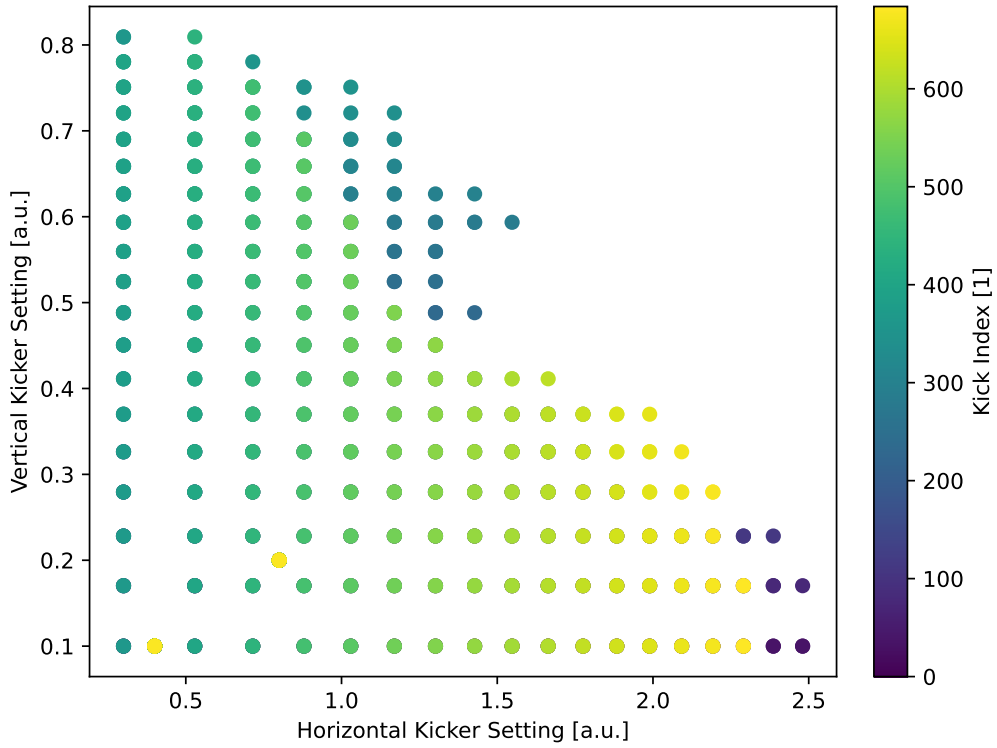


Figure 5.5 Circulating current in IOTA while quickly ramping t-parameter with chromatic compensation

kick amplitude was then increased until total beam loss as measured by the DCCT. The method to measure the aperture with this approach is detailed in section 4.5. In principle the lossless kicks from this approach could also be used for analysis of the TBT motion, but the much better statistics from grid-style scans means this was not often done.

There were two main sextupole configurations studied in the course of the TBT measurments. The first was the minimum chromaticity compensation setpoint mentioned above. To reduce the measured impact of the sextupoles on the dynamic aperture, an optimization of the sextupole configurations was undertaken. Using the remaining four families of sextupoles, four independent knobs which all preserved the first order chromatic compensation were generated and used as the variables for a bayesian optimization. The targets for this optimization were the apertures as measured by the logistic fits on the circulating curreint as described in section 4.5. The resulting optimized sextupole configuration was nicknamed "lilac" based on the color of trace in the optimization output, and has carried forward. The

| Sextupole Family | Chromatic I | Chromatic $K_3$ | Lilac I | Lilac $K_3$ |
|---|---|---|---|---|
| sa1 | 0 | 0 | -0.77 | -8.8127 |
| sc1 | 0.805 | 9.2132 | 1.171 | 13.4021 |
| sc2 | -2.11 | -19.6412 | -1.826 | -16.9975 |
| sd1 | 0 | 0 | -0.263 | -3.0100 |
| se1 | 0 | 0 | 0.254 | 2.9070 |
| se2 | 0 | 0 | 0.81 | 9.2705 |

Table 5.1 Table of sextupole current settings and effective thin lens strength

eperimental sextupole configurations following the IOTA naming conventions are given in table 5.1, in applied current and calculated integrated sextupole term.

### 5.3 Conservation of Nonlinear Invariants

A direct verification of proper implementation of the NIO system would be conservation of the analytically predicted invariants. The same approach was used in section 3.2 for evaluation of insert configurations. To evaluate the invariant expressions, transverse momentum coordinates must be reconstructed as described in section 4.3, and the fitted coordinates needed to be normalized by the bare lattice Courant-Snyder functions at the virtual BPM location. Like the transfer matrices, these quantities were extracted from the design lattice fitted to by LOCO. To benchmark the method, the Courant-Snyder invariants were calculated for the same kicks. For reasonable comparison to the equivalent Courant-Snyder invariant, the first order effect on the lattice functions due to the NIO insert were simulated using quadrupoles in place of the full nonlinear elements. The calculations of the Courant-Snyder invariants used this normalization as opposed to the bare lattice functions. To avoid apparent invariant changes due to any linear coupling, the sum of the horizontal and vertical invariants (the normalized Hamiltonian) was used for comparison [39, p.179]. Figure 5.6 shows the resulting calculated invariant quantities TBT for two kicks. These parameters are normalized to the value at the first turn. Since the decoherence reduces the amplitude of the centroid signal, the invariant quantities also necessarily reduce. The TBT BPM position uncertainty also impacts the invariant uncertainty. The left plot shows a good result for measured conservation, where both nonlinear predicted invariants show relatively

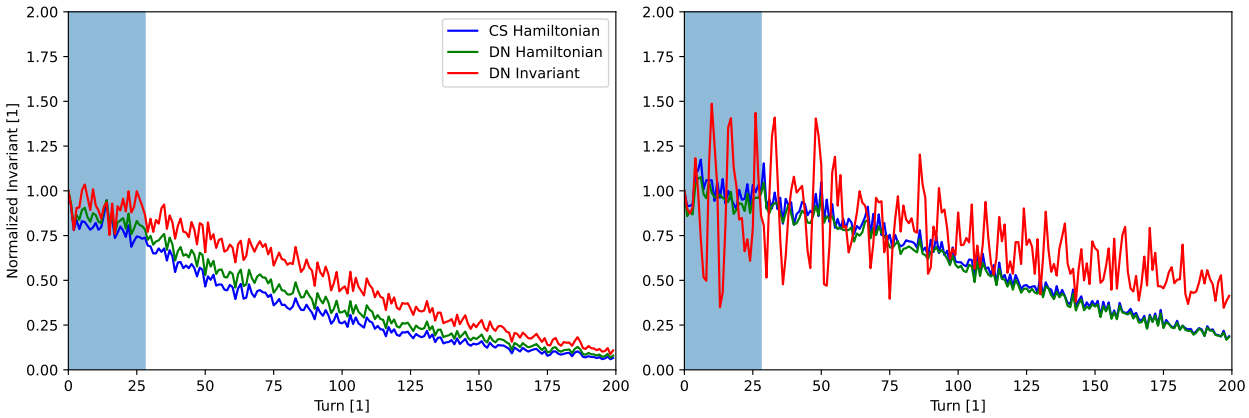


Figure 5.6 TBT calculated invariant quantities, left plot shows general good conservation of all invariant quantities, right plot shows poor conservation of DN second invariant

small deviation from their predicted values. The right plot shows a case where the second DN invariant is not conserved at all. We see large oscillations about a central value, this is a characteristic signature of an arbitrary value calculated from the dynamical variables. These responses were for the same lattice condition with different kick amplitudes.

An approach to evaluating the variance of the predicted invariants is to look at the frequency spectrum of the values. For a conserved quantity, we expect the TBT noise to dominate and the frequency spectrum to be flat. For a non-conserved quantity, we expect peaks in the frequency spectrum corresponding to the oscillation. Figure 5.7 shows the FFT spectra for the same kicks as in figure 5.6. As the decoherence generates a strong zero frequency term in the spectrum, a log-log scale is used to emphasize the higher frequency spectral peaks. We can see the clear peak in the spectrum for the poorly conserved second invariant. This approach is useful as a graphical method, but does not yield an easily interpretable reduced quantity for a given kick.

To compare different amplitudes and nonlinear insert configurations we calculate the standard deviation of these values over the first 28 turns. This was selected to maximize the number of points evaluated before the decoherence becomes prominent for the broadest range of sample kicks at the cost of significant uncertainty in the metric. The first 28 turns are highlighted in Figure 5.6. Figure 5.8 shows the variation of the Courant-Snyder

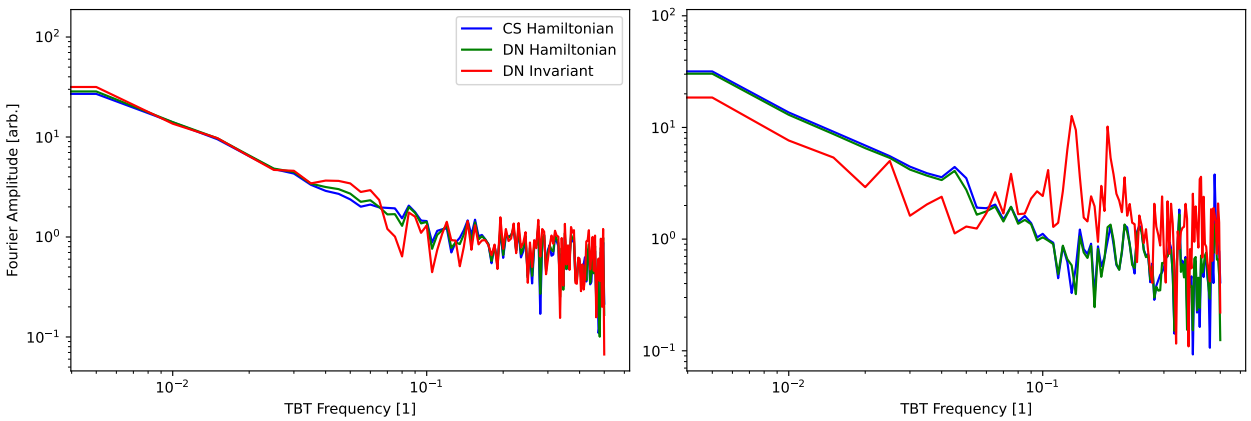


Figure 5.7 Turn based spectral composition of calculated invariant quantities for example sets

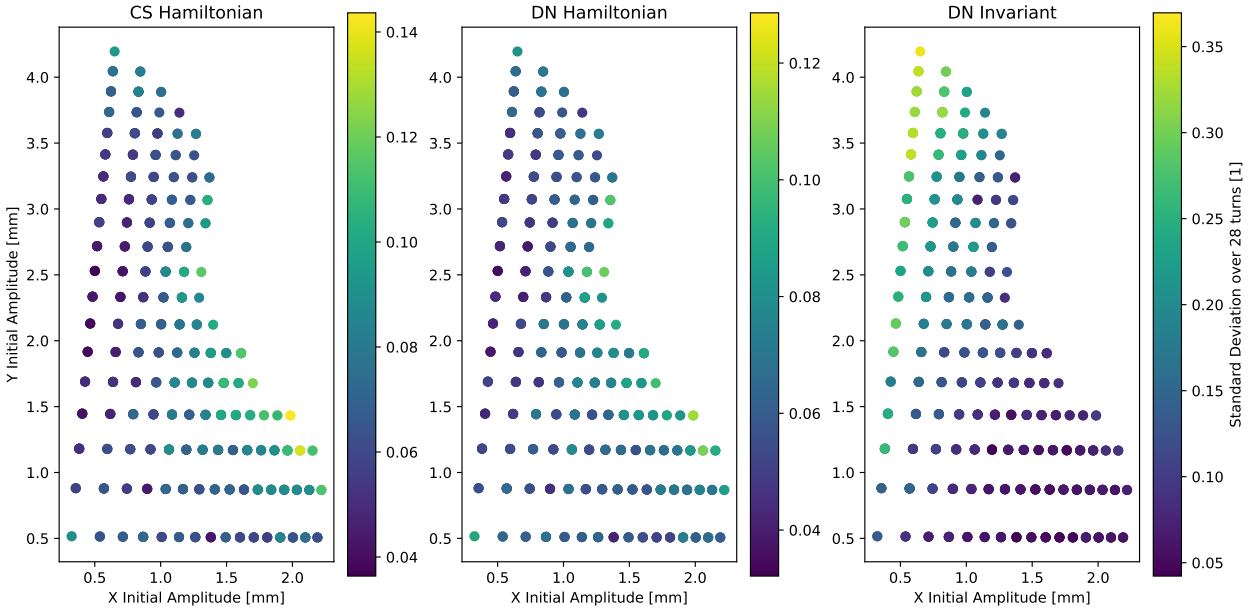


Figure 5.8 Color plot of standard deviation of analytically predicted invariants over first 28 turns, each plot has individual color scaling for better contrast but underlying metric is the same

Hamiltonian, DN Hamiltonian and DN second invariant over the first 28 turns versus the kicker setting. The lattice configuration is with the "lilac" sextupole configuration and a nominal $t = -0.238$. The coupled calibration factors are used, which results in a skewed grid from the initial Cartesian input kicker settings.

The first DN invariant (the Hamiltonian) is similar in functional form to the overall Courant-Snyder invariant. As a result these two quantities display similar levels of conser-

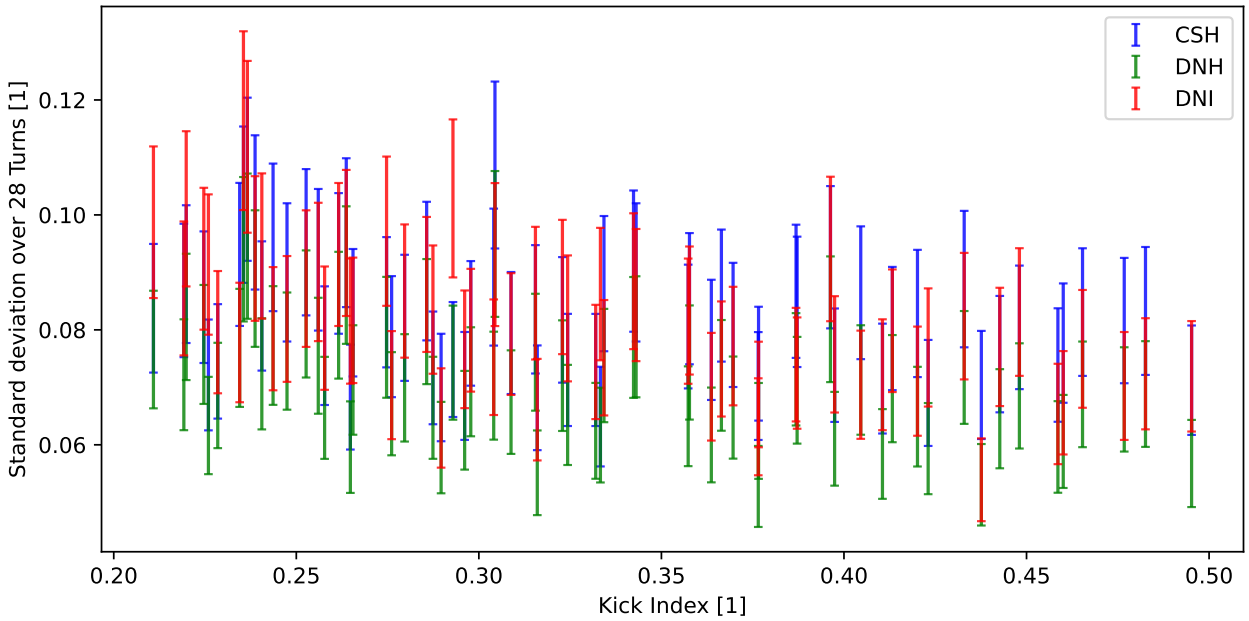


Figure 5.9 Invariant conservation for repeated kicks with same nominal amplitude as current naturally decays

vation. A better metric is looking at the conservation of the second DN invariant. Based on this plotted invariant space we see reasonable conservation of both nonlinear invariants of motion for low vertical kicks and middling horizontal kicks. Based on this observation, a collection was taken for the same kicker settings repeatedly for the full beam lifetime. Once again, the sextupoles are in the "lilac" configuration and the nonlinear $t = -0.238$. We can observe the nonlinear invariants versus current for this setting, in Figure 5.9. There is a slight reduction in overall conservation as current goes down, this is an expected effect of the decreasing signal to noise ratio we see in the BPM TBT signals. Additionally, the values are all within the statistical uncertainty for the range from about 0.33 to 0.5 mA.

This set corresponds to the best conservation of the nonlinear invariants via this method. We can compare to the predicted deviation between the conservation of the Courant-Snyder invariant with adjusted lattice functions and the nonlinear invariants in simulation for the same initial amplitudes. Table 5.2 shows the difference in the invariants in simulation and experiment. Two simulation conditions are considered, originally simulations were performed in the idealized linear lattice ("linmin" from 3.3) indicating a clear difference in conser-

| Invariant | Linmin | Nonlin | Experimental |
|---|---|---|---|
| CS Hamiltonian | $1.07\times10^{-2}$ | $5.04\times10^{-2}$ | $8.02\times10^{-2}$ |
| DN Hamiltonian | $5.59\times10^{-3}$ | $4.95\times10^{-2}$ | $6.66\times10^{-2}$ |
| DN Invariant | $6.83\times10^{-3}$ | $6.95\times10^{-2}$ | $7.54\times10^{-2}$ |

Table 5.2 Fractional Invariant conservation standard deviation for simulation and experiment with identical transverse initial conditions

vation. However, after identifying the best case conservation quantities, simulation fidelity had improved and comparative simulations with sextupole effects and expected nonlinearites ("nonlin" lattice) showed similar conservation quantites in simulation. Direct calculation of the analytical invariant quantities from fitted position data or simulation has insufficient resolution to demonstrate conservation of these invariants for a realistic lattice. We can still evaluate the topography of better and worse conservation for evaluting the interplay of NIO with perterbative nonlinearities.

### 5.4 Amplitude Dependent Detuning

A useful measurement of the nonlinearities of a system is to directly evaluate the change in tune with the amplitude. This figure of merit impacts the potential effectiveness of the Landau damping of a system. The amplitude dependent detuning was measured for different t-parameter settings ranging from $t = -0.05$ to $t = -0.41$. The resonant capture effects covered in sections 3.5 and 4.1 had a strong impact on available detuning measurements beyond $t = -0.275$. Figure 5.10 shows the detuning for a t-parameter setting of $t = -0.330$. Here the collection was a rastered grid-style scan of kicks, so many different amplitudes are sampled. Note the clustering of tunes on the third order coupling line, sextupole terms tend to drive this coupling and trap the beam on the resonance. This does not negatively impact stability, but renders us insensitive to the detuning effects from the NIO.

Figure 5.11 shows the resulting phase space for the beam on this coupling resonance. The contours are characteristic of the two-to-one ratio of the coupling tunes. While the amplitude dependent detuning from the nonlinear insert drives the beam centroid to the resonance, the resonance then dominates and we are insensitive to the NIO effects.

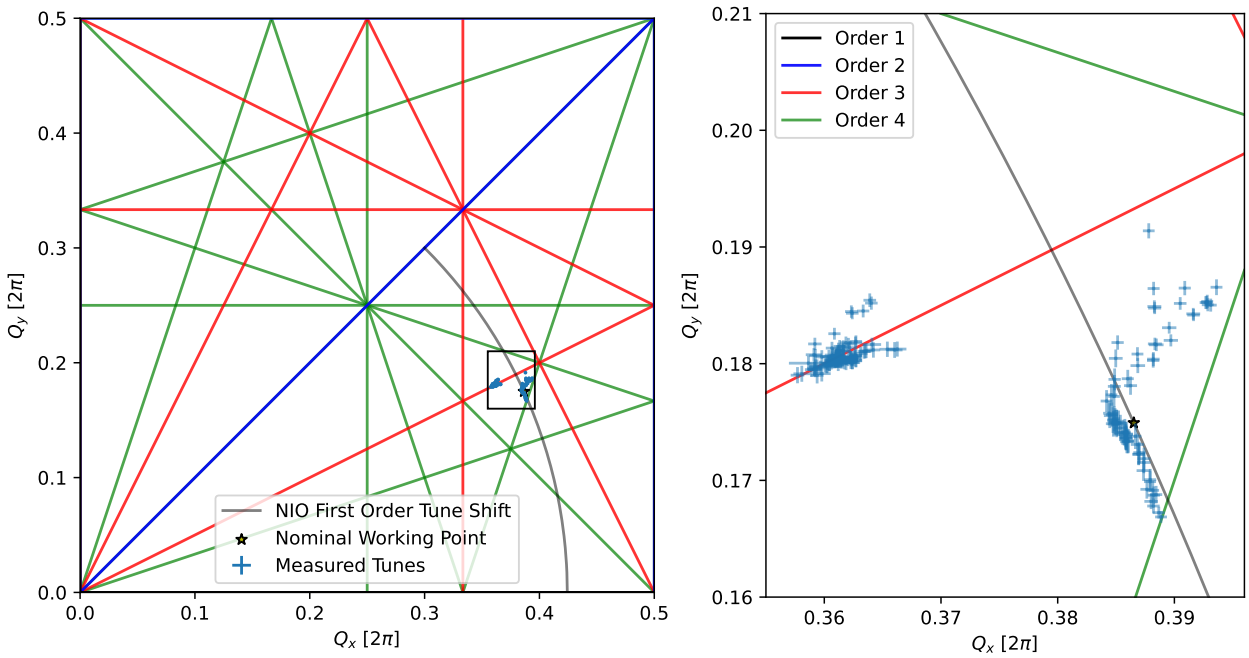


Figure 5.10 Amplitude dependent detuning for nominal $t = -0.330$, sampled for 45 turns

The $Q_x = 1/3$ horizontal resonance line also impacted the available aperture for tune measurements. Figure 5.12 shows the reconstructed phase space of a kick near this line for a NIO setting at $t = -0.140$. The characteristic triangular phase space of a third order resonance in the horizontal plane is visible. This is the same line which had to be crossed quickly when ramping the insert for collections.

Based on these constraints, to measure the maximum range of the detuning without resonant effects, a nominal working point of $t = -0.238$ was selected, which corresponds to $Q_x = 0.364, Q_y = 0.217$. Figure 5.13 shows the detuning for this point sampling 45 turns. This is quite fast and leads to some uncertainties in the tune measurements. Figure 5.14 shows a further zoomed version of the plot with errorbars indicating uncertainties of the tune measurements in each plane. The errors are vertically dominated as the decoherence in the vertical plane is much faster than in the horizontal plan. We still see resonant capture effects on fractions of the beam for this configuration. If we are dominated by TBT centroid signal before full decoherence we are sensitive to the DN NIO detuning. However, if the tune length is sampled for a long span, resonant capture of a fraction of the bunch begins

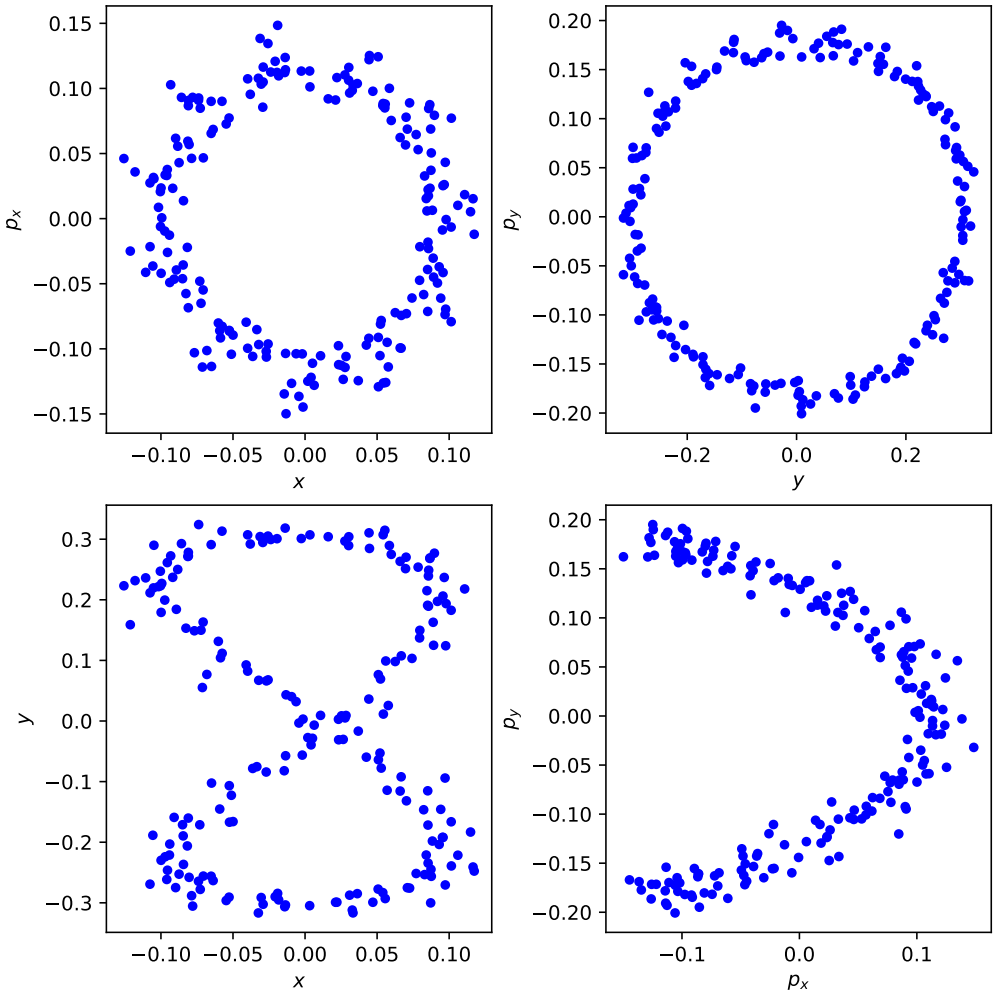


Figure 5.11 Reconstructed phase space for kicked beam captured on a second order coupling resonance

to dominate the tune measurements. Figure 5.15 shows the same tune space measurements for a TBT sample range of 190 turns. We see resonant capture near sextupole and octupole coupling lines.

We can also compare this detuning with our directly calibrated amplitude measurements. As the amplitude calibration depends on the linear lattice parameters, the direct amplitude dependent measurements were only valid for the "lilac" sextupole configuration. Figure 5.16 shows the tune in both planes plotted against the equivalent initial linear action in both planes. Each plot contains every kick so the perpendicular detuning and amplitude is visible as the low amplitude tune spread for a given combination. Simulated tunes for the

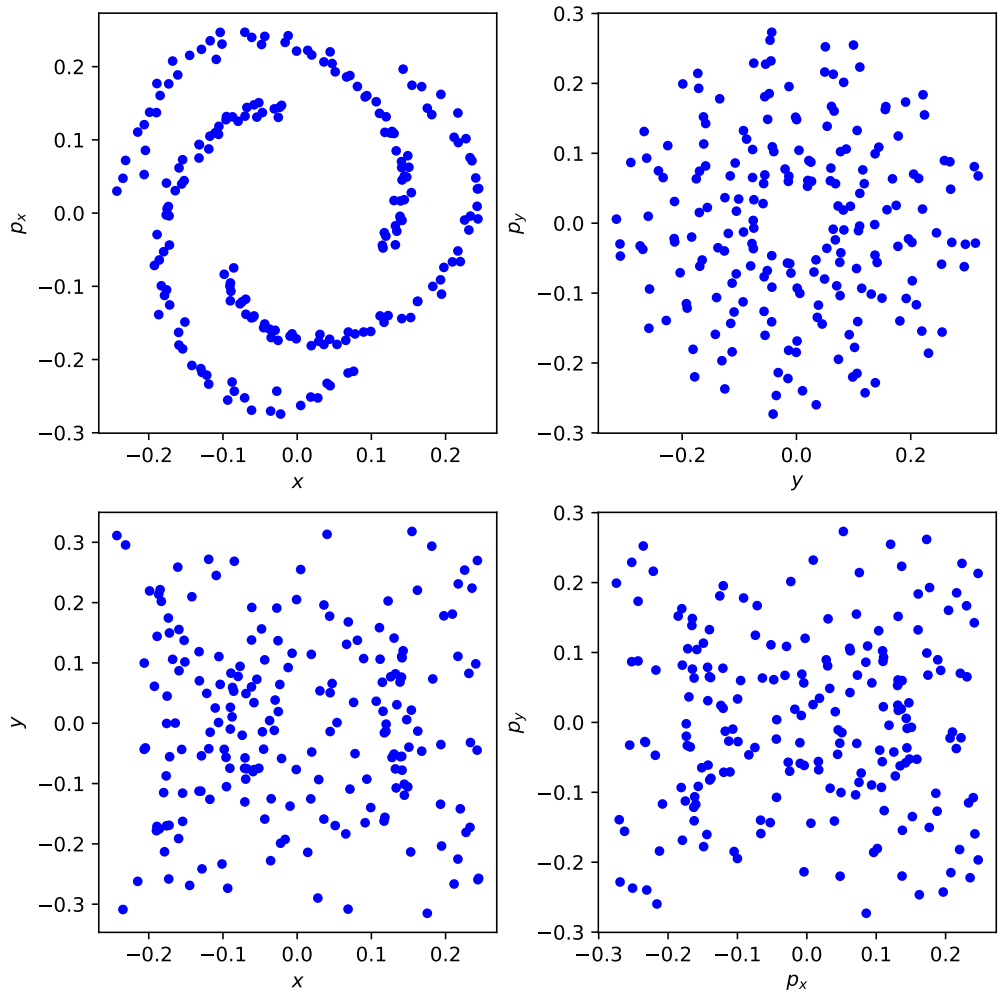


Figure 5.12 Reconstructed phase space for kicked beam with horizontal tune just above third order horizontal resonance

ideal IOTA lattice are plotted alongside. The simulated tunes were calculated using initial positions set by the calculated positions from the measured tunes. The overall direction of the detuning and the ranges are comparable, but a number of features are lacking. The horizontal and vertical detuning versus the horizontal amplitude are suppressed, the slope of the detuning versus the vertical kicks is different. We also see a slight mismatch in the origin of the detuning profiles, this indicates an imperfect bare lattice working point for the measurement configuration. This makes direct comparison of detuning a little harder, but supports the general stability of the NIO insert to perturbations in the matching lattice.

We know that the bare lattice is more complicated than the ideal situation. We can

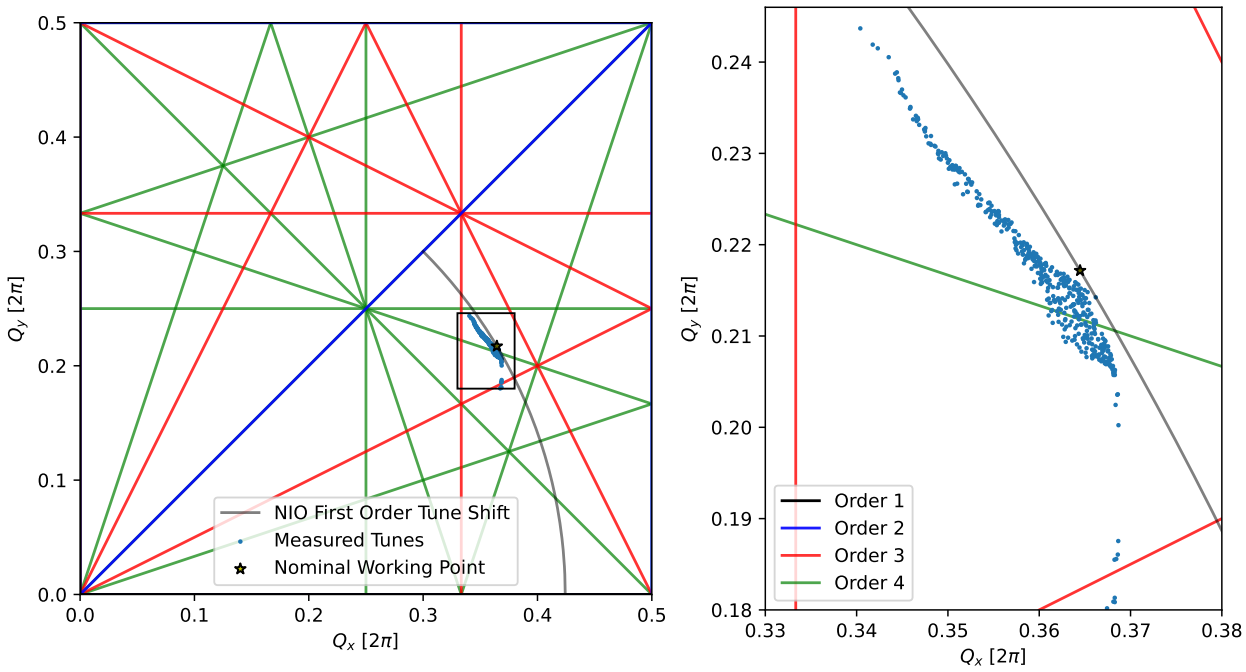


Figure 5.13 Amplitude dependent detuning for nominal $t = -0.238$, sampled for 45 turns

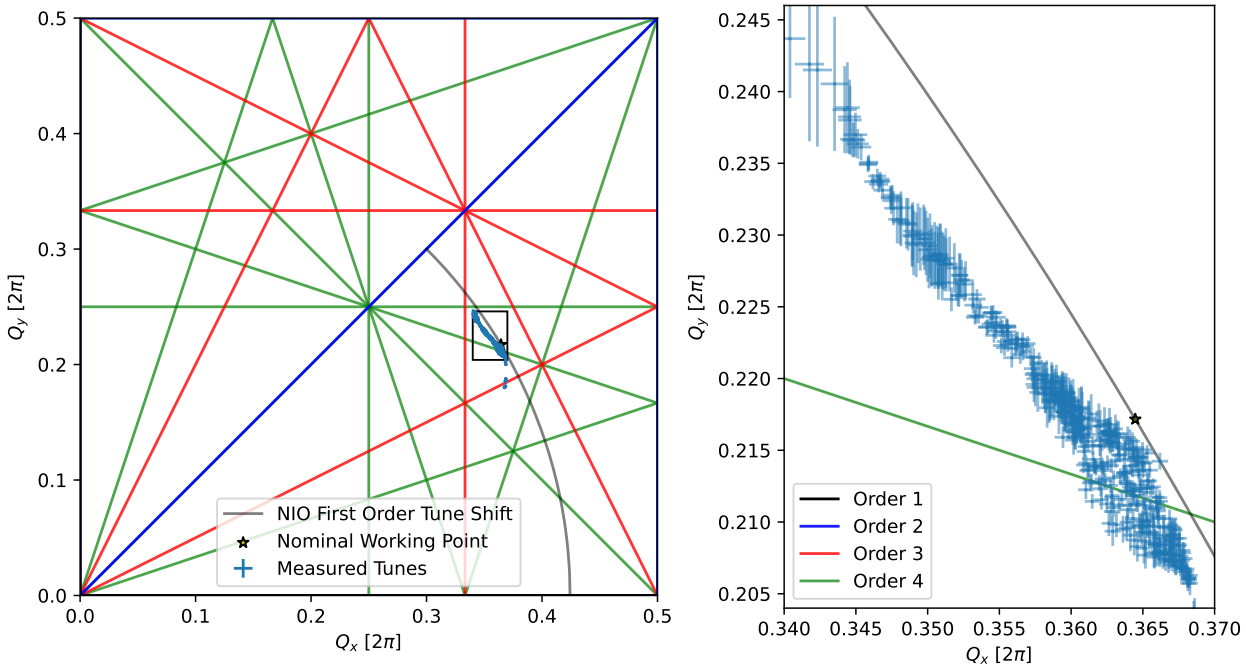


Figure 5.14 Amplitude dependent detuning for same data as figure 5.13 with a tighter zoom to emphasize the main range of tunes with uncertainties. Vertical uncertainties dominate due to very short decoherence times

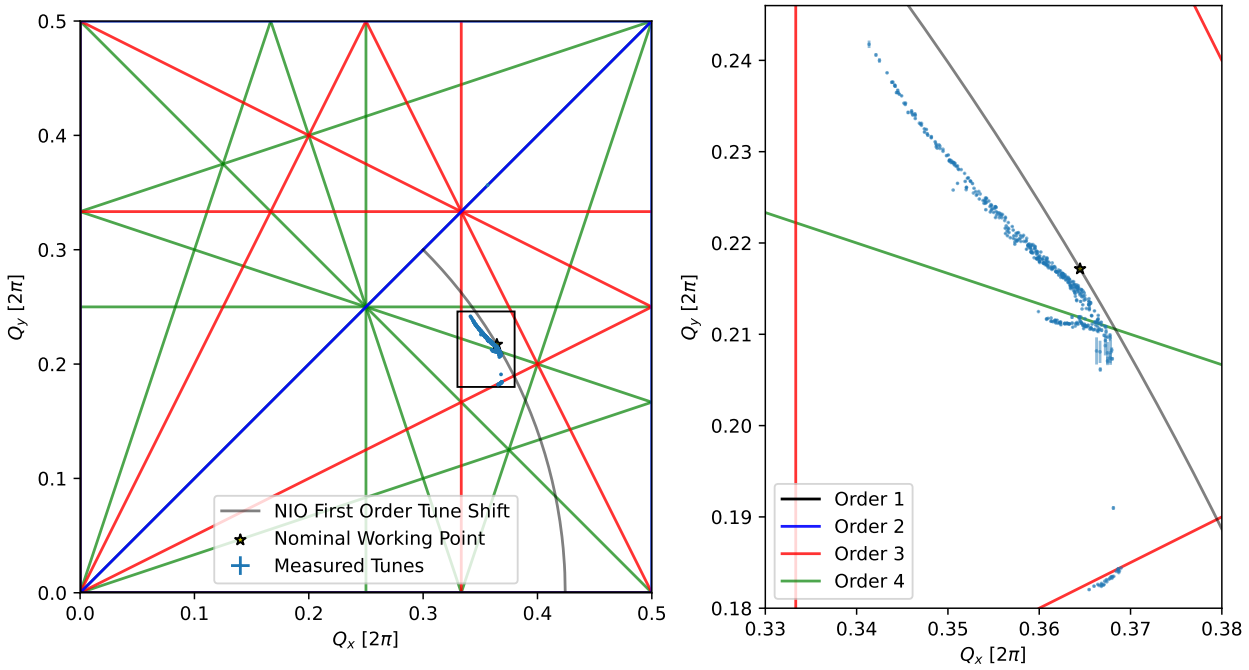


Figure 5.15 Amplitude dependent detuning for nominal $t = -0.238$, sampled for 190 turns. Resonant capture dominates tune measurements for a large fraction of tune space

introduce the sextupole nonlinearities consistent with full compensation of the chromaticities, the exact dipole mappings, and the nonlinear quadrupole fringe field effects to the lattice ("nonlin" lattice from section 3.3). Figure 5.17 shows the same tune vs amplitude plots where the simulation contains these nonlinearities. The most immediately striking effect is the reduction in the range of the tune spread versus the horizontal amplitude, and the "folding" effect which more closely matches the tune ranges.

We make one more comparison, that of the detuning with the residual nonlinearities and only the quadrupole terms of the nonlinear insert to ensure that the dominant contribution to the detuning is the NIO insert. The quadrupole terms of the nonlinear insert must be simulated in order to match the relevant working point. In Figure 5.18 the same detuning vs amplitude plots show significant deviation favoring experimental measurement of the design NIO system. The detuning is much smaller and the horizontal detuning is anti-correlated and depends on the perpendicular amplitude compared the DN detuning.

The effect is more striking in tune space, Figure 5.19 shows the simulated tune spread

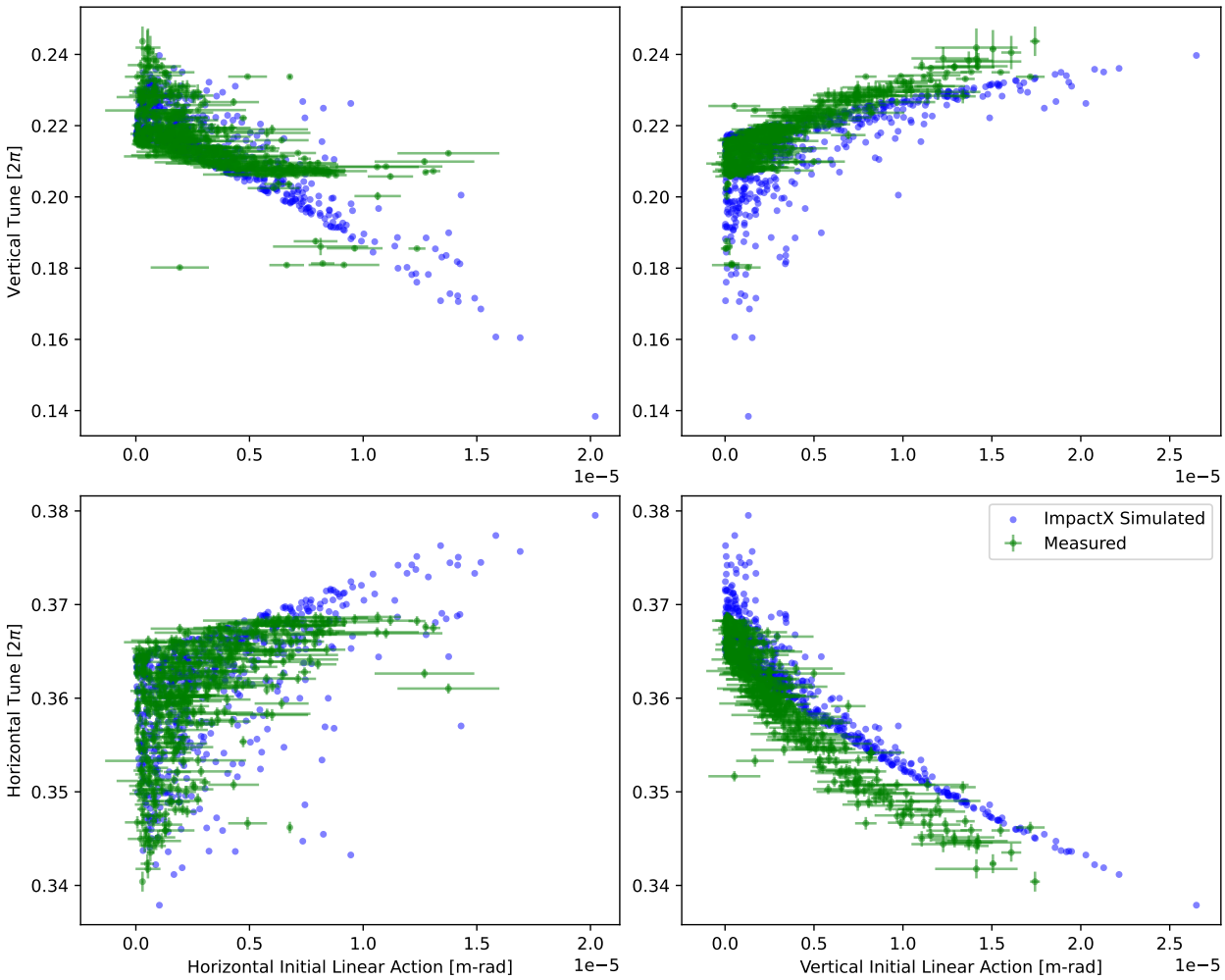


Figure 5.16 Measured centroid tune versus fitted initial linear action with simulated tunes in idealized IOTA lattice for identical initial actions

for configuration S3. Here we can clearly see the anti-correlated horizontal detuning across the opposite side of the DN tune shift.

We see significant impacts of the residual nonlinearities in the bare IOTA lattice. We can directly evaluate the amplitude dependent detuning for the bare "lilac" as well. Figure 5.20 shows this detuning. We see coherent detuning along the linear coupling resonance.

## 5.5 Measured Aperture

For evaluations of the available aperture, we first need to understand the admittance, or accepted amplitudes of our lattice. This is of course a convolution of the apertures of the machine and the beta functions at each location. In IOTA the dominant minimizing

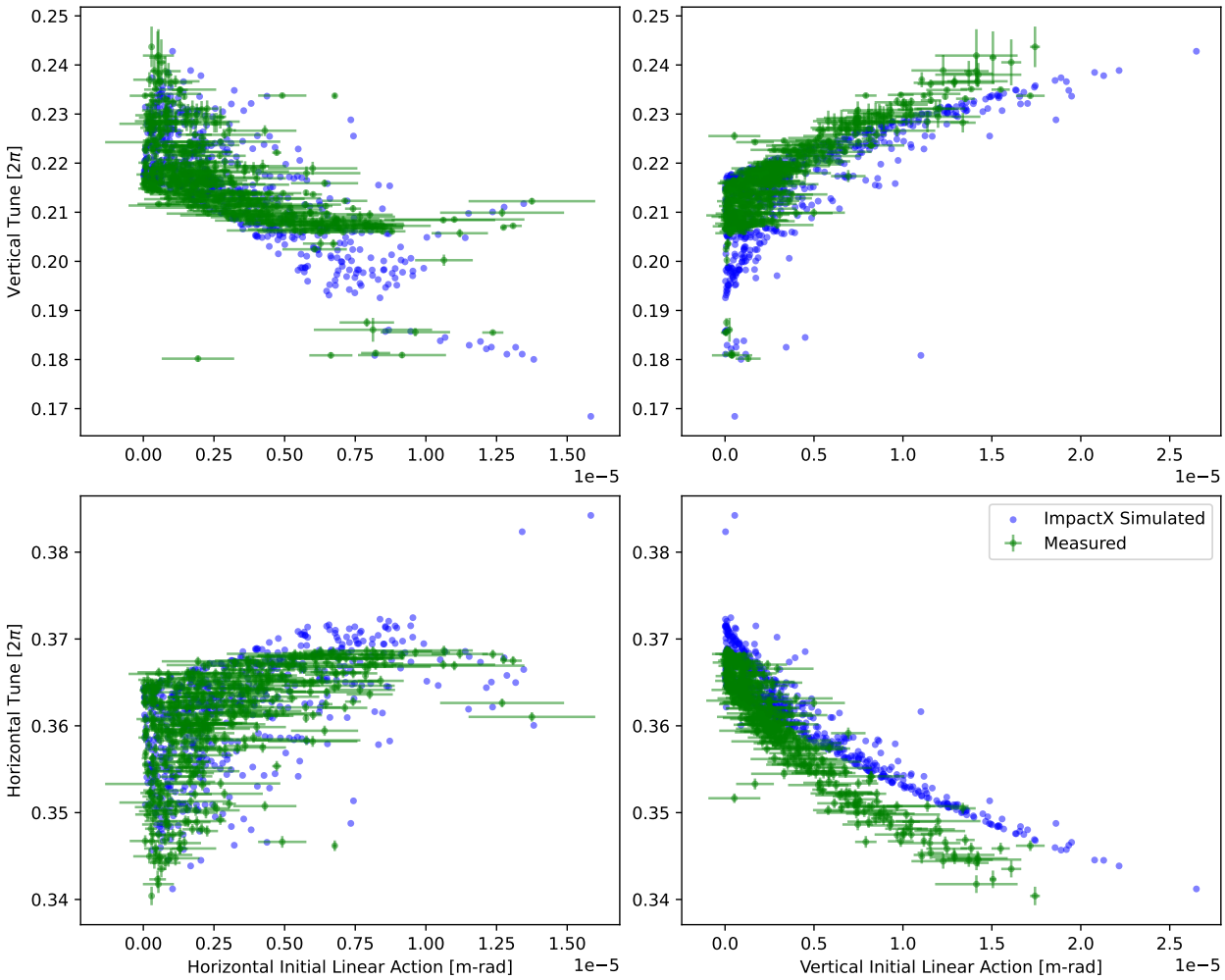


Figure 5.17 Measured centroid tune versus fitted initial linear action with simulated tunes in IOTA lattice with ad hoc nonlinearities for identical initial actions

aperture is that in the nonlinear insert. due to the small size of the nonlinear magnet poles, the aperture is constrained, nominally by the normalization due to the design beta function in the insert. Figure 5.21 shows the CAD drawings of the IOTA NIO insert vacuum chamber, at the center and the entrance. The most strict minimizing requirements are horizontal so this lemon-shaped profile was adopted to simultaneously clear the poles and provide good vacuum conductance in the insert.

Elliptical minimizing apertures at each location have been overlaid, while there may technically be extra vertical admittance beyond these ellipses, it is very narrow and simulation software typically only supports elliptical and rectangular apertures. The vacuum chamber

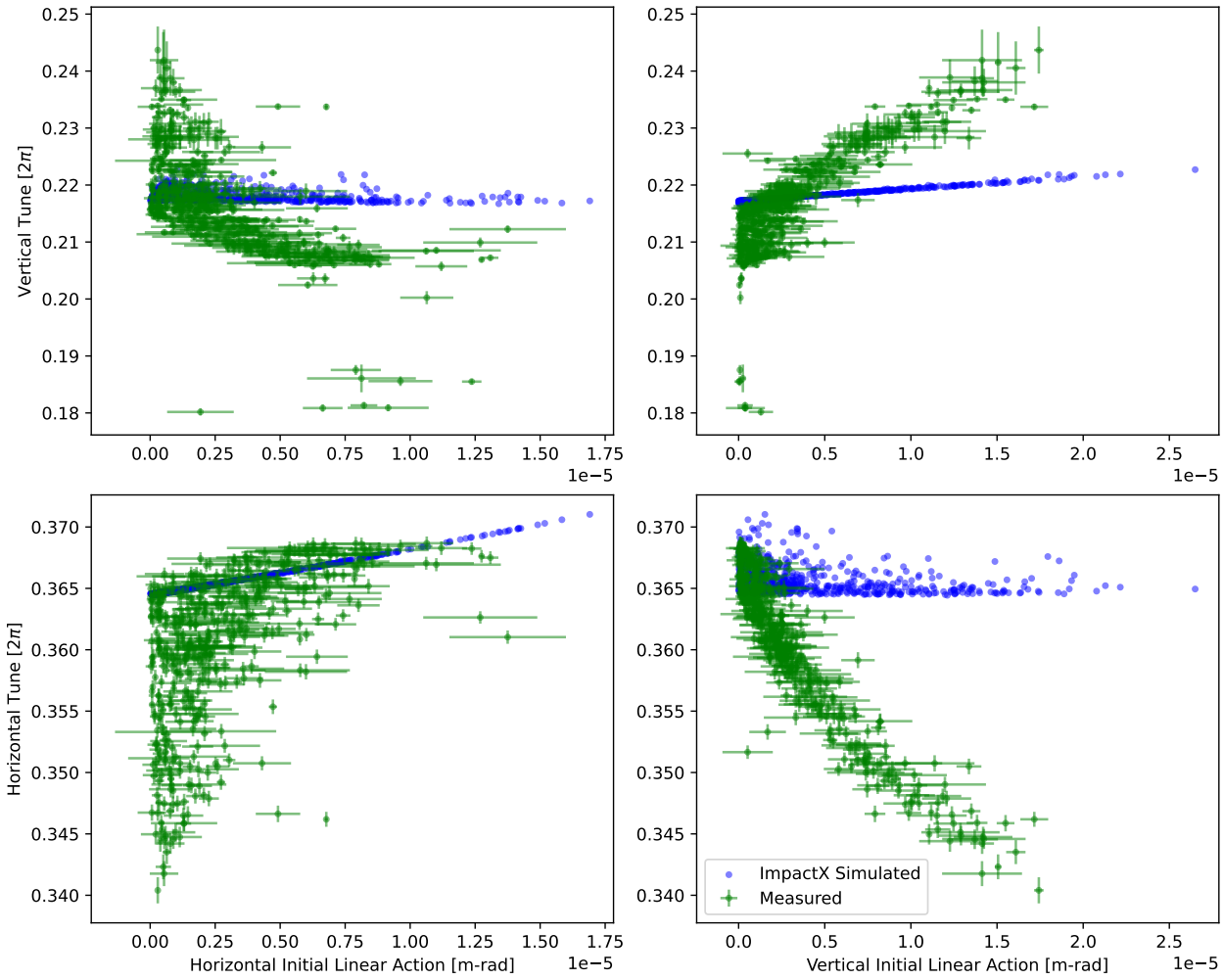


Figure 5.18 Measured centroid tune versus fitted initial linear action with simulated tunes in IOTA lattice with ad hoc nonlinearities and first order component of DN NIO insert for identical initial actions

also does not perfectly conform to the beta function scaling, so a single aperture physically defined is insufficient for the bare lattice. A combined minimizing aperture using the limits in each direction was calculated. Table 5.3 gives the relative values for each. This is a bit coarse, but the uncertainties in our closed orbit location and beta function scaling mean that accuracy below 50µm will be overprecision, so this combined minimizing aperture will be used for reference moving forward.

There is an additional aperture impact on the admittance, the undulator used for other experiments has an atypical vacuum pipe which limits the vertical admittance for low t-parameter values. The first order effect of the DN insert can be used to adjust the beta

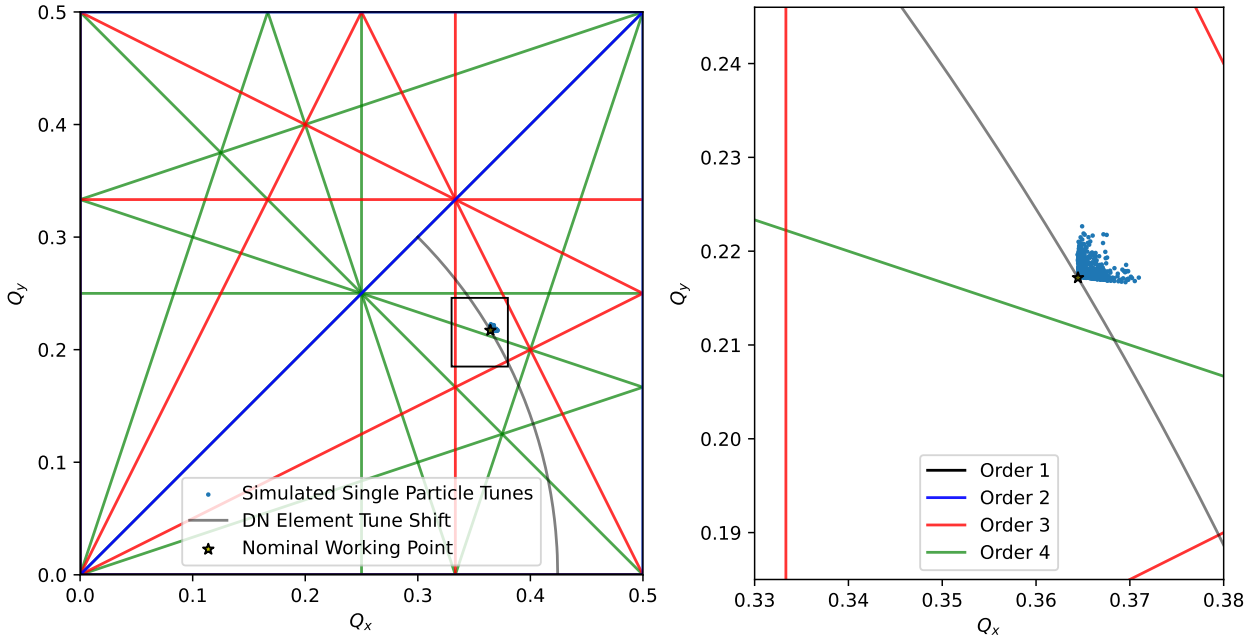


Figure 5.19 Amplitude dependent detuning for simulated IOTA lattice with ad-hoc nonlinearities and first order component of DN NIO insert

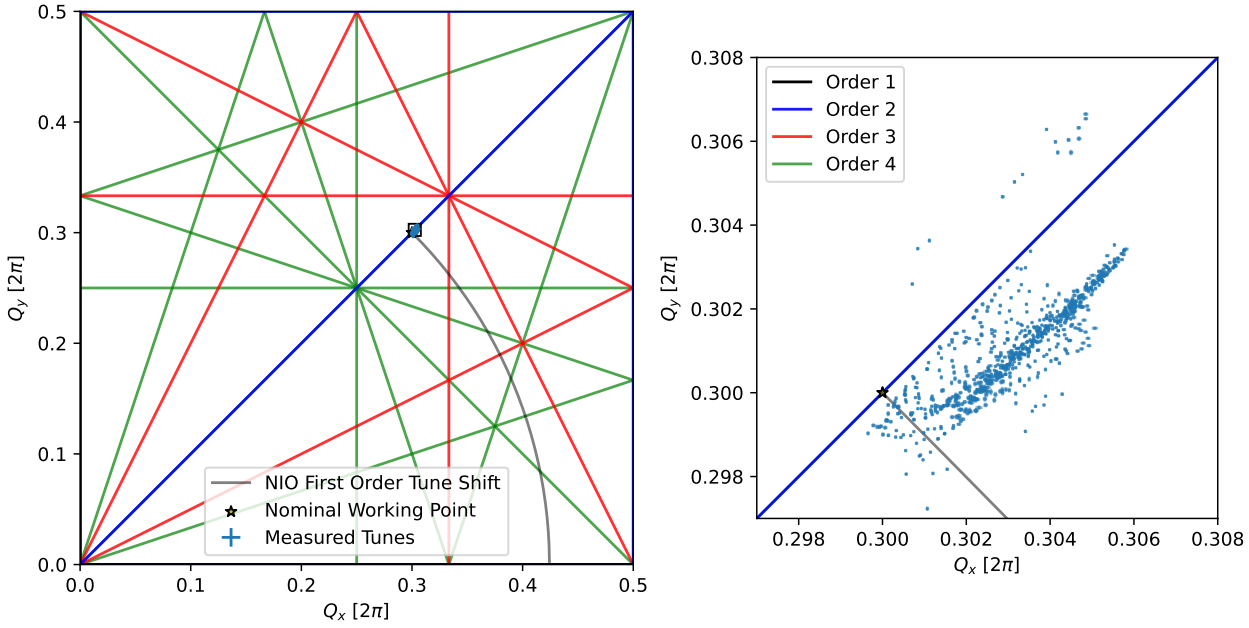


Figure 5.20 Amplitude dependent detuning for bare IOTA lattice. Evaluated for 190 turns, error bars are smaller than markers

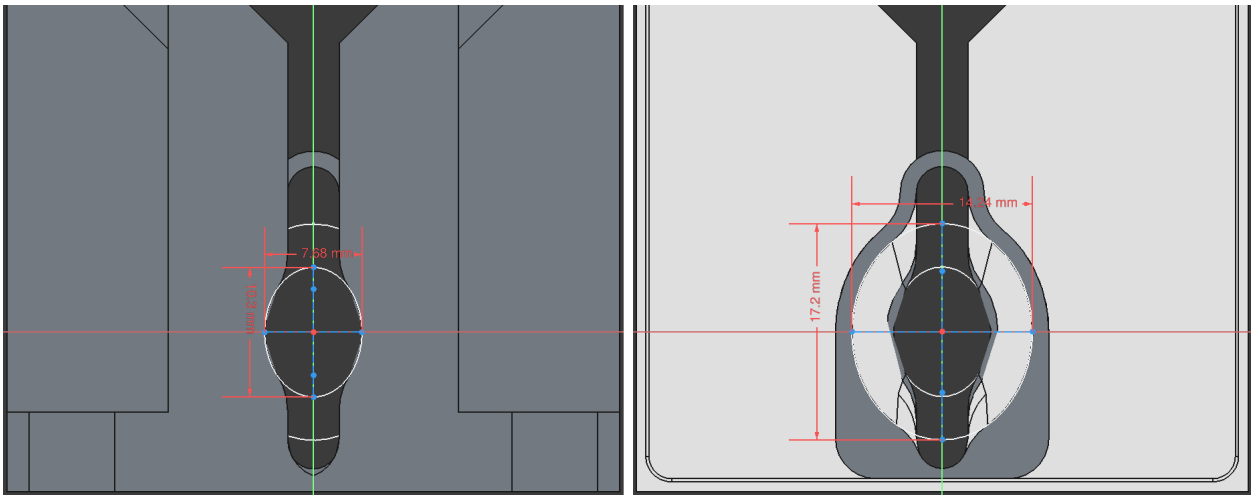


Figure 5.21 CAD drawings of IOTA NIO insert vacuum chambers, with minimizing ellipses in apertures overlaid

| **Aperture** | **X Minor Axis** [mm] | **Y Major Axis** [mm] | **Axis Ratio** [1] |
|---|---|---|---|
| Central | 3.84 | 5.15 | 0.75 |
| Edge | 7.12 | 8.60 | 0.83 |
| Combined Central | 3.84 | 5.05 | 0.76 |

Table 5.3 IOTA NIO Insert Apertures

functions, so we can see that this restriction goes away and the insert vacuum becomes the minimizing aperture for t-parameters $t < -0.2$. Before then, though we end up with a superposition of the ellipse and a flat vertical limiting aperture.

To evaluate the different sextupole configurations, full aperture scans of the bare lattice were taken for different sextupole configurations after the optimization. The losses along fixed amplitude ratio "spoke" kicks were taken as outlined in section 4.5. Figure 5.22 shows the resulting measured aperture limits. The apertures are symmetric, so the limits are mirrored twice to give a sense of the aperture in configuration space. For comparison, the admittance scaled to the center of the nonlinear insert is plotted in the thick black lines. Both the insert vacuum and the undulator contribute here, so the actual admittance restriction becomes the minimum of these overlapping contours, a vertically truncated ellipse. The uncertainties presented are the rms beam sized according to the expected emittance for

the current at loss combined with a 50µm uncertainty from the kicker amplitude. The flat vertical aperture also includes a contributed uncertainty (represented in the grey shading) from the closed orbit in the undulator. While the closed orbit is carefully controlled in the nonlinear insert, it is less well controlled in the rest of the lattice, which contributes to about a ±0.5mm uncertainty in the closed orbit at that aperture. We see significant impacts on the sextupole configuration from the sextupole fields. Without any sextupole excitation, we see significant horizontal dynamic aperture restrictions. The consistent vertical restriction is consistent with a flat vertical aperture restriction. Potentially, this means that the aperture metric systematically under evaluates physical aperture restrictions. This is not so much of a limitation for evaluating relative dynamical losses, so it was not pursued further. It does serve to emphasize that the greatest value from these loss scans is in their relative features, and not in the exact loss limits. Adding the minimum chromatic compensation sextupole complement does not adjust the aperture much, making it slightly larger. The optimization result with the "lilac" configuration shows significant gains horizontally at the cost of some vertical aperture.

Figure 5.23 shows the evolution of the aperture for a few low t-parameters in the lilac configuration. We can see here that the vertical admittance changes with the t-parameter, so they can not be strictly plotted on top of each other. We see significant horizontal restriction at $t = -0.094$. There is also significant vertical restriction at $t = -0.14$. Both of these collections are near the horizontal third order resonance, and the dynamic aperture restrictions are consistent with detuning onto the unstable sidebands of this resonance.

Figure 5.24 shows the evolution of the aperture for a selection of t-parameters beyond where the admittance is affected by the undulator vacuum, so the contours are all restricted by the same minimizing aperture in the nonlinear insert. We see reasonable aperture conservation in the vertical plane for the first few t-parameters, but the horizontal aperture shrinks to a plateau for middling t-parameters around our nominal good configuration. For larger t-parameters beyond $t = -0.33$ we begin to see a significant reduction in the aperture, and

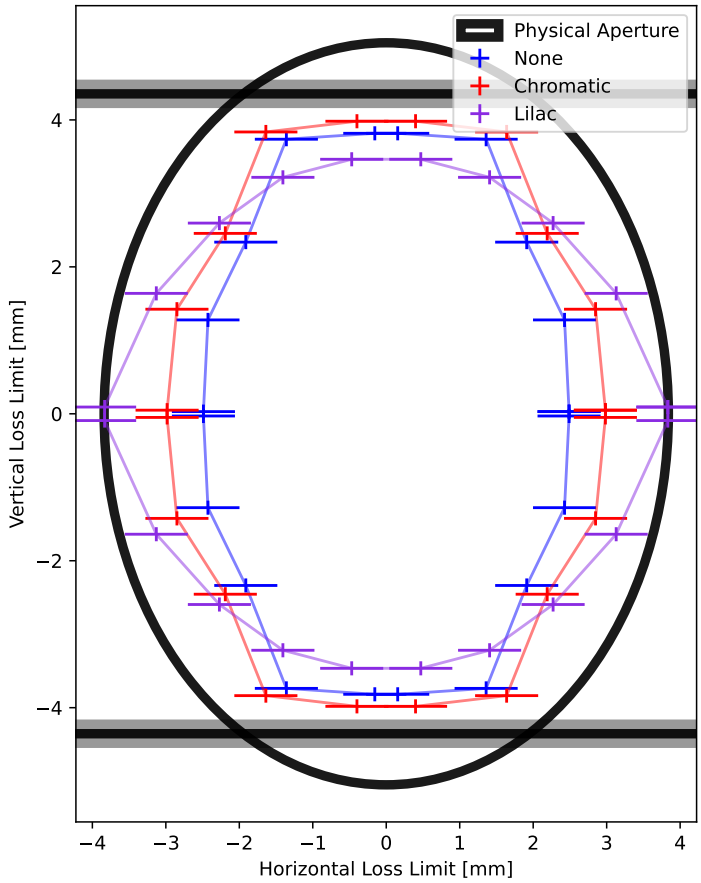


Figure 5.22 Aperture limits of different sextupole configurations for the IOTA bare lattice

approaching a t-parameter of $t = -0.45$ the kicked beam losses method becomes unreliable due to the working point losses in this region.

Figure 5.25 shows the evolution of the aperture for different t-parameters in the IOTA lattice with only chromatic compensation sextupoles. The $t = 0$ measurement here is not the same as in 5.22 as collections from the same day are preferred for the most direct comparison. There are a number of t-parameter settings below $t = -0.2$, but only the $t = 0$ setting is constrained by the undulator admittance, so only that limiting aperture is plotted instead of the separate plots in 5.23. Its relative value is not applicable for the rest of the aperture contours, e.g. the $t = -0.187$ is not near the undulator aperture at its vertical admittance settings. Here we see that the evolution is largely the same as with the lilac sextupole configuration. The horizontal aperture shrinks before the vertical, and

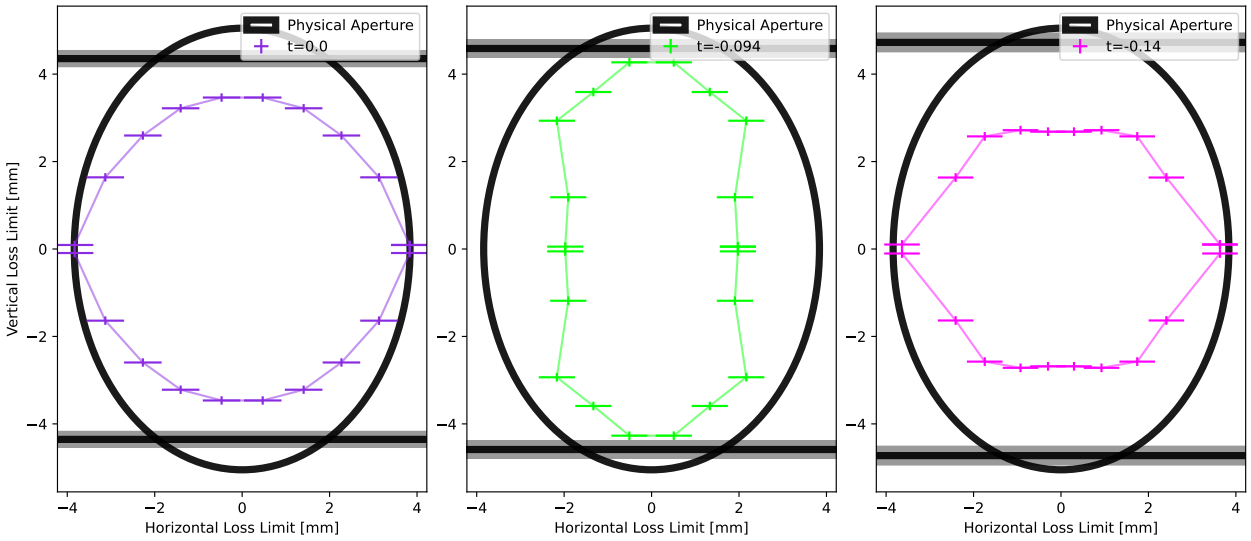


Figure 5.23 Aperture limits for the lilac sextupole configuration with different t-parameters, in the range where the vertical aperture limitation in the undulator still contributes to the admittance

both axes shrink significantly for values of the t-parameter beyond $t = -0.3$. Unfortunately, a direct comparison cannot be made since not all of the same t-parameters were sampled between these lattice configurations. Ultimately, based on the reduction of aperture in both of the widely sampled sextupole configurations near sextupole impacts, it seems that the simple optimization of dynamic aperture for the bare lattice is an insufficient condition for maximizing the available NIO aperture.

Of particular interest for the stability of the DN NIO implementation is its robustness to linear perturbations in the matching lattice. To evaluate this stability a number of orthogonal perturbations to the linear matching lattice were constructed, with a particular focus on the lattice functions in the nonlinear insert drift. To evaluate the relative effect, a consistent t-parameter of $t = -0.223$ and the lilac sextupole configuration were applied for all collections. The t-parameter was intended to be the nominal $t = -0.238$ as used for the amplitude dependent detuning and invariant conservation measurements. Unfortunately, by mistake, the calibration factor found in 4.2 was not applied. Luckily a consistent value of

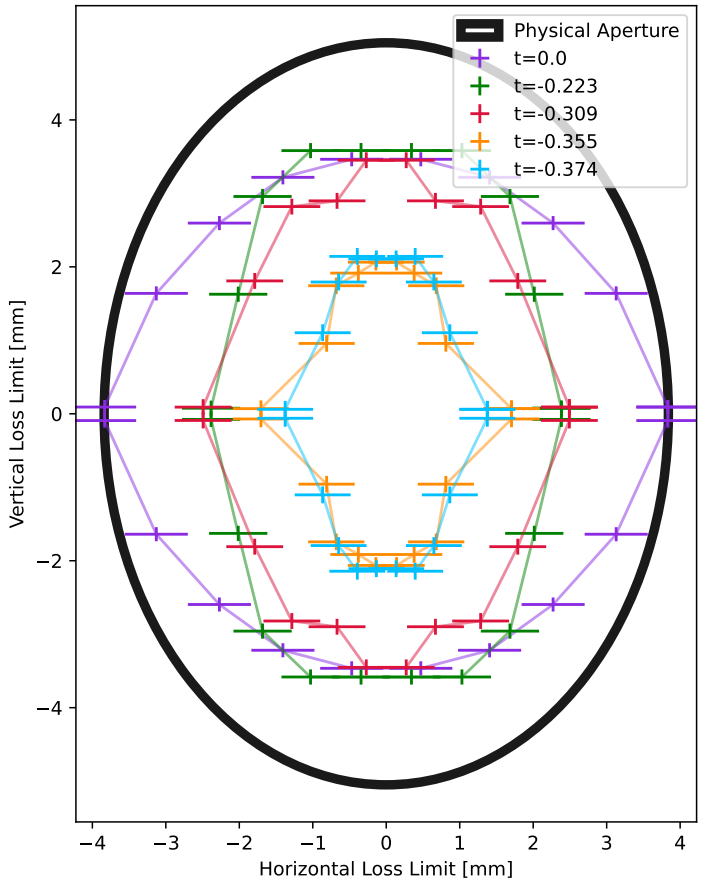


Figure 5.24 Aperture limits of different t-parameters for the IOTA "lilac" lattice

$t = -0.233$ was applied for almost all of the aperture measurments, so we can still make relative measurements. As a baseline, we should evaluate the stability of the aperture measurment for collections at different times. Figure 5.26, shows the nominal lattice aperture at $t = -0.223$ on different collection days. The 10/07 collection shows a little inconsistency vertically, but the horizontal apertures are consistent, and we will compare the measurements to the nearest base lattice which excludes the 10/07 collection moving forward.

The first comparison is the overall tune of the lattice. Nominally, this knob adjusts the phase advance in the matching lattice while leaving all the lattice functions exactly the same in the insert. This exact knob was used on a daily basis for matching the tunes of the bare lattice, usually to a $\Delta Q$ lower than $10{\times}10^{-3}$. The perturbations are then significantly worse than the level of lattice control we expect. We see general reduction of the aperture for

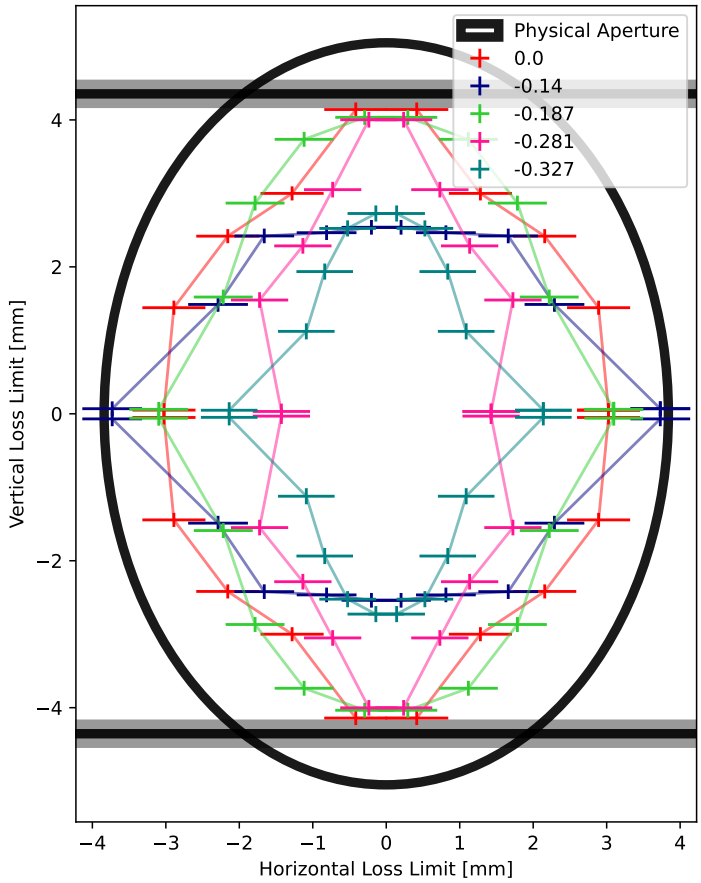


Figure 5.25 Aperture limits of different sextupole configurations for the IOTA bare lattice

mismatch of the external lattice, with slightly more losses for the increased tune.

The next comparison is adjusting the phase advance across the nonlinear insert, in this case the integer matching condition is conserved, so the overall tune still changes. The system is quite robust to these adjustments, with a sizeable reduction only for significantly reducing the phase advance. Recall that the overall phase advance through the insert is $\Phi_x = \Phi_y = 0.$, so these perturbations are a significant fraction of the overall phase advance. This can be partially understood as a poor implementation of the integration, for a symmetric mismatched phase, it simply looks like we did a worse job of matching the nominal scaling with the bare lattice beta function.

The next two perturbations we consider are the location of the minimum of the beta function $\beta^*$ longitudinally in the insert. These knobs are quite small, not quite 1 cm in a drift

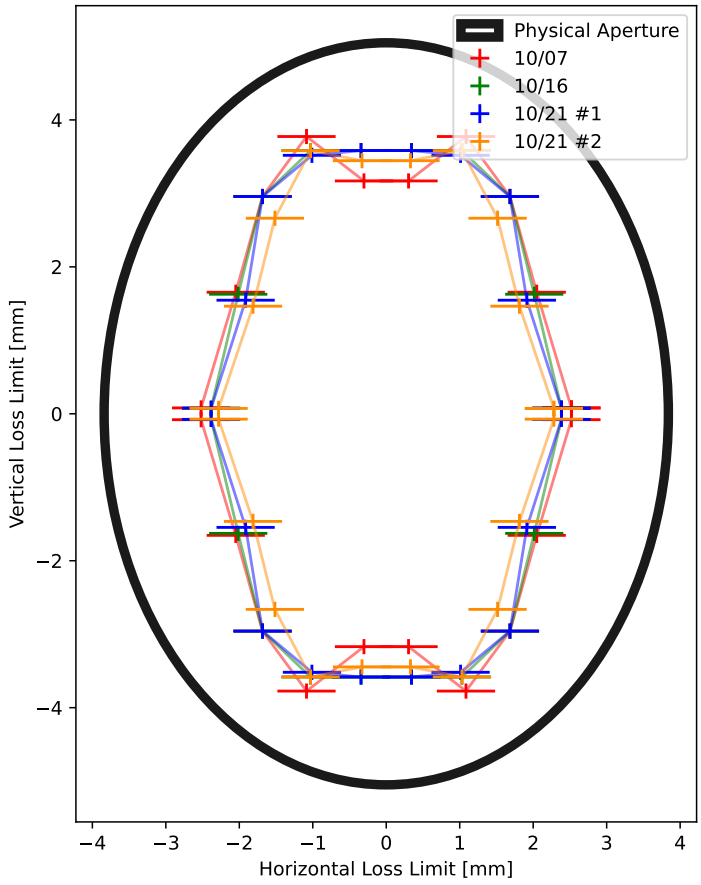


Figure 5.26 Aperture limits for $t = -0.223$ with lilac sextupole settings on multiple collection days

of 1.8 m, but we already see significant reduction in the aperture with these samples. This was one of the main knobs used for increasing the beam lifetime at the integer resonance discussed in section 5.6. The second knob considered here is the amplitude of the dispersion function through the NIO insert. Once again these knobs are quite small, but we see some reduction of the aperture for the most aggressive knob. This is the only comparative perturbation collection with non $t = -0.223$ conditions, the two last points in the dispersion comparison were taken at the properly calibrated $t = -0.238$. However, we see no significant reduction in aperture for the $+2\times10^{-2}$ collection, so the comparison is likely reasonable.

Additionally, an effect related to the configuration space of the NIO system may shrink the admittance. For larger t-parameters, the configuration space begins to take on an "hourglass" shape, so for a given horizontal axis position, parts of the beam off the median symmetry

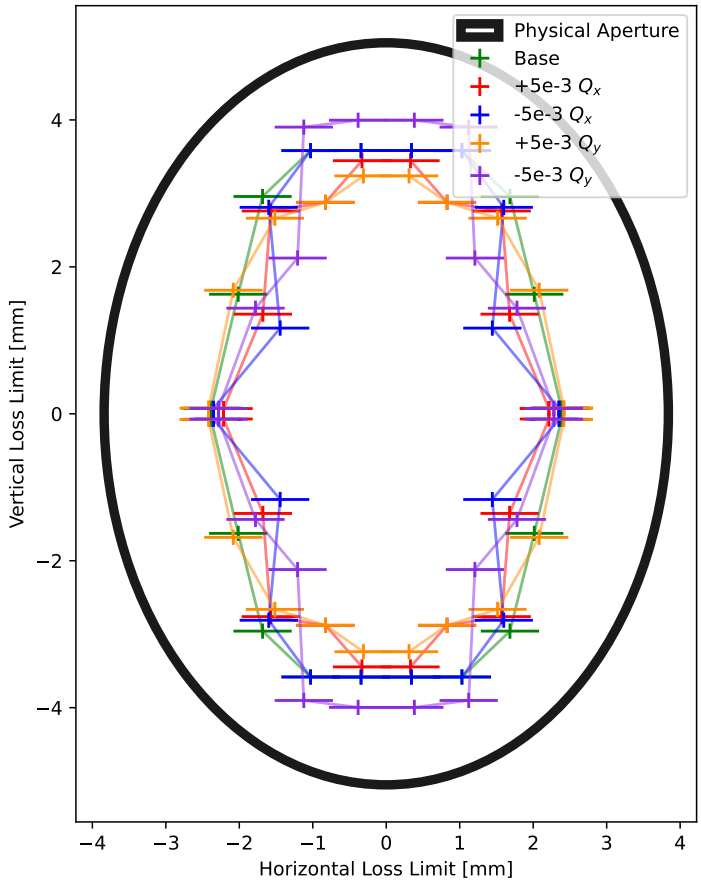


Figure 5.27 Aperture limits for perturbations of the bare lattice phase advance in the matching section outside of the insert with $t = -0.223$

line may have larger horizontal offsets and be lost on the minimizing aperture. Figure 5.30 shows the case for a simple simulation ("toy" lattice in section 3.3) of only the nonlinear insert and a matching matrix. We see losses on the central aperture changing near the horizontal axis for large displacements. This is a strictly nonlinear effect, for a linear system the admittance for this single aperture case would simply be the aperture scaled by the beta function. The majority of suspected dynamic aperture losses occurred at t-parameters where this effect is present in simulation, so it is unlikely to impact these measurements. For future experiments, a full aperture model of IOTA should be constructed and evaluated with DN impacts in tracking simulations, but this is unfortunately beyond the scope of this thesis work.

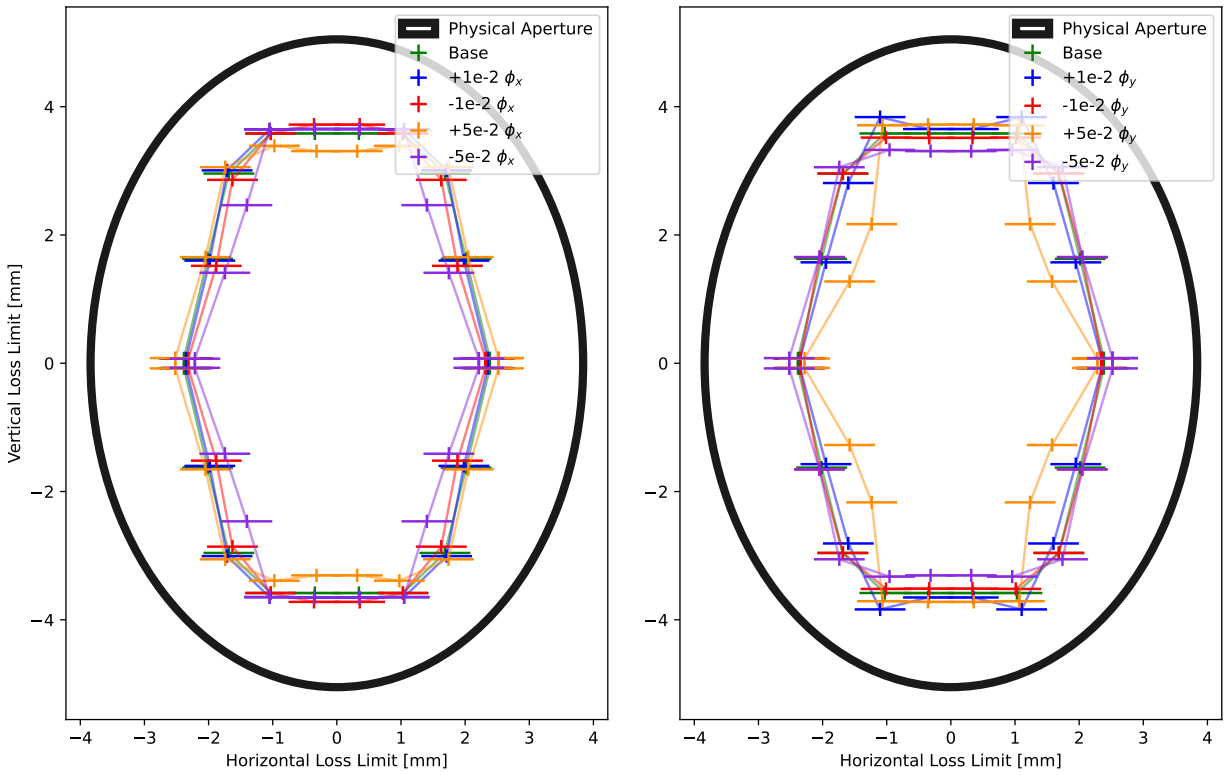


Figure 5.28 Aperture limits for perturbations of the bare lattice phase advance across the nonlinear insert with $t = -0.223$

## 5.6 Nonlinear Stability at Integer Resonance

The synchrotron camera images were used for evaluation of beam stability at the integer resonance condition. To make this observation, the t-parameter was incremented while logging the time dependence of the synchrotron radiation profiles. Based on the calibration of the t-strength from the linear working point in section 4.2, settings crossing the vertical integer resonance were selected. The linear system is fundamentally unstable at this tune, but the NIO system retains stability. Measurements supporting stability in these conditions are strong evidence for the NIO system. To evaluate stability, the lifetime of the beam was evaluated at each t-parameter setting. Beam current was low due to a restricted dynamic aperture and normal beam lifetime, so the DCCT measurements were insensitive and intensity was evaluated from the synchtrotron images. Section 4.6 describes the methods to extract the lifetime from the synchtrotron images.

The topography of the DN system is useful here in tuning the measurements and deter-

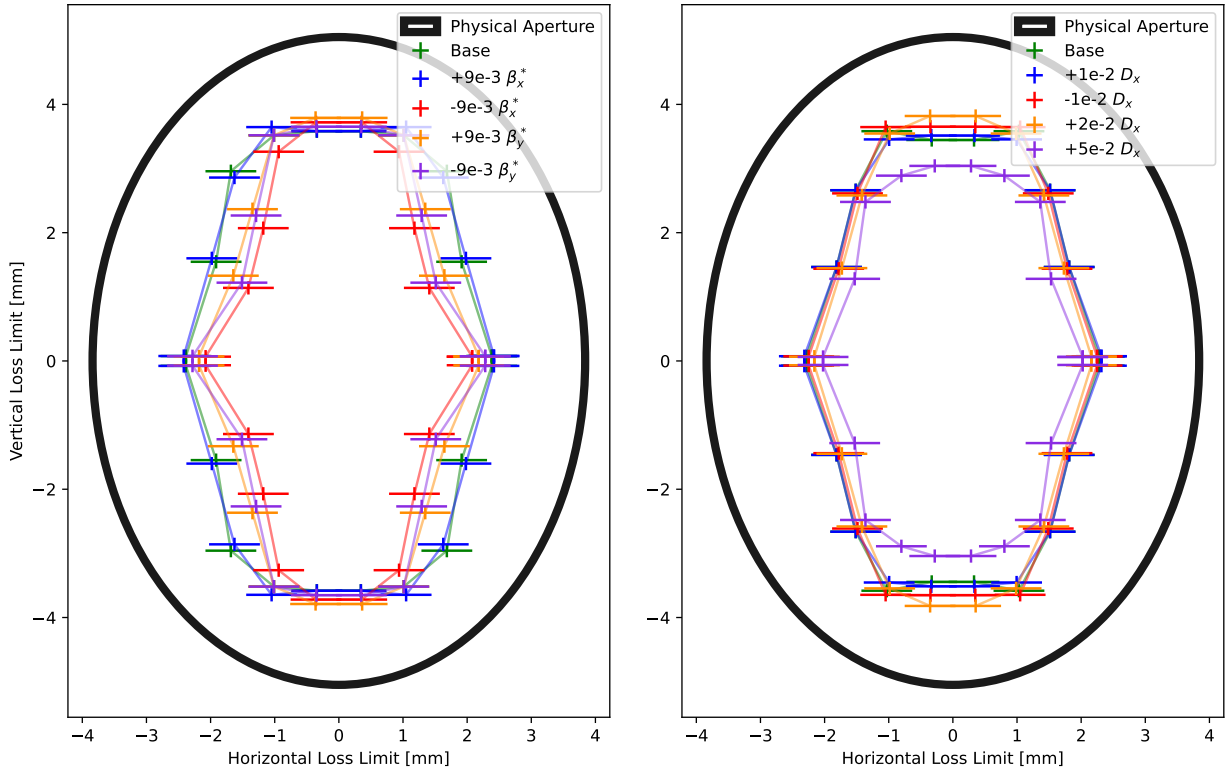


Figure 5.29 Aperture limits for perturbations of the $\beta^*$ location and the dispersion across the nonlinear insert

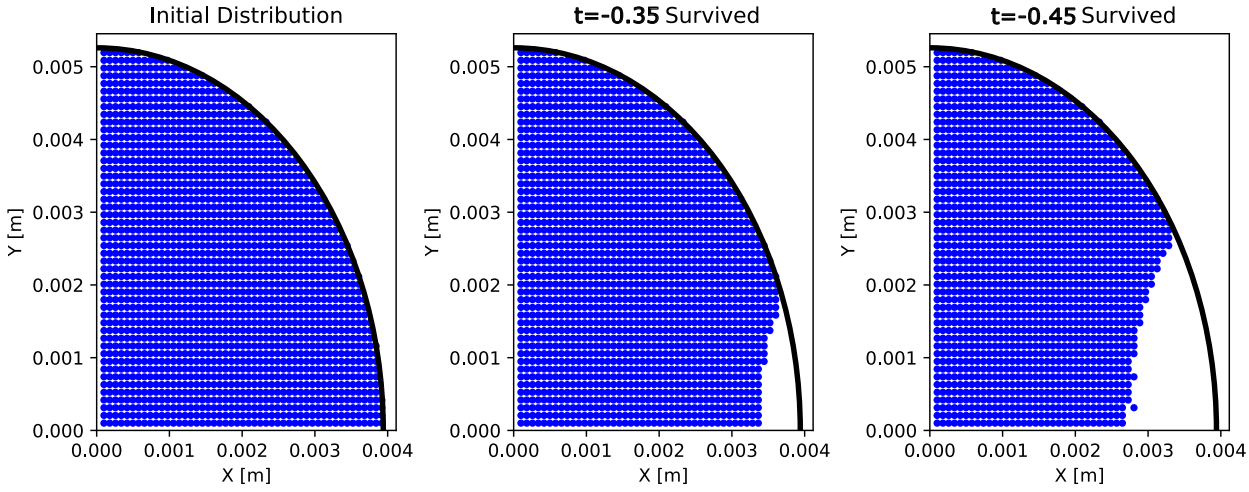


Figure 5.30 Evolution of admittance for a simple thin lens DN system

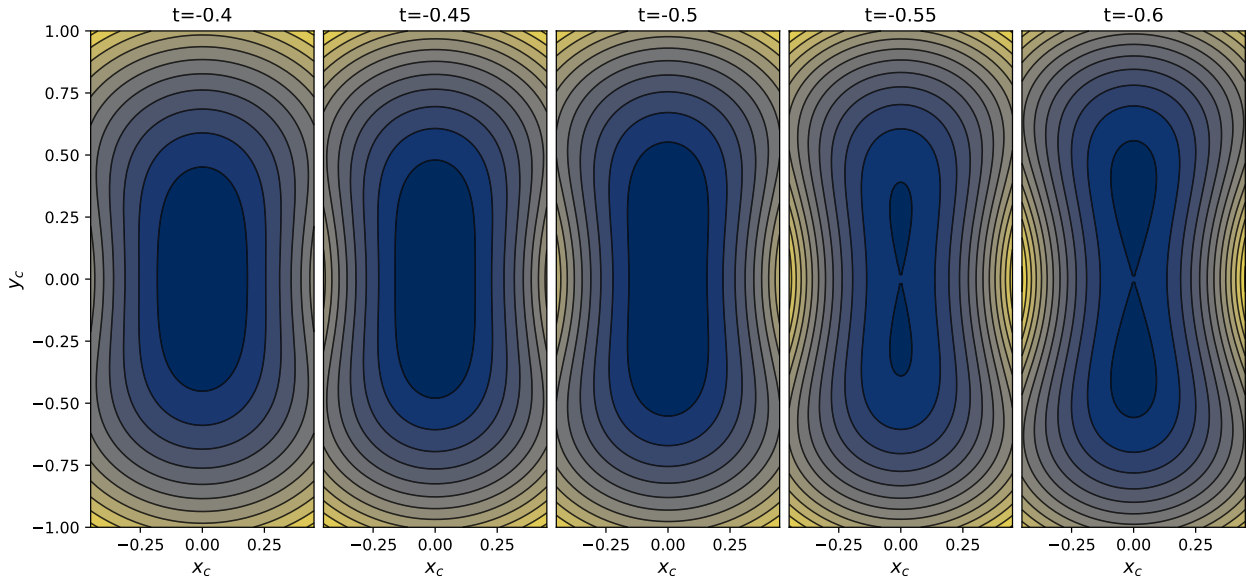


Figure 5.31 Analytical potential contours crossing integer resonance

mining the working point. At strengths of the nonlinear insert beyond the integer resonance, the origin of the system becomes an unstable fixed point. Two new stable fixed points are present above and below the origin. The result in the machine is the slow splitting of the beam into two stable "beamlets" about these new fixed points. By evaluating when the beam becomes fully split, an upper limit on the crossing of the integer resonance location can be set. Figure 5.31 shows the analytical potential contours for t-parameters crossing the vertical integer resonance. We see the new minima split and move vertically away from the origin.

Figure 5.32 shows the raw images in all of the cameras for a t-parameter just beyond the integer resonance condition. Here we see the characteristic distribution about the two new fixed points. Based on the calibration of the step size between t-parameter settings and the location of the splitting of the beam, we can attach a nominal t-parameter of $t = -0.525 \pm 0.0019$ to these profiles. The asymmetry in the beam distribution is another characteristic feature of operation at and beyond the integer resonance with the DN NIO system. Small deviations in the closed orbit means the beam distribution tends to oscillate between the two main potential wells over relatively slow timescales, yielding a visible "flickering" of

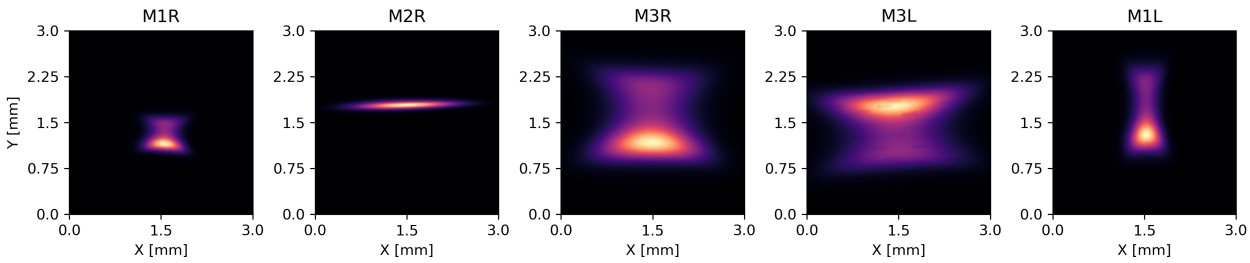


Figure 5.32 Example sychrotron radiation profiles for all cameras, t-parameter $t = -0.525$

the distribution during operation. By evaluating many profiles over time for the same t-parameter, a more even distribution can be obtained, and is the approach used moving forward.

In addition to evaluating the integer resonance, the synchrotron profiles could be used for fine tuning the closed orbit through the insert. Varying the closed orbit knobs to arrive at an equal distribution of beam in the top and bottom beamlets is a clear indicator of proper alignment about the center of the insert. Additionally, the characteristic lattice functions in the nonlinear insert could be adjusted. Figure 5.33 shows a comparison of the synchrotron profile of the beam for two different manual optimizations. The left plot is the nominal IOTA lattice with best manual optimization for beam centering in the nonlinear insert. Here many images at the same t-parameter are combined to smooth out this slow scale flickering mentioned above. The plot on the right shows the same set t-parameter optimized for best lifetime, here the beam is less centered in the DN potential. Less obvious from this plot is the fact that the t-parameter scaling suffers some drift, the location of the integer resonance based on the topology changes with respect to the setpoint t-parameter for different collections. The strong dependence of the tune on the t-parameter and the resolution and repeatability of our power supplies means the topology is a more accurate indicator of the resonance crossing than tune based methods in this regime. Additionally, the strong suppression of the dynamic aperture in these regions, means kicked beam tune

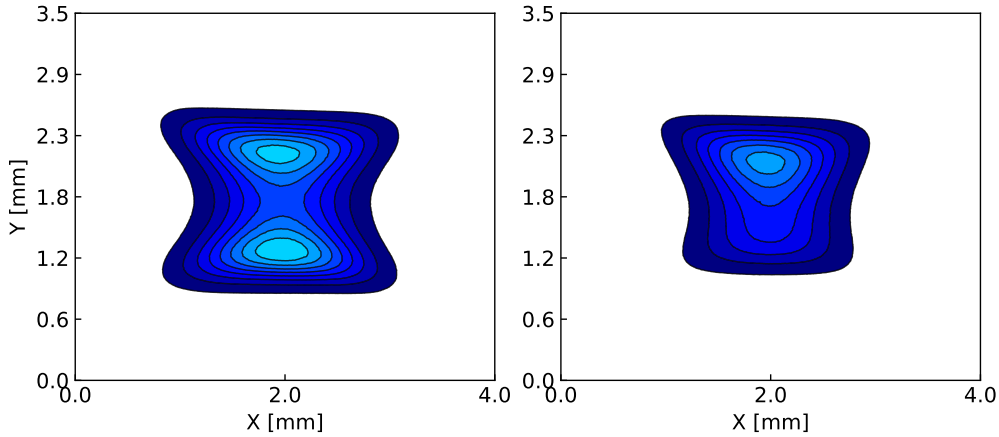


Figure 5.33 Sychrotron radiation profiles for the nominal lattice, and lattice optimized for lifetime, in camera M3R, t-parameter $t = -0.525$

measurements are unavailable.

Figure 5.34 shows the fitted lifetimes for the beam as the integer resonance is crossed for the well centered lattice configuration. The red circled points correspond to the synchtrotron profiles plotted in Figure 5.35, which were used to set the upper limit on the integer resonance crossing indicated in the green bar, around the nominal t-parameter of $t = -0.5$. Also included for reference are some t-parameters beyond the splitting point, where two separately stable orbiting beamlets propagate in the machine. The camera exposure had to be changed during the course of the measurements, as continuing beam loss reduced the signal. This means that only the relative intensity for a given exposure setting could be evaluated, and the absolute circulating current values were not available.

Figure 5.36 shows the fitted lifetimes for the beams at the integer resonance after manual optimization for best lifetime. We see some significant improvement for lifetimes up to and at the integer resonance limit. Once again, the red circled points correspond to beam profiles in Figure 5.37. Here a slightly broader range of nominal t-parameters is selected to show the full transition from the almost perfectly elliptical profile through to the widely separated beamlets. As the orbit centering is imperfect in this lattice we can see an asymmetric current distribution in the beamlets, as the lower beamlet in the last plot contains a larger fraction of the total circulating beam.

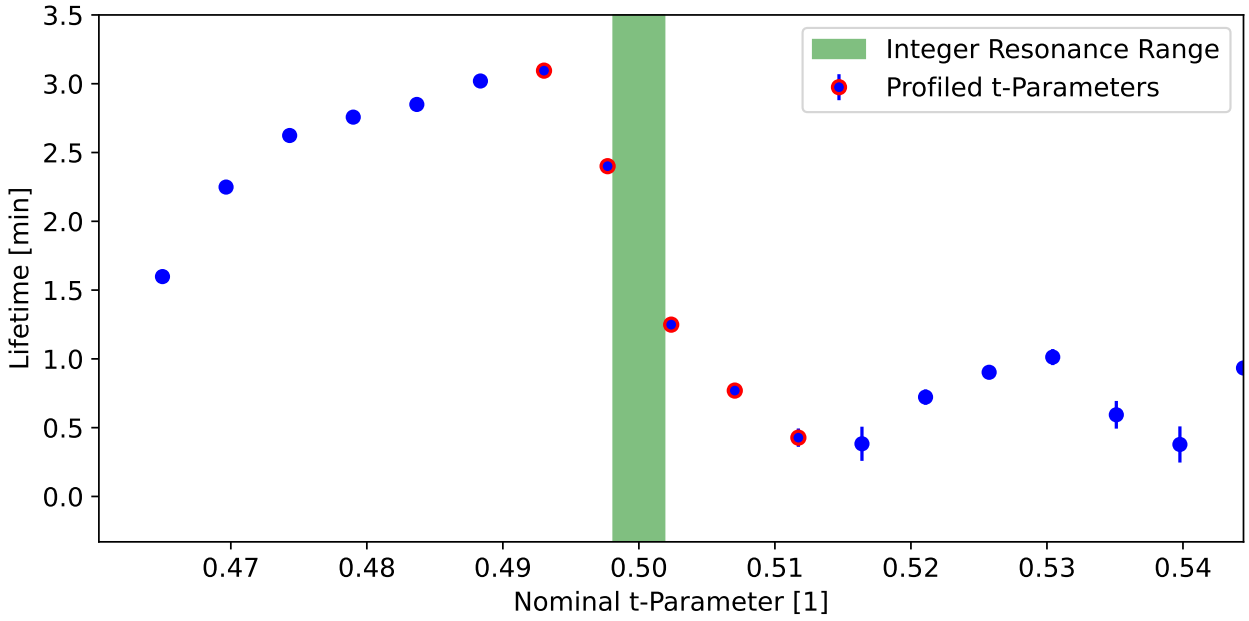


Figure 5.34 Fitted lifetimes from synchrtron radiation intensity for beam crossing integer resonance, in nominal IOTA lattice with manual centering in NIO potential.

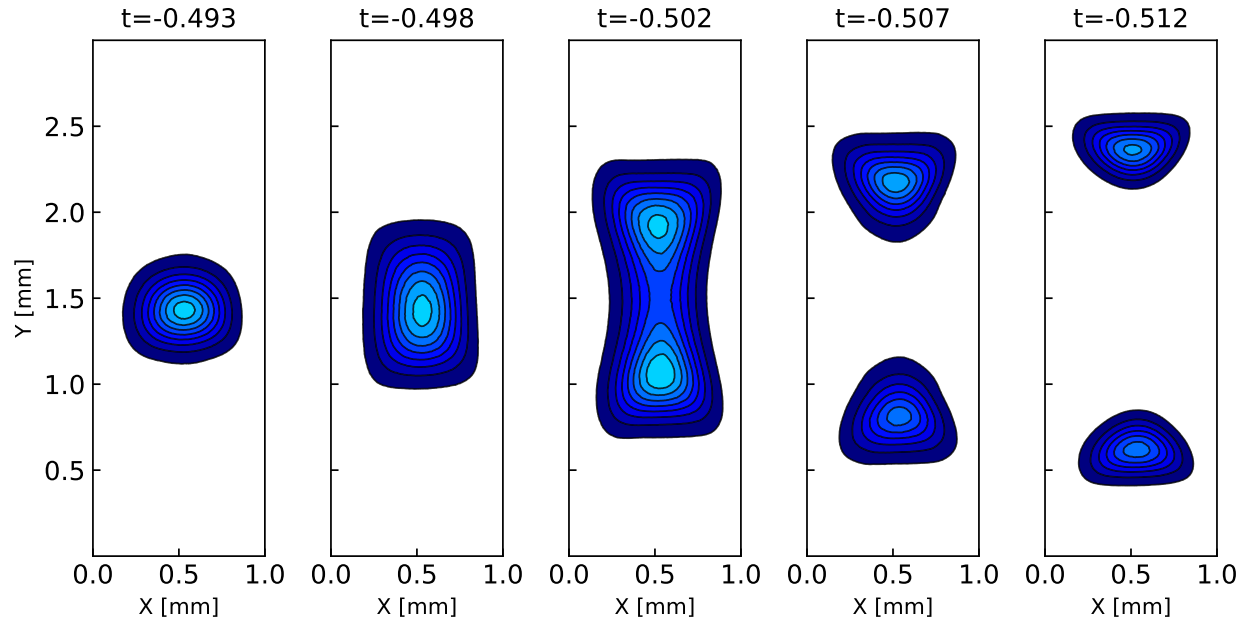


Figure 5.35 Synchrotron radiation profiles for crossing the integer resonance, the original stable fixed point splits to two new fixed points which move away from the origin with the t-strength.

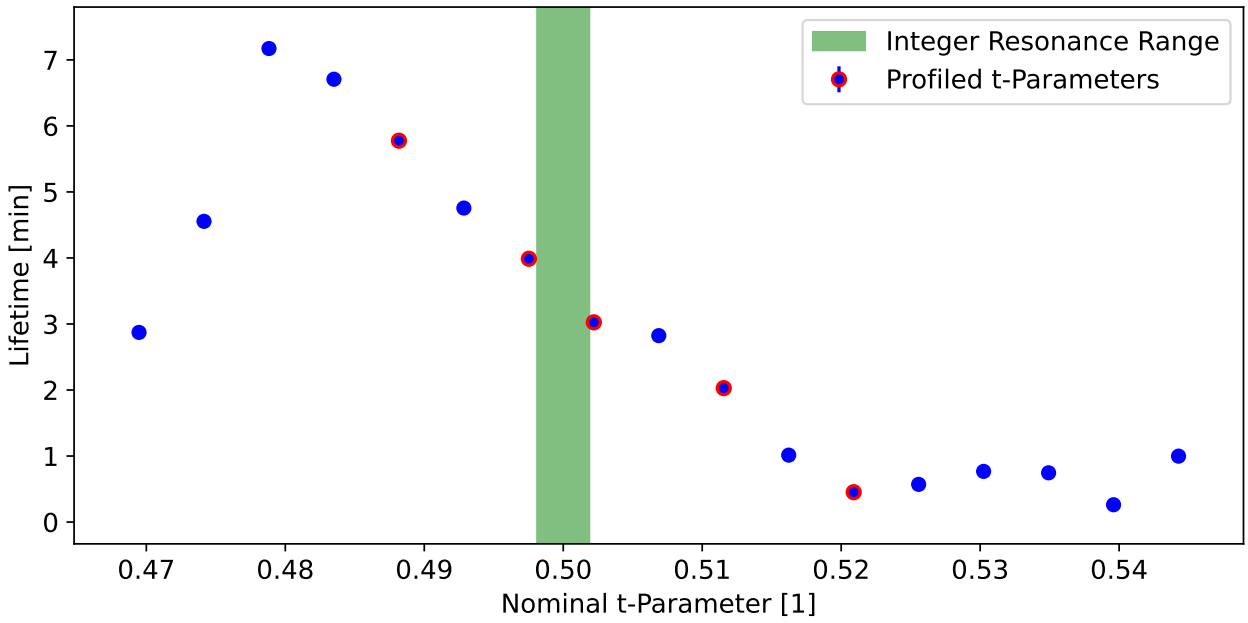


Figure 5.36 Fitted lifetimes from synchrtron radiation intensity for beam crossing integer resonance, in lattice optimized for best lifetimes near integer resonance.

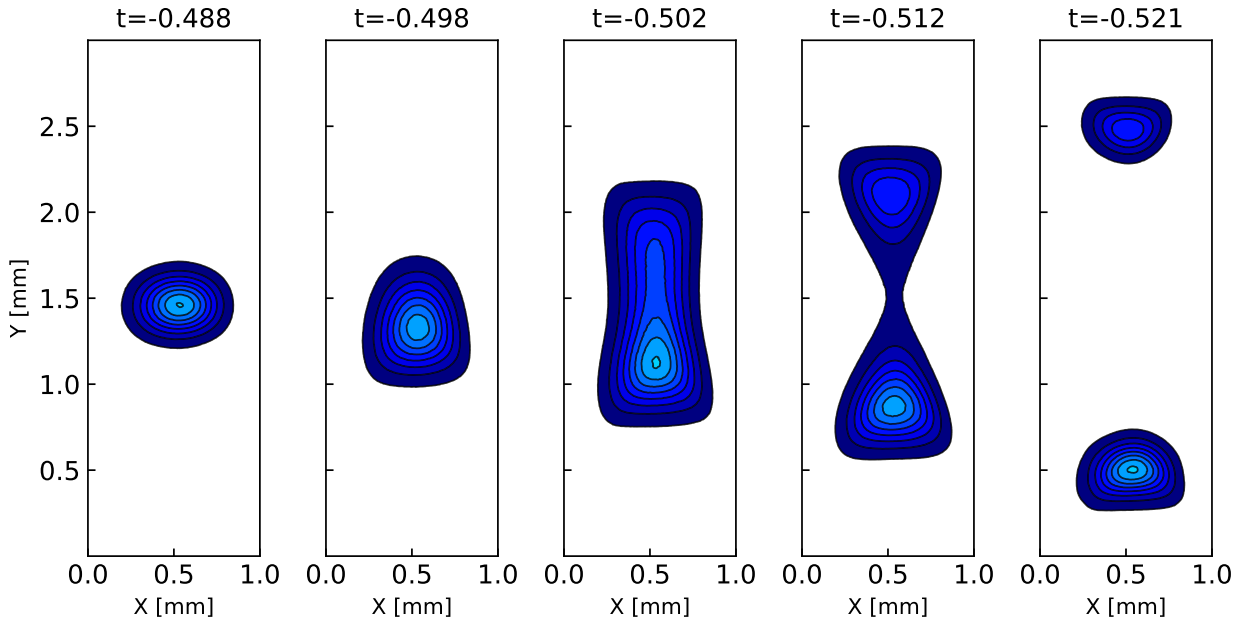


Figure 5.37 Synchrotron radiation profiles for crossing the integer resonance, the original stable fixed point splits to two new fixed points which move away from the origin with the t-strength.

The lifetime measurements on the order of minutes corresponds to millions of turns, and indicates asymptotic stability of particles at the integer resonance where the nonlinear focusing terms dominate.

# CHAPTER 6

## SUMMARY AND CONCLUSION

The following is a brief summary of my major developments in experimental beam dynamics studies in IOTA and contributions to a deeper understanding of nonlinear integrable optics for particle accelerators. The experimental measurements in IOTA provided substantial new data on the NIO system, and motivated an extensive set of supporting simulations for further understanding of the dynamics.

Kicked beam measurements of the low emittance electron beam allowed turn-by-turn reconstruction of the dynamics in the accelerator. Fast decoherence due to strong amplitude dependent detuning from the NIO system complicated measurements of relevant quantities and required extensive verification of analysis algorithms. Supporting tracking simulations further verified that measurements of the centroid of the realistic IOTA beam closely matched the action of a single particle with identical amplitudes, even with strong nonlinearites. Virtual BPM reconstruction was implemented for analyzing the phase space and calibrating the amplitude of individual kicks. Initially, direct verification of conservation of the analytically predicted invariant quantities was attempted. The current IOTA configuration demonstrated clear variance in this quantity, especially with regards to the second invariant of the NIO system. Further investigating the regions of best conservation yielded results which indicated insufficient sensitivity to definitively demonstrate this conservation. Supporting tracking simulations with nonlineaities of the form expected in the bare IOTA lattice were similarly insensitive to this exact conservation evaluation consistent with the measured quantities. Amplitude dependent detuning measurements showed a significant tune footprint and impacts of perturbative nonlinearities in the form resonant capture of fractions of the bunch were well measured. Initial deviations from the predicted tune footprint were remedied with simulations including the expected residual nonlinearites.

The transverse aperture of the system was measured using kicked beam losses. The bare lattice aperture showed significant effects from the sextupole configuration in the lattice, and

an effort to minimize this was undertaken. Evaluation of the aperture for different relative strengths of the integrable nonlinearites showed a slight reduction in aperture for a broad range of the strength, comparable to the aperture effects of the base sextupole configurations. For relative nonlinear strengths beyond two-thirds of the tune shift to the integer resonance, the aperture reduced significantly. Measurements of the aperture of the NIO system with various linear matching lattice perturbations demonstrated good robustness to a variety of knobs, indicating that the system is generally stable to typical lattice perturbations.

By increasing the relative strength of the integrable nonlinearities in the system, the expected shift in the working point to the vertical integer resonance was demonstrated. In this configuration, the unique nonlinear focusing dominates, and the circulating beam is not entirely lost. Nonlinear perturbations and imperfections in the implementation of the NIO potential means that the dynamic aperture shrinks substantially in this condition. However, the circulating beam within this aperture demonstrates measurable macroscopic lifetimes on the order of minutes. This corresponds to millions of turns and is indicative of asymptotic stability of particles within this aperture. This stability is only possible due to the nonlinear focusing from the NIO insert. Additionally, by further increasing the strength of the nonlinearites, the central fixed point on the closed orbit splits into two separate orbits which move vertically away from the original point. This was measured as two separate, stable "beamlets" which moved apart with increasing nonlinear insert strength. This effect is a unique characteristic of the NIO system studied and is direct support of reasonable matching to the NIO condition.

Overall, strong evidence of the unique dynamics of the NIO system was observed, though detuning, the topology of the phase space, and unique stability and behaviour beyond the integer resonance. The system proved to be reasonably robust and stable in operation, even with significant linear and nonlinear perturbations. The strong detuning and reasonable aperture of the NIO system are promising steps towards implementation in an operational user-focused accelerator. Importantly, the dominant shortcomings of the current configura-

tion in the form of strong sextupole perturbations were identified as a significant limiting factor on the NIO system, which will be leveraged in further experiments at IOTA.

# APPENDIX A

## COMMON LONGITUDINAL COORDINATE RELATIONSHIPS

We would like to briefly consider the exact relationships between the canonical longitudinal coordinates $p_t$ and $\delta$. Starting with the ImpactX definition of $p_t$ in eq. A.1 and the reference particles total energy $E_o$, we can rearrange to the total energy of the particle $E$ in eq. A.2.

$$p_t = \frac{E_o - E}{p_o c} \tag{A.1}$$

$$E = \sqrt{p_o^2 c^2 + (mc^2)^2} - p_t p_o c \tag{A.2}$$

We can now perform a similar sequence with the definition of $\delta$ in eq. A.3 to arrive a the total energy in eq. A.4.

$$\delta = \frac{p - p_o}{p_o} \tag{A.3}$$

$$E = \sqrt{p_o^2 c^2 (1 + \delta) + (mc^2)^2} \tag{A.4}$$

Setting these expressions equal to each other and squaring to remove the roots results in eq. A.5.

$$p_t^2 p_o^2 c^2 - 2 p_t p_o c E_o + p_o^2 c^2 + (mc^2)^2 = p_o^2 c^2 + p_o^2 c^2 (2\delta + \delta^2) + (mc^2)^2 \tag{A.5}$$

Subtracting like terms and dividing by $p_o^2 c^2$ yields eq. A.6.

$$p_t^2 + \frac{2 p_t E_o}{p_o c} = 2\delta + \delta^2 \tag{A.6}$$

We can now use the fact that the reference particle momentum is the definition of the trajectory, we can use the relationship in A.7 to arrive at eq. A.8.

$$\beta_o E_o = p_o c \tag{A.7}$$

$$p_t^2 - \frac{2p_t}{\beta_o} = 2\delta + \delta^2 \tag{A.8}$$

In the paraxial approximation, both $p_t$ and $\delta$ are small so $p_t^2 \ll p_t$ and $\delta^2 \ll \delta$ and the relationship in eq. A.9 holds.

$$p_t \approx -\beta_o \delta \tag{A.9}$$

For the exact relationship we can start with eq A.5 and divide by $p_o^2 c^2$ without subtracting all terms to arrive at eq. A.10.

$$p_t^2 - \frac{2p_t E_o}{p_o c} + 1 = (1+\delta)^2 \tag{A.10}$$

Substituting eq. A.7 and rearranging we arrive at eq. A.11, where the sign of the root can be determined from the initial sign of the $p_t$ term.

$$\delta = \pm\sqrt{p_t^2 - \frac{2p_t}{\beta_o} + 1} - 1 \tag{A.11}$$

The inverse transformation is can be obtained from eq. A.6 to arrive at eq. A.12. Once again, the sign of the root can be determined from the inital sign of $\delta$.

$$p_t = \pm\sqrt{\delta^2 + 2\delta + \frac{1}{\beta_o^2}} + \frac{1}{\beta_o} \tag{A.12}$$

# APPENDIX B

## SECOND GENERATION DANILOV-NAGAITSEV INSERT MAGNET

The second iteration of the DN integrable insert makes a few different design decisions from the first. The largest change is a reduction from 18 equally spaced lenses to 11 in an equi-phase spaced configuration. As discussed in 3.2 we see similar quality of conservation of the analytically predicted invariants in this configuration with fewer elements. In this configuration, the central elements are more closely packed, and the relative integrated strength of the elements becomes the same. Figure B.1 shows the integration of the nominal potential with the equi-phase elements.

The dense central packing requires differently shaped individual lenses, with shorter magnets in the center to minimize longitudinal cross-talk.

The other major change in the insert design is a signifcantly icreased physical aperture. There are two ways to accomplish this, the first is increasing the geometric DN c-parameter. This naturally increases the radius of the good field region, but also effectively reduces the nonlinearities the beam is sensitive to. In the case of the new insert, the c-parameter is increased to $c = 0.014\sqrt{\text{m}}$. The other adjustment is changing the contour in the magnetic potential used for the pole face. Contours further from the origin can be selected, which naturally increases the minimum aperture.

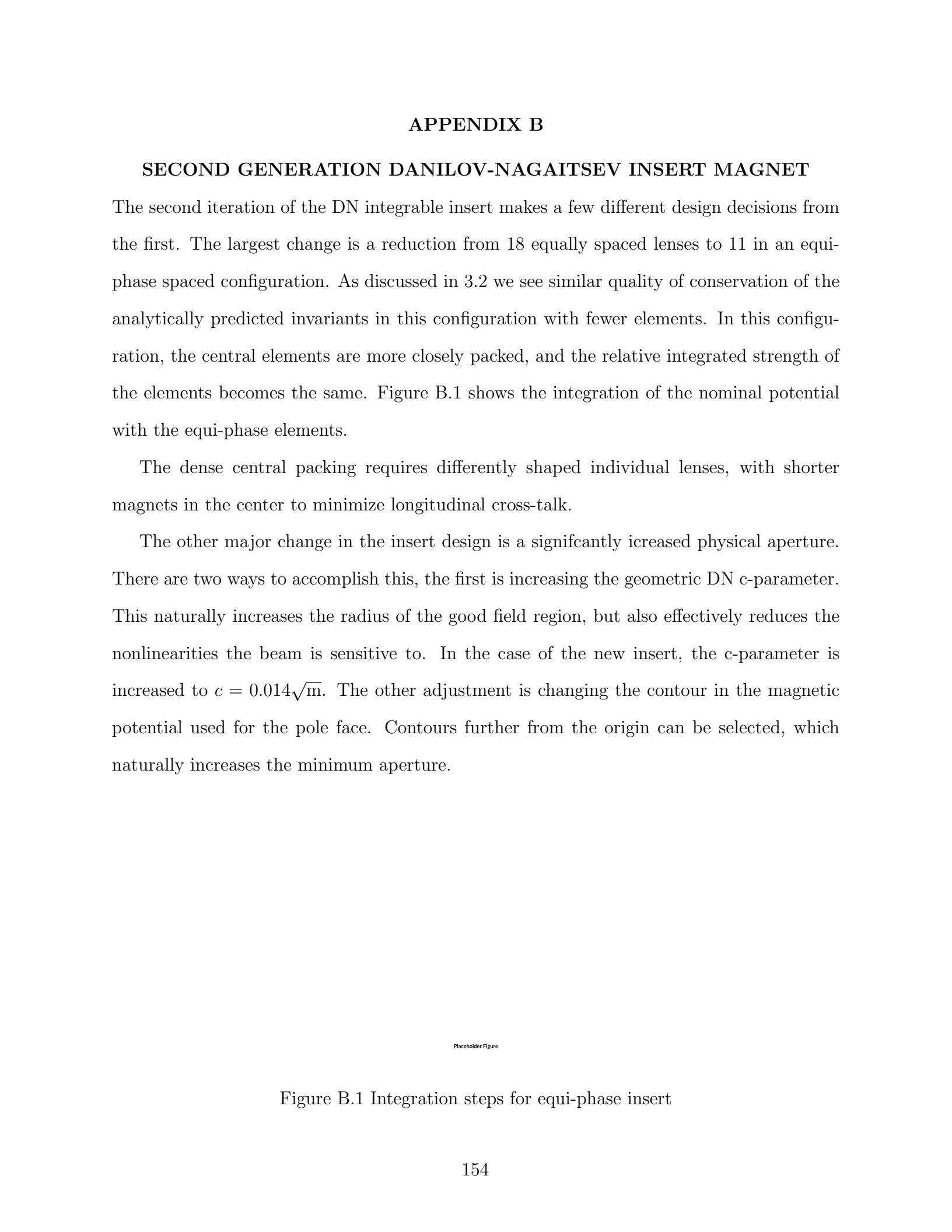


Figure B.1 Integration steps for equi-phase insert

# APPENDIX C

## OCTUPOLE MAGNETIC FIDUCIALIZATION

This covers the magnetic field measurments for fiducialization and centering of the octupole insert.

# APPENDIX D

## SEXTUPOLE ERROR IDENTIFICATION

This covers the beam and field based methods to evaluate the error in the sextupole magnets.

# BIBLIOGRAPHY


[1] P. Adamson et al. "The NuMI Neutrino Beam". In: *Nuclear Instruments and Methods in Physics Research Section A: Accelerators, Spectrometers, Detectors and Associated Equipment* 806 (Jan. 2016), pp. 279–306. ISSN: 01689002. DOI: 10.1016/j.nima.2015.08.063. arXiv: 1507.06690 [physics]. URL: http://arxiv.org/abs/1507.06690.

[2] Paul W. Allison, Joseph D. Sherman, and David B. Holtkamp. "An Emittance Scanner for Intense Low-Energy Ion Beams". In: *IEEE Transactions on Nuclear Science* 30.4 (Aug. 1983), pp. 2204–2206. ISSN: 1558-1578. DOI: 10.1109/TNS.1983.4332762. URL: https://ieeexplore.ieee.org/abstract/document/4332762.

[3] Luis W. Alvarez et al. "Berkeley Proton Linear Accelerator". In: *Review of Scientific Instruments* 26.2 (Feb. 1, 1955), pp. 111–133. ISSN: 0034-6748. DOI: 10.1063/1.1771253. URL: https://doi.org/10.1063/1.1771253.

[4] S. Antipov et al. "IOTA (Integrable Optics Test Accelerator): Facility and Experimental Beam Physics Program". In: *Journal of Instrumentation* 12.03 (Mar. 2017), T03002. ISSN: 1748-0221. DOI: 10.1088/1748-0221/12/03/T03002. URL: https://dx.doi.org/10.1088/1748-0221/12/03/T03002.

[5] Sergey A. Antipov et al. *Stripline Kicker for Integrable Optics Test Accelerator*. June 30, 2016. DOI: 10.48550/arXiv.1607.00023. arXiv: 1607.00023 [physics]. URL: http://arxiv.org/abs/1607.00023. Pre-published.

[6] R. Baartman. "Quadrupole Shapes". In: *Physical Review Special Topics - Accelerators and Beams* 15.7 (July 30, 2012), p. 074002. DOI: 10.1103/PhysRevSTAB.15.074002. URL: https://link.aps.org/doi/10.1103/PhysRevSTAB.15.074002.

[7] R Bartolini et al. "Algorithms for a Precise Determination of the Betatron Tune". In: (1996). URL: https://cds.cern.ch/record/309235.

[8] R Bartolini et al. "Tune Evaluation in Simulations and Experiments". In: *Part. Accel.* 52.3–4 (1996), pp. 147–177. URL: http://cds.cern.ch/record/292773.

[9] S. S. Baturin. "Hamiltonian Preserving Nonlinear Optics". In: *Physica D: Nonlinear Phenomena* 439 (Nov. 1, 2022), p. 133394. ISSN: 0167-2789. DOI: 10.1016/j.physd.2022.133394. URL: https://www.sciencedirect.com/science/article/pii/S0167278922001488.

[10] Richard A. Beth. "Complex Representation and Computation of Two-Dimensional Magnetic Fields". In: *Journal of Applied Physics* 37.7 (June 1, 1966), pp. 2568–2571. ISSN: 0021-8979. DOI: 10.1063/1.1782086. URL: https://doi.org/10.1063/1.1782086.

[11] I. Borchardt et al. “Calculation of Beam Envelopes in Storage Rings and Transport Systems in the Presence of Transverse Space Charge Effects and Coupling”. In: *Zeitschrift für Physik C Particles and Fields* 39.3 (July 1, 1988), pp. 339–349. ISSN: 1431-5858. DOI: 10.1007/BF01548283. URL: https://doi.org/10.1007/BF01548283.

[12] D Broemmelsiek et al. “Record High-Gradient SRF Beam Acceleration at Fermilab”. In: *New Journal of Physics* 20.11 (Nov. 2018), p. 113018. ISSN: 1367-2630. DOI: 10.1088/1367-2630/aaec57. URL: https://doi.org/10.1088/1367-2630/aaec57.

[13] D L Bruhwiler, J R Cary, and S Shasharina. “Symplectic Propagation of the Map, Tangent Map and Tangent Map Derivative through Quadrupole and Combined-Function Dipole Magnets without Truncation”. In: ().

[14] D D Caussyn et al. “Experimental Beam Dynamics at the Third Integer Resonance”. In: ().

[15] CERN OMC Team. *PyLHC*. CERN. URL: https://github.com/pylhc.

[16] M. Church, S. Nagaitsev, and P. Piot. “Plans for a 750 MeV Electron Beam Test Facility at Fermilab”. In: *2007 IEEE Particle Accelerator Conference (PAC)*. 2007 IEEE Particle Accelerator Conference (PAC). June 2007, pp. 2942–2944. DOI: 10.1109/PAC.2007.4440628. URL: https://ieeexplore.ieee.org/document/4440628.

[17] E. D Courant and H. S Snyder. “Theory of the Alternating-Gradient Synchrotron”. In: *Annals of Physics* 3.1 (Jan. 1, 1958), pp. 1–48. ISSN: 0003-4916. DOI: 10.1016/0003-4916(58)90012-5. URL: https://www.sciencedirect.com/science/article/pii/0003491658900125.

[18] Frederick Cropp et al. “FAST Low-Energy Beamline Studies: Toward High-Peak 5D Brightness Beams for FAST-GREENS”. in: *Instruments* 7.4 (Dec. 2023), p. 42. ISSN: 2410-390X. DOI: 10.3390/instruments7040042. URL: https://www.mdpi.com/2410-390X/7/4/42.

[19] V. Danilov and S. Nagaitsev. “Nonlinear Accelerator Lattices with One and Two Analytic Invariants”. In: *Physical Review Special Topics - Accelerators and Beams* 13.8 (Aug. 25, 2010), p. 084002. ISSN: 1098-4402. DOI: 10.1103/PhysRevSTAB.13.084002. URL: https://link.aps.org/doi/10.1103/PhysRevSTAB.13.084002.

[20] V.V. Danilov and E.A. Perevedentsev. “Two Examples of Integrable Systems with Round Colliding Beams”. In: *Proceedings of the 1997 Particle Accelerator Conference (Cat. No.97CH36167)*. Proceedings of the 1997 Particle Accelerator Conference (Cat. No.97CH36167). Vol. 2. May 1997, 1759–1761 vol.2. DOI: 10.1109/PAC.1997.750998. URL: https://ieeexplore.ieee.org/abstract/document/750998.

[21] Gaston Darboux. “Sur un Probléme de Mécanique”. In: *Archives Néerlandaises*

*des Sciences Exactes et Naturelles* 2.6 (1901), pp. 371–376. URL: https://www.biodiversitylibrary.org/item/157010#page/389/mode/1up.

[22] Laurent Deniau et al. *The MAD-X Program Users Reference Manual*. Version 5.08.01.

[23] Nathan Eddy et al. "Beam Instrumentation at the Fermilab IOTA Ring". In: *Proceedings of the 8th International Beam Instrumentation Conference*. International Beam Instrumentation Conference. Vol. IBIC2019. [object Object], 2019, 7 pages, 3.187 MB. ISBN: 978-3-95450-204-2. DOI: 10.18429/JACOW-IBIC2019-MOBO02. URL: http://jacow.org/ibic2019/doi/JACoW-IBIC2019-MOBO02.html.

[24] D. Edstrom et al. "IOTA Proton Injector Beamline Installation". In: *IOTA Proton Injector Beamline Installation**. IOTA Proton Injector Beamline Installation*. US DOE, May 5, 2023. DOI: 10.2172/1973433. URL: https://www.osti.gov/servlets/purl/1973433/.

[25] D. A. Edwards and L. C. Teng. "Parametrization of Linear Coupled Motion in Periodic Systems". In: *IEEE Transactions on Nuclear Science* 20.3 (June 1973), pp. 885–888. ISSN: 1558-1578. DOI: 10.1109/TNS.1973.4327279. URL: https://ieeexplore.ieee.org/document/4327279.

[26] Étienne Forest. "Geometric Integration for Particle Accelerators". In: *Journal of Physics A: Mathematical and General* 39.19 (May 12, 2006), pp. 5321–5377. ISSN: 0305-4470, 1361-6447. DOI: 10.1088/0305-4470/39/19/S03. URL: https://iopscience.iop.org/article/10.1088/0305-4470/39/19/S03.

[27] Étienne Forest and Janko Milutinović. "Leading Order Hard Edge Fringe Fields Effects Exact in $(1 + \delta)$ and Consistent with Maxwell's Equations for Rectilinear Magnets". In: *Nuclear Instruments and Methods in Physics Research Section A: Accelerators, Spectrometers, Detectors and Associated Equipment* 269.3 (June 20, 1988), pp. 474–482. ISSN: 0168-9002. DOI: 10.1016/0168-9002(88)90123-4. URL: https://www.sciencedirect.com/science/article/pii/0168900288901234.

[28] L. N. Hand and W. K. H. Panofsky. "Magnetic Quadrupole with Rectangular Aperture". In: *Review of Scientific Instruments* 30.10 (Oct. 1, 1959), pp. 927–930. ISSN: 0034-6748. DOI: 10.1063/1.1716386. URL: https://doi.org/10.1063/1.1716386.

[29] F.J. Harris. "On the Use of Windows for Harmonic Analysis with the Discrete Fourier Transform". In: *Proceedings of the IEEE* 66.1 (Jan. 1978), pp. 51–83. ISSN: 1558-2256. DOI: 10.1109/PROC.1978.10837. URL: https://ieeexplore.ieee.org/abstract/document/1455106.

[30] S. Henderson et al. "The Spallation Neutron Source Accelerator System Design". In: *Nuclear Instruments and Methods in Physics Research Section A: Accelerators, Spectrometers, Detectors and Associated Equipment* 763 (Nov. 2014), pp. 610–673.

ISSN: 01689002. DOI: 10.1016/j.nima.2014.03.067. URL: https://linkinghub.elsevier.com/retrieve/pii/S0168900214003817.

[31] Jarmo Hietarinta. "Direct Methods for the Search of the Second Invariant". In: *Physics Reports* 147.2 (Mar. 1, 1987), pp. 87–154. ISSN: 0370-1573. DOI: 10.1016/0370-1573(87)90089-5. URL: https://www.sciencedirect.com/science/article/pii/0370157387900895.

[32] Axel Huebl et al. "Next Generation Computational Tools for the Modeling and Design of Particle Accelerators at Exascale". In: *Proceedings of the 5th North American Particle Accelerator Conference* NAPAC2022 (2022), 5 pages, 0.729 MB. ISSN: 2673-7000. DOI: 10.18429/JACoW-NAPAC2022-TUYE2. arXiv: 2208.02382 [physics]. URL: http://arxiv.org/abs/2208.02382.

[33] Eric Jacobsen. "On Local Interpolation of DFT Outputs". In: (). URL: http://www.ericjacobsen.org/FTinterp.pdf.

[34] Jorge V. José and Eugene J. Saletan. *Classical Dynamics: A Contemporary Approach*. Cambridge University Press, Aug. 13, 1998. 702 pp. ISBN: 978-0-521-63636-0. Google Books: Eql9dRQDgvQC.

[35] Sergei Kladov et al. *Near-Infrared Noise in Intense Electron Bunches*. Feb. 10, 2025. DOI: 10.48550/arXiv.2412.13482. arXiv: 2412.13482 [physics]. URL: http://arxiv.org/abs/2412.13482. Pre-published.

[36] Glen R. Lambertson. "Charged Particle Extracting Magnet for an Accelerator". U.S. pat. 3323088A. Individual. May 30, 1967. URL: https://patents.google.com/patent/US3323088/en.

[37] A. Langner and R. Tomás. "Optics Measurement Algorithms and Error Analysis for the Proton Energy Frontier". In: *Physical Review Special Topics - Accelerators and Beams* 18.3 (Mar. 3, 2015), p. 031002. DOI: 10.1103/PhysRevSTAB.18.031002. URL: https://link.aps.org/doi/10.1103/PhysRevSTAB.18.031002.

[38] Jacques Laskar, Claude Froeschlé, and Alessandra Celletti. "The Measure of Chaos by the Numerical Analysis of the Fundamental Frequencies. Application to the Standard Mapping". In: *Physica D: Nonlinear Phenomena* 56.2 (May 1, 1992), pp. 253–269. ISSN: 0167-2789. DOI: 10.1016/0167-2789(92)90028-L. URL: https://www.sciencedirect.com/science/article/pii/016727899290028L.

[39] S. Y. Lee. *Accelerator Physics*. 4th ed. World Scientific Publishing Company, 2018. ISBN: 978-981-327-467-9.

[40] Edwin M McMillan. *Some Thoughts on Stability in Nonlinear Periodic Focusing Systems*. UCRL-17795. Lawrence Radiation Laboratory, Sept. 5, 1967.

[41] J D McNevin, R B Agustsson, and F H O'Shea. "Mechanical Design and Manufacturing of a Two Meter Precision Non-Linear Magnet System". In: North American Particle Accelerator Conference. 2016.

[42] Chad Mitchell. *Complex Representation of Potentials and Fields for the Nonlinear Magnetic Insert of the Integrable Optics Test Accelerator*. July 31, 2019. DOI: 10.48550/arXiv.1908.00036. arXiv: 1908.00036 [physics]. URL: http://arxiv.org/abs/1908.00036. Pre-published.

[43] Chad E. Mitchell, Robert D. Ryne, and Kilean Hwang. "Bifurcation Analysis of Nonlinear Hamiltonian Dynamics in the Fermilab Integrable Optics Test Accelerator". In: *Physical Review Accelerators and Beams* 23.6 (June 15, 2020), p. 064002. DOI: 10.1103/PhysRevAccelBeams.23.064002. URL: https://link.aps.org/doi/10.1103/PhysRevAccelBeams.23.064002.

[44] Jürgen Moser. "Is the Solar System Stable?" In: *The Mathematical Intelligencer* 1.2 (June 1, 1978), pp. 65–71. ISSN: 0343-6993. DOI: 10.1007/BF03023062. URL: https://doi.org/10.1007/BF03023062.

[45] Sergei Nagaitsev, A. Valishev, and V. Danilov. *Nonlinear Optics as a Path to High-Intensity Circular Machines*. July 23, 2012. DOI: 10.48550/arXiv.1207.5529. arXiv: 1207.5529 [physics]. URL: http://arxiv.org/abs/1207.5529. Pre-published.

[46] Sergei Nagaitsev and Timofey Zolkin. "Betatron Frequency and the Poincar\'e Rotation Number". In: *Physical Review Accelerators and Beams* 23.5 (May 8, 2020), p. 054001. DOI: 10.1103/PhysRevAccelBeams.23.054001. URL: https://link.aps.org/doi/10.1103/PhysRevAccelBeams.23.054001.

[47] Matthew Newville et al. *LMFIT: Non-Linear Least-Squares Minimization and Curve-Fitting for Python*. Zenodo, July 19, 2025. DOI: 10.5281/zenodo.16175987. URL: https://zenodo.org/records/16175987.

[48] F H O'Shea et al. "Measurement of Non-Linear Insert Magnets". In: Particle Accelerator Conference. Pasadena, CA, 2013.

[49] F H O'Shea et al. "Non-Linear Inserts for the IOTA Ring". In: (2017).

[50] Finn O'Shea et al. "Non-Linear Magnetic Inserts for the Integrable Optics Test Accelerator". In: *Proceedings of the 6th Int. Particle Accelerator Conf.* IPAC2015 (2015), 4 pages, 0.587 MB. DOI: 10.18429/JACOW-IPAC2015-MOPMN010. URL: http://jacow.org/ipac2015/doi/JACoW-IPAC2015-MOPMN010.html.

[51] P. N. Ostroumov, V. N. Aseev, and A. A. Kolomiets. "Application of a New Procedure for Design of 325 MHz RFQ". in: *Journal of Instrumentation* 1.04 (Apr. 2006), P04002. ISSN: 1748-0221. DOI: 10.1088/1748-0221/1/04/P04002. URL: https://dx.doi.

org/10.1088/1748-0221/1/04/P04002.

[52] Andreas Reiter, Rahul Singh, and Oleksandr Chorniy. "Statistical Treatment of Beam Position Monitor Data". In: *Nuclear Instruments and Methods in Physics Research Section A: Accelerators, Spectrometers, Detectors and Associated Equipment* 890 (May 2018), pp. 18–27. ISSN: 01689002. DOI: 10.1016/j.nima.2018.02.046. arXiv: 1609.01332 [physics]. URL: http://arxiv.org/abs/1609.01332.

[53] Alexander Romanov et al. "Lattice Correction Modeling for Fermilab IOTA Ring". In: *Proceedings of the 5th Int. Particle Accelerator Conf.* IPAC2014 (2014), 3 pages, 0.447 MB. DOI: 10.18429/JACOW-IPAC2014-TUPRO058. URL: http://jacow.org/IPAC2014/doi/JACoW-IPAC2014-TUPRO058.html.

[54] H.B. Rookhuizen et al. "Magnetic Devices of the Amsterdam Pulse Stretcher Ring AmPS". in: *Conference Record of the 1991 IEEE Particle Accelerator Conference*. Conference Record of the 1991 IEEE Particle Accelerator Conference. San Francisco, CA, USA: IEEE, 1991, pp. 2366–2368. ISBN: 978-0-7803-0135-1. DOI: 10.1109/PAC.1991.164968. URL: http://ieeexplore.ieee.org/document/164968/.

[55] R Roussel et al. "Xopt: A Simplified Framework for Optimization of Accelerator Problems Using Advanced Algorithms". In: ().

[56] Yu M Shatunov et al. "Project of a New Electron-Positron Collider VEPP-2000". In: ().

[57] Giulio Stancari et al. "Undulator Radiation of Single Electrons: Coherence Length and Quantum-Optical Properties". In: *JACoW* IPAC2024.FERMILAB-CONF-24-0228-AD (July 1, 2024). DOI: 10.18429/JACoW-IPAC2024-MOPG06. URL: https://www.osti.gov/biblio/2446917.

[58] Wai-Ming Tam. "Characterization of the Proton Ion Source Beam for the High Intensity Neutrino Source at Fermilab". PhD thesis. Jan. 1, 2010. URL: https://ui.adsabs.harvard.edu/abs/2010PhDT.....14T.

[59] Marion Vanwelde et al. *Review of Coupled Betatron Motion Parametrizations and Applications to Strongly Coupled Lattices*. Oct. 31, 2022. DOI: 10.48550/arXiv.2210.11866. arXiv: 2210.11866 [physics]. URL: http://arxiv.org/abs/2210.11866. Pre-published.

[60] Stephen Webb et al. *Suppressing Transverse Beam Halo with Nonlinear Magnetic Fields*. FERMILAB-CONF-13-738-AD. Fermi National Accelerator Laboratory (FNAL), Batavia, IL (United States), June 1, 2013. URL: https://www.osti.gov/biblio/1845710.

[61] Stephen D. Webb et al. *Chromatic and Dispersive Effects in Nonlinear Integrable Op-*

*tics*. May 18, 2015. DOI: 10.48550/arXiv.1504.05981. arXiv: 1504.05981 [nlin, physics:physics]. URL: http://arxiv.org/abs/1504.05981. Pre-published.

[62] R C Webber and G Apollinari. "Overview of the High Intensity Neutrino Source Linac R&D Program at Fermilab". In: ().

[63] E. T. Whittaker and G. Robinson. *The Calculus Of Observations*. Blackie and Son Limited, 1924. 416 pp. URL: http://archive.org/details/calculusofobserv031400mbp.

[64] Andrzej Wolski. *Beam Dynamics In High Energy Particle Accelerators*. World Scientific, Jan. 21, 2014. 606 pp. ISBN: 978-1-78326-279-3. Google Books: 8c63CgAAQBAJ.

[65] Haruo Yoshida. "Construction of Higher Order Symplectic Integrators". In: *Physics Letters A* 150.5 (Nov. 12, 1990), pp. 262–268. ISSN: 0375-9601. DOI: 10.1016/0375-9601(90)90092-3. URL: https://www.sciencedirect.com/science/article/pii/0375960190900923.

[66] P. Zisopoulos, Y. Papaphilippou, and J. Laskar. "Refined Betatron Tune Measurements by Mixing Beam Position Data". In: *Physical Review Accelerators and Beams* 22.7 (July 8, 2019), p. 071002. ISSN: 2469-9888. DOI: 10.1103/PhysRevAccelBeams.22.071002. URL: https://link.aps.org/doi/10.1103/PhysRevAccelBeams.22.071002.

[67] Panos Zisopoulos. *PZiso/PyNAFF*. June 30, 2023. URL: https://github.com/PZiso/PyNAFF.

[68] T. Zolkin. "Sector Magnets or Transverse Electromagnetic Fields in Cylindrical Coordinates". In: *Physical Review Accelerators and Beams* 20.4 (2017). DOI: 10.1103/PhysRevAccelBeams.20.043501.